Study of Ion Beam Interaction with Materials and Nanostructure Fabrication

Submitted in partial fulfillment of the requirements

of the degree of

Doctor of Philosophy

of the
Indian Institute of Technology Bombay, India
and
Monash University, Australia

by

Bhaveshkumar Kamaliya

Supervisors:

Mohammed Aslam (IIT Bombay)

Rakesh G. Mote (IIT Bombay)

Jing Fu (Monash University)

The course of study for this award was developed jointly by
Monash University, Australia and the Indian Institute of Technology Bombay, India
and was given academic recognition by each of them.
The programme was administrated by The IITB-Monash Research Academy

(2021)

In memory of my father

&

To my mother

With love and eternal gratitude

Copyright Notice

© Bhaveshkumar Kamaliya (*2021*).

Notice 1

Under the Copyright Act 1968, this thesis must be used only under the normal conditions of scholarly fair dealing. No results or conclusions should be extracted from it, nor should it be copied or closely paraphrased in whole or in part without the written consent of the author. Proper written acknowledgement should be made for any assistance obtained from this thesis.

Notice 2

I certify that I have made all reasonable efforts to secure copyright permissions for third-party content included in this thesis and have not knowingly added copyright content to my work without the owner's permission.

Declaration

I declare that this written submission represents my ideas in my own words and where other's ideas or words have been included, I have adequately cited and referenced the original sources. I also declare that I have adhered to all principles of academic honesty and integrity and have not misrepresented or fabricated or falsified any idea/data/fact/source in my submission. I understand that any violation of the above will be cause for disciplinary action by the Institute and can also evoke penal action from the sources which have thus not been properly cited or from whom proper permission has not been taken when needed.

Bhaveshkumar Kamaliya

11th June 2021

Table of Contents

List of Figures **ix**

List of Tables **xvii**

List of Symbols and Abbreviations **xix**

Abstract **xxv**

Chapter 1 Introduction **1**

1.1 Background 1

1.2 Motivation 1

1.3 Objectives 7

1.4 Organization of the report 7

Chapter 2 Literature Review **9**

2.1 Focused ion beam 9

2.1.1 FIB: primary functions and important parameters 10

2.1.2 FIB: applications and capabilities 14

2.2 Self-organized nanostructures by ion beam irradiation 15

2.2.1 Broad ion beam induced nanostructures 16

2.2.2 Focused ion beam induced nanostructures 20

2.2.2.1 Nanoripples/nanowires 21

2.2.2.2 Nanodots 26

2.2.2.3 Nanoholes 28

2.2.3 Molecular dynamics (MD) simulations for self-organization 30

2.3 Summary 32

Chapter 3 Improved Enhancement Factor for SERS using Broad Ion Beam Induced Self-Organized Gold Nanocones **33**

3.1 Introduction 33

3.2 Experimental details 36

3.3 Results and discussion 38

3.3.1 Morphology investigations via atomic force microscopy (AFM) 38

3.3.2 Characterizations via scanning electron microscopy (SEM) 41

3.3.3 Optical reflectance by UV-Visible spectroscopy 43

3.3.4 Optical simulations for a hybrid tri-layered system for improved SERS response using gold nanocones 44

3.3.4.1 FDTD simulations setup: design and graphene modelling 45

3.3.4.2 Improved enhancement factor (EF) for SERS 48

3.3.4.3 Effect of nanohole and nanocone-tip radius on EF 51

3.3.4.4 Comparison of other dielectric spacing materials with graphene 52

3.4 Summary 54

Chapter 4 Enhanced Light Trapping by Focused Ion Beam (FIB) Induced Self-Organized Nanoripples on Germanium (100) Surface 57

4.1 Introduction 57

4.2 Experimental details 60

4.3 Results and discussion 62

4.3.1 SEM analysis 62

4.3.2 Measurement of optical absorption by nanoripples 66

4.3.3 3D topography generating and porosity calculations 68

4.3.4 Simulation of optical absorption by nanoripples 69

4.3.5 Theoretical absorption calculations using porosity analysis 70

4.3.6 The effect of incidence angle and nanorippled layer thickness 75

4.3.7 Field distribution in the nanostructures using FDTD simulations 78

4.4 Summary 81

Chapter 5 Tailoring Surface Self-Organization for Nanoscale Polygonal Morphology on Germanium 83

5.1 Introduction 84

5.2 Experimental details 88

5.3 Results and discussion 89

5.3.1 Characterization of morphological evolution using SEM and AFM 91

5.3.2 Nanostructures with complex morphologies by varying parameters 99

5.3.2.1 Zigzag nanostructures by single-pass scan 100

5.3.2.2 Circularly concentric zigzag nanostructures 102

5.3.2.3 Corrugated, nano-mushrooms and nanohole-needle shaped structures 103

5.3.3 Investigation on the mechanism of self-organization 104
5.3.3.1 Characterizations via transmission electron microscopy (TEM) 104
5.3.3.2 Characterizations via Raman spectroscopy 111
5.3.4 Optical absorption 114
5.4 Summary 116
Chapter 6 Focused Ion Beam Induced Self-Organization: Investigations by Molecular Dynamics Simulations 117
6.1 Introduction 117
6.2 Molecular dynamics (MD) simulations 119
6.3 Results and discussion 123
6.3.1 Temperature evolution 123
6.3.2 Crystallinity changes 127
6.3.3 Demonstrating FIB induced self-organization 130
6.3.4 Proposed mechanism of polygon formation via viscous-fingering 132
6.4 Summary 134
Chapter 7 Conclusions and Outlook 137
7.1 Conclusions 137
7.2 Directions for future research and developments 140
References 143
Publications 157
Acknowledgements 159

List of Figures

Figure 1.1 (a) Macro-scaled ripple patterns on the sand dune, (b) micrograph of leaf-venation in *Viburnum mole* plant leaf [7], (c) sub-micron size ripples in glass substrate [8], and (d) TEM cross-section image of ripples on the Si surface. The arrow shows the ion beam incidence direction [9]. 2

Figure 1.2 Micrographs of self-organized nanostructures formed by ion beam irradiation. (a) Nanoripples on strontium titanate [10], (b) transparent aluminium nanowires [11], (c) silicon nanodots [12] and (d) gold nanowires [13]. 3

Figure 1.3 Nanofabrication by focused ion beam. (a) FIB-CVD schematic and (b) the SEM image of metal (Pt) deposition as well as material removal using FIB milling. "IIT" is produced on the silicon substrate with deposition of Pt and by removing Si material using the FIB milling process. 5

Figure 1.4 Schematic of FIB milling process via pixel scanning. 5

Figure 2.1 (a) FIB Schematic, (b) Dual-beam FIB/SEM system. 10

Figure 2.2 Basic functions FIB a) milling, b) deposition, c) implantation and d) imaging [30]. 11

Figure 2.3 Illustration of beam overlap with different pixel sizes. The pixel size is lesser than the beam size for positive beam overlap, whereas it is greater than the beam size for negative beam overlap. 14

Figure 2.4 Examples of fabricating different nanostructures by FIB. (a) Nanoholes array milled through SOI wafer (Silicon on Insulator wafer) by FIB milling [35], (b) nano-rotor (Complex 3D structure) by FIB–CVD method [36] and (c) self-organized nanoripples by ion beam bombardment [31]. 15

Figure 2.5 Schematic diagrams to understand surface imbalance during ion beam erosion of the surfaces: (a) the surface minima erodes faster than, (b) the surface maxima because the energy has to travel fewer distances (solid lines) to sputter nearby atoms than the local maxima. (See points A and A’) [9,41]. (c) The process of pattern formation [42]. 16

Figure 2.6 Broad ion beam induced nanostructures on surfaces. (a) transparent aluminium nanowires [11], (b) silicon nanodots [12] and (c) gold nanowires [13]...................19

Figure 2.7 Nanoripples on $LaAlO_3$ (100) surface, $SrTiO_3$ (100), and Al_2O_3 (0001) induced by 30 *keV* Ga^+ focused ion beam with ion flux of 1.9×10^{15} *ions/cm²s* [40]. 21

Figure 2.8 (a) FIB and (b) AFM micrographs of the self-organized ripples created by FIB with ion dose 1.3×10^{17} *ions/cm²*, incident angle of 55° and energy 50 *keV*. The amplitude of nanoripples is 10 *nm* [46] 22

Figure 2.9 FIB induced nanoripples on germanium surface. SEM images showing that the ripples tend to orient towards the fast scan direction, as indicated by red arrows [49]. 25

Figure 2.10 SEM images of FIB induced Ga droplets on the surface of GaAs at different incident angles of the ion beam [50]. Droplets over the edge and trench of the scanned region are shown with varied incident angles: (a) 0°, (b) 17°, (c) 35°, (d) 50°. Corresponding SEM images inside a trench are shown in (e)-(h). (i) The diameter of nanodroplets with the function of the incident angle of the ion beam. The scale bar is 1 μm. 26

Figure 2.11 FIB induced nano and micro dots. (a) Indium nanodots on InP (100) surface [54] and (b) nanodots on beryllium surface [55]..27

Figure 2.12 SEM images of nanoholes induced by (a) FIB irradiation and (b) broad ion beam irradiation [56]. Cross-sectional TEM images of nanoholes induced by (c) FIB irradiation and (d) broad ion beam irradiation..29

Figure 2.13 The screenshot of the simulation box, initially wavelength was 50 *nm* (a) before impact and (b) after the impact of 1000 ions. (c) cross-section of grown ripple after 1000 ion dose (the solid line indicates the initial state of ripple) [58]. ..30

Figure 3.1 Schematic of the IBS experiment. Sample (Au-on-quartz or silicon wafer) on a rotating sample holder under ion beam irradiation. 37

Figure 3.2 AFM images for gold nanostructures. (a) The bare gold surface, (b) obtained nanoripples without sample rotation during IBS, and (c) obtained nanocones with sample rotation during IBS. (d & e) shows the three-dimensional representation of (b & c). (f & g) 3D representation of nanocones acquired via AFM from different angles.. 39

Figure 3.3 AFM images for silicon nanostructures. (a) The bare silicon surface, (b) obtained densely distributed nanocones without sample rotation during IBS, and (c) obtained sparsely distributed nanocones with sample rotation during IBS. (d) & (e) represents the three-dimensional views for (b) & (c), respectively. (f & g) are high-resolution images for obtained nanocones in (c).. 40

Figure 3.4 SEM images of gold and silicone surfaces. (a & c) bare surfaces and (b & d) nanostructures formed with sample rotation during IBS. 42

Figure 3.5 UV-vis reflection spectra of nanocones and bare surfaces: (a) for gold surface and (b) for silicon surface. 43

Figure 3.6 Design of proposed tri-layered system of gold-nanocone/graphene/gold-nanohole for SERS device; (b) different geometrical positions of a nanocone tip with respect to the nanoholes considered for FDTD simulations; (c) FDTD simulation setup when the nanocone is at the nanoholes edge. Nanocone is set with height 90 *nm*, tip radius 20 *nm*, base radius 150 *nm* and cone angle 40°................ 47

Figure 3.7 (a) Enhancement factor $(|E|/|E|)^4$ at *xz*-plane, *yz*-plane and *xy*-plane for different geometrical positions of the nanocone-tip with respect to the nanohole. Dashed white lines indicate geometrical shapes and interfaces between the layers. *xz* - and *yz* - planes: graphene layer from $z = -1$ to 0 *nm*, gold nanohole layer is from $z = 0$ to 10 *nm*. 49

Figure 3.8 Enhancement factor versus the number of graphene layers as a spacer. 50

Figure 3.9 Change in EF with an increase in the nanohole radius at a constant nanocone-tip radius of 20 *nm*.. 51

Figure 3.10 Change in EF with an increase in the nanocone-tip radius at a constant nanoholes radius of 20 *nm*... 52

Figure 3.11 Enhancement factor versus dielectric materials. 53

Figure 4.1 Schematic of FIB processing. (a) The scanning at 90° angle with the surface and the arrow showing left to right scanning direction, (b, c & d) raster scanning strategies with the pixel method for 0%, –50% & +50% beam overlap (BO). 61

Figure 4.2 SEM images of nanoripples fabricated at fixed dose [$\sim 5 \times 10^{17}$ *ion/cm*^{2}] and different beam overlaps (a) 0%, (b) −25%, (c) −50%, (d) −100%, (e) −150%, (f) −200%, and (g) −250%. Inset images represent FFT for corresponding SEM image. 63

Figure 4.3 (a) Cross-sectional SEM image of nanoripples for beam overlap −250% and (b) 3D nanorippled surface generated from SEM image, (c) tilted SEM image from the cross-section for −250% beam overlap. 65

Figure 4.4 (a) Absorption spectra of germanium surface with nanoripples: experimental (solid line), simulated by FDTD method (dashed line) and porosity based theoretical prediction (dotted line); (b) absorption spectra of bare germanium surface: experimental (solid line), simulated by FDTD method (dashed line).......................67

Figure 4.5 Illustration of the 3D surface (created from SEM image). As indicated by dotted lines, the thickness of the nanorippled region is divided into steps of dz = 5 nm. 68

Figure 4.6 Set-up of FDTD simulations for nanoripples. 70

Figure 4.7 Calculated refractive index and porosity vs. the height of nanoripples, inset shows multiple light reflections through nanoripples. 71

Figure 4.8 Schematic of propagation amplitude of EM wave through multilayer (N layers) having complex effective refractive index n. The number of interfaces is $N+1$. In subscripts, I, R and T represent incident, reflected and transmitted waves for corresponding interfaces. For each layer, the thickness is taken as $dz = 5\ nm$ and for substrate $dz = 500\ \mu m$. 73

Figure 4.9 (a) Absorption spectra for germanium nanoripples with the angular incidence of light. The plot in (b) shows the variation in absorptance with the angle of incidence for 900 nm wavelength..76

Figure 4.10 Simulated absorptance spectra for four different thicknesses (250, 290 (original), 350 and 400 *nm*) of nanorippled germanium layer on bulk Ge substrate; and simulated absorptance spectra for the bare Ge wafer. 78

Figure 4.11 Two-dimensional (2D) electric field intensity ($|E|^2$) distribution at wavelength (a) 350 *nm*, (b) 500 *nm* and (c) 900 *nm* for nanoripples across planes *xz*-plane ($y = 0$), *yz*-plane ($x = 0$) and *xy*-plane (1 *nm* above nanoripples). The dashed white line indicates a germanium surface, and the colour-bar shows electric field intensity ($|E|^2$). 79

Figure 4.12 Light absorption per unit volume for nanoripples (left column) and bare germanium surface (right column) for incident wavelength (a) 350 *nm*, (b) 500 *nm* and (c) 900 *nm* across *xz*-plane ($y = 0$). The dashed white line indicates a germanium surface profile, and the colour-bar shows absorption density in *watt/µm*^{3}. 80

Figure 5.1 Overview with the cross-sectional schematic for the phenomenon to manipulate the morphology of nanoholes: (a) conventional milling dominant FIB machining and (b) self-organization driven nanofabrication. 91

Figure 5.2 Schematic for morphology evolution, scanning strategies and SEM images. 3D representation for morphology evolution of nanoholes from circular (a) to polygonal (b). Inset images in (a & b) are cross-sectional views for 3D schematics. Scanning grids for (c) square, (d) triangle, and (e) hexagon geometries. The corresponding SEM images for the transition from (*i*) circular nanoholes to (*ii*) polygonal nanoholes such as (f) square, (g) triangular, and (h) hexagonal nanoholes with an increase in dwell time from 0.1 *ms* to 1.8 *ms* on 10-pass FIB scan. The scale bar represents 200 *nm*. 92

Figure 5.3 Scanning grids used in the stream files for (a) pentagon, and (b) octagon shaped nanostructures with corresponding SEM images (c) pentagon, and (d) octagon nanoholes, respectively. The orange arrow shows a raster scanning direction. Blue dotted lines are for the guide representing peripheral pixels. (e) Tilted image for hexagonal nanoholes at 20° angle (inset is at 40° angle). The scale bars represent 200 *nm*. 95

Figure 5.4 Evolution of hexagonal nanostructures with an increase in dwell time and dose. The scale bar represents 200 *nm*. 96

Figure 5.5 (a) Evolution of nanoholes with increasing beam overlaps (BO). (b) The circularity of nanoholes for the square grid with an increase in the beam overlap...97

Figure 5.6. (a) Evolution of nanoholes with increasing dwell time. (b) Protrusion of the self-organized nanostructures represented by the average height as a function of dwell time from the line profile of the AFM image in (d). (d) 3D representation of the AFM image acquired of the patterned region. 99

Figure 5.7 Single-pass scan for zigzag nanostructures, (a) serpentine scan and (b) raster scan. Red arrows represent the direction of serpentine and raster scans. 100

Figure 5.8 Effect of a number of passes for a fixed dose of 4.03×10^{14} *ions/cm*^{2}. The left side of each image represents single-pass serpentine scan, and the right side of each image represents a 10-pass serpentine scan. 101

Figure 5.9 Effect of a number of passes for a fixed dose of 1.01×10^{16} *ions/cm*^{2}. The left side of each image represents single-pass serpentine scan, and the right side of each image represents a 10-pass serpentine scan. 101

Figure 5.10 Evolution of hexagon-like and V-shaped nanostructures with dose (red lines represent geometric shapes), (a) low dose of 4.03×10^{14} *ions/cm*^{2}, (b) intermediate dose of 1.61×10^{15} *ions/cm*^{2}, and (c) high dose of 1.01×10^{16} *ions/cm*^{2}................102

Figure 5.11 Complex-shaped self-organization (a) Corrugated, (b) Nano-mushrooms (inset, tilted at 30°), and (c) dual-nanostructures resembling nano-holes connected with nano-needles (inset, tilted at 30°). 103

Figure 5.12 (a) SEM image of a patterned array of square nanostructures where the TEM lamella was prepared, (b) SEM image of protected layer deposition on the patterned area of (a), (c) FIB milling for preparation of lamella, (d) SEM images of the lamella lift-out, and (e) STEM image in of the prepared lamella. 105

Figure 5.13 (a) Cross-sectional TEM image of nanostructures. (b_1 & b_2) High-resolution TEM image and EDS elemental map for nanostructure showing a clear distinction between germanium with coated carbon and platinum. (c-e) Selected area electron diffraction (SAED) patterns for different regions: at the bulk (c), at the apex of nanostructure (d) and below the nanostructures (e). The indices for dc-Ge are indicated in white (c & e), and that for hd-Ge are indicated in red (e). 106

Figure 5.14 The EDS mapping of elements through a cross-section of the nanostructures. 107

Figure 5.15 Azimuthally averaged intensity profile for the selected area diffraction ring pattern at the apex of nanostructures.. 108

Figure 5.16 Radial distribution function calculated for the selected area electron diffraction ring pattern at the apex of nanostructures. 109

Figure 5.17 Raman spectra for (a) bare germanium and (b) the nanostructured Ge surface. 112

Figure 5.18 UV-Vis absorptance spectra for bare germanium and germanium nanostructures. 115

Figure 6.1 The perspective 3D view of the MD simulation set-up with different regions in the simulation domain and FIB region at the top... 122

Figure 6.2 (a) The ion beam intensity across the diameter of for the radial distribution of ions. (b) The representation for a typical ion distribution in the beam cross-section corresponding to parameters in (a).. 124

Figure 6.3 (a) The evolution of the temperature, from the MD simulation of Ga^+ FIB irradiation on Ge for the sputter region, shows the temperature spike with each ion impingement. Inset is the magnified view of temperature at the end of the irradiation time. (b) Snapshots illustrating the time evolution of temperature distribution on the yz-plane of the sputter region. The scale bars are of 4 *nm*. 126

Figure 6.4. The 3D view of sliced sputter region for the atomic displacement (a) before and (b) after irradiation. The cross-sectional view of the sputter region for atomic displacement (c) before irradiation (at t = 30 *ps*) and (d) after irradiation (at t = 1060 *ps*)... 128

Figure 6.5 Effect of irradiation on the RDF (Radial distribution function) of the sputter region for damage in crystallinity due to Ga^+ FIB irradiation on the Germanium surface. 129

Figure 6.6 3D sliced view of the sputter region for the crystallinity changes due to Ga^+ FIB irradiation on the Germanium surface. 130

Figure 6.7 Top view of self-organization simulation via four FIB spots. The snapshots are after irradiation of (a) 150 ions per spot and (b) 200 ions per spot. These top views of the germanium crystal region are of the scale 20 *nm* × 20 *nm*. 131

Figure 7.1 Schematic for fabrication of Gee-nanodots/Graphene/Ge-nanostructures for LSPR in IR region......141

Figure A.1 Diffraction spots in the electron diffraction pattern below the nanostructures (i.e., for the SAED pattern shown in Figure 5.13(e) of the main text). The numbering indicates the spots that are indexed in Table A.1. 155

List of Tables

Table 2.1 Important contributions for the theoretical understanding of ripple formation. . 17

Table 3.1 Energy-dispersive X-ray spectroscopy (EDX) results for bare surface and nanostructured surfaces. 42

Table 6.1 Parameters for the SW potential used the MD simulations [71]....................... 121

Table A.1 Comparing the measured interplanar distances with calculated values for (*hkl*) indices of dc-Ge and hd-Ge. For any diffraction spot, if the calculated d-spacing values of both the phases match with the measured d-spacing value, then the closest interplanar distance is shown with red coloured indices....................................... 156

List of Symbols and Abbreviations

γ_j	Admittance of EM waves
Δ	Thickness of graphene layer
δ_J	Phase difference of EM waves
$\varepsilon_{\parallel}, \varepsilon_{\perp}$	In-plane and out-plane permittivities
ϵ_0	Space permittivity
μ_0	Space permeability
σ	Conductivity
τ	Relaxation time
ω	Angular frequency
2D, 3D	Two-dimensional and three-dimensional
AFM	Atomic Force Microscopy
Al_2O_3	Aluminium oxide
ALD	Atomic Layer Deposition
Ar	Argon
Au	Gold
BFAST	Broadband Fixed Angle Source Technique
BO	Beam Overlap
C	Carbon
$^{\circ}C$	Degree Celsius
CNT	Carbon nanotubes
CVD	Chemical Vapour Deposition

d	Beam size
D_x^I, D_y^I	coefficients of the ion-induced diffusion for *x* and *y* directions
e	Electron charge
$\lvert E \rvert^2$	Electric field intensity
EDX	Energy-dispersive X-ray spectroscopy
E_F	Fermi energy
EF	Enhancement Factor
EM	Electromagnetic
eV	Electronvolt
FDTD	Finite-difference time-domain
FEG-SEM	Field Emission Gun-Scanning Electron Microscope
FFT	Fast Fourier Transform
FIB	Focused Ion Beam
FWHM	Full Width at Half Maximum
Ga	Gallium
GaAs	Gallium arsenide
Ge	Germanium
h	Height
$\hbar$	Plank constant
$h(r,t)$	Height at a position $r = (x,y)$ and time *t*
HAADF	High Angle Annular Dark-Field
HFW	Horizontal Field Width
IBS	Ion Beam Sputtering

IR	Infrared
K	Kelvin
k_b	Boltzmann constant
keV	Kilo-electronvolt
kV	Kilo-volt
$LaAlO_3$	Lanthanum aluminate
LAMMPS	Large-scale Atomic/Molecular Massively Parallel Simulator
LMIS	Liquid Metal Ion Source
LSPR	Localized Surface Plasmon Resonance
mA	Milliampere
$mbar$	Millibar
MCB	Makeev, Cuerno, and Barabasi
MD	Molecular dynamics
MEMS	Micro-Electro-Mechanical Systems
m_i	Atomic mass of ith atom
ms, μs, ps	Millisecond, microsecond and picosecond
n_2	Refractive index of bulk germanium
NA	Numerical Aperture
n_{air}	Effective refractive index of air
n_{eff}	Effective (average) refractive index
n_j	Effective refractive index of each layer
NEMS	Nano-Electro-Mechanical Systems
n-GaAs	n-Type gallium arsenide

nm, µm, cm	Nanometer, micrometer and centimeter
OVITO	Open visualization tool
p	Pixel size
P%	Percentage porosity
PBC	Periodic Boundary Conditions
PML	Perfectly Matched Layer
Pt	Platinum
R, T	Reflectance and transmittance
RDF	Radial distribution function
rpm	Revolutions per minute
s	Second
SAD	Selected Area Diffraction
SEIRAS	Surface-Enhanced Infrared Absorption Spectroscopy
SEM	Scanning Electron Microscopy
SERS	Surface-enhanced Raman scattering
Si	Silicon
SiO_2	Silicon dioxide
$SrTiO_3$	Strontium titanate
STEM	Scanning Transmission Electron Microscopy
SW	Stillinger−Weber
S_x, S_y	Sputter roughness parameters for x and y-directions
T	Temperature in Kelvin
TEM	Transmission Electron Microscopy

TFSF	Total-Field Scattered-Field
THz	Terahertz
TiO_2	Titanium dioxide
t_m	Melting point temperature
UV-Vis	Ultraviolet-visible
V_0	Average erosion rate
v_i	Velocity of *i*th atom
v_x, v_y	ion-induced roughening coefficients for *x* and *y*-directions
x, y, z	Cartesian coordinates: *x, y* and *z* coordinates
ZBL	Ziegler–Biersack–Littnark

Abstract

This work aims at the fabrication of novel nanoscale structures using ion beam induced self-organization. Sparsely distributed and self-organized gold-nanocones are fabricated by broad argon ion beam sputtering on the gold and silicon surfaces with grazing incident angle. The rotation of the sample with respect to the vertical axis has been found to influence the morphology of the obtained nanostructures. Ion beam irradiation of the gold sample leads to the formation of nanoripples when the sample is held stationary; otherwise, nanocones are formed if the sample is rotated during irradiation. A hybrid gold-nanocone/graphene/gold-nanohole based surface-enhanced Raman scattering (SERS) sensor is proposed and shown to exhibit an enhancement factor of 10^9 via finite-difference time-domain (FDTD) simulations.

The gallium ion (Ga^+) focused ion beam (FIB) was used to enable the formation of the self-organized nanoripples on the germanium (100) surface. During the fabrication, the overlap of the scanning beam is varied from zero to negative value and found to influence the orientation of the nanoripples. The evolution of nanostructures with the variation of beam overlap is investigated. Parallel, perpendicular, and randomly aligned nanoripples with respect to the scanning direction are obtained via manipulation of the scanning beam overlap. The enhanced light trapping leading to the high absorption of light is confirmed by the experimental studies as well as the numerical simulations FDTD method. About 95% broadband absorptance is measured in the visible electromagnetic region for the nanorippled germanium surface. The reported light absorption enhancement can significantly improve the efficiency of germanium-silicon based photovoltaic systems.

The tailoring of the surface self-organization to realize periodic and protruding nanoscale polygonal morphologies on the germanium (100) surface was demonstrated with the aid of FIB induced self-organization. The morphologic evolution in the nanoholes has been found to be sensitive with the ion dose, and the optimized conditions produce protruding polygonal geometries such as squares, triangles, hexagons, pentagons, and octagons. With further modulation, the unusual nanostructures such as corrugated shaped, mushroom shaped and dual-nanostructures resembling nanoholes connected with nano-needles are fabricated. The systematic investigation of the morphology evolution and underlying mechanism was carried out using electron microscopy, atomic force microscopy (AFM), Raman spectroscopy and molecular dynamics (MD) simulations. The bombardment of energetic ions on the germanium surface causes the site-specific thermal spike forming the localized melting zones followed by the phase transitions enabling confined viscous-flow at the walls of nanoholes as revealed by microscopy, Raman spectroscopy and molecular dynamics (MD) studies. The confined viscous-flow provides reorganization of the surface atoms by the occurrence of viscous-fingering at the nanoscale, enabling the geometrical makeover for the nanoholes to convert the circular holes into the polygonal holes. The demonstrated strategies not only provide precise nanoscale control in the ion beam induced self-organization but also provides advancement in the field of focused ion beam fabrication process by first-of-its-kind control and manipulation at a level of individual FIB spots, offering a unique capability to surmount the barriers concerning miniaturization efforts in the field of nanofabrication. The nanoscale control over the material self-organization promises to inspire novel, fast and easy methods for 3D nanoscale and sub-nanoscale geometries for use in photonic integrated circuits (PICs), photodiodes, bio-sensing, and microfluidics.

Chapter 1

Introduction

1.1 Background

The surface topography at micro/nano-scale strongly influences the optical, electrical, and magnetic properties of materials. Photolithography and e-beam lithography are widely used nanofabrication processes. The fabrication of three-dimensional (3D) structures at nanoscale faces tremendous challenges using these conventional lithography-based processes due to multi-stage processing, resist layer requirement and the need for masks during each stage of operations. To overcome these limitations of the conventional lithography-based nanofabrication processes, learning and exploiting the self-organization phenomenon present in nature could be beneficial in terms of simplicity as well as cost-effectiveness without losing on the quality of the outcomes. The self-organization is known as the process where surface or material undergo interplay of competitive dynamics leading to the formation of ordered arrays of objects or morphologies [1]. In nature, the occurrence of such self-organization are ranging from ripples on sand dunes (Figure 1.1(a)), a network of veins in leaf structures by leaf-venation (Figure 1.1(b)) to molecular and atomic arrangements [1]. Mimicking this natural self-organization phenomenon artificially to create varied geometries and morphologies could be useful in the advancement of materials science by opening up the new avenues in the field of nanofabrication [2–4].

1.2 Motivation

The nanopatterning using ion beam sputtering (IBS) technique has been getting attention for its capability of forming nanostructures via self-organization of the surface atoms [5,6]. The advantage of this technique is the possibility of nanostructures on a large area with a single step and mask-less process. During the ion beam irradiation on the surface, the curved surfaces are formed with an increase in the roughness, and atoms on the concave regions tend to erode faster than those from the convex regions [5]. The occurrence of such a selective surface erosion and its competition with a surface diffusion induced by ion beam sputtering results in reorganization of the surface atoms, and thus, the nanostructures are formed [5,6].

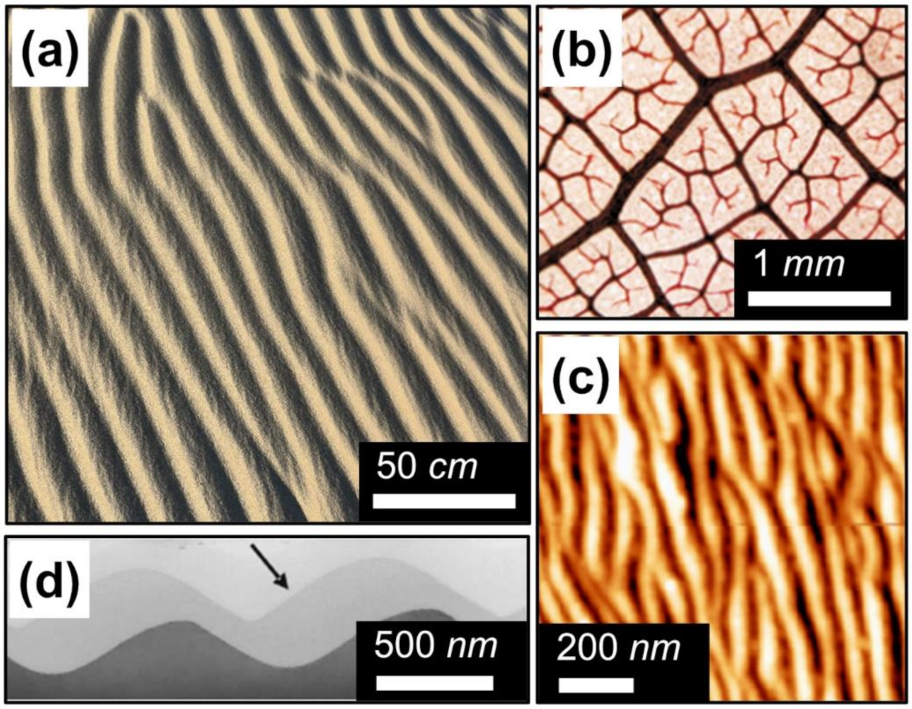

Figure 1.1 (a) Macro-scaled ripple patterns on the sand dune, (b) micrograph of leaf-venation in *Viburnum mole* plant leaf [7], (c) sub-micron size ripples in glass substrate [8], and (d) TEM cross-section image of ripples on the Si surface. The arrow shows the ion beam incidence direction [9].

The self-organization on the surface during ion beam irradiation resembles the natural phenomena of the wave-like pattern created due to wind on the sand dunes, as seen in Figure 1.1(a & c) [8]. The observations of sub-micron scale ripples created on the Si surface by argon ion beam sputtering (IBS) exhibit the similarities with the macro-scaled ripples or wave-patterns in nature on the sand dunes, as seen in transmission electron microscopy (TEM) image (Figure 1.1(d)) [9]. A variety of nanostructures can be fabricated by self-organization (Figure 1.2) such as nanoripples on strontium titanate [10], transparent and conducting aluminium nanowires [11], nanodots on silicon surface [12] and gold nanowires [13].

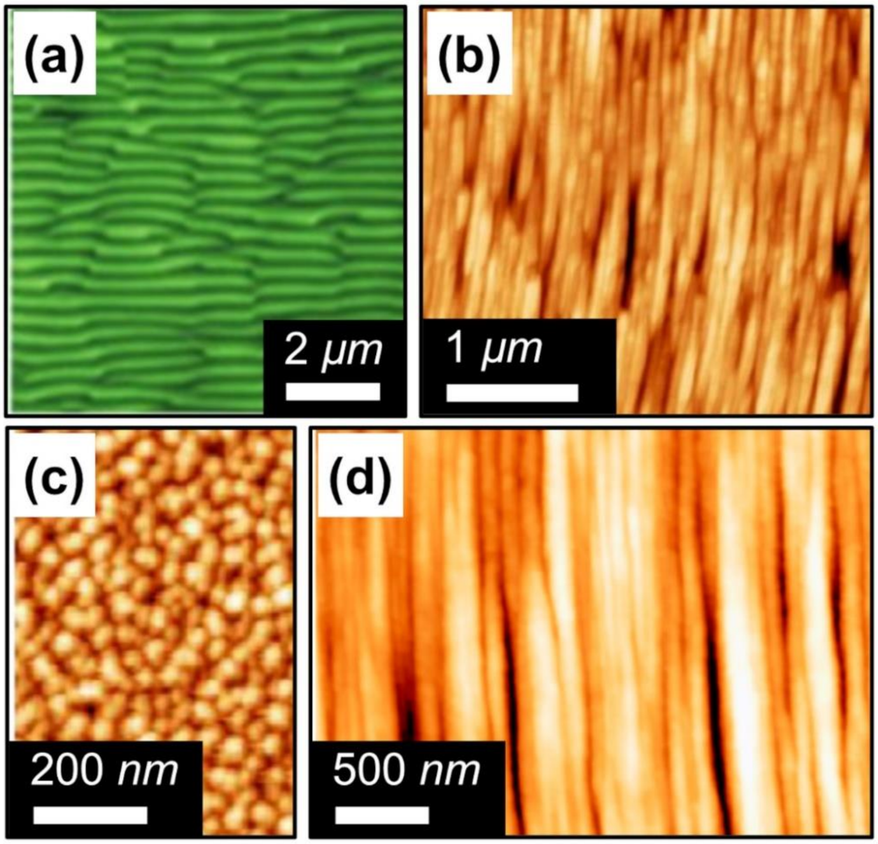

Figure 1.2 Micrographs of self-organized nanostructures formed by ion beam irradiation. (a) Nanoripples on strontium titanate [10], (b) transparent aluminium nanowires [11], (c) silicon nanodots [12] and (d) gold nanowires [13].

The self-organization on the ion beam irradiation for the strontium titanate leads to the formation of nanoripples on the surface [10]. The ripple formation was found to be prominent with a higher beam current. However, the ripples are not uniform in any case and even wavelength is not uniform throughout the selected area; also, the faceted features were present. The grazing angle (82° with respect to the surface normal) ion beam irradiation on the polycrystalline aluminium film provided transparent and conducting aluminium nanowires [11]. The conductivity of the aluminium nanowires was dependent on the irradiation dose, enabling the possibilities for tuning the conductivity of transparent metal nanowires. Researchers have also demonstrated quasi-periodic silicon nanodots via ion beam induced self-organization.

Researchers have reported the ion beam induced self-organization of nanoripples and nanodots on various surfaces [14–17]. However, the lack of control over structures in terms of periodicity and uniformity limits their application. There is also a lack of reports on the morphology controlled self-organized geometries such as squares (and other higher-order polygons) with periodic spacing. Hence, fabricating 3D structures with higher aspect ratios is a challenge. Instead of broad ion beam sources, the use of focused ion beam (FIB) – a beam of energetic ions focused with beam diameter around 10 *nm* – can be beneficial to overcome the limitations of broad ion beam assisted self-organization. FIB can be used both for imaging and micro/nano-fabrication [18]. Primarily, the focused ion beam assisted direct milling process (Figure 1.3(a)) and chemical vapour deposition (CVD) process (Figure 1.3(b)) have been widely used for three-dimensional (3D) nano-fabrication strategies [19,20]. The advantage of the focused ion beam milling process for nanofabrication is that the process is a single step and mask-less. However, direct milling-based FIB nanofabrication is slow, and nanostructures with a feature size of a few nanometers (e.g., features of dimensions lesser than that of the ion beam size) are challenging.

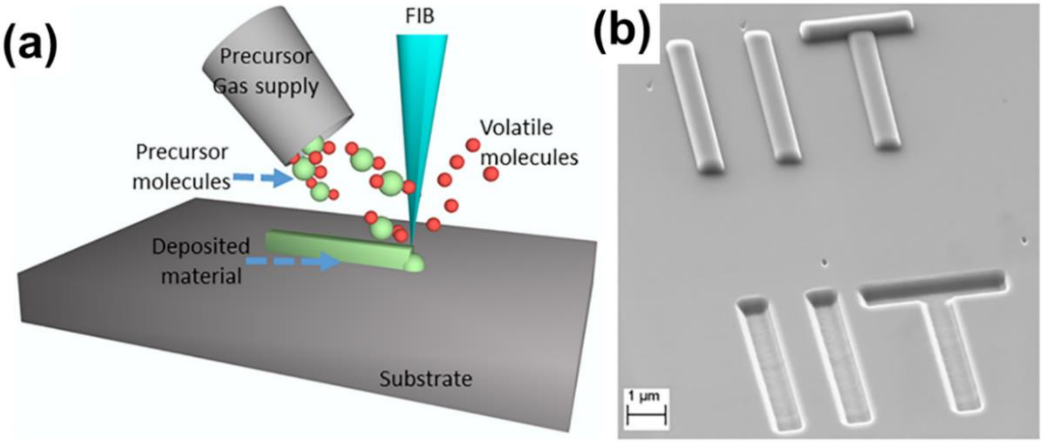
(a)
FIB
Precursor
Gas supply
Precursor
molecules
Volatile
molecules
Deposited
material
Substrate
(b)
1 µm

Figure 1.3 Nanofabrication by focused ion beam. (a) FIB-CVD schematic and (b) the SEM image of metal (Pt) deposition as well as material removal using FIB milling. “IIT” is produced on the silicon substrate with deposition of Pt and by removing Si material using the FIB milling process.

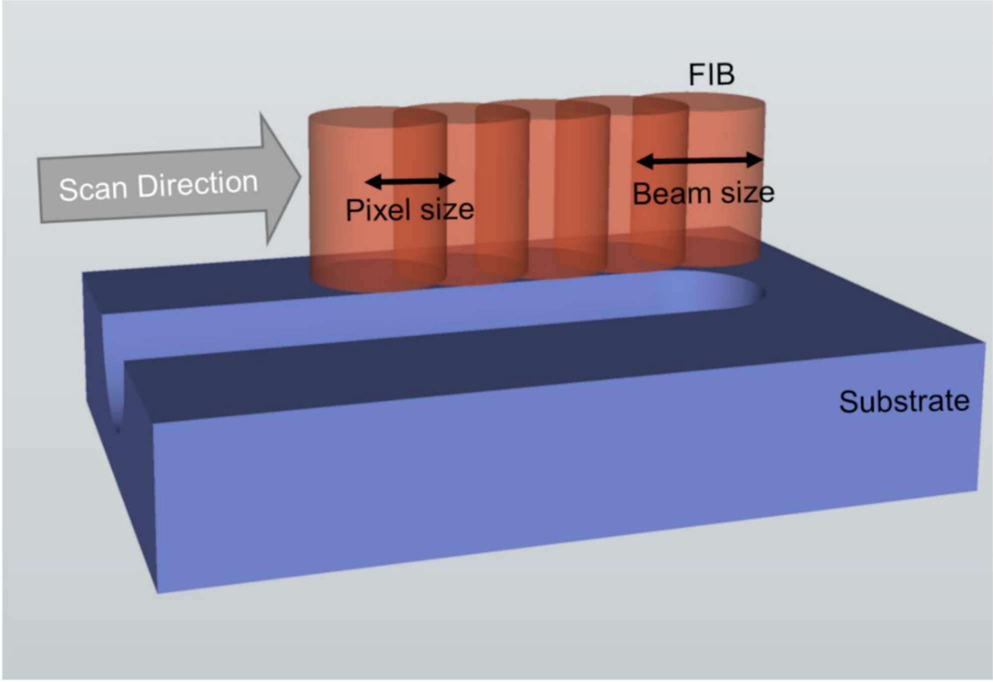
FIB
Scan Direction
Pixel size
Beam size
Substrate

Figure 1.4 Schematic of FIB milling process via pixel scanning.

As shown in Figure 1.4, the fabrication strategy to create nanostructures using a focused ion beam (FIB) is to sputter away the material for the desired geometrical shape, to produce the designed structures by dwelling pixel by pixel, known as a direct milling process [21–

25,19,26–28]. Direct milling by FIB is slow due to the requirement of pixel-by-pixel scanning with enough dwell time to erode the materials up to the desired depth, which depends on the effective sputter yield of the material for the particular ion beam source [21–24]. In order to produce well-defined nanostructures with dimensions of the same order or lesser order of the diameter of the ion beam is practically not possible using focused ion beam milling [22,24,29]. Recently, the FIB technique has attracted researchers towards its capability to form well-ordered nanostructures and sub-nanometer structures via self-organization of the surface atoms after FIB irradiation. Self-organization of nanostructures using focused ion beam with optimized beam parameters may lead towards overcoming both the significant limitations, namely, (i) low-periodicity and lack of variety in morphologies of broad ion beam based self-organization and (ii) limitations in size and slow process by the milling-based FIB nanofabrication method. Under the influence of the focused ion beam, self-organization of the surface can lead to novel structures and morphologies, which is promising due to its high-throughput capabilities.

The proposed research aims at studying ion beams and their interactions with materials for novel 3D nanostructure fabrication. Based on beam geometries and scanning strategies, controlled ion beam irradiation is expected to significantly tune the surface morphology with characteristic topographical features. Periodicity and precision in the size of self-organized nanostructures can enable them to be served as functional nanostructures and exhibit novel structures required for surface plasmonics, photonics, microfluidics, template for nanoparticle/nanowire patterning and sensing.

1.3 Objectives

There is a need to develop a fast and easy fabrication method for creating 3D nanostructures that can have the potential to miniaturize functional nanoscale devices in the future. The focused ion beam assisted nanofabrication is a promising technique; however, conventional direct milling-based methods are limited by speed, and the features having a size lesser than the beam size can’t be created. In order to develop novel strategies, ion-material interactions need to be understood. The proposed research is aimed at the capabilities of the focused ion beam (FIB) for self-organization to achieve control on the processes for periodic 3D nanostructures on the material surfaces. The control on surface reorganization through ion-material interactions is proposed to be achieved by the optimization of FIB parameters for characteristic surface evolutions. The knowledge acquired from the research will be applied for the fabrication and nanoscale control of self-organization for novel 3D nanostructures.

The work aims at the following objectives:

- Study the ion-solid interactions for self-organization of surfaces.
- Understanding the mechanism behind controlled self-organization.
- Achieving nanoscale control over the morphology of self-organized nanostructures by utilizing a focused ion beam.
- Develop novel and 3D nanostructures on the surfaces.

1.4 Organization of the report

The report is organized in the following manner. Chapter 2 represents a literature review on focused ion beam instrumentation and relevant ion beam induced self-organization for nanostructures. Chapter 3 includes the fabrication of nanocones on silicon and gold surfaces with argon ion beam sputtering. The use of broad ion beam induced gold nanocones for a hybrid gold-nanocone/graphene/gold-nanohole based surface-enhanced Raman scattering (SERS) sensor has been proposed by optical simulations. Chapter 4 presents easy control on the alignment of the focused ion beam induced germanium nanoripples. The anti-reflecting properties of nanoripples are studied by theoretical calculations, optical simulations, and experimental measurements. The enhanced light trapping by focused ion beam (FIB) induced self-organized nanoripples on germanium (100) surface has been demonstrated. Chapter 5 presents the evolution of focused ion beam induced 3D periodic polygonal nanostructures on germanium (100) surface. Morphological characteristics of periodic nanostructures are studied by scanning electron microscopy (SEM) and atomic force microscopy (AFM). The phase transformation and self-organization mechanism are discussed using transmission electron microscopy (TEM) and Raman spectroscopy. Chapter 6 contains molecular dynamics (MD) simulations for investigation on FIB induced self-organization of germanium nanostructures. Gallium ion impingement of 2 keV has been carried out to study its interaction with germanium crystal at the ion bombardment site with an estimation of temperature evolution and crystallographic changes. Chapter 7 includes conclusions and an outlook for future research.

Chapter 2

Literature Review

In this chapter, a review of the broad and focused ion beam induced self-organization has been carried out. The survey aims to understand ion-solid interactions for self-organization processes; thus, the literature review was carried out with an emphasis on achieving morphology control at the nanoscale using broad and focused ion beam as per the objectives defined in the previous chapter (Chapter 1). The morphological dependence of ion beam induced self-organization with the operating parameters has been discussed. The potential use of a focused ion beam for the novel and complex nanostructures has been hypothesized based on the literature study. Also, the reports on the atomistic simulations of ion beam irradiation induced damage on materials are discussed.

2.1 Focused ion beam

Focused ion beam (FIB) has been widely used as a nano/micro fabrication and imaging tool [19,20]. It is analogous to the scanning electron microscope (SEM), where the electron source gets replaced by the ion source and the lens system is modified accordingly. In FIB, the electrostatic lens system and gun are different than the SEM. The schematic of the FIB is given in Figure 2.1(a). A liquid metal ion source (LMIS) is at the top of the FIB column to produce ions. Gallium is commonly used as an ion source because of its low melting point (32° *C*), high mass and low volatility. However, argon, indium, neon, etc., can also be used as an ion source. By applying a high electric field, ions are evaporated from LMIS and are focused within a narrow beam by the electrostatic lens system. Passing through the deflector plate and apertures, the ion beam reaches the sample surface. Upon impact of focused ions on the surface, elastic and inelastic collisions happen. The elastic ion-atom collision removes surface atoms, which is called a sputtering process, while inelastic ion-atom collision results in the production of secondary electrons and x-rays. These secondary electrons are then detected, amplified, and analyzed to produce images of the sputtered surface. Thus in-situ imaging is also possible by FIB. In general, for simultaneous imaging, the column of an electron beam is attached along with the ion beam. Therefore, it is called a dual-beam FIB/SEM system, as seen in Figure 2.1(b).

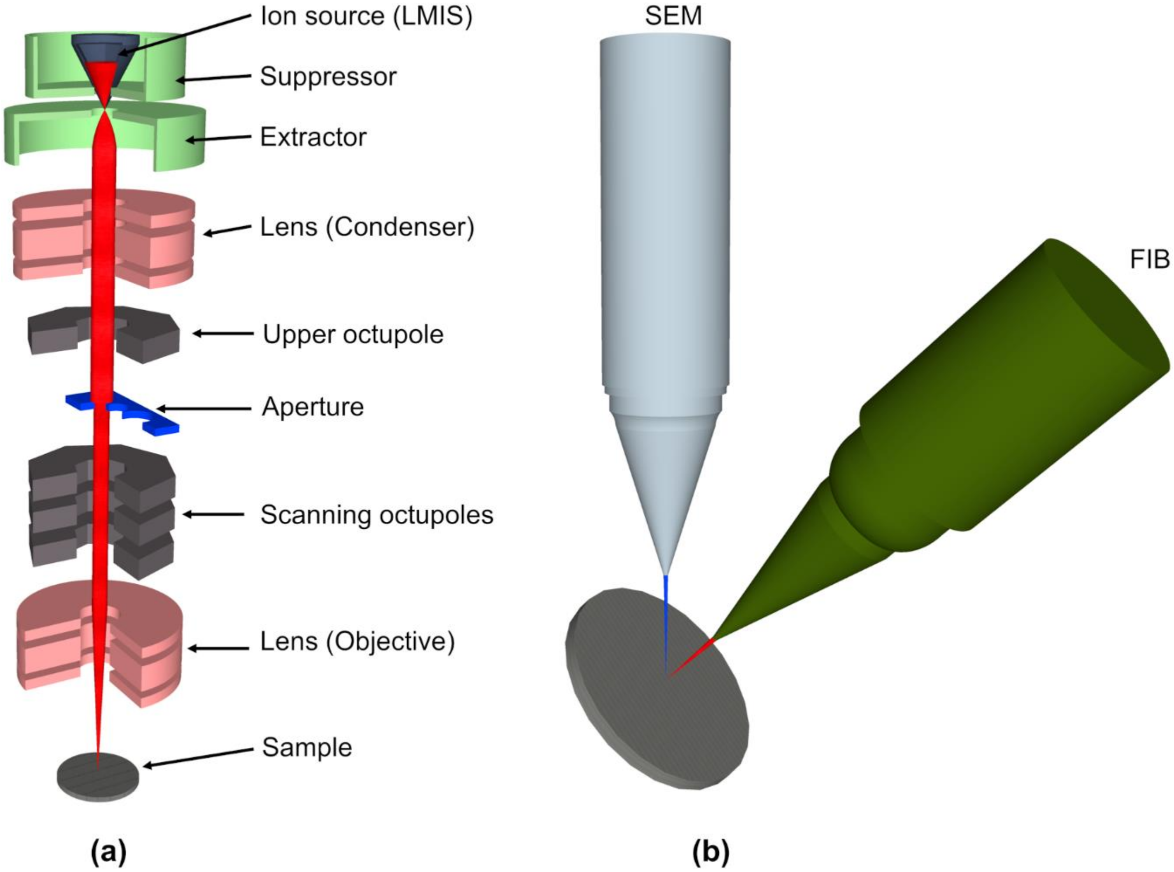
Ion source (LMIS)
Suppressor
Extractor
Lens (Condenser)
Upper octupole
Aperture
Scanning octupoles
Lens (Objective)
Sample
(a)
SEM
FIB
(b)

Figure 2.1 (a) FIB Schematic, (b) Dual-beam FIB/SEM system.

2.1.1 FIB: primary functions and important parameters

Bombardment of FIB on the surface of the substrate mainly results in physical effects like (i) sputtering of surface atoms either in neutral or ionized form, (ii) electron emission, (iii) displacement of atoms in the solids (damage, defect creation), (iv) photon emission and (v) ion beam induced chemical reaction at the selected site. These effects can lead to four basic functionalities of the focused ion beam, namely, 1. Milling (by sputtering and etching), 2. Deposition, 3. Implantation, and 4. Imaging (See Figure 2.2).

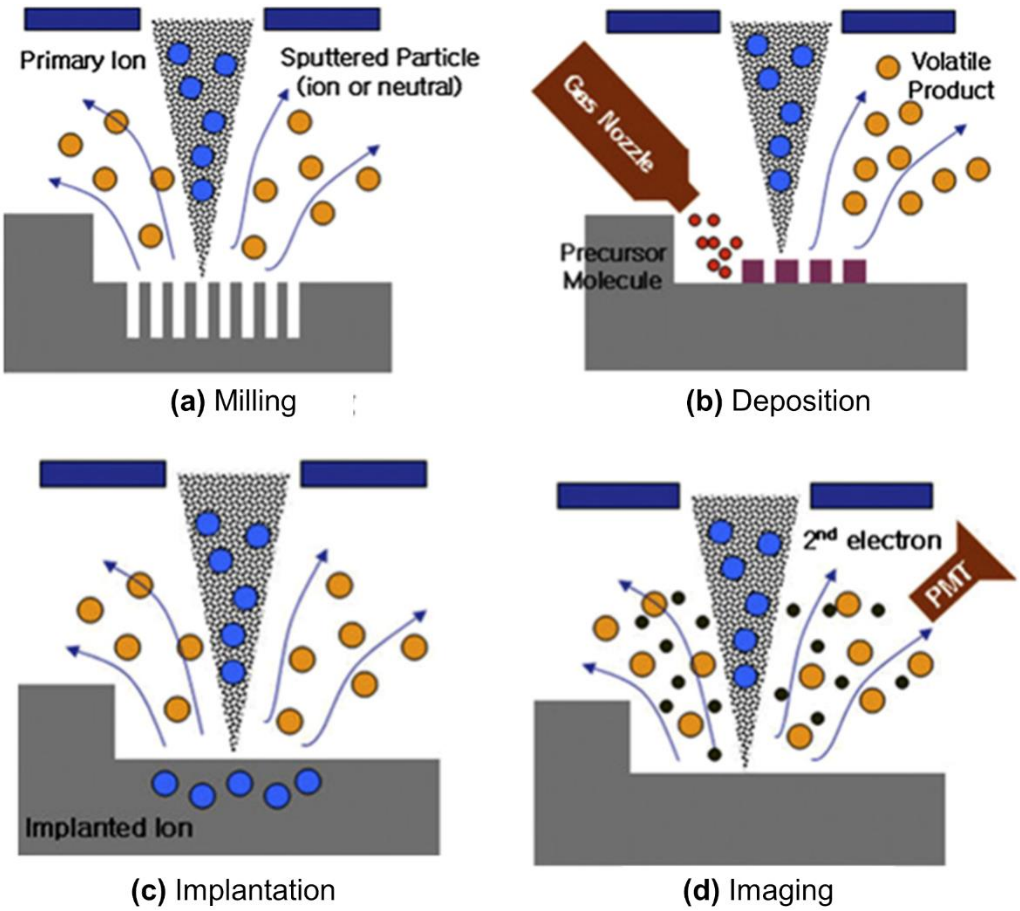
Primary Ion
Sputtered Particle (ion or neutral)
(a) Milling
Gas Nozzle
Volatile Product
Precursor Molecule
(b) Deposition
Implanted Ion
(c) Implantation
2nd electron
PMT
(d) Imaging

Figure 2.2 Basic functions FIB a) milling, b) deposition, c) implantation and d) imaging [30].

Selective area milling of the surface atoms happens by sputtering the atoms due to high energy FIB bombardment, and 2D as well as 3D nano/micro-structures can be fabricated [30]. Deposition can be achieved by inserting some precursor molecules (mainly gases) in the chamber near the ion beam spot. The interaction of ion beam, surface atom and precursor lead to a chemical reaction, and the resultant product gets deposited on the surface.

This process can also be called FIB−CVD (FIB − Chemical Vapour Deposition) [30]. The FIB-CVD process is highly suitable for the fabrication of 3D functional nanostructures [30]. When the ion beam is bombarded with much higher kinetic energy such that ions get penetrated up to a certain depth on the surface, they get implanted on the surface as an impurity atom and make the crystalline surface amorphous. This is called the implantation process. The implantation process is mainly used in the semiconductor industry for doping intrinsic semiconductors with impurity atoms.

FIB process involves important parameters associated with the operation such as ion beam energy (i.e., acceleration voltage), beam current, dwell time, ion dose (i.e., ion flux or ion fluence), incident angle, beam overlap, etc. Optimization of these parameters depending on the substrate material and desired FIB operation is essential while doing the FIB fabrication process. These crucial FIB parameters are defined as follow,

- Energy (Acceleration voltage):

  To extract and accelerate the ions from LMIS, an acceleration voltage is applied. The energy and velocity of the ions depend on the applied acceleration voltage. It is usually expressed as kV or keV. The penetration range inside the material will be higher for the ions accelerated with higher acceleration voltage. In general, the acceleration voltage of 30 kV is used [21,30].

- Beam current:

  The aperture size and condenser lens control the beam current through the ion beam column. For the higher beam current, the aperture will allow an increased number of ions to pass through the column, and thus, the diameter (beam size) of the beam will be higher.

Hence, a smaller beam current is required for the higher resolution, but the smaller beam current will significantly decrease the throughput. The unit of beam current is *nA* or *pA*.

- Dwell time:

  The duration of beam irradiation at each position (pixel) is known as dwell time. Generally, the dwell time is in the range from *μs* to *ms*. The higher value of dwell time leads to an increased depth of the milling features.

- Ion dose:

  The number of ions bombarded per unit area is known as ion dose. The product of total dwell time and beam current is proportional to the number of ions bombarded on the surface. Ion dose is expressed with unit $ions/cm^2$.

- Incident angle:

  Ion impingement angle onto the target sample is known as an incident angle or the angle of incidence. The angle of incidence is defined with respect to the surface normal of the sample substrate.

- Beam overlap:

  As shown in Figure 1.4, during FIB scanning on the surface, after the set dwell time, the beam position is moved to the next pixel position (depending on the set pixel size) towards the scanning direction. When FIB is moved, the beam is blanked until it is positioned at the next pixel position. The beam overlap is defined by the step size (pixel size), as illustrated in Figure 2.3.

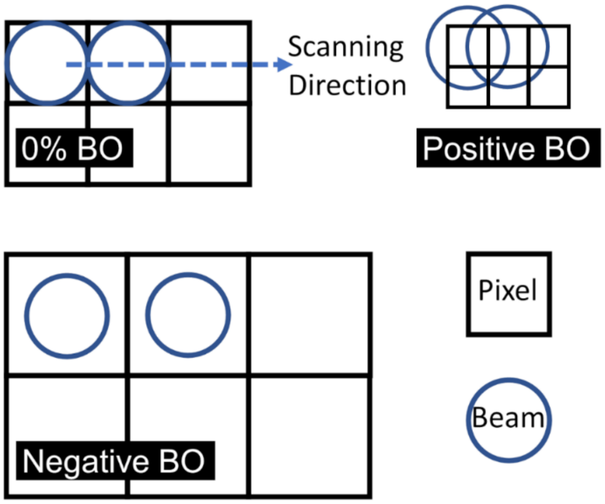

Figure 2.3 Illustration of beam overlap with different pixel sizes. The pixel size is lesser than the beam size for positive beam overlap, whereas it is greater than the beam size for negative beam overlap.

2.1.2 FIB: applications and capabilities

The focused ion beam is widely used in the areas of fabrication, surface modification and surface analysis. Nano/micro photonic crystals, MEMS/NEMS devices, TEM sample preparation, 2D/3D micro/nano-structure fabrication, mechanical machining tools, biological tools, microfluidics, etc., are the applications where fabrication capabilities of FIB have been utilized. Milling and deposition are two main tools of FIB which enable us to create simple (planner) as well as complex (3D nanostructures) on a variety of substrates (Figure 2.4(a) & (b)) [30]. Self-organized nanoripples can also be produced by ion beam bombardment on the substrates (Figure 2.4(c)) [9,30,31]. Ion beam irradiation can also be used to modify carbon nanotubes (CNT) and graphene surfaces to generate temporary and permanent defects [32,33]. It can also be used for site-specific functionalization of graphene and CNT, which can be used to fabricate all carbon sensing devices [34]. Joining/welding of CNT and graphene has also been observed.

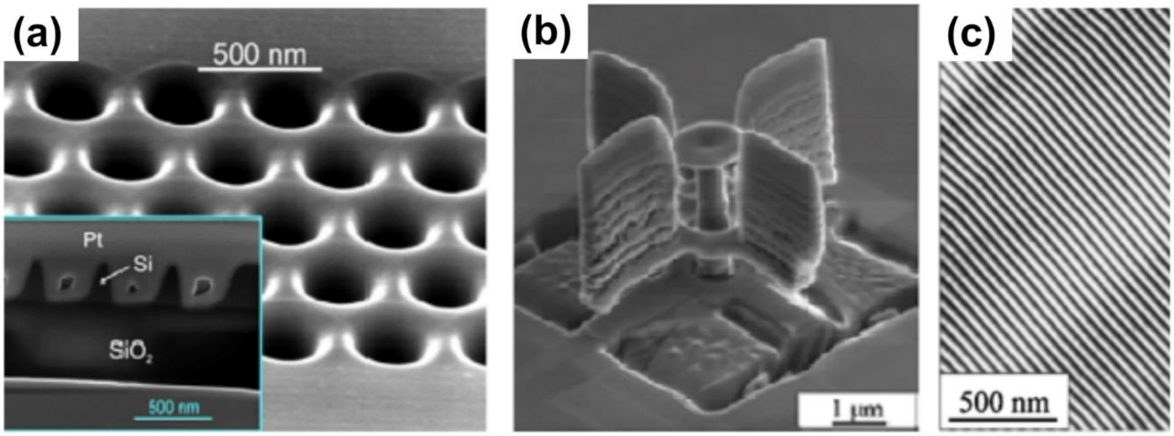

Figure 2.4 Examples of fabricating different nanostructures by FIB. (a) Nanoholes array milled through SOI wafer (Silicon on Insulator wafer) by FIB milling [35], (b) nano-rotor (Complex 3D structure) by FIB–CVD method [36] and (c) self-organized nanoripples by ion beam bombardment [31].

In a nutshell, FIB is an ideal instrument for fabricating, modifying, and imaging innovative nanostructured materials and devices. The FIB is a multipurpose tool for milling, deposition, characterizing, and tailoring the surface of nanomaterials. In a dual-beam FIB/SEM system, by using an SEM gun, in-situ imaging and characterization can also be done simultaneously while FIB is running. 2D as well as complex (3D) nano/micro-structures can be fabricated on the variety of substrates using milling and deposition features of FIB.

2.2 Self-organized nanostructures by ion beam irradiation

The study of nanostructures and sub-nanometer-sized structures is of great interest today because of their novel applications and efficient performance. Two ion beam irradiation approaches can be mainly followed: (1) broad ion beam irradiation and (2) focused ion beam irradiation. Both the approaches have advantages and disadvantages based on the governing processes and due to the difference in energy imparting on the surface. Hence, it is useful to survey the self-organization processes owing to both these approaches.

2.2.1 Broad ion beam induced nanostructures

Ion beam sputtering (IBS) is one of the most explored techniques to fabricate nanostructures by self-organization of surfaces under the irradiation of energetic ions [9]. Submicron ripples and nano/micro-dots on the surfaces are repeatedly reported to be formed after ion beam sputtering [9,31,37–40]. Ripple orientation hugely depends on the incidence angle and the ion beam projectile direction. Ion beam sputtering induces surface erosion and strain on the substrate. It creates surface energy disequilibrium, which leads to relaxation and self-organization of surface atoms to minimize surface energy. And, as a result, nanostructured ripples are created on the substrates [31,37–40]. Important structural features of ripples like wavelength, height, period, and orientation depend on the irradiation parameters like type of ion, ion doses, angle of incidence, the energy of ion, and irradiation duration.

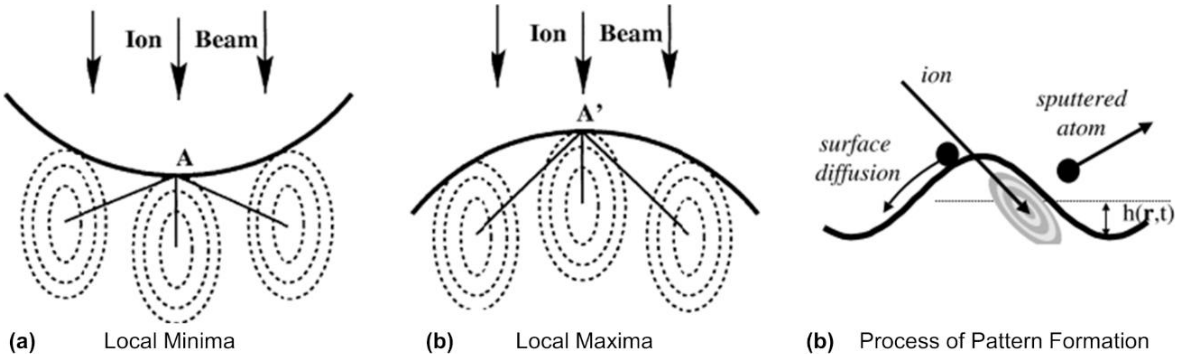

Figure 2.5 Schematic diagrams to understand surface imbalance during ion beam erosion of the surfaces: (a) the surface minima erodes faster than, (b) the surface maxima because the energy has to travel fewer distances (solid lines) to sputter nearby atoms than the local maxima. (See points A and A') [9,41]. (c) The process of pattern formation [42].

Table 2.1 Important contributions for the theoretical understanding of ripple formation.

Year	Contribution	Reference
1969	Theoretical understanding of ion sputtering mechanism and sputtering yield	Sigmund P. [43]
1973	Surface roughening mechanism leading to ripple formation.	Sigmund P. [44]
1988	Theory for ripple surface formation with Bradley & Harper's second-order linear equation and wavelength dependence on temperature and ion flux	Bradley and Harper [5]
2002	Ion-induced smoothing and morphological evolution of ripples on amorphous surfaces	Makeev, Cuerno, and Barabasi [41]
2014	Modification of Sigmund model accord with surface energy distribution of ion sputtering via MD simulations	Bradley and Hans [45]

Important contributions for the development of ripple formation theory are listed in Table 2.1. Sigmund did the first theoretical understanding for the sputtering process of energetic ions on the substrate and formation of nanostructures in 1973 [9,44]. Sigmund suggested that on sputtering of the ions with the off-normal angle to the surface, the sputtering rate at the site depends on the curvature of the local site (Figure 2.5(a) & (b)). When the curvature of the surface is formed due to erosion by ion sputtering, the further sputtering depends on the local surface rate, which is now different at the different surface curvatures. At the surface minima, further erosion will be faster than the surface maxima, creating one surface minima adjacent to the surface maxima. This leads to the creation of wave-like ripples and increases the roughness of the surface (Figure 2.5(c)). Such instabilities on the surfaces are the cause of nanostructure formations [9,44,45]. The sputtering behaviour can be expressed by the proportionality relation of the probability of sputtering with the curvature of the surface as,

$$\frac{\partial h}{\partial t} = S_x \frac{\partial^2 h}{\partial x^2} + S_y \frac{\partial^2 h}{\partial y^2} \tag{2.1}$$

Where S_x and S_y are sputter roughness parameters for x and y-direction and h is the height of the surface, which is taken as $h(r,t)$ at a position $r = (x,y)$ and time t. The changes in h over time occur based on the roughing and smoothing processes depending on parameters and curvature after erosion, as seen in Figure 2.5. Based on Sigmund's work Bradley and Harper developed the first model for low amplitude ripple formation [44,45]. Modified Makeev, Cuerno, and Barabasi theory (MCB theory) introduce an ion-induced smoothing mechanism via preferential sputtering without mass movement on the surface [44–46,5,41]. Which, on the latest modification by Bradley and Harper's second-order linear equation, is proposed to explain the smooth-ripple phase transition occurring at a critical ion-incidence angle [45]. The equation can be given as,

$$\frac{\partial h}{\partial t} = -V_0 + \gamma\frac{\partial h}{\partial x} + v_x\frac{\partial^2 h}{\partial x^2} + v_y\frac{\partial^2 h}{\partial y^2} - D_x^I\frac{\partial^4 h}{\partial x^4} - D_y^I\frac{\partial^4 h}{\partial y^4} \tag{2.2}$$

Where V_0 is the average erosion rate. The second term for the uniform motion of the surface features along the x-direction. Parameters v_x and v_y are ion-induced roughening coefficients, which were originally calculated by Bradley and Harper [5,45]. The value of v_y is always negative, but v_x is initially negative at a lower incidence angle and it increases to become positive at a higher incidence angle. D_x^I and D_y^I are the coefficients of the ion-induced diffusion in the x and y directions. Such a diffusion mechanism originates from selective sputtering, as discussed earlier, and it does not involve actual mass movement. Bradley and Harper have proposed that the wavelength dependence of ripple to be related to the temperature and the ion flux at high temperature and low ion flux to be expressed as,

$$\lambda \sim (fT)^{-\frac{1}{2}} exp\left(\frac{-\Delta E}{2k_B T}\right) \tag{2.3}$$

Where f is ion flux, T is temperature, $\triangle E$ is thermal activation energy and k_B is Boltzmann constant. This type of behaviour has been experimentally confirmed by many researchers [17]. In the following sections, the experimental reports of broad ion beam and FIB induced nanostructures are reported.

The self-organization driven by a broad ion beam has been widely demonstrated to create nanoscale and microscale structures via irradiation on different surfaces (see Figure 2.6) such as nanowires on aluminium [11], silicon surface with nanodots [12], and nanowires on gold induced by ion irradiation [13]. The nanoripples and nano/micro-dots on the surfaces are repeatedly reported to be modulated by the optimization of ion beam incidence direction, dose and beam energy [13,31,37–39].

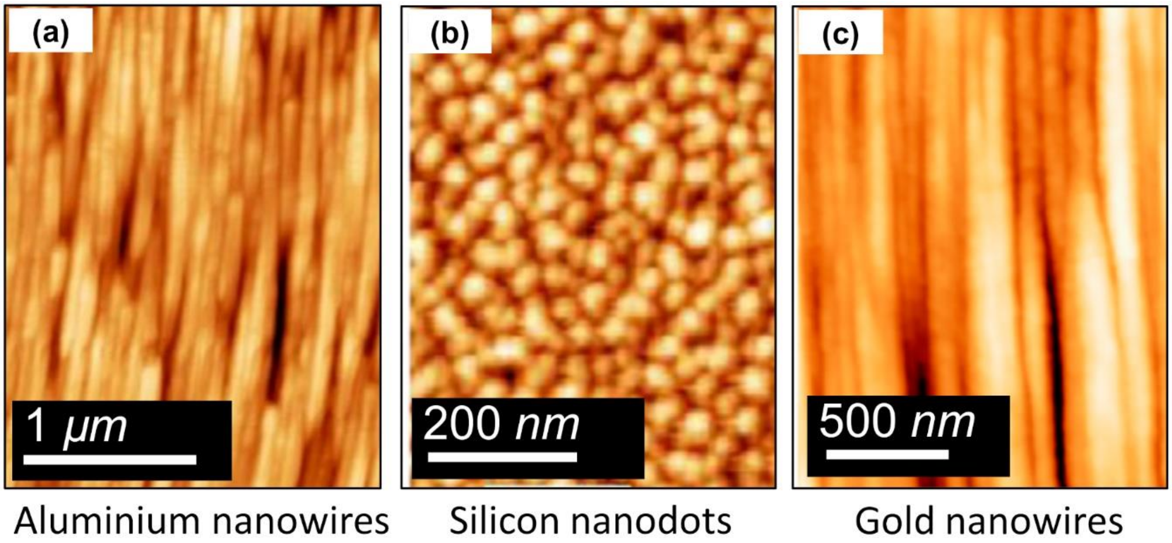

Figure 2.6 Broad ion beam induced nanostructures on surfaces. (a) transparent aluminium nanowires [11], (b) silicon nanodots [12] and (c) gold nanowires [13].

The mechanism of surface texturing is majorly explained by the theory suggested by Bradley and Harper [5] through the competition between selective erosion and surface diffusion effects [5,6]. The self-organized surfaces on the metal have beneficial electrical and optical properties such as transparent conducting aluminium nanowires [11] and gold nanowires, giving improved surface enhanced Raman spectroscopy (SERS) response [13]. Diego et al. reported that the aluminium nanowire electrodes show interesting anisotropic conductivity behavior and exhibit 40% optical transparency [11]. The enhanced optical response by gold nanowires implies their potential use in optical sensing applications [13]. It should be noted here that the self-organization process by broad ion beam is easy, faster and also it produces nanostructures over the large area on the surfaces [11–13,31,37–39]. However, the broad ion beam induced structures are having simple morphologies such as nanoripples, nanowires and nanodots; thus, it can be summarized that the formation of complex morphologies using broad ion beam irradiation is a challenge. The reports of broad ion beam and focused ion beam induced nanoripples and nanodots demonstrate the dependency of germanium nanostructure's topography on the various broad ion beam parameters such as dose, energy and angle of incidence has been studied [14–17]. The irradiation is uniform on the surface with a broad ion beam, whereas the site-specific irradiation on a finite size can be achieved using a focused ion beam. Broad ion beam source involves control parameters such as dose, energy, beam current, time, and angle of incidence. In contrast, a focused ion beam provides additional control parameters such as beam size and beam overlap. In order to attain precise nanoscale control over the self-organization, the focused ion beam can be used.

2.2.2 Focused ion beam induced nanostructures

Recently focused ion beam (FIB) has attracted many researchers towards its capability of forming well-ordered nanostructures via self-organization. Lithography by focused ion beam (FIB) has its limitations of beam diameter (least possible beam diameter is 5 to 10 *nm* depending on ion source), which limits direct writing of few nanometers and subnanometer features on the various substrates [37].

2.2.2.1 Nanoripples/nanowires

Controlled ion beam parameters lead to the formation of well-ordered and aligned self-organized nanostructures. Aligned and ordered nanoripples on surfaces like $LaAlO_3$ (100), $SrTiO_3$ (100), and Al_2O_3 (0001) induced by Ga^+ focused ion beam are shown in Figure 2.7 [40]. On the increase of ion fluence, the wavelength was observed to be increasing [40]. Datta et al. reported the real-time investigation of ripple structures on a diamond surface induced by focused ion-beam bombardment (Figure 2.8) [46].

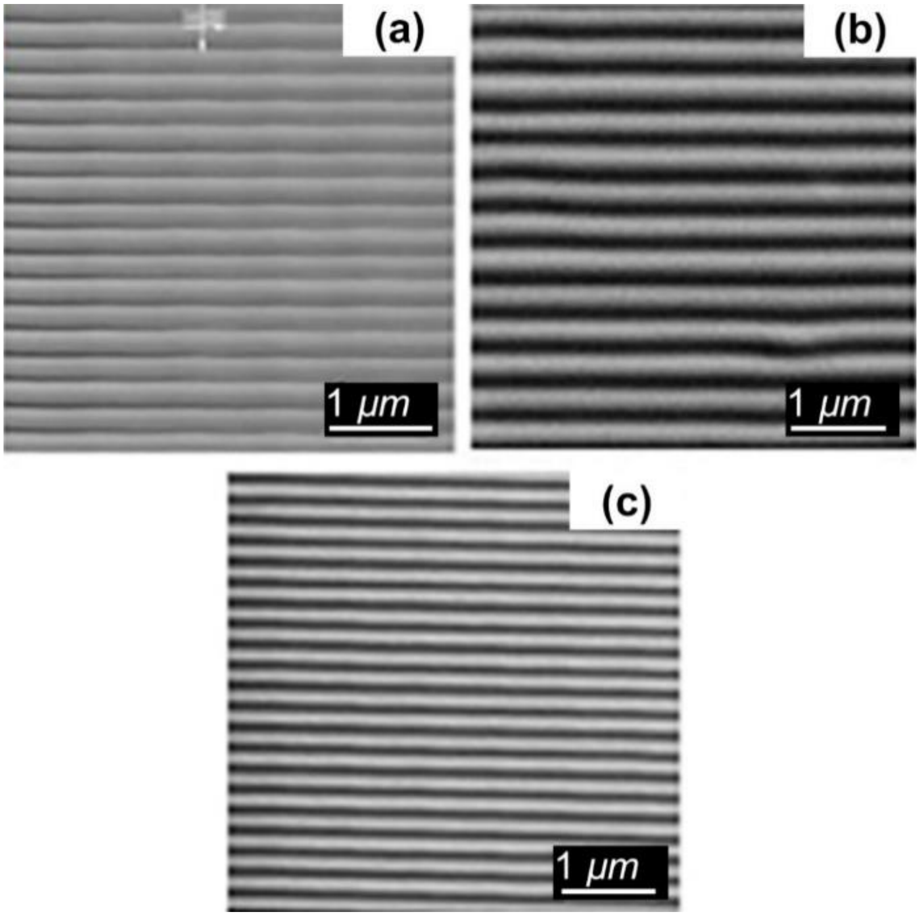

Figure 2.7 Nanoripples on $LaAlO_3$ (100) surface, $SrTiO_3$ (100), and Al_2O_3 (0001) induced by 30 *keV* Ga^+ focused ion beam with ion flux of 1.9×10^{15} *ions/cm²s* [40].

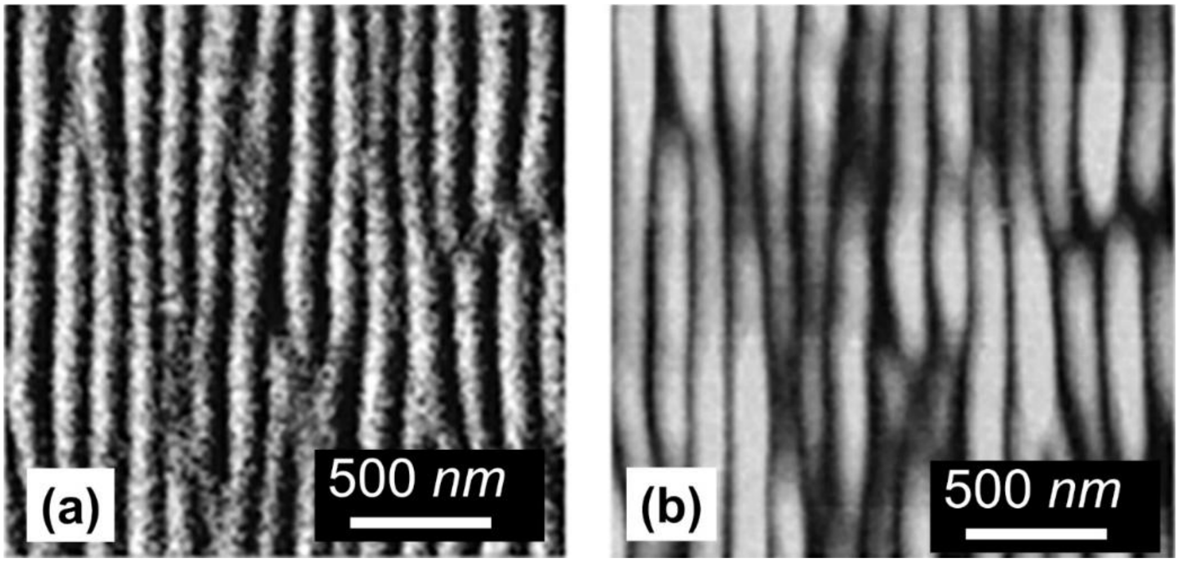

Figure 2.8 (a) FIB and (b) AFM micrographs of the self-organized ripples created by FIB with ion dose 1.3×10^{17} *ions/cm*^{2}, incident angle of 55° and energy 50 *keV*. The amplitude of nanoripples is 10 *nm* [46]

The dependency of ripple features with ion beam parameters was studied by varying parameters such as incident angle, ion beam energy and ion beam doses. At a lower incidence angle, the surface was smooth, and the nanoripples were created at 40° and 50° for 50 *keV* and 10 *keV* beam energies, respectively. With a further increase in the incident angle beyond 75°, nanoripples were broken down. Therefore, the morphological evolution of the diamond surface under the FIB bombardment can be categorized into three stages with increasing incidence angle, (i) a smooth surface, (ii) a surface with well-defined ripple topography, and (iii) a surface with broken ripple topography.

The wavelength of nanoripples was observed to be increasing with the increase in the ion beam energy; however, the ion flux did not affect the wavelength of nanoripples on the diamond surface [46]. The evolution of nanoripples wavelength, amplitude and dependency on the critical incidence angle was found to be following the predictions made by MCB theory expressed by equation 2.2 [46]. Keller et al. reported tuning and repairing of nanoripples by sequential ion beam sputtering at different angles after the formation of ripples. After the formation of the ripple of order 25 *nm* at the first step, the sample was rotated at an azimuth angle 90° and the second sputtering at a grazing angle with low energy was achieved. This resulted in increasing the order for ripples obtained after the first step of irradiation [47]. In this study, it was shown that the quality of nanoscale ripple patterns could be considerably improved by sequential ion-beam sputtering, which acts like cleaning and repairing defects. During sputtering at grazing incidence, when the ion beam is oriented parallel to the ripples, the density of topological pattern defects decreases exponentially with fluence. The authors reported 40% reduction in defect of nanoripples, keeping the order of 25 *nm* persistence. This research shows a novel way to improve nanoripples without disturbing the already obtained structures.

Aziz et al. reported an interesting evolution of nanoripples formation via ion sputtering on Si (111) surface and tried to quantify the order of ripple formation [48]. Ion irradiation with uniform energy was used in order to achieve the spontaneous formation of ripple and dot patterns. The effect of variations in fabrication conditions and ion parameters, such as current density, ion flux and ion energy, on the nanostructures formed on Si (111) surfaces were studied. It was observed that for low and high fluences, the modes of ripples were parallel and perpendicular, respectively, to the ion beam projection. In the intermediate case, the parallel ripples were being cut by the perpendicular ripples. This phenomenon also got strengthen by quantification of normalized defect density, the high defect density at intermediate state can be attributed to features that have maximum defects in ripple structures. Variation in nanoripples with ion energy was studied, and it was observed that one could get fine and ordered nanoripples for the higher bombardment energies. At 1000 *eV*, both ripple modes were observed, but only single-mode ripples were observed for other energies. The actual reason for this phenomenon has not been understood yet. However, it was clear that for higher bombardment energies, the order was high. This phenomenon of appearance of both the parallel and perpendicular ripple mode can lead to the formation of a highly ordered and closely packed 2D array of nanodots [48].

It has been known that nanoripples can be fabricated by the non-normal bombardment of FIB on surfaces. Nanoripples can be achieved with high-order and uniform amplitude with the optimization of FIB parameters depending on the surface. In general, ripple formation is explained by Bradley-Harper mechanism [5] with ion incidence on the non-normal angle beyond a certain critical angle [31,40,46]. However, Aziz et al. in 2003 reported rare and spontaneous ripple formation on normal FIB bombardment attributed to linear propagation of FIB induced micro-explosions in the FIB scanning direction [49].

The nanoripples in Figure 2.9 were fabricated on the germanium with 30 *keV* Ga^+ FIB, and the raster scanning was performed with 50% beam overlap, and the ion dose was 1.04×10^{18} ion/cm^2. The observed orientation of ripples in the direction of fast scanning was further confirmed by changing the raster scanning direction. It can be seen in Figure 2.9 that ripples are oriented in the fast scanning direction, and for the raster scanning by 90°, the ripples are aligned with the new orientation (Figure 2.9(b)). Also, for the spiral scanning from the center to the outward direction, the ripples were spirally oriented (Figure 2.9(c)). These results are interesting to create the desired patterns by varying ripples orientation, but the approach is not preferable for highly ordered nanoripples.

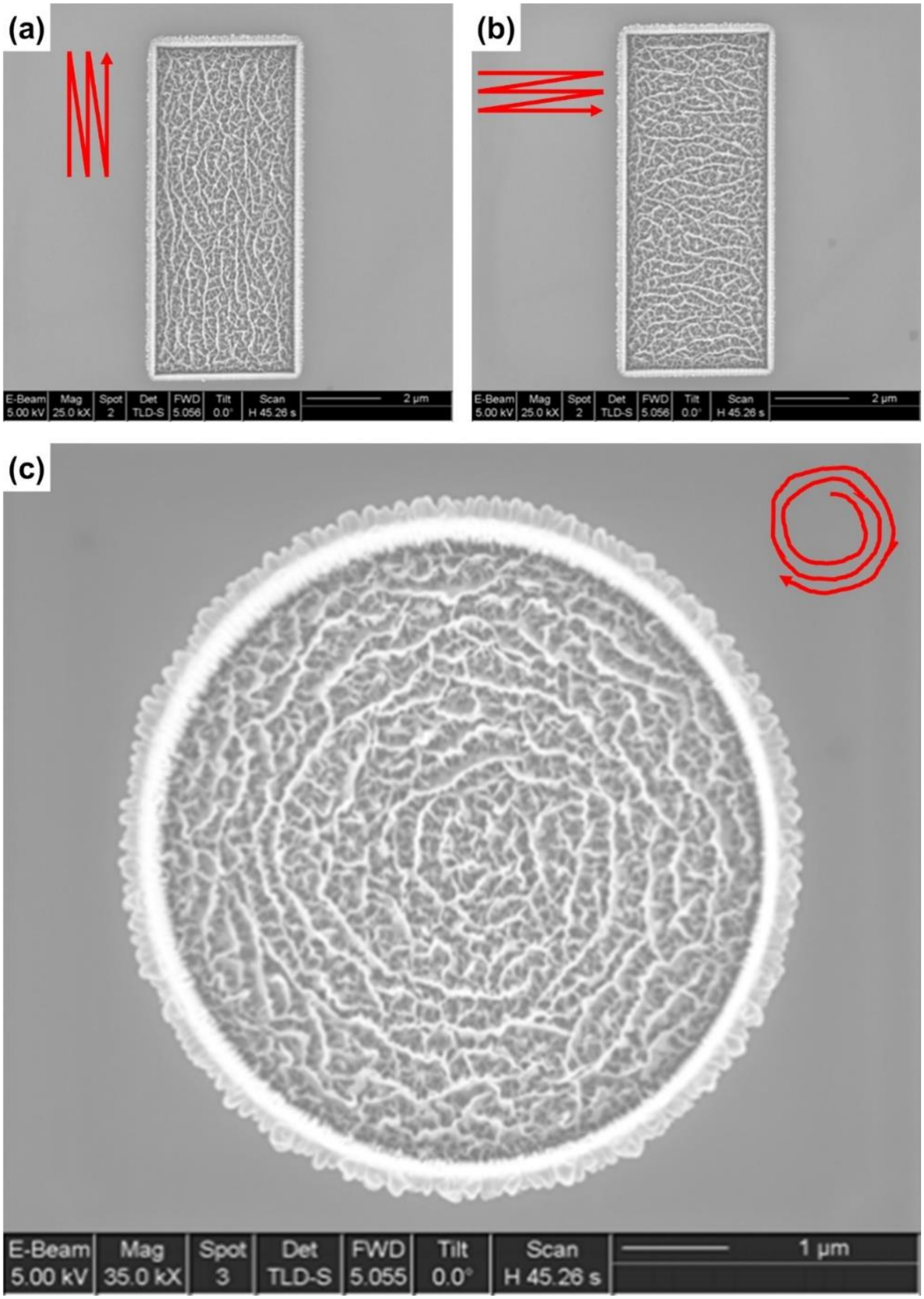
(a)
E-Beam
5.00 kV
Mag
25.0 kX
Spot
2
Det
TLD-S
FWD
5.056
Tilt
0.0°
Scan
H 45.26 s
2 µm
(b)
E-Beam
5.00 kV
Mag
25.0 kX
Spot
2
Det
TLD-S
FWD
5.056
Tilt
0.0°
Scan
H 45.26 s
2 µm
(c)
E-Beam
5.00 kV
Mag
35.0 kX
Spot
3
Det
TLD-S
FWD
5.055
Tilt
0.0°
Scan
H 45.26 s
1 µm

Figure 2.9 FIB induced nanoripples on germanium surface. SEM images showing that the ripples tend to orient towards the fast scan direction, as indicated by red arrows [49].

2.2.2.2 Nanodots

Self-organized nanostructures by FIB irradiation are not just limited to the nanorippled structures, but size and site-specific nanodroplets and nanoparticles can also be created by FIB irradiation [50–53]. Ga nanodroplets are created by raster scanning Ga^+ FIB over GaAs surface [51,50]. The incident angle of the ion beam can control the droplet diameter; increasing the incident angle decreases the size of the resultant droplets, as shown in Figure 2.10.

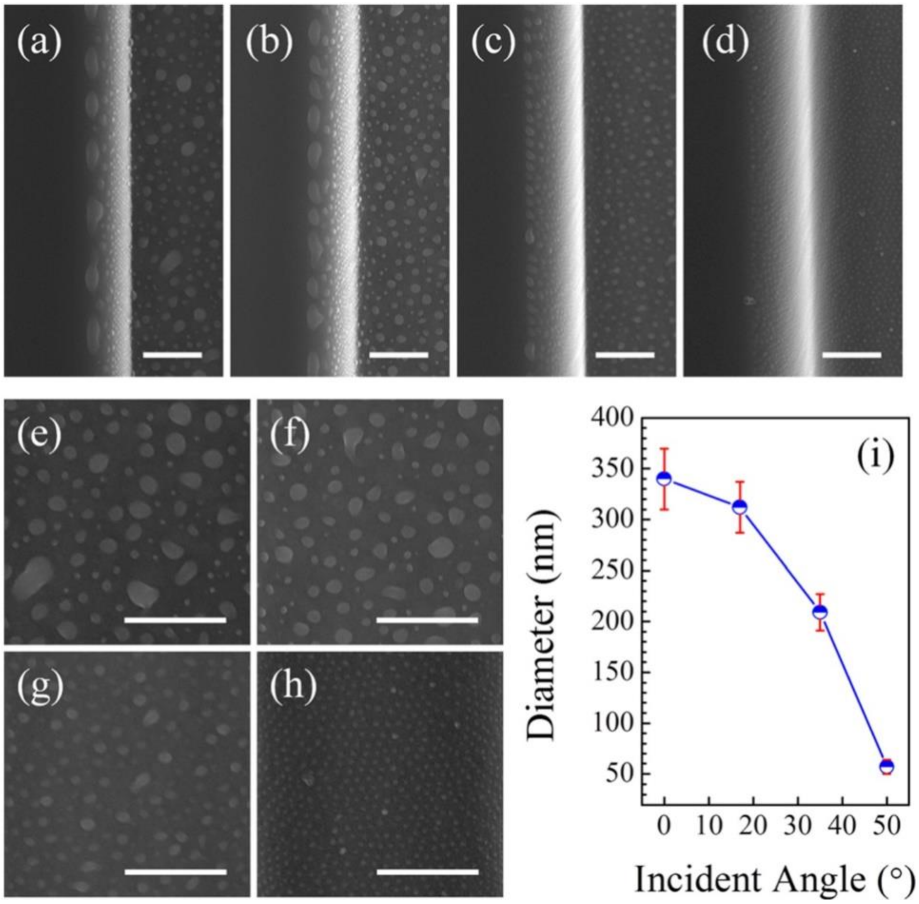

Figure 2.10 SEM images of FIB induced Ga droplets on the surface of GaAs at different incident angles of the ion beam [50]. Droplets over the edge and trench of the scanned region are shown with varied incident angles: (a) 0°, (b) 17°, (c) 35°, (d) 50°. Corresponding SEM images inside a trench are shown in (e)-(h). (i) The diameter of nanodroplets with the function of the incident angle of the ion beam. The scale bar is 1 μm.

The higher sputtering rate for As atoms from the surface of GaAs plus impinging Ga ions lead to Ga rich surface, which results in the formation of Ga droplets. An increase in the ion beam irradiation time increases the diameter of Ga droplets. These droplets are sparsely distributed over the surface, but it is important to note that they are not periodically spaced.

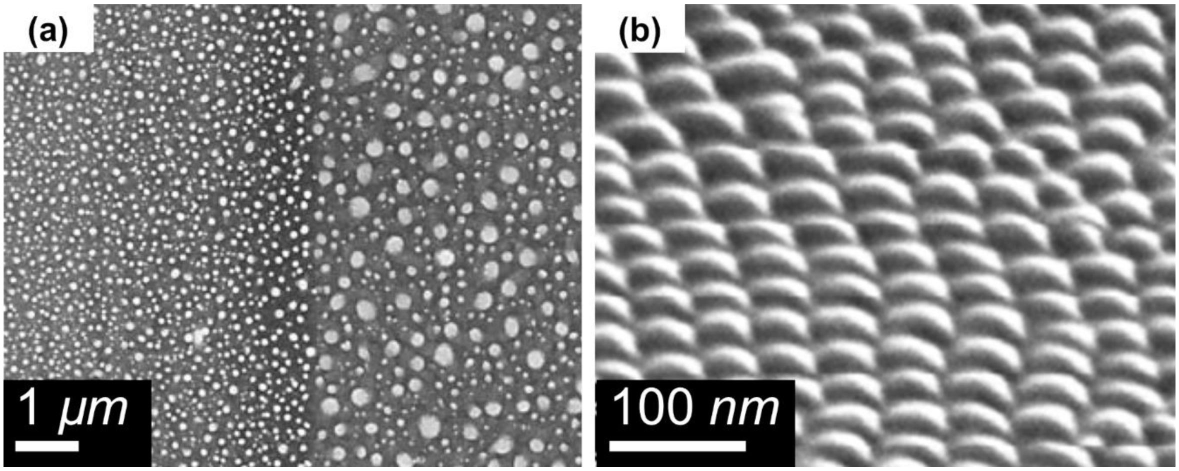

Figure 2.11 FIB induced nano and micro dots. (a) Indium nanodots on InP (100) surface [54] and (b) nanodots on beryllium surface [55].

The instinctive formation of indium nanodots on InP (100) surface via focused ion beam irradiation was reported to be uniformly distributed over the surface [54]. The formation of these nanodots was not only attributed to self-organization but also due to the surface becoming indium-rich during the ion beam irradiation. During the Ga^+ FIB irradiation in a serpentine manner, the indium atoms aggregated and formed microscale droplets on the surface (see Figure 2.11(a)). It is evident from the SEM image that the low ion fluence ($8.7 \times 10^{15}\ cm^{-2}$) created smaller dots (left), and the high fluence ($1.7 \times 10^{16}\ cm^{-2}$) resulted in bigger dots (right) due to excess aggregation. The size of the smaller nanodots is around 42 *nm* in diameter and 7 *nm* in height. Another exciting example of nanodots formation with focused ion beam induced self-organization is on the beryllium surface, as shown in Figure 2.11(b) [55]. These quasi-periodic nanodots are formed due to the differential etch rate along the polycrystalline beryllium surface during the ion beam treatment. These reports suggest the possibility of density-controlled and size-controlled nanodots with varying parameters of FIB. However, these surface structures are either quasi-periodic or sparsely distributed, and they do not form periodic arrays on the surface.

2.2.2.3 Nanoholes

Germanium is an interesting material when considered self-organization with ion beam irradiation, as it can produce nanoripples and porous surface (with nanoholes) on ion beam treatment [49,56,57]. Roman et al. studied the transformation of the smooth surface of germanium to nanohole patterns to sponge-like porous structures with fast scanning of focused ion beam [57]. The authors recognized that the formation of holes and sponge-like layers is driven by the kinetics of the ion beam induced defects and viscous flow along the exposed germanium surface. The hexagonally shaped and quasi-ordered nanohole patterns were reported on the germanium surface with Ga^+ broad ion irradiation as well as fast scanning of Ga^+ focused ion beam (see Figure 2.12) [56].

Transmission electron microscopy (TEM) images (see Figure 2.12(c & d)) show that the holes have significantly less aspect ratio and they can be termed as surface features due to low depth of around 10 *nm*. In both cases, the energy of bombarded Ga^+ ions was set as low as 5 *keV*. The dose required for the identical morphologies was five times lesser in the case of broad ion beam irradiation than that of the focused ion beam. This suggests that the surface coverage is more critical than the ion dose for this kind of nanoholes on a germanium surface. Authors have claimed that (i) the ion-induced drift and (ii) selective sputtering is the driving force behind the occurrence of surface instabilities during ion beam irradiation [57]. The instability mechanism induced by the competition between these two effects leads to the morphology evolution towards the relaxed surface having nanoholes.

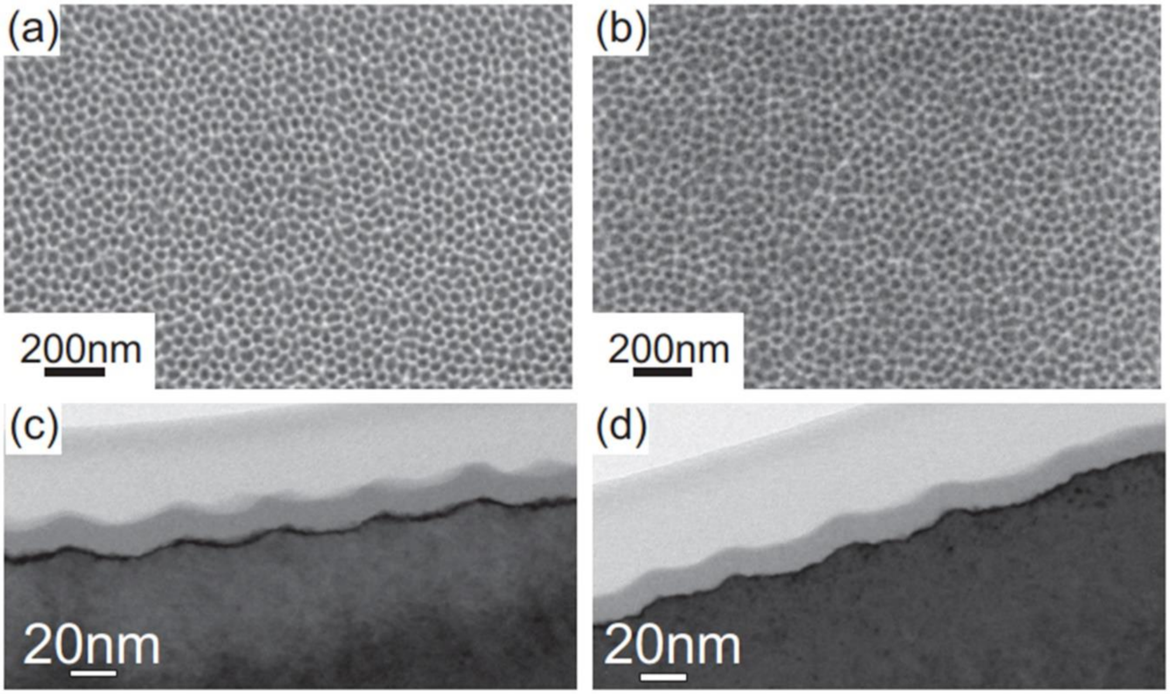

Figure 2.12 SEM images of nanoholes induced by (a) FIB irradiation and (b) broad ion beam irradiation [56]. Cross-sectional TEM images of nanoholes induced by (c) FIB irradiation and (d) broad ion beam irradiation.

Again, it should be noted that these nanodots (Figure 2.12) are surface features with a depth of about 5 to 10 *nm*, and they are quasi-periodically arranged. The nanostructures which are entirely due to self-organization without any material removal are having low-aspect-ratios [55,56]. The attempt of alignment control during the FIB induced self-organization leads to erosion of some material (Figure 2.9), and it creates quasi-aligned structures with high-aspect-ratios [49]. Hence, further optimization of FIB parameters can lead to the realization of complex morphologies with high periodicity.

2.2.3 Molecular dynamics (MD) simulations for self-organization

The atomic-level studies like classical molecular dynamics (MD) simulations are useful to investigate interactions of the energetic ion beam with materials. Sule and Heinig reported in 2009 that using the proper pseudo-potentials and the system, the MD simulation can be carried out to understand the nano-ripple formation on Si surface under non-normal Xe^+ ion beam irradiation [58]. They used Tersoff potential for Si crystal and Ziegler–Biersack–Littnark (ZBL) [59] repulsive potential for ion-atom interactions. The simulation results are shown in Figure 2.13. To reduce the simulation time, the pre-predicted erosion modal was used to create an initial simulation set up of the ripples, as shown in Figure 2.13(a). This was a sinusoidal model of generated ripples. Once simulation initiated, with impact of 1000 *ions*, the grown ripples appeared as shown in Figure 2.13(b) and cross-section in Figure 2.13(c).

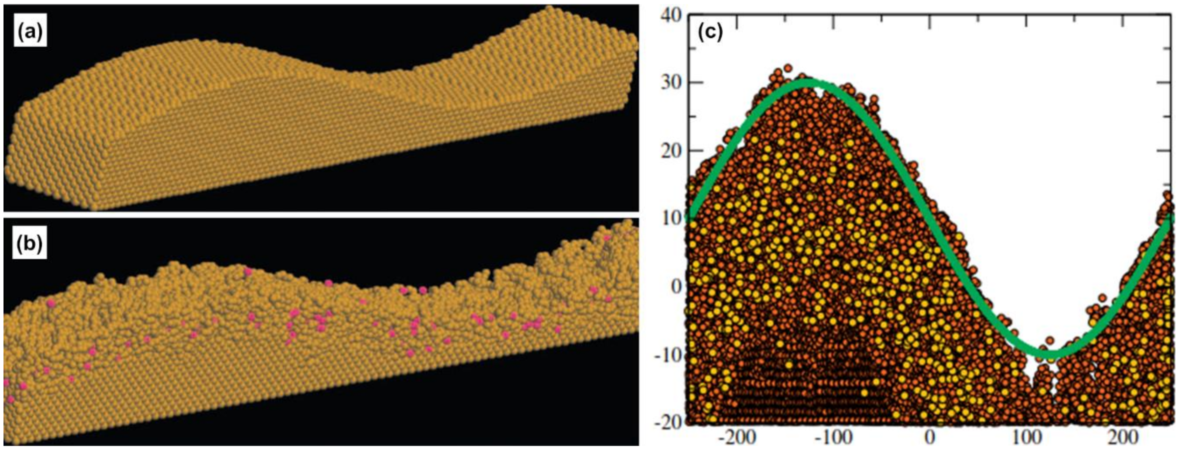

Figure 2.13 The screenshot of the simulation box, initially wavelength was 50 *nm* (a) before impact and (b) after the impact of 1000 ions. (c) cross-section of grown ripple after 1000 ion dose (the solid line indicates the initial state of ripple) [58].

With further increase of the ion dose during the above simulation, it was observed that the ripple growth was persistent, and the saturation demonstrated the wavelength and ripple height, as shown in experimental observations [46,58]. Though the above simulations appear identical to experimental observations, they are incomplete. These simulations are limited to already grown ripples, and the generation of ripples has not been considered. However, the simulations confirm that the replication of self-organized ripple induced by ion beam can be simulated with certain limitations with careful considerations and assumptions.

Attempts to study the interactions between impinging ions and the atoms of the target surface to study self-organization dynamics were reported to be made with atomistic simulations using MD methods [60–67]. The formation of nanopores via focused ion beam milling on the graphene was reported by MD simulations for the interactions of energetic ions with graphene sheets [65,66]. It was determined that not only cutting of nanopores but also joining of graphene layers at the edges of nanopores was possible using ion beam irradiation. The MD simulations can also be utilized to investigate defects and alteration of mechanical properties due to ion beam irradiation [68]. It was observed that the extent of crystallographic damage and morphology of nanoholes on the crystalline silicon substrate is dependent on the orientation of the exposed facet and incident angle of ion bombardment [67].

Recent reports on MD simulations using LAMMPS (Large-scale Atomic/Molecular Massively Parallel Simulator) for interactions of Ga^+ ion beams with germanium and silicon surfaces utilize hybrid Stillinger−Weber (SW) & ZBL potentials [59,69,70]. The interactions between Ge−Ge and Si−Si was defined by the modified Stillinger−Weber (SW) potential [70], and the high-energy collision interactions between Ga^+ and Ge atoms (or Ga^+ and Si atoms for silicon) was defined by the Ziegler–Biersack–Littnark (ZBL) potential [59,62]. The MD simulations can reveal important insights to understand the ion beam induced damage on the materials [67,67,71]. From the MD simulations, the change in the temperature due to ion beam irradiation can be predicted using the average kinetic energy of the atoms at a specific region [72]. In order to investigate the effect of the ion beam on the materials, it is required to bombard ions with a particular interval of time. This ensures that the system is stabilized against the sudden increase in temperature due to kinetic energy transfer from incident ions to the atoms of the sample [62]. The information acquired by MD simulations such as morphology evolution, crystallographic phase transformation, local heating induced effects due to temperature spike, material self-diffusion, and induced strains can be useful to predict and understand the ion beam induced self-organization process.

2.3 Summary

In summary, the fabrication of self-organized nanostructures by focused ion beam is discussed. Self-organized nanoripples, nanodots, and nanoholes have been reported to be formed by broad and focused ion beam irradiation on various surfaces. When irradiated with an ion beam, the atoms in the convex region erode faster compared to the concave regions providing selective erosion and micro-scale explosions, which lead to reorganization of the surface atoms resulting in the formation of self-organized nanostructures. The dimensions and periodicity of the self-organized nanostructures depend on the surface properties and ion beam parameters. As the low dose is required, the self-organizing process using a focused ion beam is faster compared to the FIB milling process, which gives the advantage of large throughput on nanofabrication. Though nanostructures are easy to produce with the self-organization technique, the lack of control over structures in terms of periodicity and uniformity limits their application. There is also a lack of reports on morphology controlled self-organized geometries such as squares (and other higher-order polygons) with periodic spacing. Hence, fabricating 3D complex nanostructures with higher aspect ratios such as polygonal geometries is a challenge.

Chapter 3

Improved Enhancement Factor for SERS using Broad Ion Beam Induced Self-Organized Gold Nanocones

This chapter presents sparsely distributed and self-organized gold-nanocones fabricated by broad argon ion beam sputtering on the gold and silicon surfaces with grazing incident angle. The rotation of the sample with respect to the vertical axis has been found to influence the morphology of the obtained nanostructures. The ion beam irradiation of the gold sample leads to the formation of nanoripples when the sample is held stationary; otherwise, nanocones are formed if the sample is rotated during irradiation. A hybrid gold-nanocone/graphene/gold-nanohole based surface-enhanced Raman scattering (SERS) sensor is proposed and shown to exhibit an enhancement factor of 10^9 via finite-difference time-domain (FDTD) simulations.

3.1 Introduction

Ion beam sputtering is a widely used tool as a mask-assisted dry etching tool for the fabrication of MEMS (Micro-Electro-Mechanical Systems) and electronic devices. This work aims to achieve uniformly distributed and large-scale nanostructures on metal and semiconductor surfaces using a mask-less fabrication route. Recently ion beam sputtering (IBS) technique has attracted researchers towards its capability of forming nanostructures via self-organization of the surface atoms. Surface erosion and strain induced by ion beam bombardment result in the reorganization of surface atoms to minimize the surface energy, and nanostructures are formed on the surface. During the ion erosion, the atoms in the convex region erode faster compared to the concave regions [5]. Such selective erosion and micro-scale explosions lead to reorganization of the surface atoms resulting in the formation of self-organized nanostructures. Suitable parameters of IBS lead to a mask-less fabrication of uniformly distributed nanostructures on the surface, like gold nanowires on polycrystalline gold film [13]. The authors reported that in order to produce gold nanowires, the polycrystalline gold film (thermally coated on soda-lime glass) was bombarded by a broad argon ion beam of 800 *eV* at a grazing angle (82° with respect to the surface normal), with 5.5×10^{14} *ions/cm*^{2} ion dose [13]. The technique has also been demonstrated for producing transparent and conducting aluminium nanowires [11]. In this process, the ion beam energy was kept at 800 *eV*, and the incident angle of the ion beam was 82° with respect to the surface normal. During argon ion treatment, the chamber pressure was kept at 4.4×10^{-4} *mbar*. Silicon nano-cones formation on low energy ion beam irradiation has been widely studied by researchers [73–75]. Ming Lu et al. reported 1.5 *keV* Ar^+ induced nano-cone structures on silicon (100) surface in the presence of stainless steel as a sacrificial layer kept adjacent to the exposed area of the silicon sample [73]. They reported that randomly distributed nanoscale Fe and Cr clusters were formed due to the re-deposition of sputtered atoms from stainless steel. These clusters acted as masks, and nano-cones were formed on further sputtering of silicon surface [73]. On changing the incident angle of the argon ion beam from 63° to 83°, Basu et al. reported nano-ripple transition from parallel (in this case, wave vector is parallel to projected ion beam) to perpendicular mode. However, in the intermediate state at 72.5° incident angle, nano-cones were obtained [73]. It was also reported that the nano-cone formation on silicon, by ion beam irradiation at 600^{o}, was independent on the crystallographic orientation of silicon surface but it was strongly dependent on the co-deposited elements on the surface from adjacent sacrificial metal [75]. Gold nanodots and nanocone surfaces are also interesting due to their potential applications such as local surface plasmon resonance based enhanced molecular sensing [76,77]. However, the ion beam irradiation has to be controlled, and sputtering parameters have to be optimized to get gold nanocone/nanodots over the surface.

Surface-enhanced Raman scattering (SERS) is a widely used technique to develop high sensitive molecular sensing devices using metal nanostructures [78,79]. Several nanostructures have been reported for SERS applications such as gold nanoparticles [76,80], gold nanowires [13], silver nanoparticles [81], gold nanovoids [82], and dried silver colloids [83,84]. Though metal nanospheres have been widely utilized as SERS substrates, sandwiched nanostructures with nanometer-sized gap have been shown to enhance the SERS signal significantly [13,76,78,80,82]. Hybrid nanostructures such as metal/2D-materials, metal-nanostructures/2D-materials have been studied extensively, as reported in the reference [78]. In these studies, the metals used are gold, silver, or copper and 2D-materials are graphene, single-layer molybdenum disulfide, or boron nitride. The use of graphene as an atomically thin spacer between silver nanoparticles has been shown to provide a huge improvement in the enhancement factor as the near-field enhancement and scattering depend on the geometry and the dimensions of nanomaterials [78,79,85]. Raman scattering, being a non-linear process, the direct prediction of signal by simulations is difficult. However, the signal enhancement can be estimated by measuring the extent of scattering enhancement numerically via finite-difference time-domain (FDTD) simulations. The enhancement factor (EF) is taken as [76,81],

$$\mathrm{EF} = \left(\frac{|E|}{|E_0|}\right)^4 \tag{3.1}$$

Where E is the local maximum electric field, and E_0 is the input source electric field [76,81]. Closely placed metal nanostructures undergo strong LSPR (localized surface plasmon resonance) coupling, and huge SERS enhancement can be achieved. For example, the EF of 2.1×10^6 for silver nanoparticles over graphene/silicon substrate was reported demonstrating the advantage due to graphene [81,86].

In the following sections, the formation of self-organized and sparsely distributed nanocones on the gold and silicon surface is experimentally demonstrated via argon ion beam bombardment. The effect of a sample rotation is studied on the final morphology of the nanostructures. By utilizing the morphology of obtained gold nanocones, a high enhancement factor of SERS is predicted from the hybrid gold-nanocone/graphene/gold-nanohole tri-layers system via FDTD simulations.

3.2 Experimental details

In order to get nanostructured surfaces, grazing-angle argon ion beam bombardment was performed on the gold and silicon surfaces. A gold film of 95 *nm* thickness (5 *nm* chromium for adhesion) was thermally deposited on glass using a thermal evaporator (Vacuum Coating Unit, Model 12A4D; Hind HiVac, Bangalore, India) at 1×10^{-6} *mbar* pressure. Before the experiment, silicon (100) wafers were cleaned using RCA solution. Subsequently, the silicon wafer was cleaned by ultra-sonication in an acetone bath and de-ionized water bath. Finally, before using for the experiment, the wafer was dried using nitrogen gas. At room temperature, the gold surface was treated by grazing-angle (at 82° to the surface normal) argon ion beam (KDC 40 4-cm DC ion source; Kaufman & Robinson, Inc., Fort Collins, USA) irradiation with accelerating voltage 400 *V* and current 42 *mA*. The chamber pressure was maintained at 6.1×10^{-4} *mbar*, and the specimen was irradiated for 1020 *s* to get the total ion dose of 2.168×10^{16} $ions/cm^2$. The ion beam irradiation experiment was repeated for the silicon surface with keeping source and chamber parameters the same.

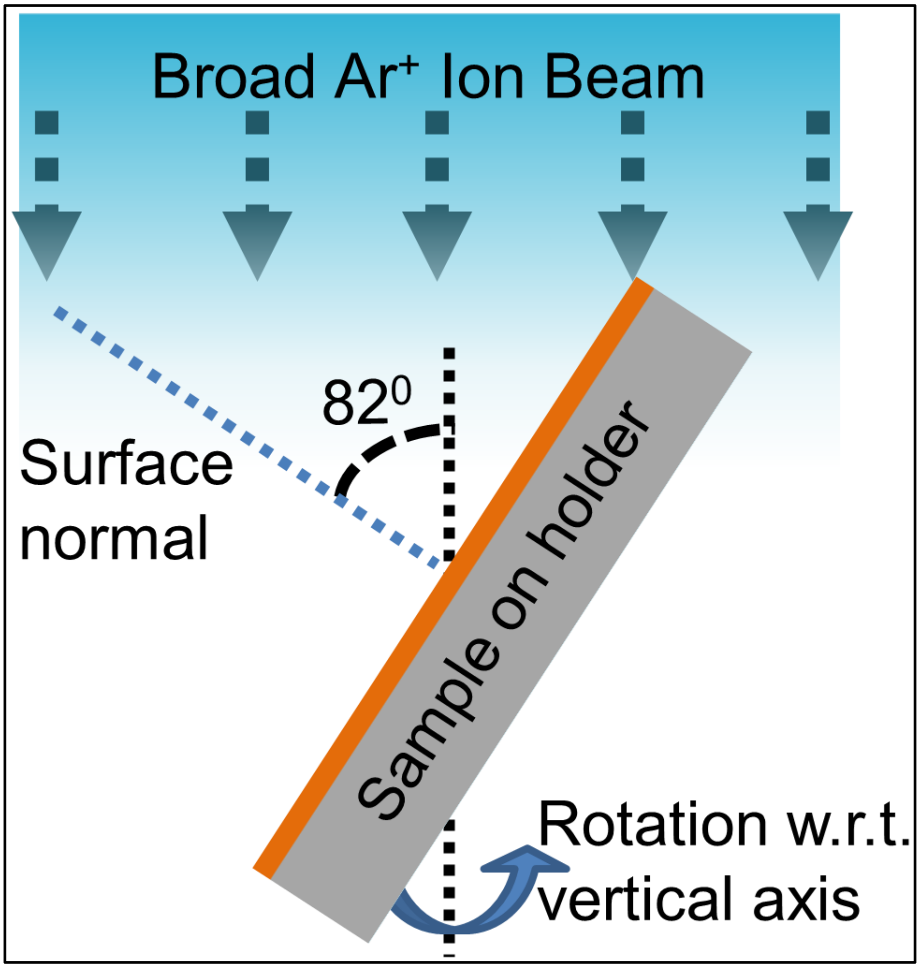

Figure 3.1 Schematic of the IBS experiment. Sample (Au-on-quartz or silicon wafer) on a rotating sample holder under ion beam irradiation.

The schematic of the experimental setup is represented in Figure 3.1. The sample holder was made up of copper, and there was a provision of rotating the sample holder on its vertical axis by 30 *revolutions per minute* (*rpm*). Hence, in order to obtain different morphologies of the nanostructures, the experiment was carried out with- and without- rotation of the sample with respect to the vertical axis.

The atomic force microscope micrographs were obtained using the Agilent 5500 scanning probe microscope (Agilent Technologies). Scanning electron microscopy (SEM) and energy-dispersive X-ray spectroscopy (EDX) was carried out for the characterization of nanostructures using the field emission gun-scanning electron microscope (FEG-SEM) model JSM-7600F FEG-SEM (JEOL Ltd.). Further UV-visible reflection characterization was performed using LAMBDA 950 UV/Vis Spectrophotometer (PerkinElmer).

3.3 Results and discussion

In order to investigate the evolution of nanostructures, the morphology investigations are crucial to carrying out using atomic force microscopy and scanning electron microscopy (SEM). Also, energy-dispersive X-ray spectroscopy (EDX) was performed to obtain the details of elements present on the surface of ion beam treated samples. As the aim is to study enhancement in the optical properties of the nanostructures, the optical absorption behavior was captured using UV-Vis spectroscopy.

3.3.1 Morphology investigations via atomic force microscopy (AFM)

Atomic force microscopy (AFM) images of the obtained structures on the gold surface can be seen in Figure 3.2. It can be observed that the formation of nanoripples (Figure 3.2(b)) occurs without rotation of sample during the ion beam sputtering, and nanocones (Figure 3.2(c & e-g)) are formed when the sample is rotated with respect to the vertical axis during ion beam irradiation. High and low-resolution AFM images at different rotational angles in Figure 3.2 show that the majority of the nanostructures are conically shaped. Though some nanostructures resemble nanodots, and others are irregularly shaped, a large proportion of the nanostructures retain the pointed geometry. Thus, in general, the shape of nanostructures could be categorized as a nanocone for numerical studies using FDTD simulations.

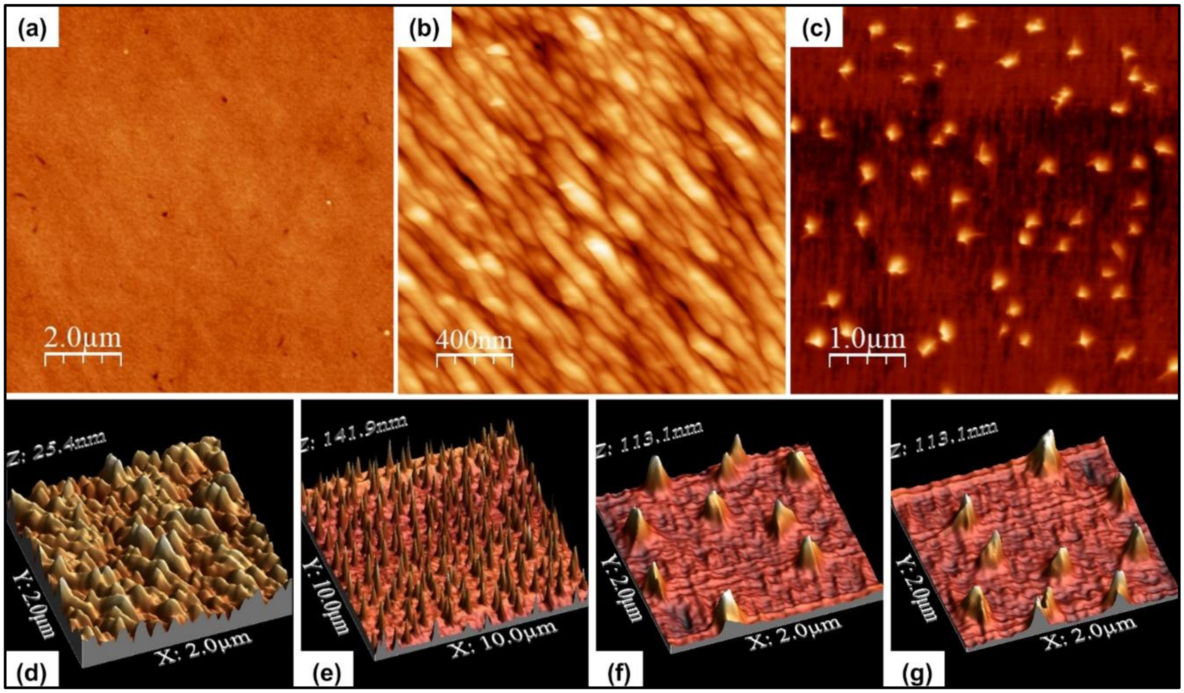

Figure 3.2 AFM images for gold nanostructures. (a) The bare gold surface, (b) obtained nanoripples without sample rotation during IBS, and (c) obtained nanocones with sample rotation during IBS. (d & e) shows the three-dimensional representation of (b & c). (f & g) 3D representation of nanocones acquired via AFM from different angles.

It is observed that the base diameter of the cone is ranging from 110 to 250 *nm*, and the height of the cone is ranging from 20 to 200 *nm*. The aspect ratio of the nanostructures is ranging from 1 to 2, and the average aspect ratio is about 1.5. The average surface roughness is 1.6 *nm* and 14 *nm* for bare and treated surfaces, respectively. When energetic ions are bombarded on the surface, surface erosion and diffusion occur, competition between them leads to the formation of convex and concave regions over the surface [5,13]. Due to the geometry of the convex region, diffusion and erosion rate for atoms on the convex surface is higher than that of the concave surface, which leads to the formation of self-organized nanostructures such as nanoripples and nanowires [5,13]. In the present work, the rotation of the specimen with respect to the vertical axis leads to the formation of broken nanoripples. And, with a suitable dose of 2.168×10^{16} $ions/cm^{2}$, conically shaped self-organized nanostructures are formed instead of nanoripples/nanowires.

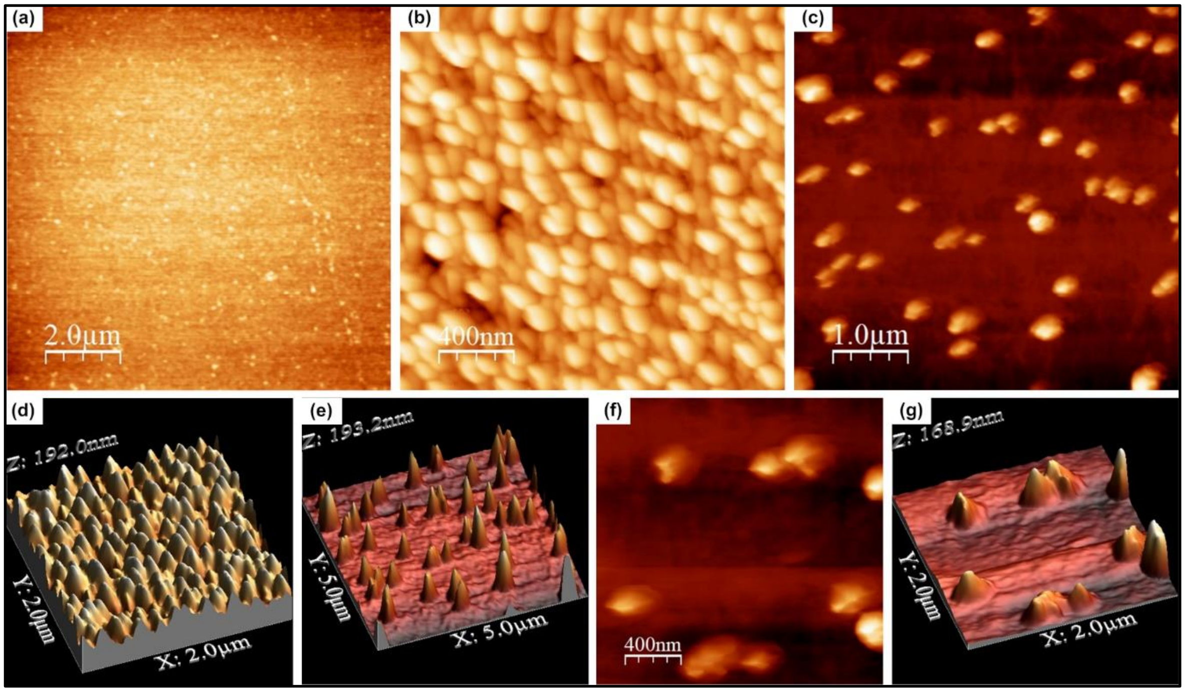

Figure 3.3 AFM images for silicon nanostructures. (a) The bare silicon surface, (b) obtained densely distributed nanocones without sample rotation during IBS, and (c) obtained sparsely distributed nanocones with sample rotation during IBS. (d) & (e) represents the three-dimensional views for (b) & (c), respectively. (f & g) are high-resolution images for obtained nanocones in (c).

In the case of the silicone surface, the surface underwent identical morphological changes in either state of sample rotation. Nanocones are observed to be formed in both the rotation conditions for silicon surface. As seen in Figure 3.3(b), silicon nano-cones are more densely distributed over the surface when the sample is steady. While nanocones are less sparsely distributed when the sample is rotated with respect to the verticle axis (Figure 3.3(c-g)).

For the silicon surface, the base diameter of the nanocone is ranging from 150 to 300 *nm*, and the height of the cone is ranging from 50 to 130 *nm*. Without rotation, the average surface roughness for nanostructured silicon was 24 *nm*. When samples were treated with rotation, the average roughness for silicon nanostructures was 27 *nm*. It is evident from the average roughness measurements that the crest and troughs of the nanostructured surface on silicon is having the same range for both the experiments and unlike the gold surface, it does not depend on the rotation condition of the sample holder.

3.3.2 Characterizations via scanning electron microscopy (SEM)

Scanning electron microscopy and energy-dispersive X-ray spectroscopy characterization of samples were carried out using the field emission gun-scanning electron microscope (FEG-SEM) model JSM-7600F FEG-SEM (made by JEOL Ltd.). Figure 3.4 shows SEM images for bare as well as nanostructured surfaces of gold and silicon. It could be observed that nanostructures are uniformly distributed on both surfaces. It is also noted that the bare surfaces are cleaned and completely smooth. While after the broad ion beam treatment, surfaces are showing some morphological changes. In these experiments, as the ion bombardment is in grazing angle (82°) with respect to the surface normal, less kinetic energy is imparted on the surface atoms. Thus, the sputtering would be relatively less compared to the situation where ion beam bombardment is normal to the surface. Therefore, the morphological evolution would be dominant by the self-organization of surface atoms instead of sputter induced structures.

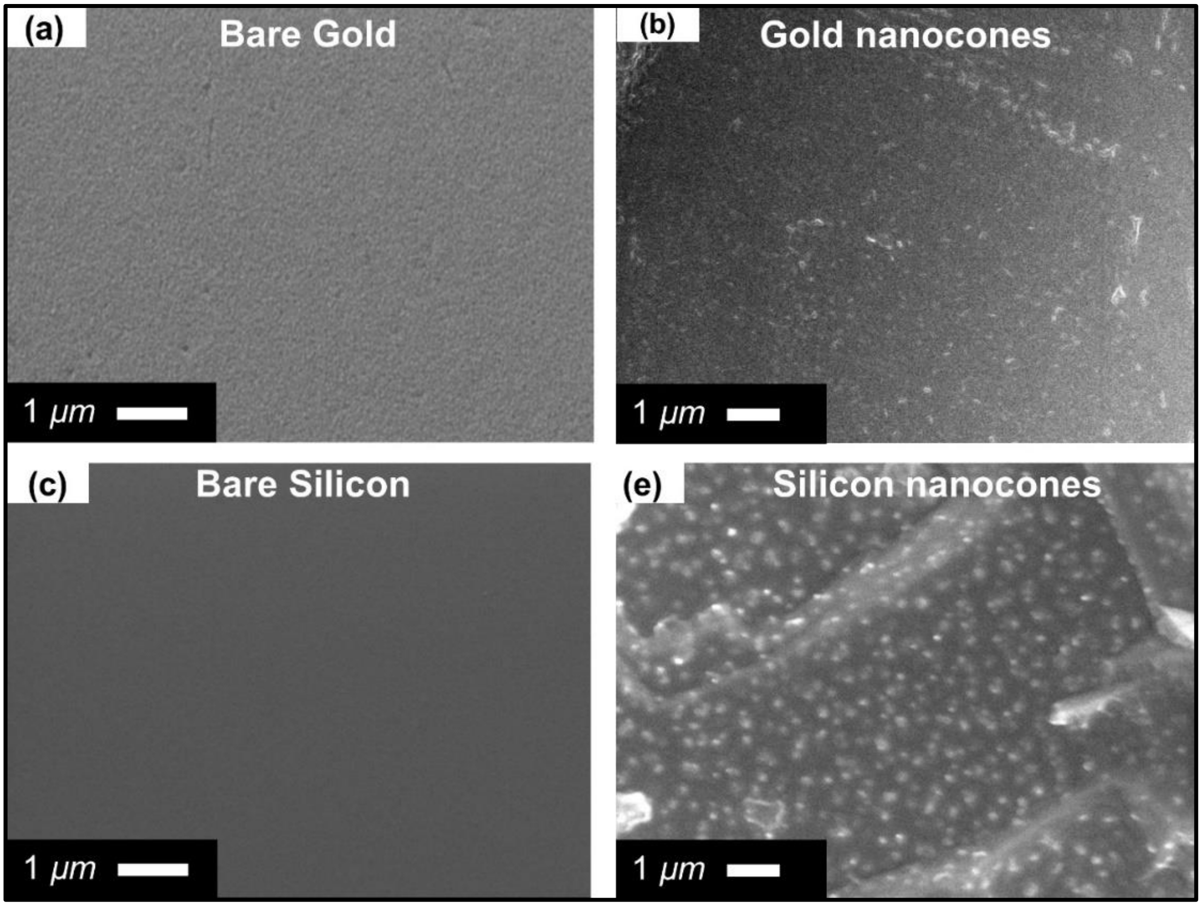
(a)
Bare Gold
1 μm
(b)
Gold nanocones
1 μm
(c)
Bare Silicon
1 μm
(e)
Silicon nanocones
1 μm

Figure 3.4 SEM images of gold and silicone surfaces. (a & c) bare surfaces and (b & d) nanostructures formed with sample rotation during IBS.

Table 3.1 Energy-dispersive X-ray spectroscopy (EDX) results for bare surface and nanostructured surfaces.

Gold surface			**Silicon surface**	
Element	Wt% (Treated surface)	Wt% (Bare surface)	Wt% (Treated surface)	Wt% (Bare surface)
C	13.87	16.07	13.17	11.21
O	--	1.68	--	--
Si	10.29	12.37	81.58	74.06
Cr	0.82	0.94	--	--
Ni	1.49	--	--	--
Cu	7.19	--	5.25	--
Au	66.34	68.57	--	--

The EDX analysis reveals an abundance of gold and silicon atoms on gold and silicon surface, respectively, after the bombardment of argon ions (see Table 3.1). Cr is present in EDX results for the gold substrate because, before thermal deposition of Au on the quartz substrate, a thin Cr layer was deposited to enhance the adhesion of Au with the substrate. The presence of C and Ni is due to the chamber contaminations. It should also be noted that copper atoms of approximately 5 weight percentage are present, post argon bombardment, on the surface of the nanostructures for both gold and silicon samples. The presence of Cu on the surfaces having nano-cones indicates that the Cu atoms sputtered from the sample holder are clustering on the sample surface and helping towards the formation of nano-cones due to selective erosion from the surface [73,75]. The appearance of nanoripples when the gold sample is not rotating suggests an additional role of self-diffusion in nanostructuring of the gold surface on the bombardment of argon ions.

3.3.3 Optical reflectance by UV-Visible spectroscopy

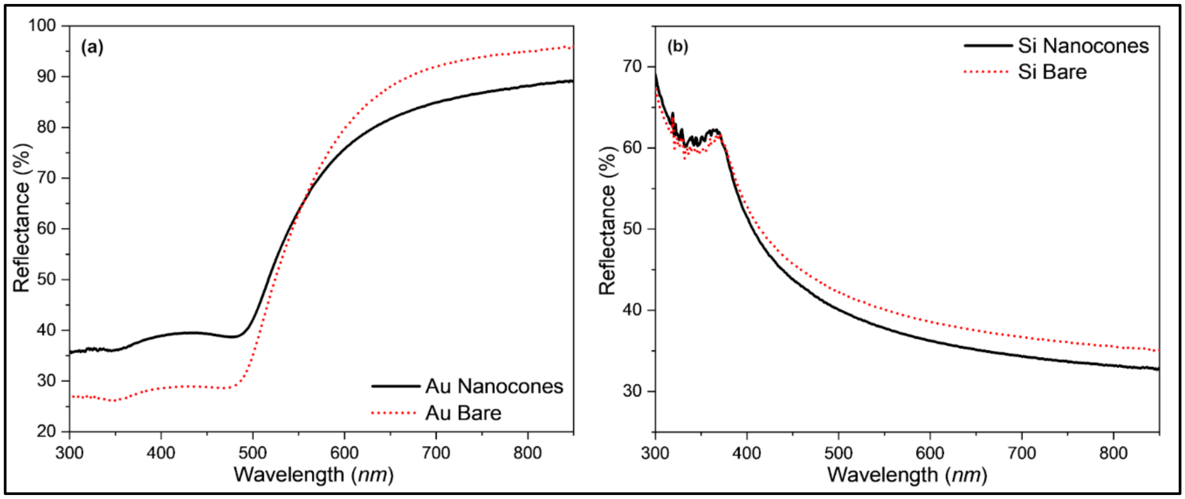

Figure 3.5 UV-vis reflection spectra of nanocones and bare surfaces: (a) for gold surface and (b) for silicon surface.

UV visible spectra were acquired in reflection mode gold structures and silicon structures. The reflection spectra for bare and nanostructured surfaces are shown in Figure 3.5. The optical reflection beyond 530 *nm* was found to be reduced for the gold nanocones compared to the bare gold surface. The optical spectroscopy revealed 7% to 10% low reflection for a gold surface having nanocones compared to bare gold surface from wavelength range 530 *nm* to 1200 *nm*, suggesting the enhanced light-matter interactions for the gold nanostructures. Whereas there was a high reflection for nano-cones compared to the bare gold surface for wavelength below 530 *nm*. In the case of silicon nanocones (Figure 3.5(b)), around 5 to 8 % suppression of reflection for the wavelength range 370 to 850 *nm*.

3.3.4 Optical simulations for a hybrid tri-layered system for improved SERS response using gold nanocones

It has been reported that nanoparticles [76,80], nanowires [13], and nanovoids [82] provide good SERS enhancement; hence, the obtained nanocones can be used for the improved the SERS sensing. In this section, in order to utilize the fabricated nanocones, the tri-layered system of gold-nanocone/graphene/gold-nanohole is proposed for SERS sensing. The performance of the proposed system is evaluated via electromagnetic simulations known as finite-difference time-domain methods using a commercially available numerical solver (Lumericals, Inc., Canada). The proposed tri-layer system could be realized then by growing the graphene on the copper substrate as outlined in reference [87] followed by deposition of a gold film on the graphene layer [88,89]. The nanoholes array can be created on the gold/graphene via employing direct milling with a focused ion beam, and the gold/graphene layer can be transferred over the gold nanocones. However, the current work is limited to the FDTD simulations for the enhancement of the SERS signal from the proposed design.

3.3.4.1 FDTD simulations setup: design and graphene modelling

As shown in Figure 3.6, the graphene is sandwiched between the gold nanocones and the gold nanoholes, which provides an ultra-small gap between the two nanostructures. The thickness of the gold nanohole layer is 10 *nm*, with a nanohole diameter of 30 *nm* and periodicity of 30 *nm* in both *x* and *y* directions. Though the theoretical thickness of graphene is 0.35 *nm*, the measurement attempts have revealed varied thickness due to instrument offsets such as probe tip-sample interactions as well as folding and wrinkling of graphene sheet [90,91]. Hence, in this study, 1 *nm* thick graphene layer was considered for numerical simulations.

There are two modelling approaches available for graphene in FDTD simulations, namely, the surface conductivity approach and the volumetric permittivity approach [92,93]. In the surface conductivity approach, the graphene sheet is defined as a two-dimensional layer with zero thickness. In contrast, the volumetric permittivity approach describes graphene with a finite thickness by expressing the conductivity in terms of volumetric anisotropic permittivity. In our simulations, there is a requirement of defining a finite gap between the nanocone-tip and nano-hole. Due to the positive permittivity of the graphene in the visible range [79,93], it behaves like a dielectric material for the visible light. Hence, in order to account for the finite gap between the two plasmonic structures, the graphene layer is modelled via volumetric permittivity with a finite thickness of 1 *nm*. Fermi energy dependent conductivity of graphene can be expressed using Drude-like approximation [93,94] as follow,

$$\sigma(\omega) = \frac{ie^2 E_F}{\pi\hbar\,(\omega + i\tau^{-1})} \tag{3.2}$$

Where σ is conductivity, ω is angular frequency, e is electron charge, E_F is Fermi energy, $\hbar$ is Plank constant and τ is the relaxation time. Considering charge carrier concentration of 3×10^{13} cm^2 in the graphene, the Fermi level was taken as 0.64 *eV*. The relaxation time is 0.64 *ps*. In order to simulate the graphene layer numerically, the in-plane and out-plane permittivity were defined by the following expression [93,94],

$$\varepsilon_{\parallel} = \varepsilon_{\perp} + \frac{i\sigma(\omega)}{\varepsilon_0 \omega \Delta} \tag{3.3}$$

Where $\varepsilon_{\parallel}$ is in-plane permittivity (along *xy*-plane), $\varepsilon_{\perp}= 2.5$ is out-plane permittivity (along the *z*-axis) and Δ is the thickness of the graphene layer (1 *nm*). In the visible range, the real part of permittivity for graphene is positive; hence, graphene behaves like a dielectric in the visible spectrum of light.

As nanocones are randomly spaced over the surface (Figure 3.2(c & e-g)), three possible geometrical configurations are considered for the FDTD simulations: nanocone is – (i) far from the nanohole, (ii) at the center of the nanohole, and (iii) at the edge of the nanohole (as shown in Figure 3.6(b)). The tip of nanocone is positioned at $x = 0$, $y = 0$ and $z = -1$ *nm*. A view from the *xz* plane in Figure 3.6(c) represents the FDTD simulation setup employed for the study. A TFSF (Total-Field Scattered-Field) source was used to excite the structures in the small domain around the nanocone-tip in order to capture the field enhancements. Using TFSF source allows small simulation regions, as only scattered field reaches up to the boundaries after passing through TFSF source region. The simulation domain was terminated with the perfectly matched layer (PML) boundaries with 32 layers in *x* and *y* directions to completely absorb the scattered field that is coming out of the TFSF source. 8 PML layers were set for *z*-boundaries in order to lessen the requirement of memory.

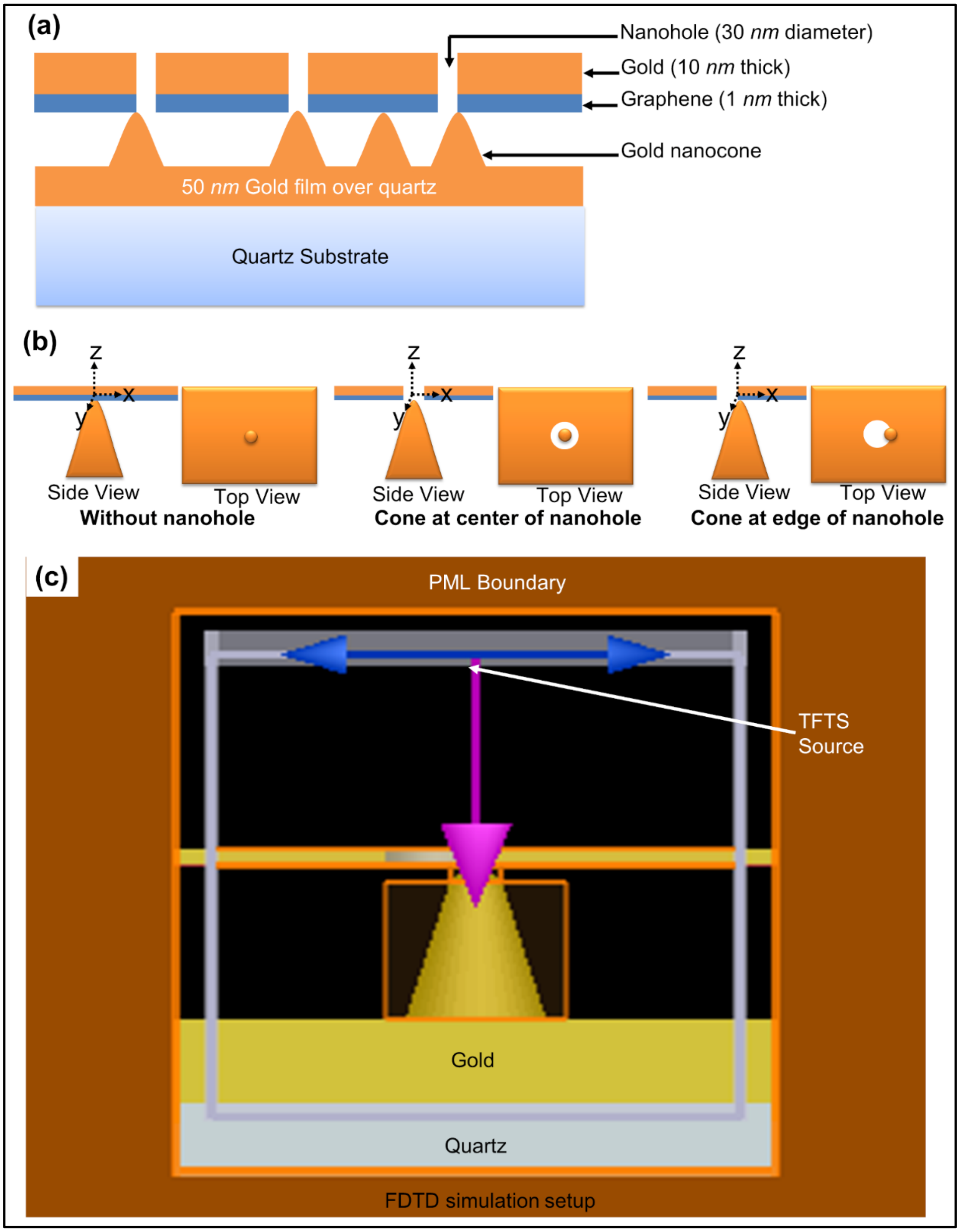
(a)
Nanohole (30 nm diameter)
Gold (10 nm thick)
Graphene (1 nm thick)
Gold nanocone
50 nm Gold film over quartz
Quartz Substrate
(b)
z
x
y
Side View
Top View
Without nanohole
Side View
Top View
Cone at center of nanohole
Side View
Top View
Cone at edge of nanohole
(c)
PML Boundary
TFTS Source
Gold
Quartz
FDTD simulation setup

Figure 3.6 Design of proposed tri-layered system of gold-nanocone/graphene/gold-nanohole for SERS device; (b) different geometrical positions of a nanocone tip with respect to the nanoholes considered for FDTD simulations; (c) FDTD simulation setup when the nanocone is at the nanoholes edge. Nanocone is set with height 90 *nm*, tip radius 20 *nm*, base radius 150 *nm* and cone angle 40°.

In order to take account of 1 *nm* thick graphene, the fine mesh was used along the thickness of the graphene layer. The fine mesh of 0.5 *nm* was set near the cone tip. However, for the graphene, the FDTD mesh was set at 0.05 *nm* in the *z*-direction (along the thickness), and the mesh in *xy*-plane was set at 0.5 *nm*. The ultra-fine mesh along the thickness of the graphene provided 20 mesh points in the graphene layer. The optical constants for quartz were taken from reference [95], and those for gold were taken from reference [96]. Convergence testing was performed to confirm the stability of simulations.

The enhancement factor (EF) is calculated by collecting electric field distribution across three different planes such as *xz* ($y = 0$), *yz* ($x = 0$) and *xy* ($z = -1$ *nm*, at the tip of nanocone) using the formula in equation 3.1. Provided the flexible nature of the top two layers (nanohole array and graphene), it is possible that the upper layers would bend downwards, where the adjacent nanocones in the bottom layer are far apart, or there are nanodots smaller in height compared to adjacent nanocones. However, in the current study, the ideal situations of flat top layers are considered to avoid modelling of a curved graphene layer in the numerical simulations.

3.3.4.2 Improved enhancement factor (EF) for SERS

The maximum enhancement factor, obtained by FDTD simulations, along *xz*-plane ($y = 0$), *yz*-plane ($x = 0$) and *xy*-plane ($z = -1$ *nm*, at tip of nanocone) can be seen in the Figure 3.7(a). The proposed tri-layered system, utilizing the geometry of the fabricated gold-nanocones, provides strong LSPR coupling between the cone tip and the hole edge and leads to high electric field confinement, which increases the SERS enhancement factor. For the configuration where the nanocone is at the edge of the nanohole, the maximum EF of 1.05×10^9 for *yz*-plane and 5.8×10^8 for *xz*-plane are achieved with 600 *nm* wavelength excitation.

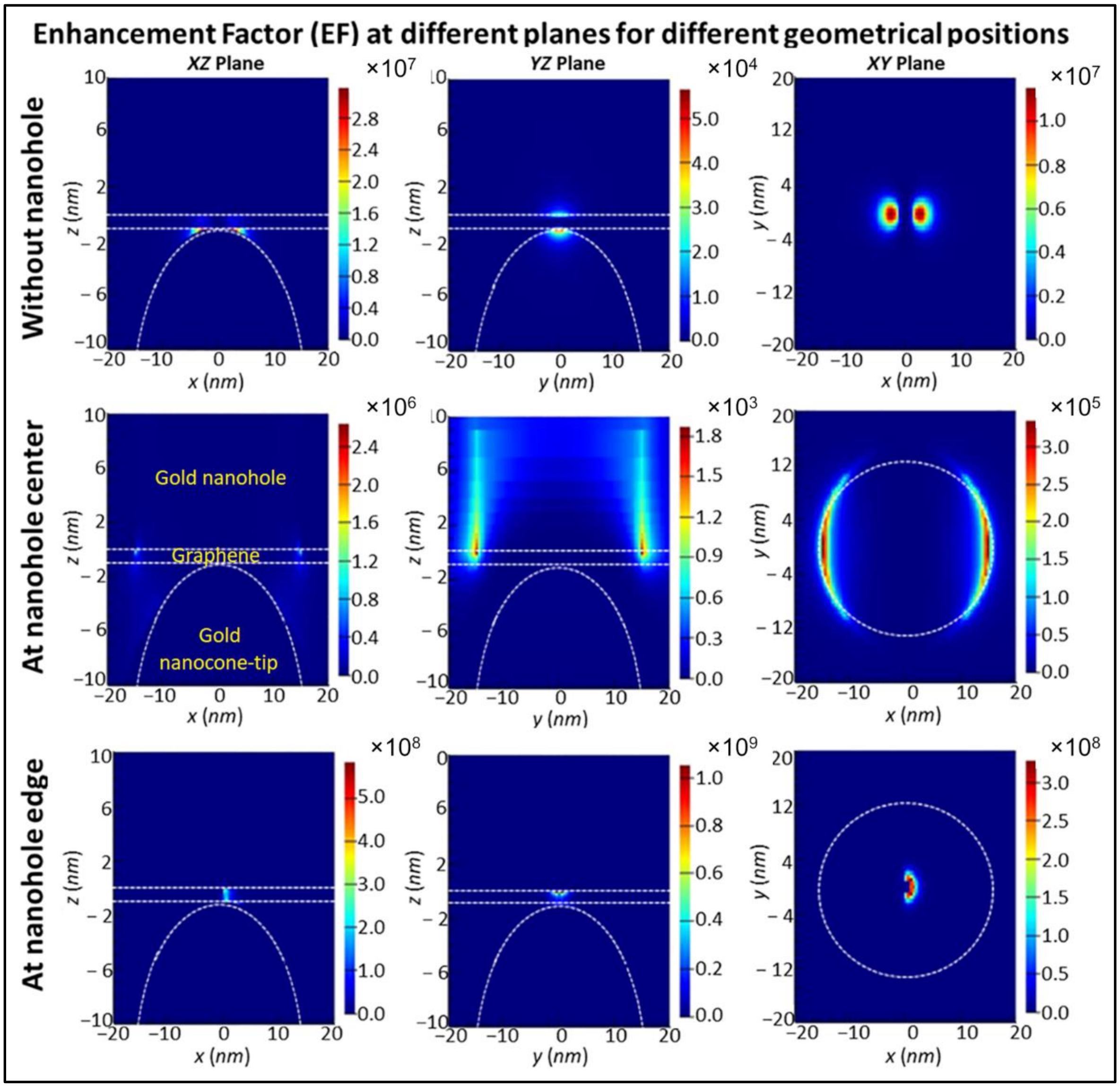

Figure 3.7 (a) Enhancement factor $(|E|/|E|)^4$ at *xz*-plane, *yz*-plane and *xy*-plane for different geometrical positions of the nanocone-tip with respect to the nanohole. Dashed white lines indicate geometrical shapes and interfaces between the layers. *xz* - and *yz* -planes: graphene layer from $z = -1$ to 0 *nm*, gold nanohole layer is from $z = 0$ to 10 *nm*.

The EF of 1.05×10^9 is almost three orders higher in magnitude than the experimentally reported 2.1×10^6 for silver nanoparticles on graphene/silicon substrate [86]. The field at the tip of the nanocone interacts with the field at the edge of the nanohole and provides a stronger enhancement in the scattered field. Graphene in the *nm* gap between the nanocone tip and hole edge leads to an enhanced field due to the highly coupled localized field from the plasmonic structure [79]. The current design predicts 10^3 times enhancement in SERS than previously reported Au/Graphene/Au structures [79]. Also, when compared with the reported SERS enhancement factor of 1×10^7, the current design predicts two order higher enhancement factor than the theoretical prediction for adjacent (1 *nm* apart) gold nanoparticles [80].

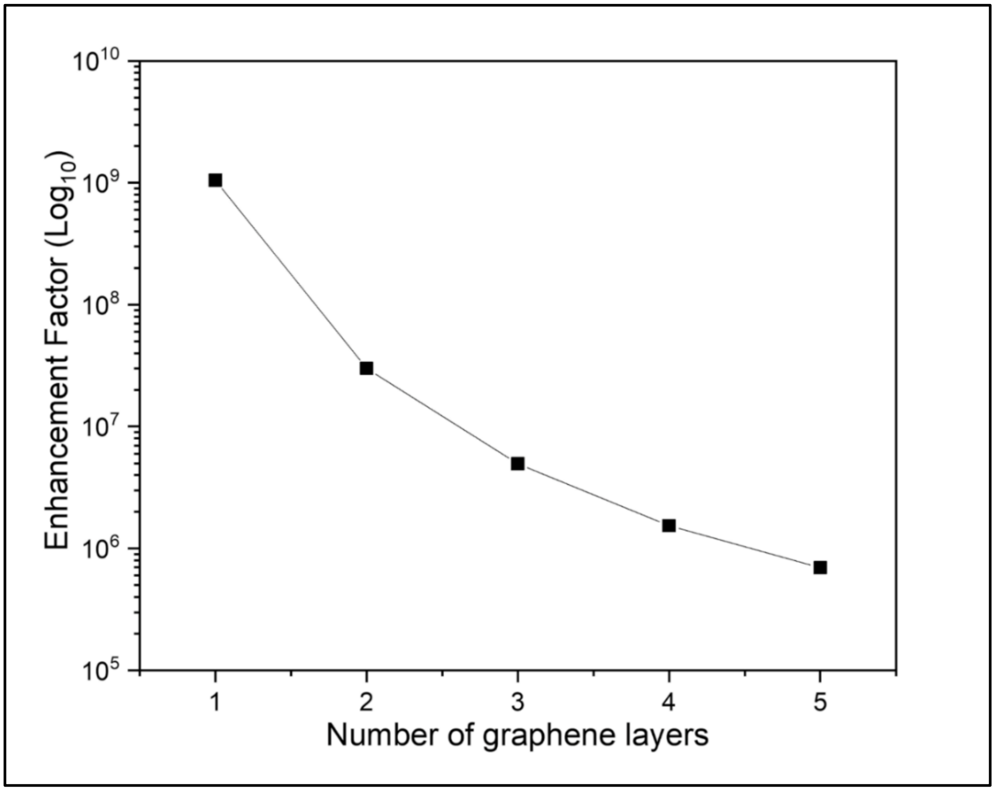

Figure 3.8 Enhancement factor versus the number of graphene layers as a spacer.

It was found that with increase in the number of graphene layers (see Figure 3.8) between the nanocone and nanoholes, the EF tends to decrease (i.e., ~10^5 for 5 layers). For the multi-layer graphene configuration, the gap between the two nanostructures increases, leading to a decrease in the near-field confinement. Thus, the decreased EF for multilayer graphene is attributed to the increased gap between the plasmonic structures and the increased opacity of the medium.

3.3.4.3 Effect of nanohole and nanocone-tip radius on EF

In order to check the effect of nanohole diameter on the enhancement factor, the radius of nanohole was varied from 10 to 25 *nm* with a constant nanocone-tip radius of 20 *nm* for the case when the geometrical position of nanocone is at the edge of nanohole. The enhancement factor as a function of the nanohole diameter is plotted in Figure 3.9. It can be observed from Figure 3.9 that the optimum nanohole radius is 20 *nm* for the highest EF of 1.29×10^9. This implies that with a fixed cone-tip radius, changing the hole-radius provides optimum SERS. Hence, it is better to choose the nanohole radius equivalent to that of nanocone-tip.

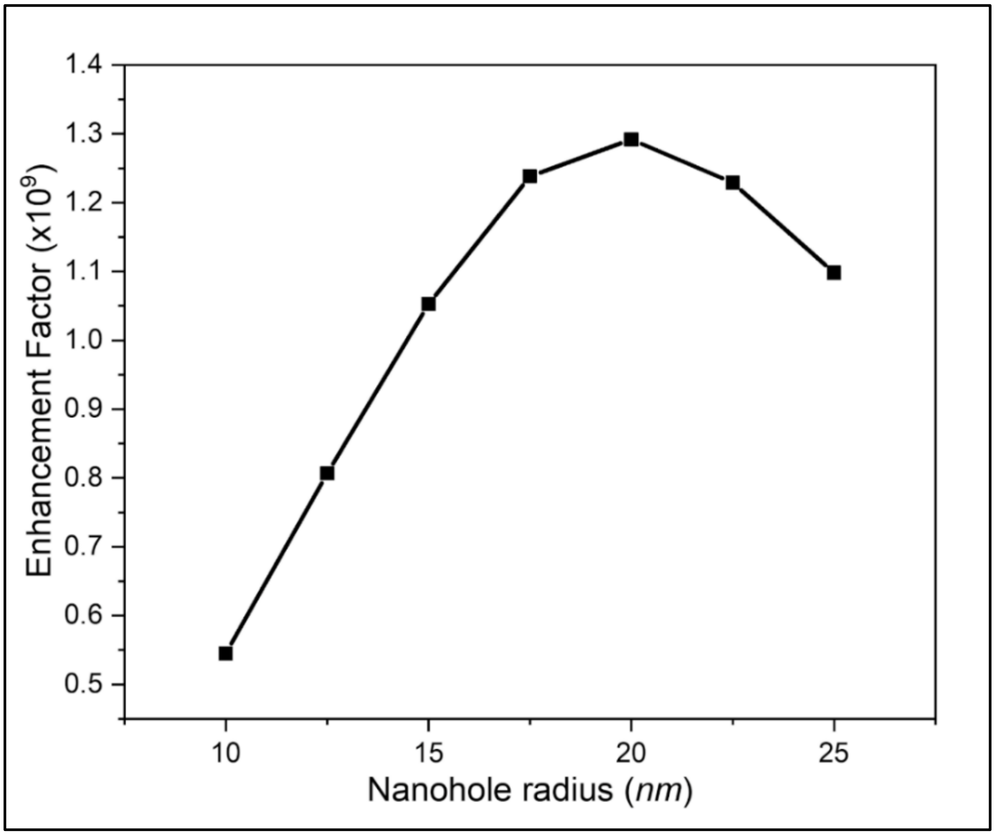

Figure 3.9 Change in EF with an increase in the nanohole radius at a constant nanocone-tip radius of 20 *nm*.

Similarly, when the nanocone-tip radius is varied with a constant nanohole radius of 20 *nm*, it was found that the EF increases with increasing the nanocone-tip radius (Figure 3.10). For a nanocone-tip radius of 20 *nm*, any deviation in the nanohole radius from 20 *nm* results in the reduction of EF. This suggests that, for a given nanocone-tip radius, if the radius for the nanohole is the same as that of the nanocone-tip, the projected cross-section for both the nanostructures is the same, and the EF is maximum.

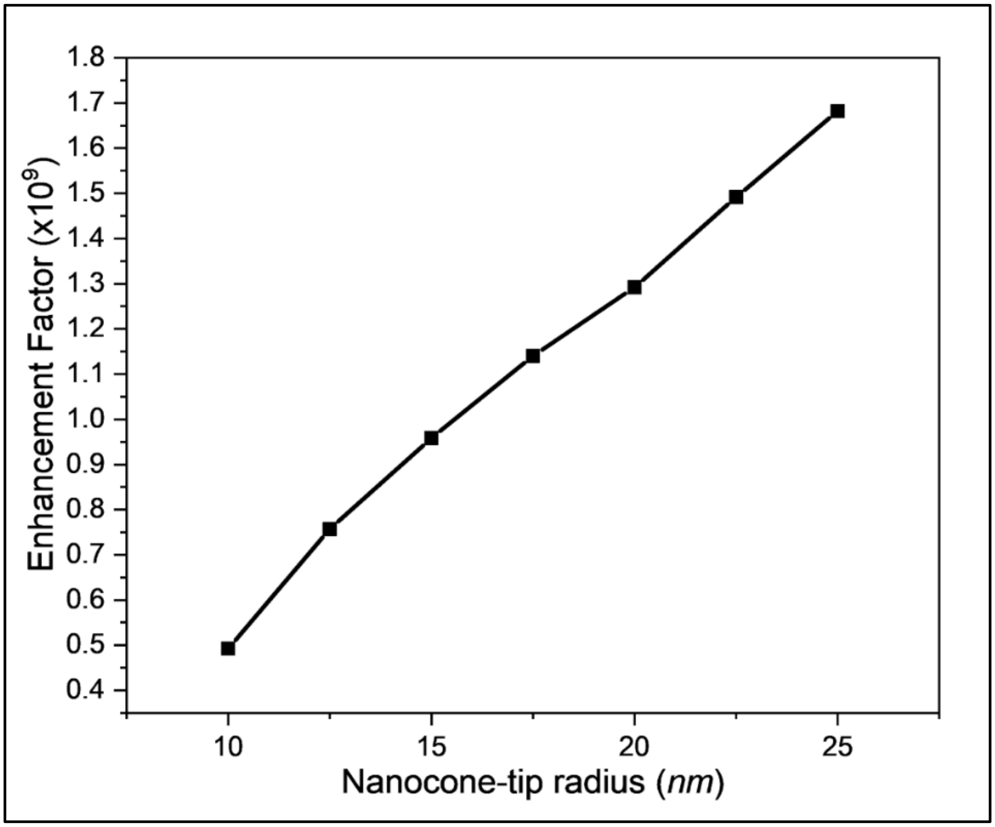

Figure 3.10 Change in EF with an increase in the nanocone-tip radius at a constant nanoholes radius of 20 *nm*.

3.3.4.4 Comparison of other dielectric spacing materials with graphene

The purpose of using graphene is to provide the atomically thin space between the nanocone-tip and the nanoholes in order to get a highly concentrated electric field between two plasmonic structures, which provides a high enhancement factor. It should be noted that the graphene in the current study is taken as 1 *nm* thick, but if the actual graphene layer thickness of 0.35 *nm* was used instead of 1 *nm* in the simulations, the EF was found to be as high as 1.45×10^{13} due to ultra-small spacing enabling more significant field confinement between plasmonic structures. However, as mentioned before, to have a realistic system, 1 *nm* thick graphene layer was considered for all the simulations due to experimental reports of wrinkling of graphene sheet [90,91].

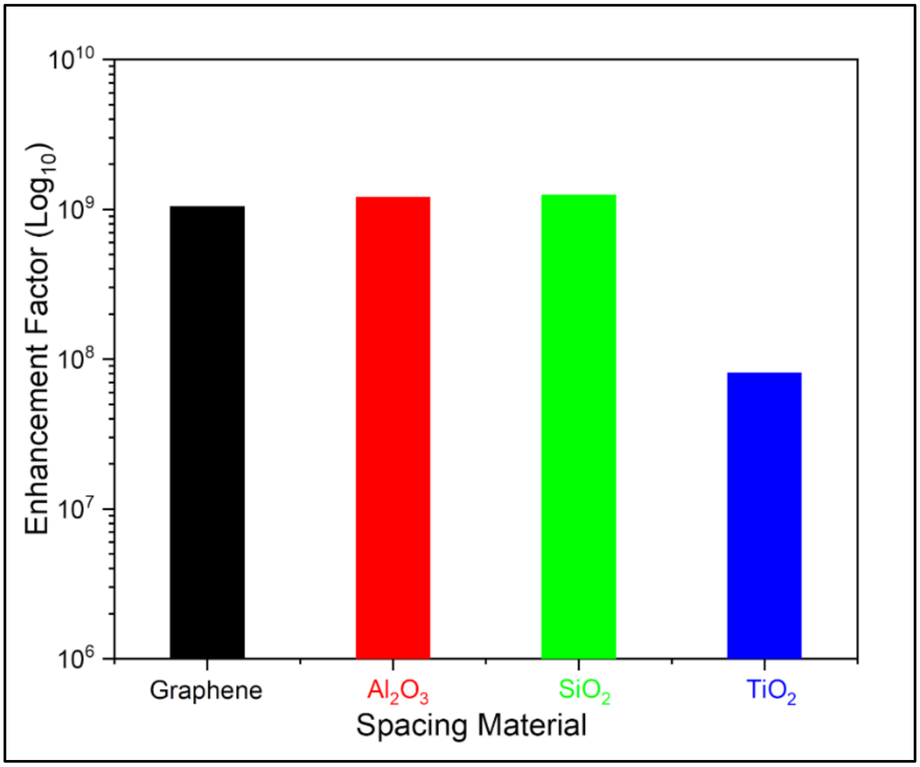

Figure 3.11 Enhancement factor versus dielectric materials.

Due to the positive permittivity of the graphene in the visible range [79,93], it must be noted that it behaves like a dielectric material. Hence, it is useful to compare EF obtained by the use of graphene as a spacer with the use of other dielectric materials as a spacer. The FDTD simulations were performed by replacing the graphene with Al_2O_3, SiO_2, and TiO_2 thin films. The optical constants for Al_2O_3 and SiO_2 are taken from the reference [95]; for TiO_2 from the reference [96]. The thickness of the dielectric layer was kept the same as the graphene layer thickness (i.e., 1 *nm*) considered in Figure 3.7. It is found that the EF values for Graphene, Al_2O_3, SiO_2 and TiO_2 are 1.05×10^9, 1.21×10^9, 1.25×10^9 and 8.14×10^7, respectively (see Figure 3.11). When Al_2O_3 and SiO_2 are used as a spacing layer, the value of EF is close to that obtained by the graphene layer of 1 *nm* thickness. However, for TiO_2 the EF is observed to be reduced to the order of 10^7 (Figure 3.11). It is seen from the simulated results that the enhancement factor is nearly the same for the spacing layers Al_2O_3, SiO_2 and graphene. However, the conformal (pinhole-free) coating of Al_2O_3, SiO_2 and TiO_2 with a thickness of 1 *nm* is difficult to achieve by atomic-layer-deposition (ALD). In general, the conformal and pinhole-free ALD deposition of oxide material would require the thickness to be at least a few *nm* [97–99]. Hence, it can be concluded that for improved EF, the graphene is advantageous over the ALD deposited oxide thin films as it provides sub-nanometer thick dielectric media between the two plasmonic nanostructures in the visible range.

3.4 Summary

The formation of self-organized nanocones by argon ion beam bombardment on the rotating gold and silicon surfaces at a glancing incident angle was demonstrated. AFM and SEM micrographs confirmed the formation of nanostructures on the surfaces. It has been observed that the rotation of the sample during ion beam sputtering plays a significant role in defining the final morphology of the nanostructures. Provided the large diameter of the ion beam source, this technique is suitable to produce nano-cones on the large surface area. Such nanostructures are ideal for anti-reflection enhancement in solar cell, photo-catalytic and surface plasmon based sensing applications.

A hybrid tri-layered gold-nanocone/graphene/gold-nanohole structure is proposed and numerically investigated with FDTD simulations. It is found that, for the chosen nanocone-tip radius, the enhancement factor is highest when the radius of the nanohole is the same as that of the nanocone-tip. The results obtained from numerical simulations reveal that the proposed structure gives a high SERS enhancement factor of the order of 10^9 for the graphene layer of 1 *nm* thickness. Hence, the proposed hybrid plasmonic design has the potential to provide a highly sensitive SERS signal, and it would be useful for efficient molecular sensing.

Chapter 4

Enhanced Light Trapping by Focused Ion Beam (FIB) Induced Self-Organized Nanoripples on Germanium (100) Surface

In this chapter, enhanced light trapping by self-organized nanoripples on a germanium surface is demonstrated. The enhanced light trapping leading to the high absorption of light is confirmed by the experimental studies as well as the numerical simulations using finite-difference time-domain (FDTD) method. The gallium ion (Ga^+) focused ion beam (FIB) was used to enable the formation of the self-organized nanoripples on the germanium (100) surface. During the fabrication, the overlap of the scanning beam is varied from zero to negative value and found to influence the orientation of the nanoripples. The evolution of nanostructures with the variation of beam overlap is investigated. Parallel, perpendicular, and randomly aligned nanoripples with respect to the scanning direction are obtained via manipulation of the scanning beam overlap. 95% broadband absorptance is measured in the visible electromagnetic region for the nanorippled germanium surface. The reported light absorption enhancement can significantly improve the efficiency of germanium-silicon based photovoltaic systems.

4.1 Introduction

Recently, the research on germanium-based nanostructures has gained significant attention due to the potential applications in optical trapping, terahertz (THz) signal emission and plasmonic response in the mid-infrared region of the electromagnetic spectrum [100–103]. The optical trapping is significantly enhanced by the nanostructures like nanopyramids [100] and nanoporosity [101] over germanium. The authors reported that the array of nanopyramid achieved enhanced radiation absorption in the wavelength range of 500 to 800 *nm* [100]. The enhancement is attributed mainly to the multiple reflections in the nanostructured domain. The nanostructured germanium is also shown to exhibit terahertz radiation emission [102] even though germanium is an indirect bandgap semiconductor. Researchers have achieved a three- to five-fold increase in the amplitude of terahertz radiation emitted from the nanostructured germanium surface as compared to the bare-germanium surface. It is surprising that germanium being the indirect bandgap semiconductor, emits terahertz radiation comparable to the direct bandgap semiconductor n-GaAs (n-type GaAs) [102]. Nanostructured germanium also has the potential to be used as an efficient mid-infrared plasmonic detector due to enhanced local surface plasmonic resonance [103]. The quasi-random nanostructures of silicon fabricated using the wrinkle lithography technique [104], which are morphologically similar to the germanium nanoripples, have been reported to achieve absorption enhancement by a factor of 1.6 in the 800 to 1200 *nm* wavelength range. However, maximum absorption was reported to be 80% in the case of silicon quasi-random nano-wrinkles.

The focused ion beam (FIB) technique is extensively used by researchers to form nanostructures and sub-nanostructures via self-organization on different surfaces such as nanoripples on germanium [49,105], titanium [106], diamond [46], $LaAlO_3$, $SrTiO_3$, Al_2O_3 [40]; nanowires on InP [54], antimony [107]; nanofins on platinum [108] and nanodots on InI_3 [54]. When ions are bombarded on the surface, selective surface erosion occurs, and the atoms from concave regions erode faster than those from the convex regions [5]. Competition between selective surface erosion and surface diffusion induced by ion beam sputtering leads to re-organization of the surface atoms, and thus the nanostructures are formed [5,6]. The germanium nanopyramids [100] arrays were fabricated using FIB milling, whereas the nanoripples can be formed by self-organization of the surface atoms due to the bombardment of the focused ion beam. The self-organizing operation using a focused ion beam is relatively fast compared to the FIB milling giving the advantage of large throughput. The controlled orientation of self-organized nanoripples is useful as a template for functional nanostructure-based applications like the growth of plasmonic metal nanoparticles [109], aligned nanowires on the nanoripples surface [110], and to align anisotropic liquid crystal molecules [111]. When nanoripples are used as a template for aligning metal nanorods and nanowires, the plasmonic properties would be dependent on the polarization of the incident light, and the differently oriented nanoripples on the same surface could lead to the multi-responsive plasmonic system. The optical absorption of ordered and periodic nanoripples could be expected to depend on the polarization of the incidence light. The formation of self-organized nanoripples on germanium induced by FIB bombardment was first reported by Zhou and Aziz et al. [49]. They reported the instantaneous formation of nanoripples for the ion dose of $\sim 5.2 \times 10^{17}$ ion/cm^2 and revealed that the nanoripples are aligned in the direction of beam scanning. So far, the broad ion beam induced formation of nanoripples and nanodots has been studied in detail [14–17]. Researchers have studied the dependency of germanium nanoripples topography on the various broad ion beam parameters such as dose, energy and angle of incidence [14–17]. The ion bombardment in the case of broad ion beam sputtering is uniform on the surface, whereas, in the case of FIB, the scanning of an ion beam of some definite size is performed. It is believed that the formation of nanoripples and their preferred orientation in the scanning direction is due to selective sputtering of the concave surface and propagating micro-explosions in the direction of scanning [49,112,113]. However, the resulting topography prediction and its control are still less explored, and the effect of beam overlap on the morphology of FIB induced germanium nanoripples has not been studied.

Compared to the control parameters involved in the case of broad ion beam such as dose, energy, beam current, time, and angle of incidence; there are two additional control parameters involved in the case of FIB induced nanostructures (1) beam size and (2) beam overlap (proportional to the distance between two adjacent spots). The effect of beam overlap on the morphology of FIB induced germanium nanoripples has not been studied yet. Hence, this chapter aims to check the dependency of ripple orientation and morphology on the beam overlap.

This study investigates the formation of self-organized nanoripples on germanium (100) surface by raster scanning of FIB. The study proposes and establishes a novel fabrication route for switching nanoripple alignment by changing the scanning beam overlap. The strong dependency of nanoripple's orientation with the beam overlap is observed by a Fast Fourier Transform (FFT) of the microscopic images obtained via scanning electron microscopy (SEM). Further, the optical behaviour of the nanoripples like light trapping and the reflectance is studied using finite-difference time-domain (FDTD) simulations and verified experimentally. The nanoripples are shown to exhibit enhanced light absorption.

4.2 Experimental details

The focused ion beam (FIB)-scanning electron microscope (SEM) system (Auriga® compact; Carl Zeiss) was used for Gallium ion (Ga^+) irradiation. Throughout the experiment, the ion beam current was set at 100 *pA*, and the corresponding beam size (i.e., the beam diameter measured as the full width at half maximum (FWHM)) was 30 *nm*. The FIB with 30 *keV* beam energy was scanned in a raster scanning manner on the germanium (100) surface. The FIB was aligned with the surface normal, and the raster scanned on the sample as shown by the arrow in Figure 4.1. In the present work, the evolution of nanostructures on germanium (100) with the variation of Ga ion beam overlapping has been studied. The beam overlap was varied from 0% to −250% in order to investigate the evolution of ripple morphology.

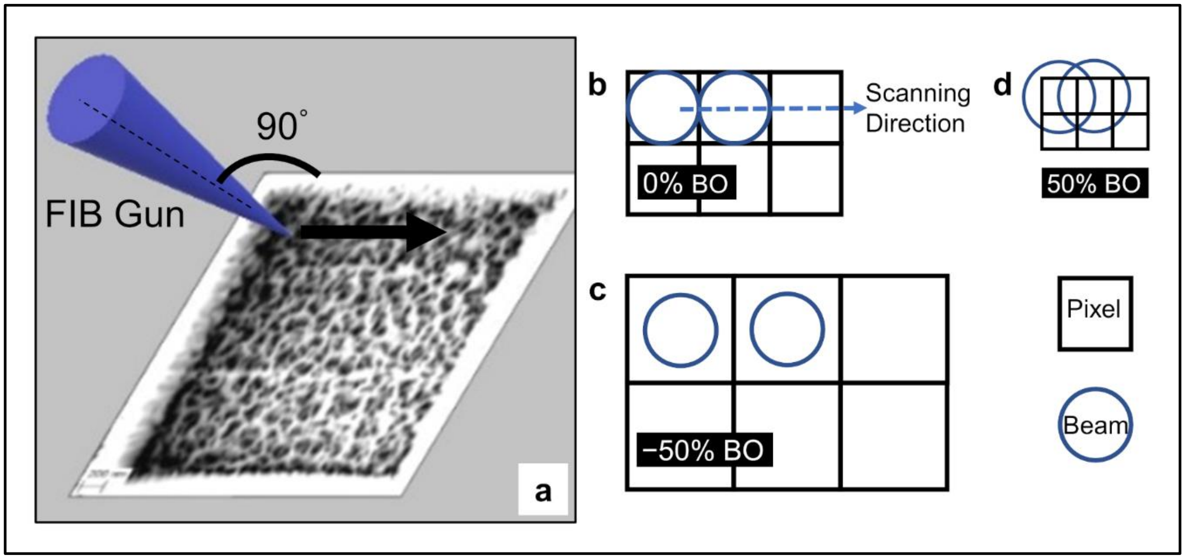

Figure 4.1 Schematic of FIB processing. (a) The scanning at 90° angle with the surface and the arrow showing left to right scanning direction, (b, c & d) raster scanning strategies with the pixel method for 0%, –50% & +50% beam overlap (BO).

The scanning leads to the self-organized formation of nanoripples over the germanium surface. The nanoripples were obtained at several rectangular regions of 5.76 μm^2 by varying the beam overlap and its dwell time. The beam overlap is given by the relation $\frac{d-p}{d}$, where d = beam size and p = pixel size. Thus, by varying the pixel size, the beam overlap can be changed as shown in Figure 4.1(b & c), where the square of the side 30 *nm* and the circle of the diameter 30 *nm* represents pixel size and beam size, respectively. For example, for beam overlaps 0%, −50% and −250%, the number of pixels would be 80×80, 53×53 and 23×23, respectively, for the given exposure area. In this study, the beam overlap was varied from +0% (i.e., high magnification) to −250% (i.e., low magnification). In order to get the fixed ion dose per unit area ($\sim 5.66 \times 10^{17}$ *ion/cm*^{2}), the dwell time in each case was varied in the range of 0.018 - 0.1 *s*. For example, the dwell time was set to 0.0081 *s*, 0.018 *s* and 0.1 *s* for the beam overlap 0%, −50% and −250%, respectively, in order to obtain a constant dose per unit area.

4.3 Results and discussion

As the nanostructuring with formation of ripples is expected from the focused ion beam irradiation, the morphology investigation by electron microscopy is vital. Hence, the investigation on the morphology evolution of the FIB induced nanoripples was carried out by scanning electron microscopy. To check the optical absorption characteristics of the nanoripples, the reflectance was measured using a micro UV-vis spectrometer. Also, the investigation on the enhanced optical absorption was performed both with theory and optical simulations.

4.3.1 SEM analysis

Figure 4.2 shows the SEM images of nanoripples formed instantaneously after Ga^+ FIB irradiation of 5.66×10^{17} *ion/cm*^{2} for different beam overlaps. Careful observation of SEM results reveals that for extreme negative beam overlap of −250% (as seen from Figure 4.2(g)), the prominent ripples are aligned in parallel with the raster scanning direction. It can be noticed that on increasing the beam overlap from −200% to −25% (Figure 4.2(b-f)), the prominent nanoripples change their direction of orientation. Nanoripples are randomly oriented for −100%, −50%, and −25% beam overlap (Figure 4.2(b-d)). However, in the case of 0% beam overlap (Figure 4.2(a)), most of the nanoripples are aligned perpendicular to the raster scanning direction.

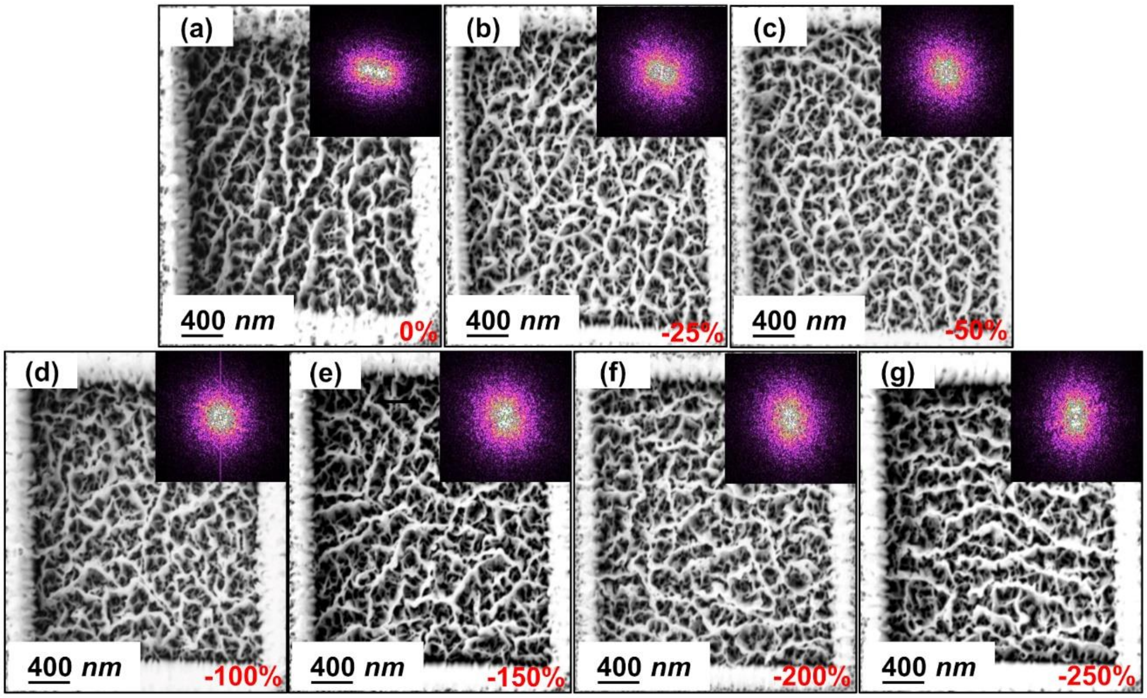

Figure 4.2 SEM images of nanoripples fabricated at fixed dose [~5×10^{17} *ion/cm*^{2}] and different beam overlaps (a) 0%, (b) −25%, (c) −50%, (d) −100%, (e) −150%, (f) −200%, and (g) −250%. Inset images represent FFT for corresponding SEM image.

The orientation pattern of the nanoripples is also confirmed by the two-dimensional fast Fourier transform (FFT) of the corresponding SEM image, as shown in the inset of Figure 4.2(a-g). The broad range of spatial frequencies are lying in the elliptical domain, which has a major axis parallel to the raster scanning direction, as seen in the inset of Figure 4.2(a). This suggests that the nanoripples are oriented perpendicular to the scanning direction for 0% beam overlap. However, for the −200% and −250% beam overlaps, the spatial frequency domains have a major axis perpendicular to the raster scanning direction, which implies that the prominent nanoripples are oriented parallel to the scanning direction.

The literature on the FIB induced nanoripples reports that the nanoripples tend to align in the raster scanning direction [49]. It is interesting to note here that even in the case of non-linear scanning directions such as a spiral scanning direction, the nanoripples are aligned in the spiral fashion [49,114]. However, here, a novel phenomenon has been observed that nanoripples are formed parallel to the scanning direction only for the extreme negative beam overlap. In contrast, they are formed perpendicular to the scanning direction for zero beam overlap. In between the extremely negative and zero beam overlapping conditions, they are oriented randomly. This implies that the orientation of nanoripples is strongly dependent on the ion beam overlap, and it is possible to manipulate the orientation of nanoripples by simply changing the beam overlap. According to the mechanism proposed by Bradley et al. [5], the formation of nanoripples is attributed to the fact that the sputtering of the concave region is higher than that of the convex region, creating an imbalance on the contour. Bellon and Wilson [112,113] observed that even a small dose of ion beam bombardment on germanium could create large microscale explosions. Such selective sputtering and the occurrence of micro-explosions are considered to be the mechanisms behind the formation of the nanoripples [49]. The reason for the occurrence of aligned nanoripples in the direction of scanning is due to the overlapping and propagating microscale explosions, in the direction of scan, during the FIB bombardment [49,112,113]. As discussed in the experimental section, for the fixed dose of 5.66×10^{17} ion/cm^2, the number of pixels per patterned rectangle are 80×80 and 23×23 for 0% and −250% beam overlap, respectively. This implies that the ion dose per pixel (i.e., ion dose for each spot of FIB bombardment) is 8.84×10^{13} ion/cm^2 and 1.07×10^{15} ion/cm^2 for 0% and −250% beam overlap respectively. Hence, the number of ions bombarded for each spot of FIB bombardment in the case of 0% and −250% beam overlap are 7262 and 625 ions, respectively, giving about twelve times dose per pixel for −250% beam overlap compared to 0% beam overlap. Such a high dose, in the case of extreme negative beam overlap, leads to greater microscale explosions and the ripple orientation is largely decided by the propagation direction of microscale explosions. This enables alignment of the larger nanoripples in the raster scanning direction.

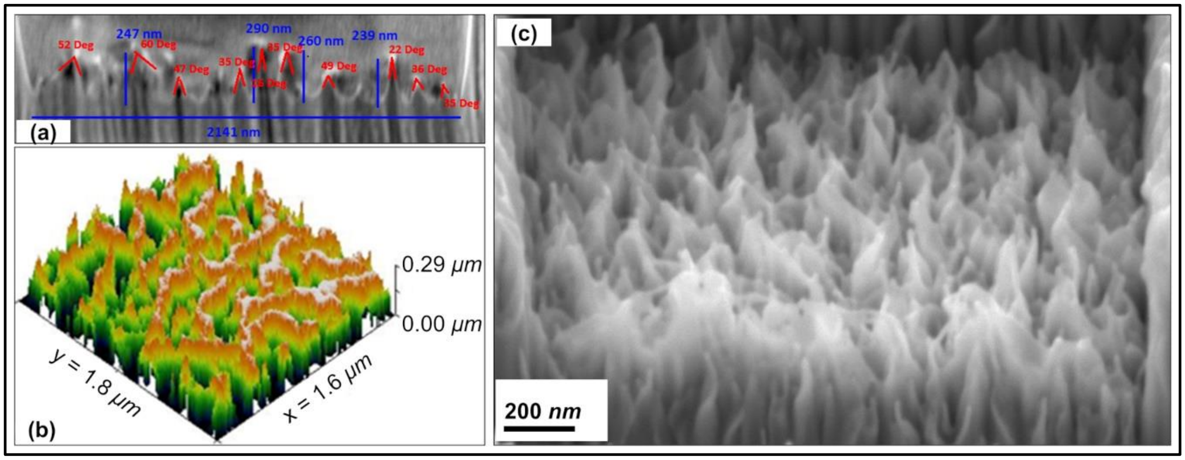

Figure 4.3 (a) Cross-sectional SEM image of nanoripples for beam overlap −250% and (b) 3D nanorippled surface generated from SEM image, (c) tilted SEM image from the cross-section for −250% beam overlap.

In order to study the detailed topography of nanoripples, SEM cross-sectional imaging is performed for the case of −250% beam overlap. The germanium nanorippled surface is first coated with a protective layer of platinum about 500 *nm* in thickness using the FIB-CVD method, and then it is sectioned with the aid of FIB milling for SEM imaging. The nanorippled topography thus obtained is as shown in Figure 4.3(a). Measurements from the cross-sectional image yield the maximum height of nanoripples to be 290 *nm*, whereas the maximum ripple angle to be 60°. The average ripple angle is about 38.7°. The nanoripples orientation parallel to the scanning direction can be seen in the tilted cross-sectional SEM image in Figure 4.3(c).

4.3.2 Measurement of optical absorption by nanoripples

Experimental reflection spectrum was obtained using J&M Micro UV-Vis microscope spectrometer with an objective lens of 50X magnification at a numerical aperture (NA) of 0.65. The halogen lamp was used as a white light source, and it was coupled with optical fibre in order to illuminate the sample. The reflected spectrum from the sample is normalized with respect to reflection from a protected silver mirror (from Thorlabs Inc.).

The reflection measurements are carried out in the wavelength range of 350-900 nm. The obtained absorption spectra ($100 - Reflection\%$) are plotted for the germanium surface with- and without-nanoripples in Figure 4.4(a) and Figure 4.4(b), respectively. The optical absorptance of the nanorippled area is 90-95% in the wavelength range of 430-720 nm. However, for the bare germanium, the light absorption is around 45% in the 400 to 900 nm wavelength range. It is worth noting that the thickness of the germanium wafer used in the current study is 400 μm, which is more than 400 times the maximum wavelength (900 nm). Though the absorptance is enhanced for the nanorippled germanium, the bulk-germanium thickness does not influence the spectral behaviour.

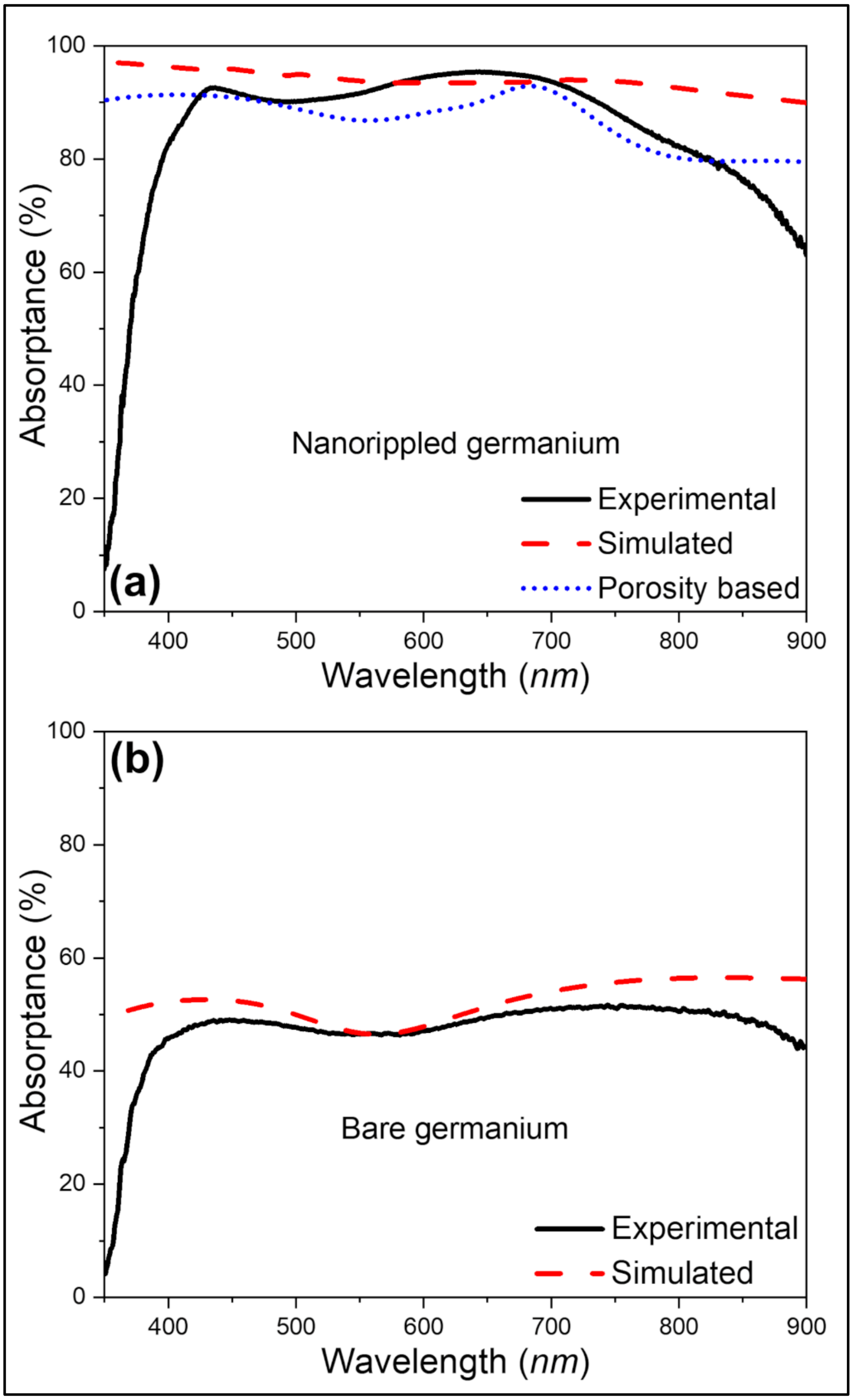

Figure 4.4 (a) Absorption spectra of germanium surface with nanoripples: experimental (solid line), simulated by FDTD method (dashed line) and porosity based theoretical prediction (dotted line); (b) absorption spectra of bare germanium surface: experimental (solid line), simulated by FDTD method (dashed line).

4.3.3 3D topography generating and porosity calculations

It can be observed from the SEM image (Figure 4.2(g)) that the nanoripples with maximum heights correspond to the respective pixels with maximum intensities in contrast to the other regions of the nanorippled surface. Similarly, the region with the lowest height corresponds to the respective pixels with the lowest intensities. To create a 3D surface profile from a 2D grayscale SEM image, an open-source image analysis tool Gwyddion is used [115].

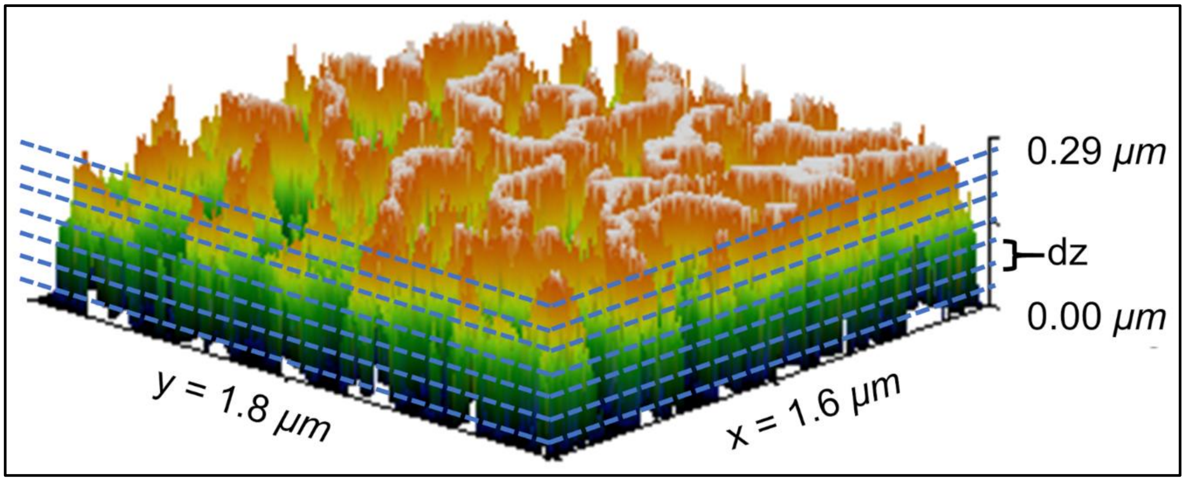

Figure 4.5 Illustration of the 3D surface (created from SEM image). As indicated by dotted lines, the thickness of the nanorippled region is divided into steps of *dz* = 5 *nm*.

The maximum height of the nanoripples for −250% beam overlap is 290 *nm* (from Figure 4.3(a)). Thus, 290 *nm* height is assigned to the pixel with the highest intensity, and 0 *nm* height is assigned to the pixel with the lowest intensity for defining the 3D surface profile. Accordingly, the pixels with intermediate intensities are assigned the linearly scaled heights corresponding to the intensities of the respective pixels. The final 3D image for −250% beam overlap is shown in Figure 4.3(b). As shown in Figure 4.5, the nanorippled region is vertically divided into 58 layers giving a thickness of 5 *nm* for each. The porosity at each layer is calculated analytically by taking the ratio of the volume of the pore to the volume of material, i.e., $P(\%) = \frac{V_{pore}}{V_{material}} \times 100$. The porosity of the substrate germanium layer, having no pores, was taken as zero. Further, for wavelength range 350 *nm* to 900 *nm* the effective refractive index at each layer was derived from porosity using Yoldas's mixing rule. The complex refractive index constants for germanium were used from reference [95].

4.3.4 Simulation of optical absorption by nanoripples

Electromagnetic field distribution throughout the nanostructures is simulated by the FDTD method using a commercially available numerical solver (Lumerical Inc., Canada). The nanoripples for −250% beam overlap were modelled in FDTD simulations using three-dimensional (3D) topography shown in Figure 4.5. The FDTD simulations for Ge nanoripples were carried out with the plane wave source, as seen in the simulation set-up represented in Figure 4.6. Optical simulation of the typical surface is carried out in the wavelength range 350 to 900 *nm* using the normally incident plane wave source. The spatial domain of the simulation region is discretized with a fine mesh of 5 *nm*. The periodic boundary conditions (PBC) are set along the *xy*-plane, and perfectly matched layer (PML) boundary conditions are set along the propagation direction. Bulk germanium is used as a substrate for the nanorippled layer in such a way that it extends the bottom boundary of the simulation domain to replicate the realistic situation. The wavelength-dependent complex dielectric constants for germanium were taken from the reference [116] for the wavelength range 350-900 *nm*.

The absorption spectra obtained from the FDTD simulations for the nanorippled and bare germanium surfaces are shown in Figure 4.4(a) and Figure 4.4(b), respectively. A higher absorptance of 95-97% in the visible range for the nanoripples is close to the reported values for germanium nanopyramid arrays [100]. As seen in Figure 4.4(a) and Figure 4.4(b), the experimentally measured absorption spectra for the nanorippled and bare germanium co-relate well with the simulated results. A comparison with morphologically similar silicon nano-wrinkles [104] reveals that the measured absorptance for the nanorippled germanium surface is 15-20% higher than the measured absorptance for silicon nano-wrinkles. The simulated absorptance by nanorippled germanium is 20-30% higher than the absorptance of silicon nano-wrinkles [104]. The work on germanium nanopyramid arrays by Han et al. [100] reports high absorption around 98% in the wavelength range 500 to 800 *nm* for the nanopyramid arrays. However, the absorption for the wavelengths lower than 500 *nm* has not been reported [100]. The absorptance for the nanoripples presented in this work is above 90% in the broadband wavelength range of 350 to 900 *nm*.

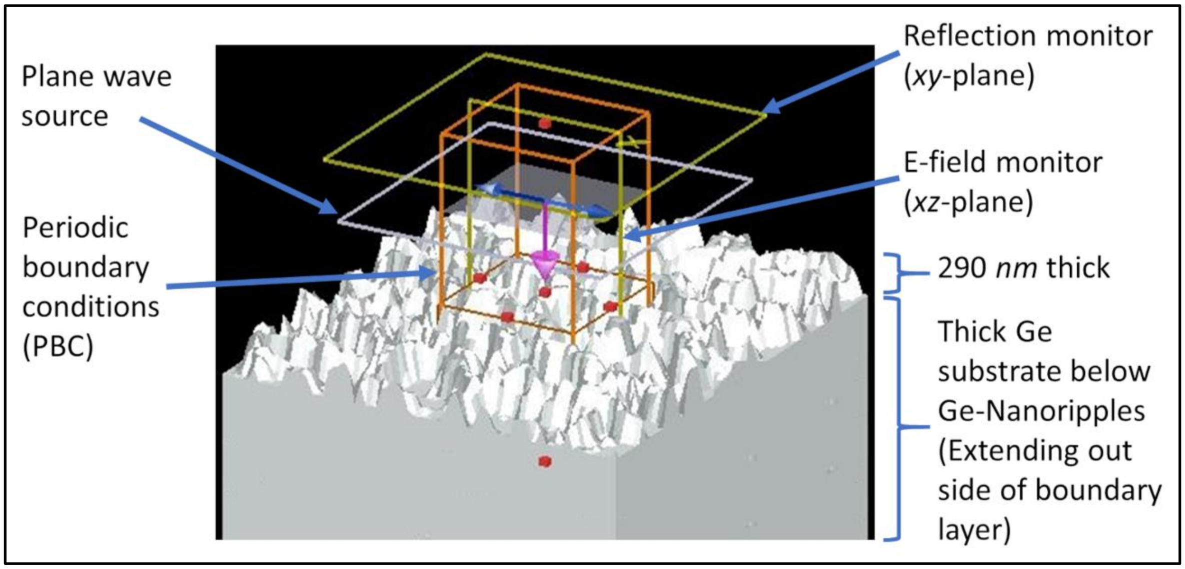
Plane wave source
Periodic boundary conditions (PBC)
Reflection monitor (*xy*-plane)
E-field monitor (*xz*-plane)
290 *nm* thick
Thick Ge substrate below Ge-Nanoripples (Extending out side of boundary layer)

Figure 4.6 Set-up of FDTD simulations for nanoripples.

4.3.5 Theoretical absorption calculations using porosity analysis

When the light is incident on vertical nanostructures, the structure scatters the light at multiple instances, which increases the probability of photon absorption as depicted schematically in the inset of Figure 4.7. The observed enhanced-light trapping could be attributed to the occurrence of multiple instances of light-scattering for the nonporous germanium surface [101].

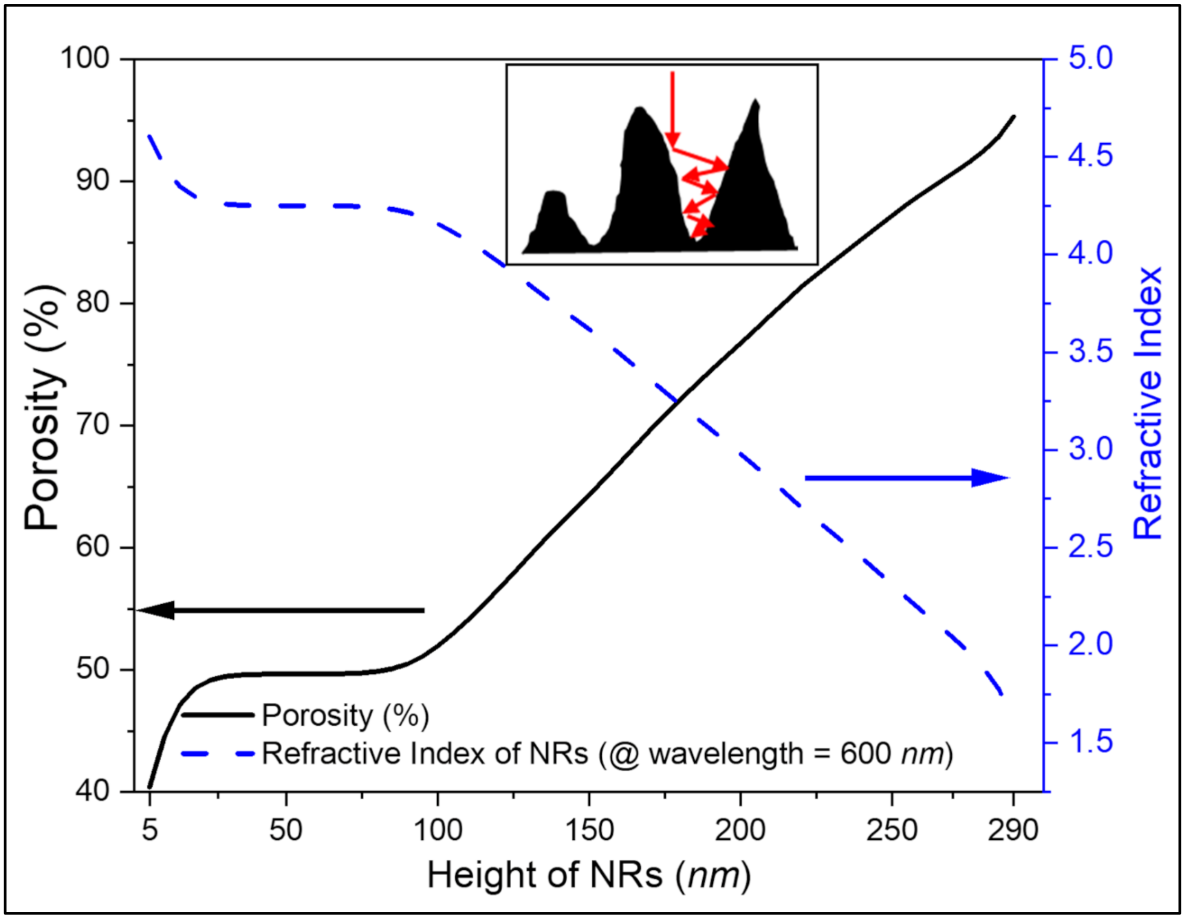

Figure 4.7 Calculated refractive index and porosity vs. the height of nanoripples, inset shows multiple light reflections through nanoripples.

It is known that the bare germanium has a high refractive index (e.g., 5.9 at 600 *nm* wavelength). Thus, a high index contrast is attained at the interface between a free space (n_{air} = 1) and the bare germanium surface. This high refractive index contrast at the interface results in high reflectance for the incident light. However, with the nanostructured germanium surface, a suppressed reflectance was observed. The suppressed reflectance can be explained by considering the graded refractive index along the thickness. It is noted that these nanostructures are narrow at the top and broad at the base. Such geometrical variation provides a graded refractive index along the height and leads to an averaged effective refractive index for the nanorippled layer of germanium. Estimation of the graded refractive index could help to explain the enhanced absorption in the nanorippled structures. The obtained nanoripples are quasi-random, and there are irregular pores in between adjacent nanoripples. Quantification of average porosity for the nanostructures will enable the calculation of the effective refractive index of the nanostructure by utilizing Yoldas's mixing rule for porous material [117]. The Yoldas's mixing rule for a porous material having air in pores is as given by,

$$n_{eff} = ((n_2^2 - 1)(1 - 0.01P) + 1)^{\frac{1}{2}} \tag{4.1}$$

Where, n_{eff} is the effective (average) refractive index of structure, P is the percentage porosity (P%) of the structure and n_2 is the refractive index of bulk germanium. The nanorippled structure is considered as a multilayer material with a total height of 290 *nm*. Each layer of the nanorippled region is set to 5 *nm* thickness. Subsequently, the porosity at each layer is calculated analytically, as described in section 4.3.3 and plotted in Figure 4.7. It is observed from Figure 4.7 that for wavelength 600 *nm,* the effective refractive index, calculated using equation (4.1), increases while going from top to bottom as the porosity decreases gradually. This provides a positive gradient of the effective refractive index for the incoming light entering from free space to the germanium substrate.

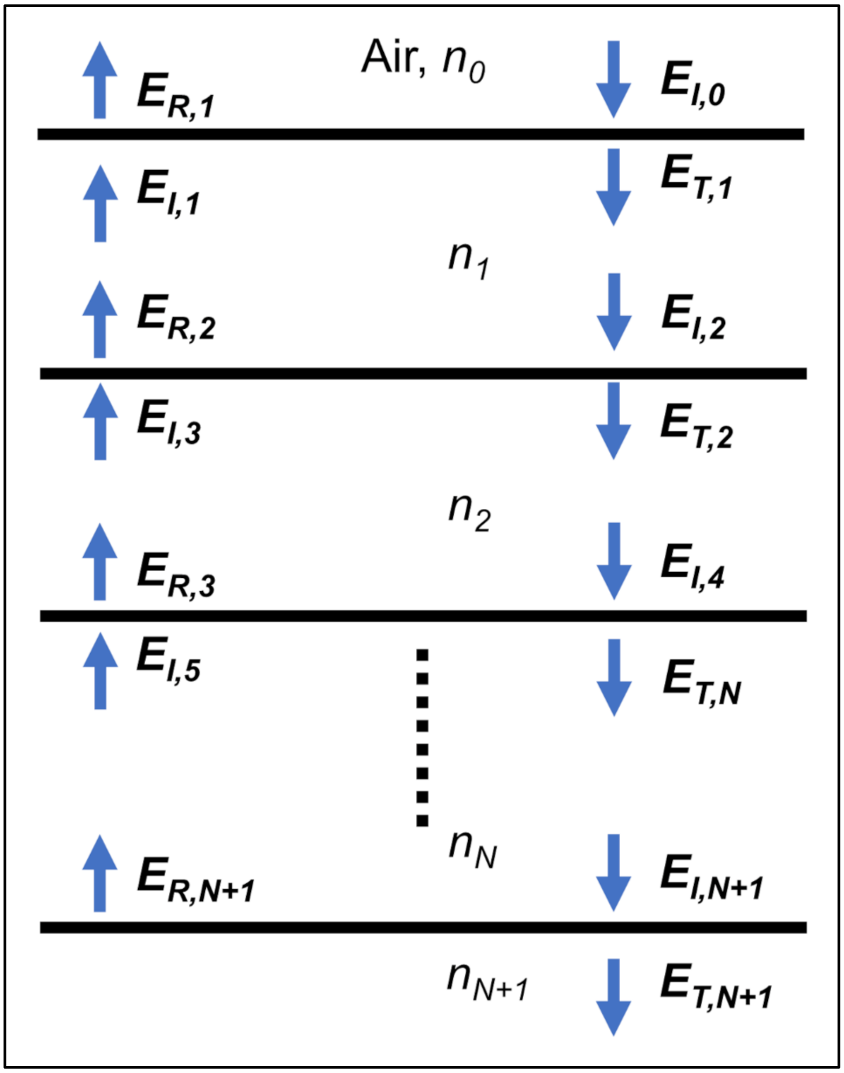

Figure 4.8 Schematic of propagation amplitude of EM wave through multilayer (N layers) having complex effective refractive index n. The number of interfaces is $N+1$. In subscripts, I, R and T represent incident, reflected and transmitted waves for corresponding interfaces. For each layer, the thickness is taken as $dz = 5\ nm$ and for substrate $dz = 500\ \mu m$.

Once the effective refractive indices of nanoporous material for the entire wavelength range are obtained, the reflectance can be calculated for the nanoporous material [118] using the transfer matrix method [119–121]. In order to employ the transfer-matrix method, the nanorippled region of the germanium surface was considered as multi-layered films stacked on each other, as shown in Figure 4.5. In this case, the electromagnetic radiation (normal incidence) is passing through multiple interfaces. Thus, the transfer matrix can be obtained for each layers giving the relationship between coefficients of electromagnetic field (Figure 4.8) on both sides [119],

$$M_j = \begin{pmatrix} \cos \delta_j & \dfrac{i \cdot \sin \delta_j}{\gamma_j} \\ i \cdot \gamma_j \cdot \sin \delta_j & \cos \delta_j \end{pmatrix} \tag{4.2}$$

Where, δ_J and γ_j are phase difference and admittance of EM wave for a layer they are given as, $\delta = \frac{2\pi}{\lambda} \cdot n_j \cdot dz_j$ degrees, and $\gamma_j = n_j \cdot \sqrt{\epsilon_0 \mu_0}$ siemens; Admittance could be calculated from the effective refractive index of each layer (n_j), free space permittivity (ϵ_0) and free space permeability (μ_0). The thickness of the layer, dz is taken as $dz_{j=1,N} = 5\ nm$ and for substrate and $dz_{N+1} = 500\ \mu m$. Here, the effective refractive index for each layer was calculated using Yoldas's mixing rule.

Thus, the total transfer matrix for *N* layers can be written as,

$$M_{total} = M_N \cdot M_{N-1} \cdot M_{N-2} \cdots\cdots M_2 \cdot M_1 = \begin{pmatrix} m_{11} & m_{12} \\ m_{21} & m_{22} \end{pmatrix} \tag{4.3}$$

Therefore, the relation between field amplitudes would be,

$$\begin{pmatrix} E_{I,0} + E_{R,1} \\ \gamma_0 (E_{I,0} - E_{R,1}) \end{pmatrix} = M_{total} \begin{pmatrix} E_{T,N+1} \\ \gamma_{N+1} E_{T,N+1} \end{pmatrix} \tag{4.4}$$

Which gives reflection coefficient (*r*) and transmission coefficient (*t*) as follow,

$$r = \frac{E_{R,1}}{E_{I,0}} = \frac{\gamma_0 (m_{11} + \gamma_{N+1} m_{12}) - (m_{21} + \gamma_{N+1} m_{22})}{\gamma_0 (m_{11} + \gamma_{N+1} m_{12}) + (m_{21} + \gamma_{N+1} m_{22})} \tag{4.5}$$

$$t = \frac{E_{T,1}}{E_{I,0}} = \frac{2\gamma_0}{\gamma_0 (m_{11} + \gamma_{N+1} m_{12}) + (m_{21} + \gamma_{N+1} m_{22})} \tag{4.6}$$

Therefore, reflectance (R) and transmittance (T) will be, $R = |r|^2$ and $T = Re\left(\frac{\gamma_{N+1}}{\gamma_0}\right)|t|^2$. Hence, the absorptance is given by ($100 - Reflection\% - Transmission\%$). The theoretical absorption spectrum, thus obtained, is plotted in Figure 4.4(a). The theoretical absorptance is around 90% from 350 to 700 *nm* wavelength range. However, the absorptance gradually decreases in the wavelength range 700 - 800 *nm* and reaches 80% value for 800 to 900 *nm* wavelength range (see Figure 4.4(a)). The graded refractive index from top to bottom of the nanorippled surface provides a smooth variation of the index from free space to the substrate. Thus, the penetration depth increases for the incoming light. Germanium being a lossy media, the increased light penetration depth provides more chance of absorption of the light, and hence the reflectance gets suppressed. The phenomenon of the graded refractive index is wavelength-independent for the wavelength range under consideration. Thus, the multilayer model validates the anti-reflection behaviour, which is also shown by the experimental measurements and the FDTD simulations.

4.3.6 The effect of incidence angle and nanorippled layer thickness

In order to check the behaviour of the absorption spectra with a change in incidence angle, the FDTD simulations are carried out with the angular incidence of light on the nanorippled germanium surface. The plane wave source with an oblique injection of light via Broadband Fixed Angle Source Technique (BFAST) was used. All other settings and simulation domain were the same as described in section 4.3.4. Figure 4.9 shows the absorptance for varied angle incidence and as a function of the incidence angle.

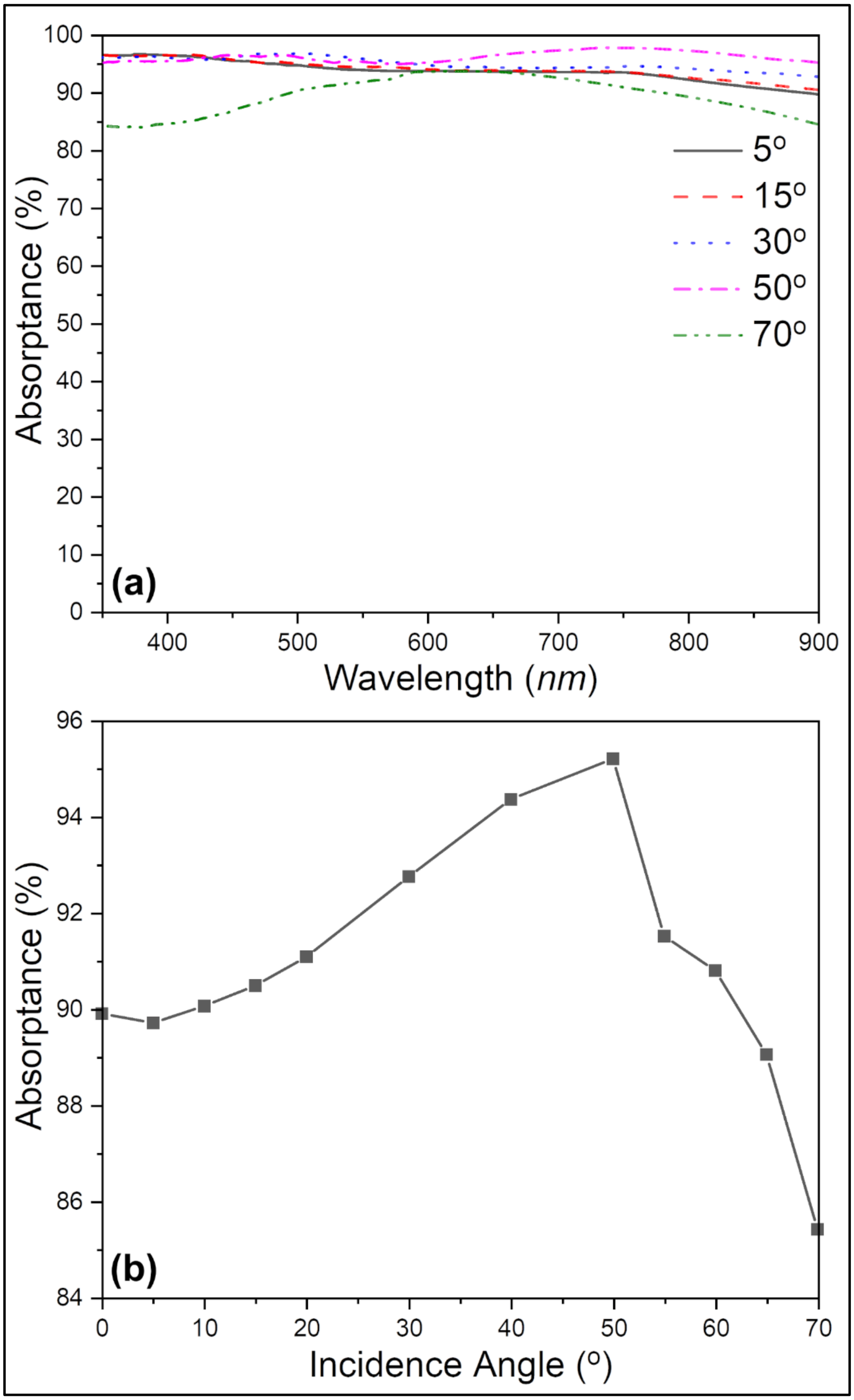

Figure 4.9 (a) Absorption spectra for germanium nanoripples with the angular incidence of light. The plot in (b) shows the variation in absorptance with the angle of incidence for 900 *nm* wavelength.

It is clear from Figure 4.9 that the absorptance increases upto 50° incidence angle and then decreases for further increase in the incidence angle. Thus, the acceptable incidence angle (Figure 4.9(b)) for the enhanced absorptance for the nanoripples structures is 50°. The results suggest that the nanoripples exhibit wide-angle broadband absorption enhancement. The wide-angle (upto 50°) absorptance behaviour of the germanium nanoripples is attributed to the smooth refractive index gradient for the light coming from free space to the nanorippled surface [122,123]. For the incidence angle below 50°, the smooth refractive index gradient ensures gradual bending of the light beam towards the surface normal, resulting in multiple internal reflections leading to suppressed reflection [122,123]. While for the glancing angle incidence, the increased scattering leads to low absorption. Further, to check the effect of layer thickness on absorption behaviour, the FDTD simulations are carried out with a varied thickness of nanorippled Ge layer. The bulk Ge is considered as a substrate below the nanorippled layer. It must be noted here that, since the bulk thickness is much larger than the illumination wavelength, in FDTD simulations, bulk Ge is considered as a semi-infinite object by applying the PML boundary layer. The geometrical shape of the nanorippled layer is considered the same as shown in Figure 4.3(b), and three different thicknesses 250, 350 and 400 *nm* are considered for the simulations. The simulated absorptance spectra for varying thickness of nanorippled area are shown in Figure 4.10.

It is seen from Figure 4.10 that the absorptance increases for the higher thickness of the nanorippled layer. However, with the FIB processing, it is difficult to get the nanoripples with the higher aspect ratios. In order to increase the depth of nanoripples, the ion dose and dwell time of the Ga beam need to be increased. The increased dose leads to sputtering of the material instead of nanoripples formation.

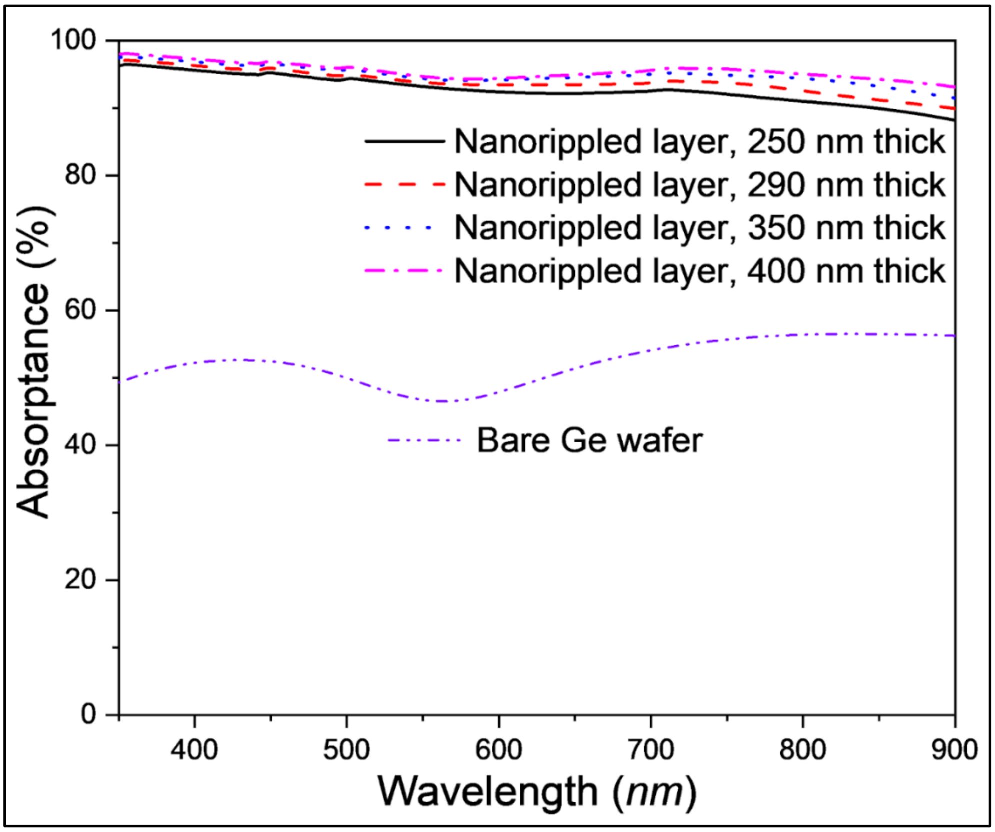

Figure 4.10 Simulated absorptance spectra for four different thicknesses (250, 290 (original), 350 and 400 *nm*) of nanorippled germanium layer on bulk Ge substrate; and simulated absorptance spectra for the bare Ge wafer.

4.3.7 Field distribution in the nanostructures using FDTD simulations

Further, the electric field distribution was investigated in the nanostructures using FDTD simulations. The electric field intensity ($|E|^2$) distribution in *xz*-plane (*y* = 0 *nm*), *yz*-pane (*x* = 0 *nm*) and *xy*-plane (near field at 1 *nm* above the nanoripple surface) is shown in Figure 4.11. The electric field intensity ($|E|^2$) is plotted for 350, 500 and 900 *nm* wavelengths (see Figure 4.11(a), (b) and (c)). Bright hot spots of the electric field intensity indicate that the electric field is trapped at positions such as on the tip of ripples and the gap between them (see Figure 4.11(a), (b) and (c)). It should also be noted that the light trapping is wavelength-independent, and in addition to the graded effective refractive index, the enhanced absorption is also attributed to the enhanced light trapping.

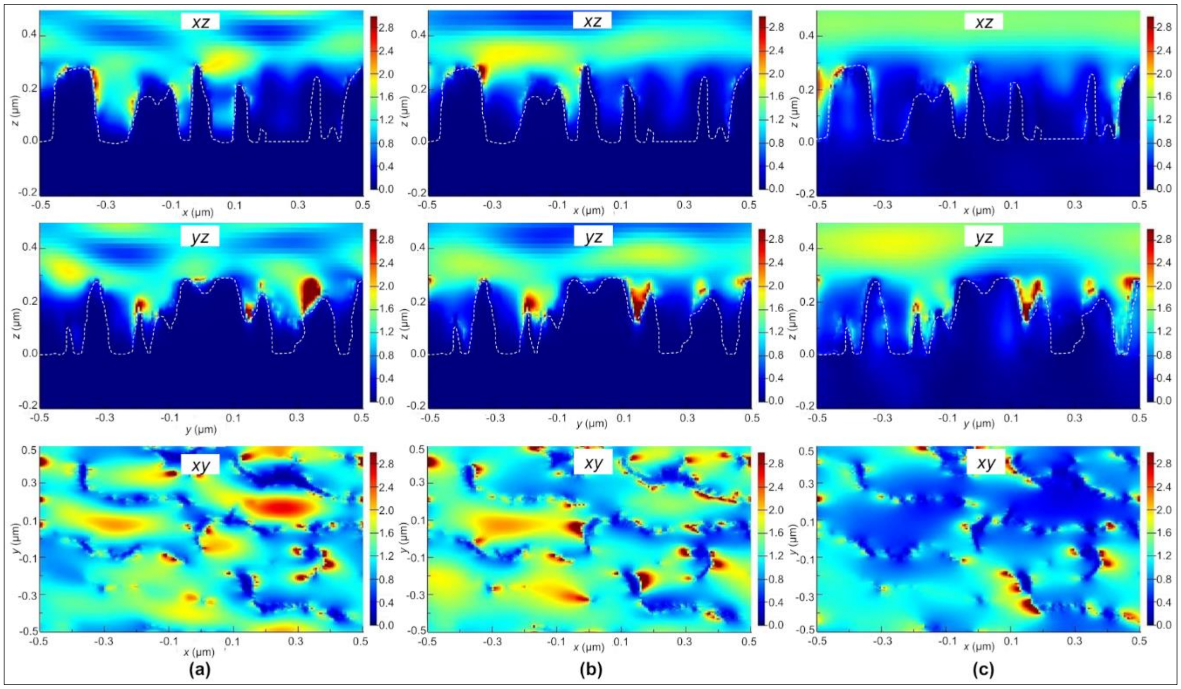

Figure 4.11 Two-dimensional (2D) electric field intensity ($|E|^2$) distribution at wavelength (a) 350 *nm*, (b) 500 *nm* and (c) 900 *nm* for nanoripples across planes *xz*-plane ($y = 0$), *yz*-plane ($x = 0$) and *xy*-plane (1 *nm* above nanoripples). The dashed white line indicates a germanium surface, and the colour-bar shows electric field intensity ($|E|^2$).

Further, the optical power absorption per unit volume is calculated by measuring the spatial absorption for each volume element in the simulation domain at different wavelengths. The optical absorption density for *xz*-plane is shown in Figure 4.12 for the nanoripples and the bare germanium. The shorter wavelengths, 350 *nm* and 500 *nm* are absorbed at the surface of the bare germanium (see Figure 4.12(a) and Figure 4.12(b)). However, for the nanorippled surface, most of the shorter wavelengths are absorbed at the tip of the nanoripples, and the rest of it gets absorbed inside the nanoripples. In case of longer wavelength (900 *nm*), after a small amount of power absorption at the tip of the nanoripples, a considerable amount of light gets absorbed inside the nanoripples, and the remaining passes to the bulk of the substrate, getting absorbed up to 200 *nm* depth (see Figure 4.12(c)). Whereas, for the bulk germanium, only some part of longer wavelength (900 *nm*) light gets absorbed up to the depth of 490 *nm*. Hence, the enhanced absorption due to the nanorippled surface is wavelength-independent.

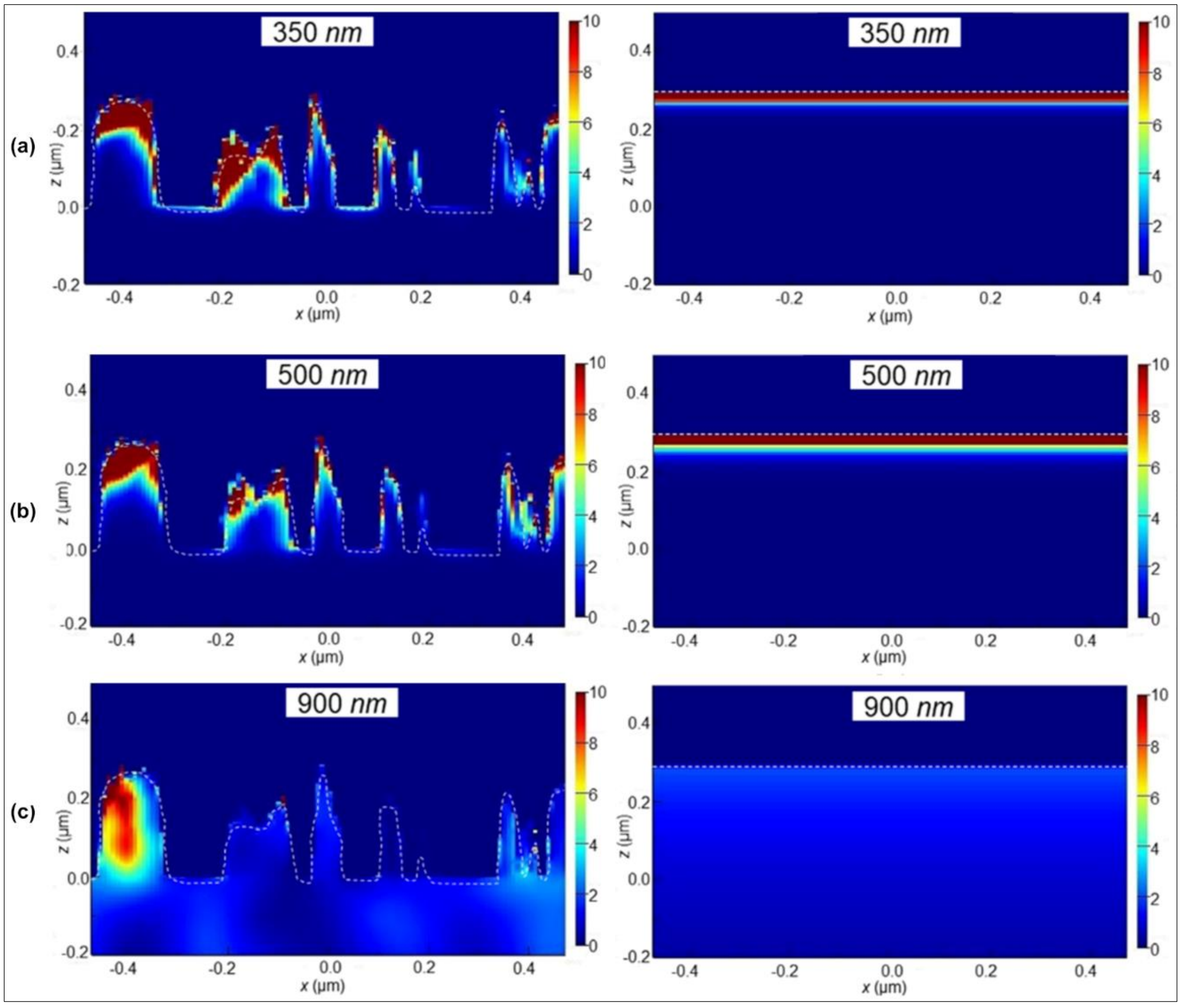

Figure 4.12 Light absorption per unit volume for nanoripples (left column) and bare germanium surface (right column) for incident wavelength (a) 350 *nm*, (b) 500 *nm* and (c) 900 *nm* across *xz*-plane ($y = 0$). The dashed white line indicates a germanium surface profile, and the colour-bar shows absorption density in *watt/µm*^{3}.

4.4 Summary

In summary, the broadband light trapping for the FIB induced germanium nanoripples both experimentally and through FDTD simulations was demonstrated. The resultant light absorptance is about 95% for the visible light range. Such broadband light absorption in nanostructured germanium can lead to higher efficiency in photovoltaic based devices. Formation of nanoripples with variant orientations such as parallel and perpendicular to the ion beam scanning direction was achieved. The results provide novel strategies to manipulate the orientation of nanoripples by simply tuning the beam overlap and thus enabling the fabrication of varied nanoripples on a defined area. Using this approach, different nanoripple orientations can be achieved at the normal incidence of the focused ion beam itself, which is advantageous over the conventional approach of varying incident angle.

Chapter 5

Tailoring Surface Self-Organization for Nanoscale Polygonal Morphology on Germanium

The research in the field of nanofabrication has been aimed at reducing the feature size of nanostructures to achieve miniaturization of the overall device size. Nanofabrication through direct milling of the material with the help of a focused ion beam (FIB) has been widely utilized approach in order to create three-dimensional (3D) micro/nano-structures. However, the direct milling processes exhibit limitations in terms of size and speed due to the requirement of milling series of pixels to get the desired nanostructures. Self-organization, by exploiting the competition among various surface interactions, plays a crucial role in nanostructuring on the materials due to its easy and high-throughput capabilities. However, there is inadequate control over morphological-uniformity and periodicity at the nanoscale. This could be mitigated by attaining the nanoscale control over the ion beam irradiation induced viscous-flow on the surfaces. Herein, periodic and polygonal-shaped nanoholes on the germanium (100) surface, aided by focused ion beam (FIB) induced self-organization, are presented. The morphologic evolution in the nanoholes has been found to be sensitive with the ion dose, and the optimized conditions produce protruding polygonal geometries such as squares, triangles, hexagons, pentagons, and octagons. The bombardment of energetic ions on the germanium surface causes the site-specific thermal spike forming the localized melting zones followed by the phase transitions enabling confined viscous-flow at the walls of nanoholes as revealed by microscopy and Raman spectroscopy studies. The confined viscous-flow provides reorganization of the surface atoms by the occurrence of viscous-fingering at the nanoscale, enabling the geometrical makeover for the nanoholes to convert the circular holes into the polygonal holes. The present morphology manipulation promises to surmount the barriers concerning the size reduction efforts in the field of nanofabrication.

5.1 Introduction

Controlled and periodic germanium nanostructures exhibit significant applications in lasing [124,125], infrared surface plasmon based molecular sensing [103,126], surface-enhanced infrared absorption spectroscopy (SEIRAS) [127,128], photovoltaic [129,101], as photodetectors in optoelectronics [130,131], enhanced light trapping [103,132], and terahertz radiation (THz radiation) emission [133,102,134]. The partially amorphized Ge quantum dots encapsulated in the silicon matrix are proven to show improved lasing action making them potentially useful for application in silicon integrated technology [124,125]. Enhanced molecular sensing capabilities have been demonstrated by plasmon-enhanced infrared absorption due to an array of germanium nanostructures [103,126,135]. The work by Podolian et al. reports the demonstration of enhanced photo-voltage generated by an array of Ge-Si nanostructures on a silicon substrate, which is suitable for solar cell applications. [131]. Germanium nanostructures have been reported to achieve three-fold to five-fold increased amplitude of terahertz radiation emission as compared to the bare-germanium surface. It was surprising that germanium being the indirect bandgap semiconductor, the periodic array of germanium nanostructures gave terahertz radiation emission comparable to the direct bandgap semiconductor n-GaAs (n-type GaAs) [102]. Local surface charge collection due to the high surface area is attributed to the enhanced THz emission from the Ge nanostructures [133]. These reports suggest that the periodic arrays of nanostructures play an essential role for improved light-matter interactions such as enhanced surface plasmon based sensing and in improved terahertz emission [103,126,102].

The occurrence of ordered arrays of objects or ordered morphological features, is a widely seen phenomenon in nature known as self-organization, straddling from ripples on sand dunes to leaf venation through molecular and atomic arrangements on the surfaces and in materials [1]. Inspired by such natural occurrences, self-organization phenomena such as preferred particle assemblies on the textured surfaces, strain-induced pattern formation by surface relaxation, and energy beam induced nanopatterning by self-organization of the surface atoms are common strategies for the formation of nanoscale structures [2–4]. These self-organization processes exploit the surface characteristics like thermodynamic stabilities, surface energy and surface diffusion effects to create micro and nanoscale features. The surface perturbation through energy beams utilizing laser beam and ion beam provides the fractal-like and ripple-like surface features ranging from millimeter and micron to nanometer scale [4,11,136]. The self-organization induced by a broad ion beam has been extensively used by researchers to create nanoscale structures via irradiation on different surfaces such as transparent and conducting nanowires on aluminium [11], nanodots on silicon surface [12], and nanowires on the gold surface [13]. Ion beam irradiation on the surface induces the formation of the curved surfaces with an increase in the roughness, and atoms on the concave regions over the material surface tend to erode faster than those from the convex regions [5]. Such a selective erosion and surface diffusion on ion beam irradiation provide reorganization of the surface atoms which lead to the formation of the nanostructures on the surface [5,6]. The self-organization process by broad ion beam is faster and produces nanostructures over a large area. However, it produces simple structures such as nanoripples, nanowires and nanodots; thus, the realization of nanostructures which can have high-periodicity, complex-morphologies, and morphological-uniformity has been a challenge. To overcome these challenges and to achieve nanoscale control over the ion beam induced self-organization, focused ion beam could be a promising tool by utilizing its capability of nanoscale milling.

Conventionally, the FIB fabrication has been widely used by direct milling operation (i.e., direct writing of features on the surfaces by FIB milling process) on the material for the desired geometrical shape of the nanoscale/microscale structures [24,26,28]. The major disadvantage of the traditional FIB direct milling method for polygonal morphology is the requirement of milling the arrays of spots (pixels) to remove the material in the shape of a desired polygonal geometry [24,26,28]. This requirement of multi-pixel milling for a particular geometry imposes restrictions on the size reduction for the nanostructures. Also, it is a slow process to fabricate structures via direct milling. Employing the self-organization phenomenon to transform each pixel into the desired polygonal morphology is a promising strategy to overcome the drawbacks of the traditional direct milling process. Quasi-periodic self-organized structures have previously been fabricated by using FIB such as nanoripples on germanium [132,49] and diamond [46], nanofins on platinum [108], nanoholes on germanium [56], and nanodots on beryllium [55]. The low-aspect-ratio nanostructures are predominantly self-organized due to selective surface diffusion driven reorganization and without any material removal involved during the process [55,56]. Whereas, the high-aspect-ratio nanostructures with a slight alignment control, in addition to the self-organization, also involve some amount of material removal as a result of ion beam milling [132,49]. However, the morphologies of these nanostructures are limited to primitive shapes like nanodots or nanoripples, and these patterns are quasi-periodic. Hence, to obtain high-periodicity and complex-morphologies like polygons (i.e., fundamental building blocks of nanofabrication systems), the milling process aided by local self-organization in the vicinity of each pixel could be explored. In Chapter 4, attempts were made to achieve control on the alignment of quasi-periodic nanoripples by varying the beam overlap (BO) during the focused ion beam irradiation on the germanium surface [132]. It is established that the germanium nanoripples provide high optical absorption at the broad wavelength and incident angle range [132]. However, periodic nanostructures would have an advantage in broader application domains such as surface plasmon resonance, THz signal generations, photovoltaics, optoelectronics, bio-sensing, etc.

In the following sections, the unique formation of the periodic polygonal nanostructures is reported by controlled and nanoscale self-organization through strategic FIB scanning over the selected area on the germanium (100) surface. The strategy involves the utilization of the self-organization process to turn the circular nanoholes created by each FIB pixel into the desired polygonal morphology. Here, a novel route to fabricate polygonal nanostructures using scanning of FIB over the germanium (100) surface with negative beam overlap (BO) is presented. On scanning over a rectangular region with a predefined grid, the circular nanoholes evolved to have a unique polygonal morphology. The single-step process involves the exploitation of the viscous-flow driven self-organization process to transform the circular nanoholes into the desired polygonal morphologies such as triangles, squares, hexagons, etc. The phenomenon of morphology evolution, phase change, and underlying mechanism were investigated by scanning electron microscopy, atomic force microscopy, transmission electron microscopy and Raman spectroscopy. The obtained protruding and periodic polygonal nanostructures have a minimum feature size of around 25 *nm* and exhibit broadband optical absorptance behaviour.

5.2 Experimental details

To attain nanoscale control over the confined viscous-flow driven by the self-organization, the FIB/SEM (Focused Ion Beam/Scanning Electron Microscope) system (FEI Quanta 3D, Thermo Fisher, USA) was used for the fabrication processes. An SEM (FEI Magellan 400 Field Emission, Thermo Fisher, USA) was used for high-resolution imaging purpose. The 30 *kV* Ga^+ FIB was used to fabricate nanostructures with a beam current of 50 *pA*. During the patterning, the horizontal pixel resolution was kept at 4096 pixels with 5000*X* magnification and horizontal field width of 29.8 *µm*. This set-up provided the pixel size of 7.3 *nm*. The probe size (i.e., FWHM) for this system at 50 *pA* is 19 *nm*, which gives the distance between two neighbouring FIB spots (pitch) to be 133 *nm* for −600% beam overlap (BO). To scan the FIB in a predefined pattern of square, triangular and hexagonal grids, the interface of the stream file provided by the manufacturer was used. First, the *x* and *y* coordinates of a defined pixel grid were calculated based on the beam overlap and dimensions of the patterned area. From the *x* and *y* coordinates of the pixel grid, the pixel numbers are calculated and listed in the stream file in a manner which defines the scanning direction as the desired pattern.

Nanostructures fabricated are characterized by atomic force microscope (AFM), UV-Vis spectroscopy, micro-Raman spectroscopy and transmission electron microscopy (TEM) to understand the crystallographic effects and change in optical properties due to FIB irradiation. As the patterned regions are of area 5.5 × 5.5 μm^2, the Raman spectroscopy and UV-Vis spectroscopy measurements were taken with the help of an optical microscope attached with the spectrometer set-up. The Raman spectra were acquired using Renishaw VIS Raman set-up (Renishaw, UK) connected with a microscope and a laser source of 488 *nm* wavelength. The reflectance spectra of germanium nanostructures were acquired using J&M Micro UV-Vis microscope spectrometer (JM microsystems, Germany) with an objective lens of 50*X* magnification at a numerical aperture (NA) of 0.65. The halogen lamp was used as a white light source, and it was coupled with optical fibre to illuminate the sample. The reflected spectrum from the sample is normalized with respect to reflection from a protected silver mirror (from Thorlabs Inc.). To study the height of protruding nanostructures, the AFM characterization was performed using the Bruker Dimension Icon system. TEM (FEI Tecnai G2-F20 system, Thermo Fisher, USA) operating at 200 *kV* was used for imaging and energy-dispersive X-ray spectroscopy (EDS) characterizations.

5.3 Results and discussion

The self-organization of surfaces is governed through perturbation by means of temperature treatment, induced strains, and energetic beams [3,4]. The material surface undergoes phase transformation and surface atoms reorganize in various morphologies forming nanoscale or microscale features, with increased or decreased roughness, based on the surface kinetics during the surface perturbation treatment. In the current study, attempts are made to employ the focused ion beam induced self-organization, a phenomenon responsible for providing nanoripples [132], to transform the milled nanoholes (formed by each pixel during FIB scanning) into the polygonal nanoholes. The self-organization is attributed to the confined viscous-flow due to the thermal spike on the ion incidence during irradiation of ion beam on the germanium surface, and leads to the formation of nanoscale structures [137,138]. The control over viscous flow at the nanoscale can be a beneficial strategy for periodic nanostructures; thus, this work is aimed at achieving precise control on the self-organization process using a focused ion beam. It has been known conventionally that during FIB milling, the diameter of nanohole increases with an increase in the ion dose [19,28,139,140]. Initially, the adjoining nanoholes are far apart when milling operation with FIB is performed. The diameter of the nanoholes increases with an increase in the dose; thus, the boundaries of adjoining holes start overlapping each other. As depicted in Figure 5.1(a), when the boundaries of the adjoining nanoholes are close enough and overlap each other, the further irradiation leads to etching of the overlapped region due to ion beam assisted milling, and the wall between adjoining holes gradually undergoes erosion [139,140]. The self-organization can be effective to transform the circular nanoholes (which are formed by each pixel during milling by FIB) into the polygonal nanoholes. The self-organization is to be engineered such that when the ion beam dose is increased, the boundary wall between the adjoining nanoholes undergoes a straightening process instead of getting eroded, as represented in Figure 5.1(b).

The expected transformation process is depicted in the three-dimensional (3D) schematics (Figure 5.2(a & b)). When Ga^+ ions are bombarded at a spot on the surface, it initially creates Gaussian-shaped holes as represented in a sectional view (Figure 5.2(a & b)). For a higher dose, the walls of the adjacent holes interact with each other, and the polygonal geometries are generated, which are protruding out of the original germanium surface as schematically represented in Figure 5.2(b).

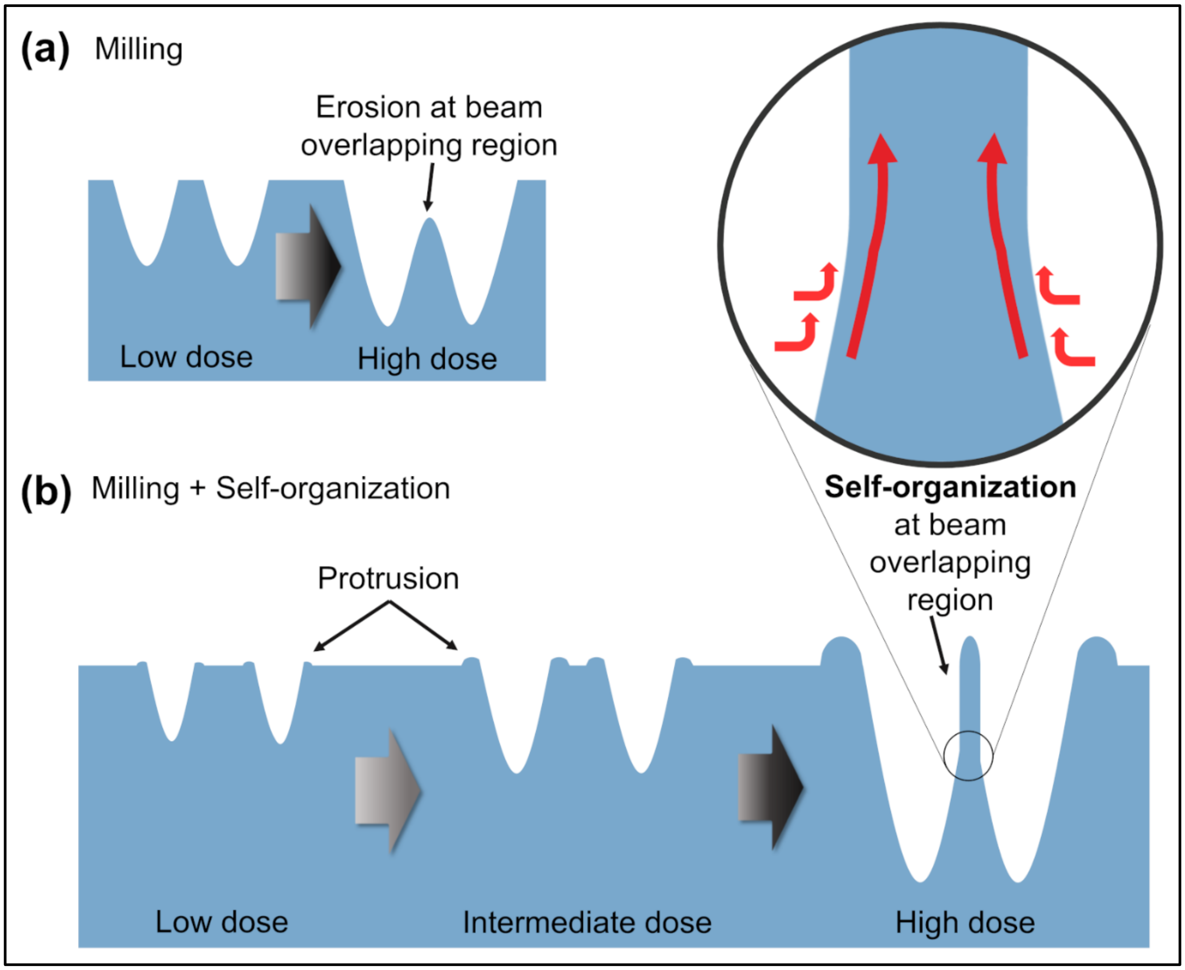

(a) Milling
Erosion at beam overlapping region
Low dose
High dose
(b) Milling + Self-organization
Protrusion
Self-organization at beam overlapping region
Low dose
Intermediate dose
High dose

Figure 5.1 Overview with the cross-sectional schematic for the phenomenon to manipulate the morphology of nanoholes: (a) conventional milling dominant FIB machining and (b) self-organization driven nanofabrication.

5.3.1 Characterization of morphological evolution using SEM and AFM

The Ga^+ FIB (dual-beam SEM-FIB system FEI Quanta 3D) was used to fabricate nanostructures at an energy 30 *kV* and beam current 50 *pA*. During the patterning, the horizontal pixel resolution was kept at 4096 pixels with 5000*X* magnification and horizontal field width of 29.8 μm. This set-up provided the pixel size of 7.3 *nm*.

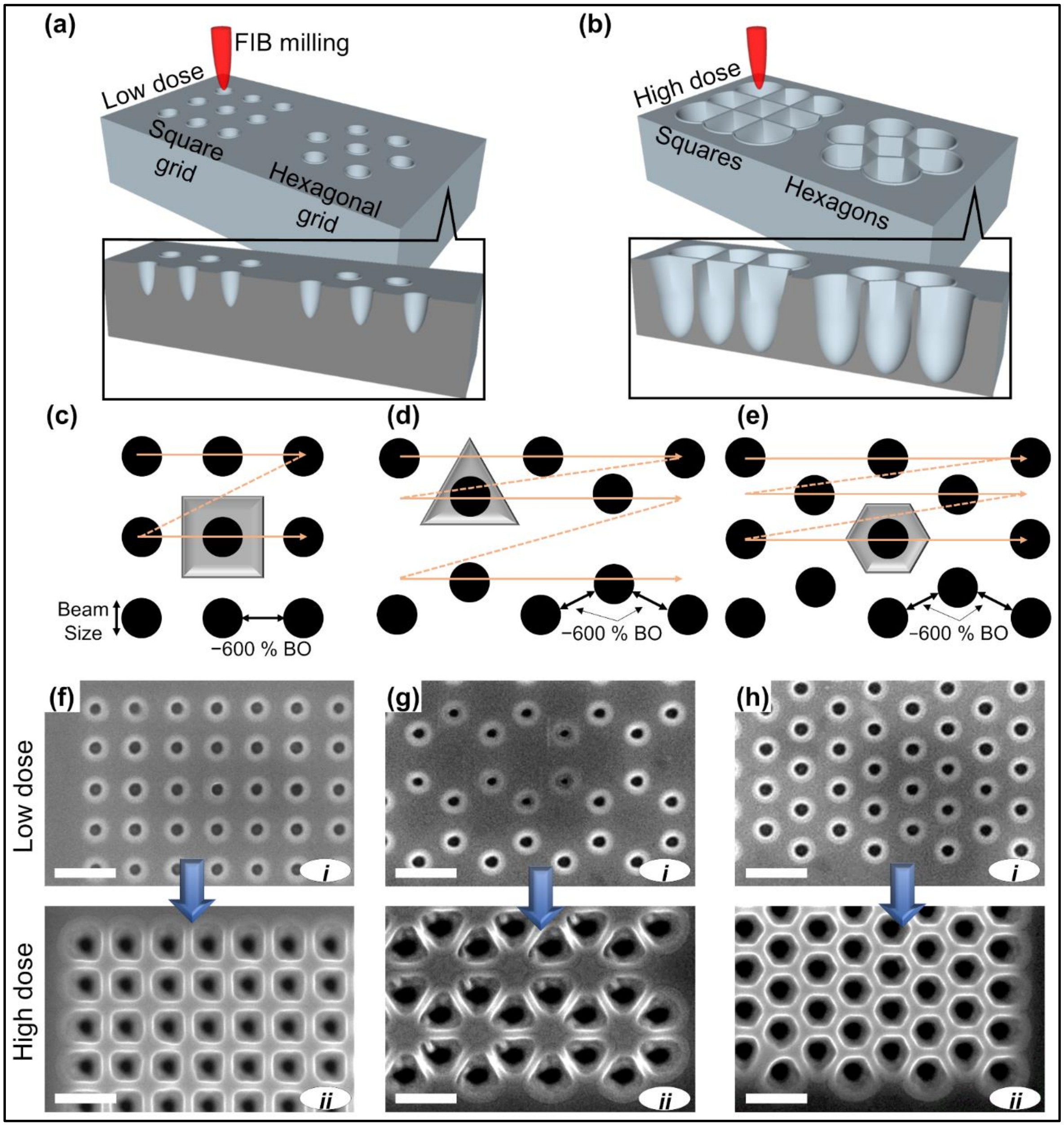
(a)
FIB milling
Low dose
Square grid
Hexagonal grid
(b)
High dose
Squares
Hexagons
(c)
Beam Size
−600 % BO
(d)
−600 % BO
(e)
−600 % BO
(f)
(g)
(h)
Low dose
High dose
i
ii

Figure 5.2 Schematic for morphology evolution, scanning strategies and SEM images. 3D representation for morphology evolution of nanoholes from circular (a) to polygonal (b). Inset images in (a & b) are cross-sectional views for 3D schematics. Scanning grids for (c) square, (d) triangle, and (e) hexagon geometries. The corresponding SEM images for the transition from (*i*) circular nanoholes to (*ii*) polygonal nanoholes such as (f) square, (g) triangular, and (h) hexagonal nanoholes with an increase in dwell time from 0.1 *ms* to 1.8 *ms* on 10-pass FIB scan. The scale bar represents 200 *nm*.

First, the *x* and *y* coordinates of a particular pixel grid were calculated based on the beam overlap and dimensions of the patterned area. From the *x* and *y* coordinates of the pixel grid, the pixel numbers are calculated and listed in the stream file in a manner which defines the scanning direction, as shown in Figure 5.2(c-e). For the square nanostructures, each pixel is surrounded by four pixel-positions, as shown in Figure 5.2(c). In a triangular pixel grid (Figure 5.2(d)), each pixel is surrounded by three adjacent pixels at a distance corresponding to the specific beam overlap. Similarly, for the hexagonal grid (Figure 5.2(e)), every pixel was surrounded by six adjacent pixels. The probe size for this system at 50 *pA* is 19 *nm*, which gives the distance between two adjacent FIB spots (pitch) to be 133 *nm* for −600% beam overlap (BO).

The transformation from circular nanohole to polygonal formation is observed for each FIB pixel based on the number of adjacent pixels in the scanning grid, as shown in Figure 5.2(f-h). The symmetry and the grid geometry led to the formation of desired polygonal nanostructures. The dwell time of 1.8 *ms* with a 10-pass scan was found to provide the best dose per spot to form the polygons such as squares, triangles, pentagons, and hexagons. The obtained square, triangular, and hexagonal nanostructures are shown in Figure 5.2(f-h). Initially, circular nanoholes transform into square, triangular and hexagonal shape at the optimized dwell time. The curved edges on the top of the hole represent protruding material as seen from SEM images in Figure 5.2(f(*i*), g(*i*) & h(*i*)). For a higher dose, the walls of the adjacent holes interact with each other, and the polygonal geometries are generated which are protruding out of the original germanium surface (see Figure 5.2(f(*ii*), g(*ii*) & h(*ii*))) as schematically represented in Figure 5.2(a & b). The thickness of the wall for polygons is around 25 *nm*, and the pitch is 133 *nm*. The tilted SEM images (at 20° and 40° angles) for hexagonal nanoholes in Figure 5.3(e) confirm the uniform formation of ordered and protruding nanostructures on the germanium surface. The higher-order complex polygonal nanostructures like pentagons and octagons are also possible to fabricate as shown in Figure 5.3(c) and Figure 5.3(d), respectively, with FIB scanning strategies detailed in Figure 5.3(a) and Figure 5.3(b). The stream file was used in a manner that defines the scanning direction, as shown in Figure 5.3(a & b) for a pentagonal pixel grid and octagonal pixel grids. It should be noted that in the case of square, triangular and hexagonal grid, all the pixels are going to generate corresponding square, triangular and hexagonal polygons due to the symmetry of the grid, as seen in Figure 5.2(c-e). Whereas, in the case of pentagonal and octagonal grids, only the central pixels are going to generate the corresponding polygonal nanohole morphologies. It should also be noted that the beam overlaps for the radial distances (radial length) and peripheral distances (side length) are different for the pentagonal and hexagonal grids (see Figure 5.3(a & b)). As the side beam overlap (BO) is smaller than the radial BO for the octagonal pixel grid. The dose has to be optimized for the suitable dwell time to get octagonal morphologies for central pixels. Here, dwell time for a central pixel was 2.2 *ms* and that for the peripheral pixel was 1.1 *ms* to get the octagonal morphology from the grid represented in Figure 5.3(b). However, in the case of pentagonal morphology, the dwell time for all the pixels was the same (i.e., 1.8 *ms*), a similar situation to the square, triangle, and hexagonal morphologies as shown in Figure 5.2(c-h).

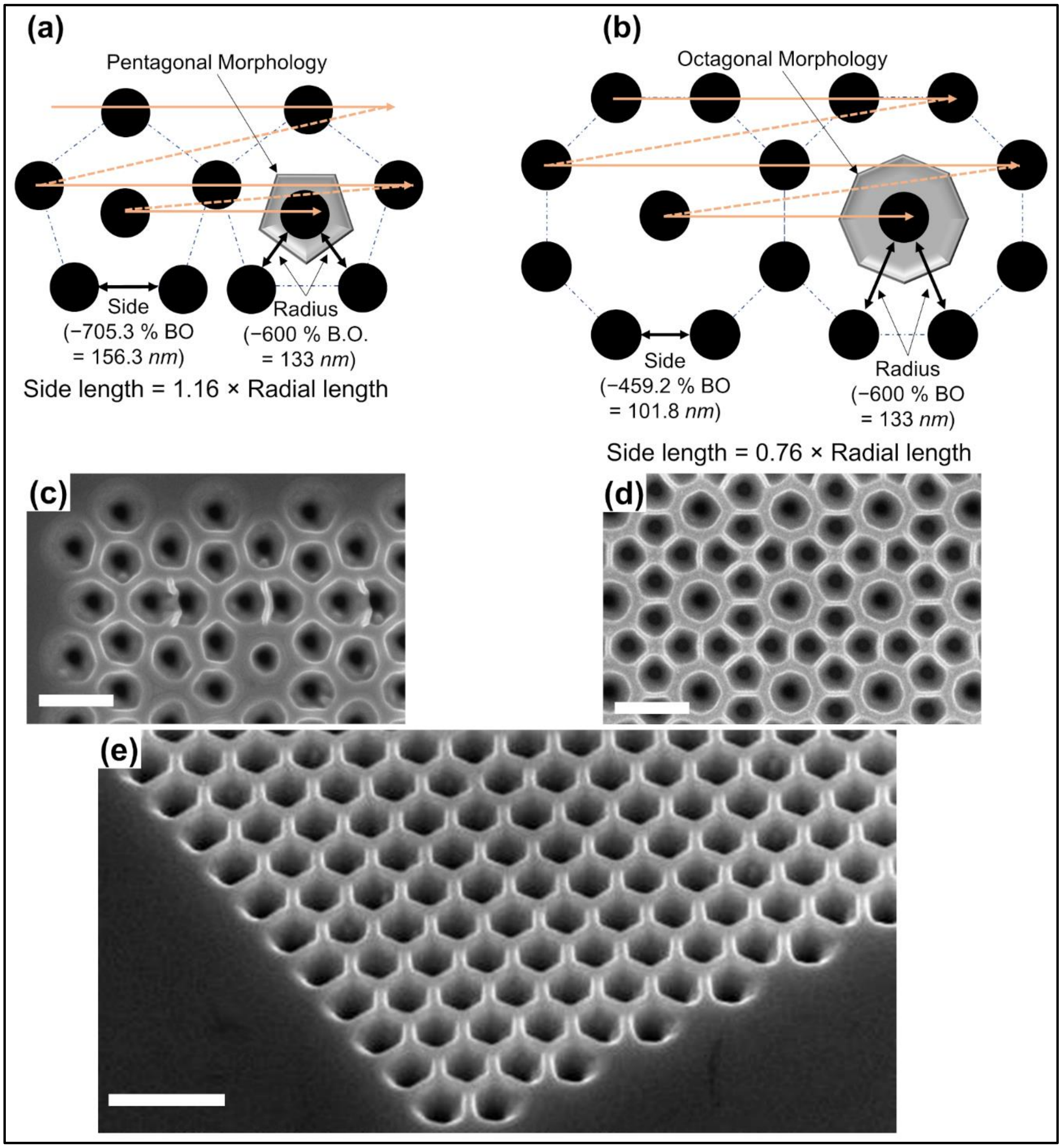
(a)
Pentagonal Morphology
Side
(−705.3 % BO
= 156.3 nm)
Radius
(−600 % B.O.
= 133 nm)
Side length = 1.16 × Radial length
(b)
Octagonal Morphology
Side
(−459.2 % BO
= 101.8 nm)
Radius
(−600 % BO
= 133 nm)
Side length = 0.76 × Radial length
(c)
(d)
(e)

Figure 5.3 Scanning grids used in the stream files for (a) pentagon, and (b) octagon shaped nanostructures with corresponding SEM images (c) pentagon, and (d) octagon nanoholes, respectively. The orange arrow shows a raster scanning direction. Blue dotted lines are for the guide representing peripheral pixels. (e) Tilted image for hexagonal nanoholes at 20° angle (inset is at 40° angle). The scale bars represent 200 *nm*.

In order to find the optimum dose for the formation of proper polygonal nanostructures, the evolution of square and hexagonal nanostructures was observed with an increase in the dwell time for a fixed area. Figure 5.4 shows the SEM images of the hexagonal nanostructures generated from raster scanning of FIB with different doses per area. With a probe size of 19 *nm* (for 50 *pA* beam current), the beam overlap was set to −600% in x- and y-direction, offering a pitch size of 133 *nm*. To get different doses over the $5.5 \times 5.5\ \mu m^2$ area, the dwell time was varied from 0.001 to 0.025 *s*. It can be observed from Figure 5.4 that the nanoholes are circular for the low dose (2.08×10^{15} *ions/cm*^{2}) as the boundaries of adjacent spots are too far and do not interact with each other. When the dose increased, the boundaries of adjacent nanoholes began to interact with each other. And on the further increase in the dose, the hexagonal nanoholes are formed at a dose of 3.74×10^{16} *ions/cm*^{2}.

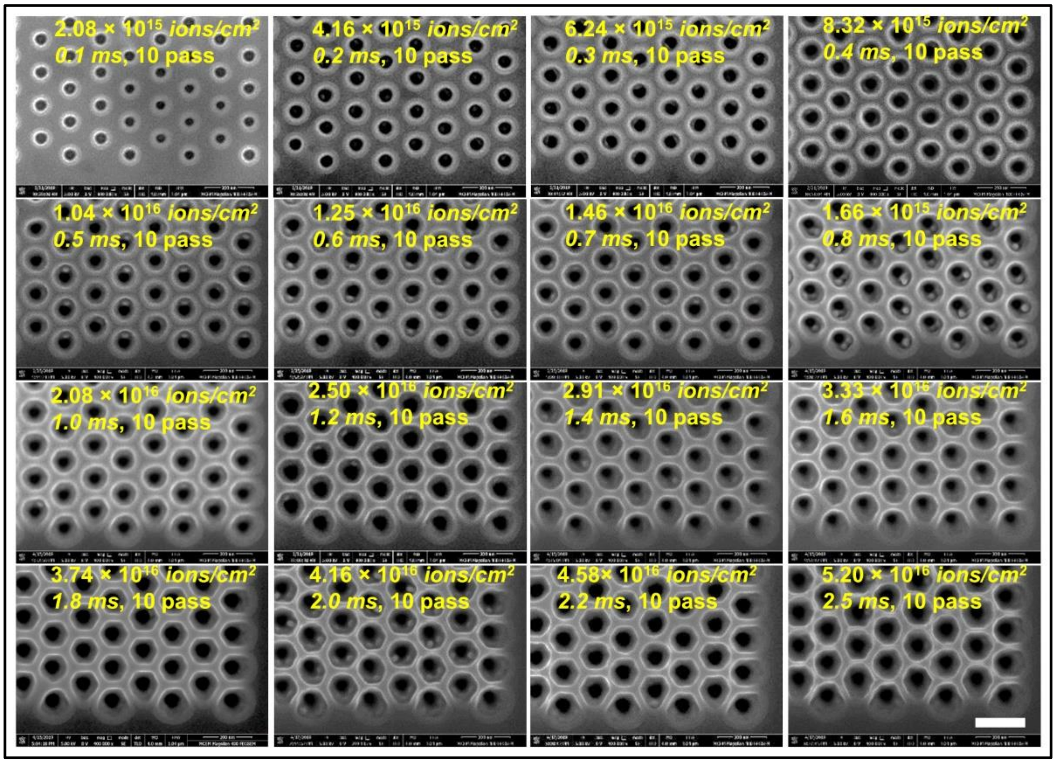
2.08×10^{15} ions/cm^2
0.1 ms, 10 pass
4.16×10^{15} ions/cm^2
0.2 ms, 10 pass
6.24×10^{15} ions/cm^2
0.3 ms, 10 pass
8.32×10^{15} ions/cm^2
0.4 ms, 10 pass
1.04×10^{16} ions/cm^2
0.5 ms, 10 pass
1.25×10^{16} ions/cm^2
0.6 ms, 10 pass
1.46×10^{16} ions/cm^2
0.7 ms, 10 pass
1.66×10^{15} ions/cm^2
0.8 ms, 10 pass
2.08×10^{16} ions/cm^2
1.0 ms, 10 pass
2.50×10^{16} ions/cm^2
1.2 ms, 10 pass
2.91×10^{16} ions/cm^2
1.4 ms, 10 pass
3.33×10^{16} ions/cm^2
1.6 ms, 10 pass
3.74×10^{16} ions/cm^2
1.8 ms, 10 pass
4.16×10^{16} ions/cm^2
2.0 ms, 10 pass
4.58×10^{16} ions/cm^2
2.2 ms, 10 pass
5.20×10^{16} ions/cm^2
2.5 ms, 10 pass

Figure 5.4 Evolution of hexagonal nanostructures with an increase in dwell time and dose. The scale bar represents 200 *nm*.

The demonstrated methodology provides a highly controlled manipulation of the single-spot FIB milling process to realize the optimized morphology of the nanoholes. The achieved morphological control can lead to the advancement of a fast and easy fabrication procedure for desired polygonal nanoholes through engineering of each circular hole.

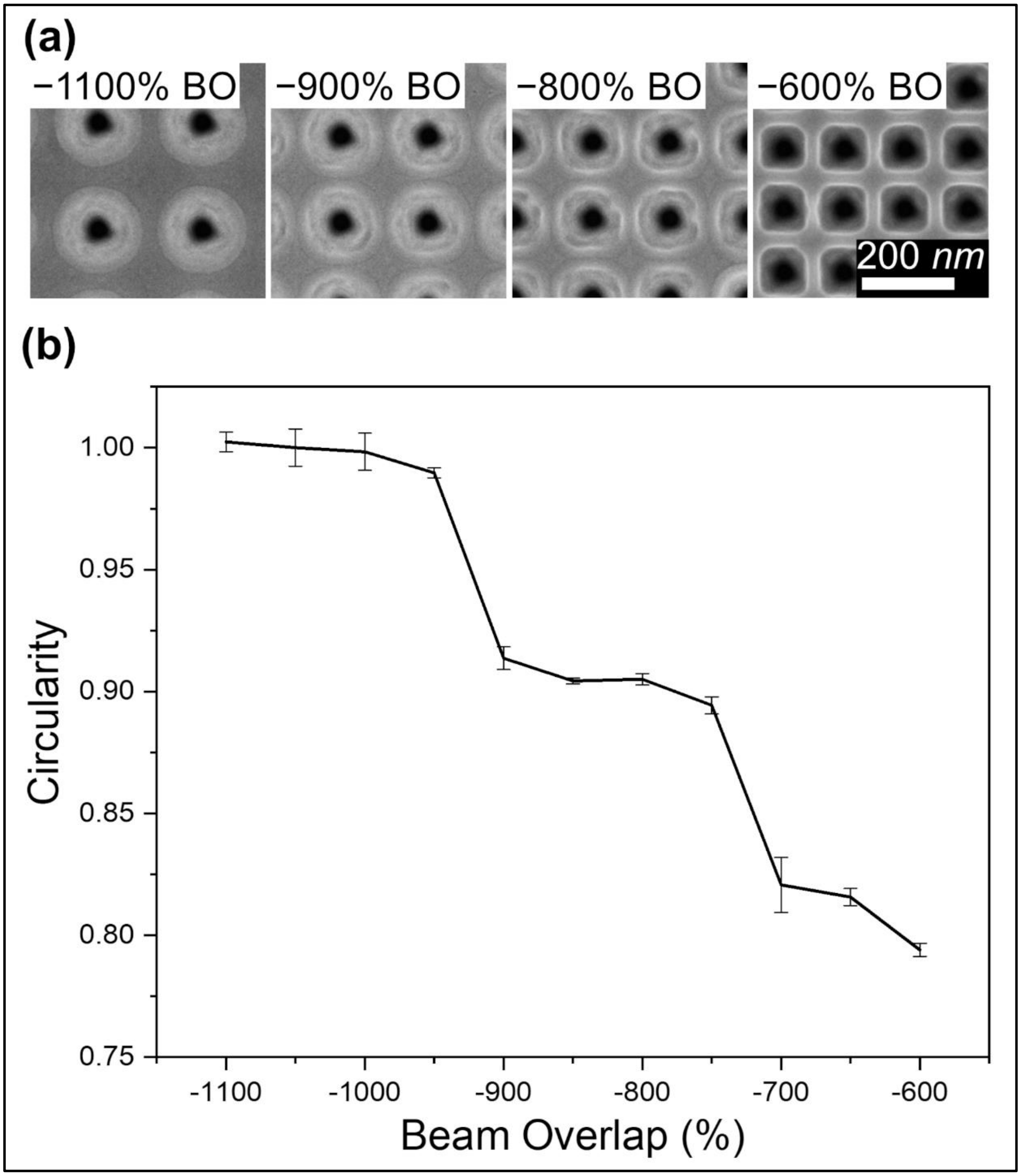

Figure 5.5 (a) Evolution of nanoholes with increasing beam overlaps (BO). (b) The circularity of nanoholes for the square grid with an increase in the beam overlap.

In order to investigate the effect of beam overlap, the phenomenon of morphology evolution from circular to square nanoholes was confirmed by the change in circularity with varied beam overlap using 1.8 *ms* dwell time and 10-pass scan as shown in Figure 5.5. It is observed (Figure 5.5(a)) that for the lowest beam overlap (−1100%), the nanoholes are far apart and are circular as they do not interact with each other. With an increase in the beam overlap (i.e., decrease in distance between adjacent pixels), the nanoholes come closer to each other, and their adjoining walls start to get reshaped due to interactions of the irradiation-affected boundaries of adjoining nanoholes. For the beam overlap of −600%, square nanoholes are formed. Thus, the beam overlap of −600% is ideal for getting the polygonal nanostructures for the present FIB parameters and instrument. The circularity of the two-dimensional geometry can be defined by equation,

$$Circularity = \frac{4\pi \cdot \mathrm{Area}}{Perimeter^2} \tag{5.1}$$

Thus, using the above equation, the phenomenon of morphology transformation from circular to square nanoholes was also confirmed by the change in circularity with varied beam overlap, as shown in Figure 5.5(b). Initially, for the circular nanoholes the circularity is 1 (at −1100% BO), and with the increase in BO the circularity decreases to 0.78 (at −600% BO), indicating the confirmation for the square nanohole formation. In order to check the formation of morphologically proper square nanostructures with the optimum dose, the evolution of square nanostructures was studied with an increase in the dwell time, as shown in Figure 5.6(a). To check the protrusion of walls with an increase in the irradiation time, the AFM micrograph was obtained for the FIB patterned region shown in Figure 5.6(a). As shown in the AFM micrograph of the patterned area (in the inset of Figure 5.6(b)), the nanostructures are found to protrude out of the germanium surface; and the height of the protrusion increases with an increase in the dose. The height obtained through the line profile (Figure 5.6(b)) suggests that the increase in the dwell time leads to an increase in the height of the protrusion of nanostructures. This indicates that the structures are formed due to self-organization on FIB irradiation.

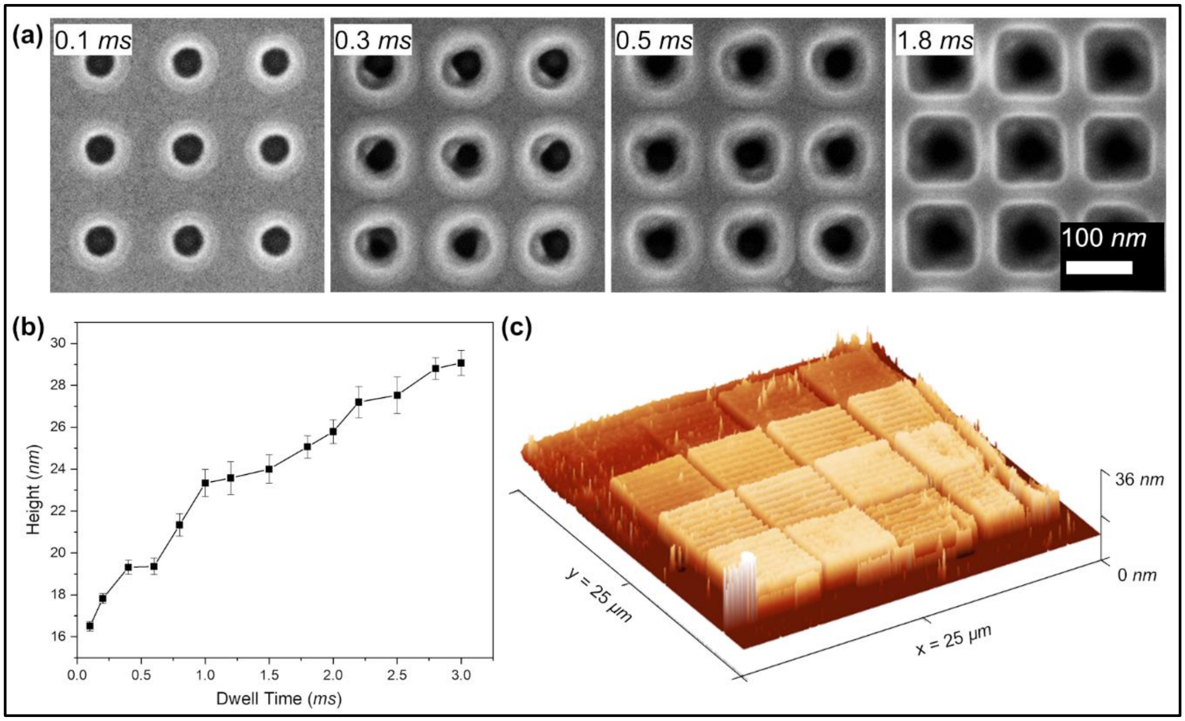

Figure 5.6. (a) Evolution of nanoholes with increasing dwell time. (b) Protrusion of the self-organized nanostructures represented by the average height as a function of dwell time from the line profile of the AFM image in (d). (d) 3D representation of the AFM image acquired of the patterned region.

5.3.2 Nanostructures with complex morphologies by varying parameters

In order to produce the complex morphologies of nanostructures, the FIB parameters were varied for differential scanning over the target surface. On changing the number of passes for particular scanning operation and by changing scanning direction, the formation of zigzag and corrugated morphologies was obtained. In addition to the complex morphologies, this study revealed vital information on morphology optimization for desired nanostructures.

5.3.2.1 Zigzag nanostructures by single-pass scan

In order to check the effect of raster scan versus serpentine scan, the single-pass scan was performed, as shown in Figure 5.7. It is observed that the raster scan has a similar effect as a serpentine scan such that the V-shape is pushed away in the direction opposite to the scan propagation. Hence, the raster scan can provide half the pitch for a zigzag wall than that of the serpentine scan. This method is effective in getting the desired zigzag morphology.

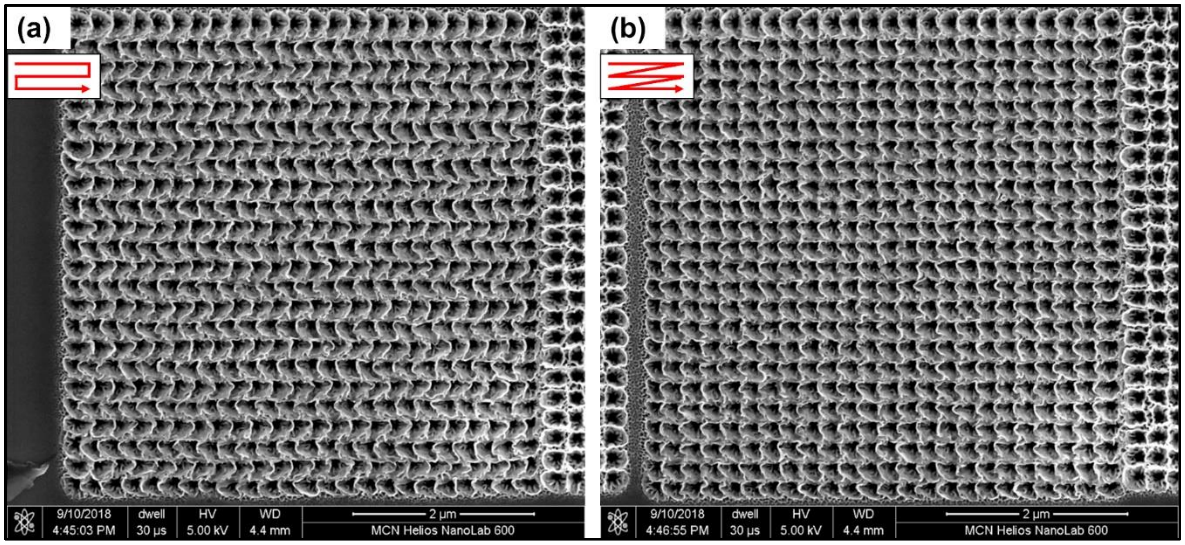
(a)
9/10/2018 4:45:03 PM
dwell 30 µs
HV 5.00 kV
WD 4.4 mm
2 µm
MCN Helios NanoLab 600
(b)
9/10/2018 4:46:55 PM
dwell 30 µs
HV 5.00 kV
WD 4.4 mm
2 µm
MCN Helios NanoLab 600

Figure 5.7 Single-pass scan for zigzag nanostructures, (a) serpentine scan and (b) raster scan. Red arrows represent the direction of serpentine and raster scans.

The effect of a number of scan-passes on the nanostructure geometry was investigated during low and high-dose serpentine scans. As shown in Figure 5.8, the low dose serpentine scan with single-pass and 10-pass shows no effect of the passes on the final circular geometry of nanoholes. However, for the high dose, the number of passes significantly influence the final geometry of the nanoholes (Figure 5.9).

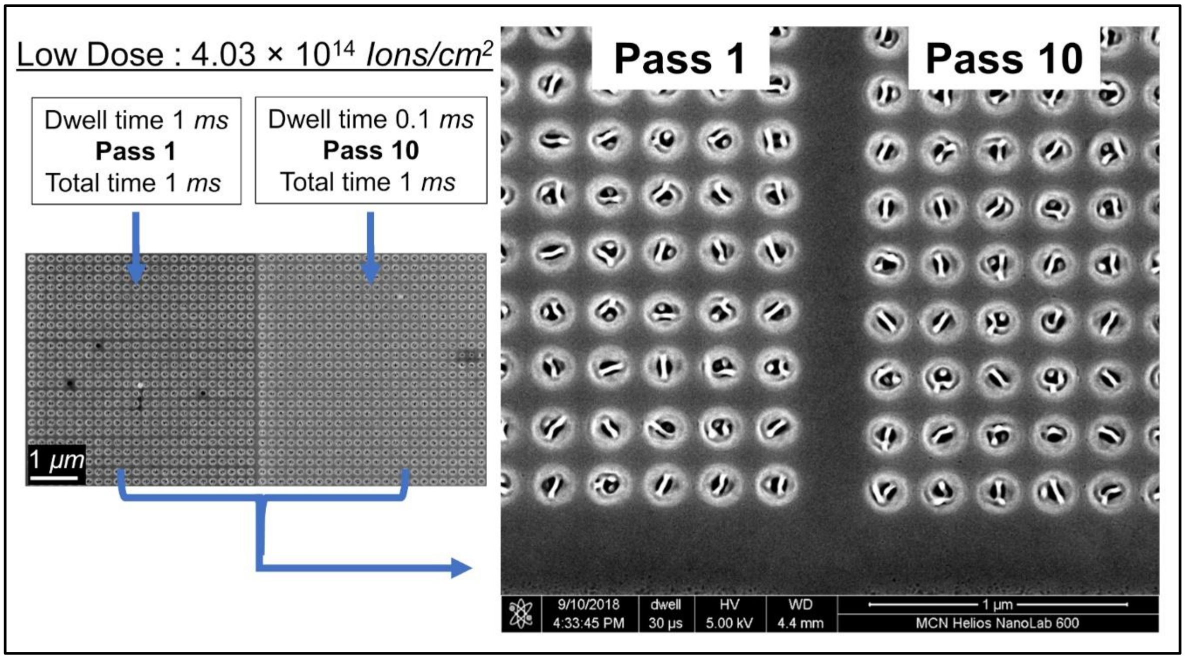
Low Dose : 4.03 × 10^14 Ions/cm^2
Dwell time 1 ms
Pass 1
Total time 1 ms
Dwell time 0.1 ms
Pass 10
Total time 1 ms
1 µm
Pass 1
Pass 10
9/10/2018
4:33:45 PM
dwell
30 µs
HV
5.00 kV
WD
4.4 mm
1 µm
MCN Helios NanoLab 600

Figure 5.8 Effect of a number of passes for a fixed dose of 4.03 × 10^{14} *ions/cm*^{2}. The left side of each image represents single-pass serpentine scan, and the right side of each image represents a 10-pass serpentine scan.

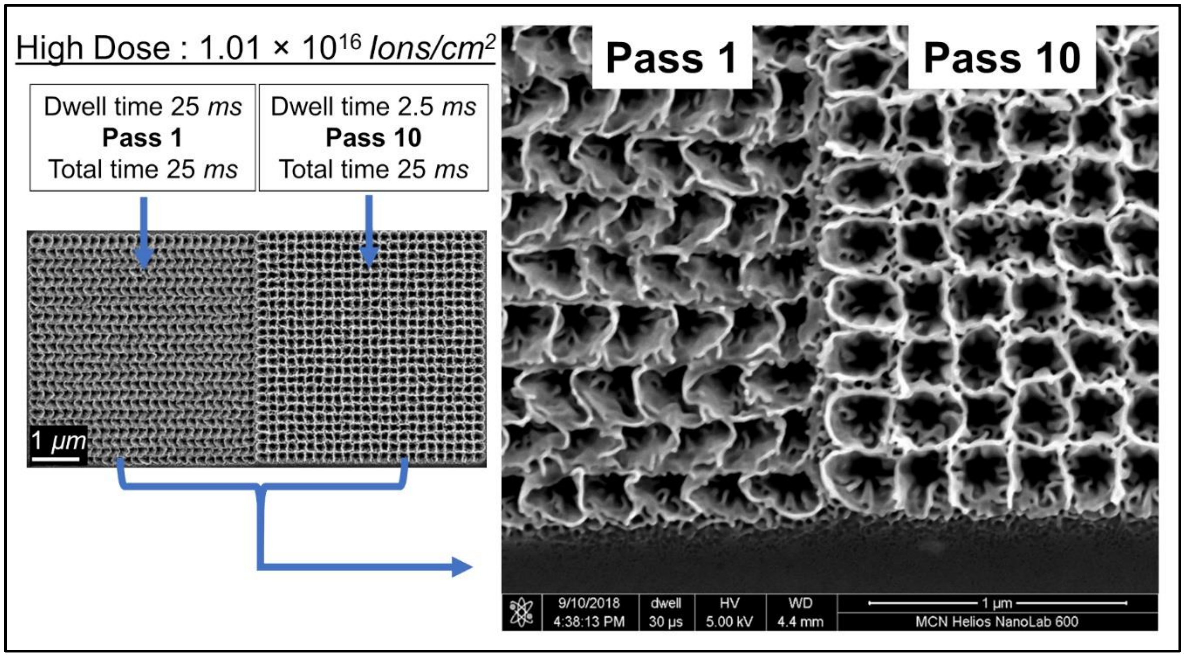
High Dose : 1.01 × 10^16 Ions/cm^2
Dwell time 25 ms
Pass 1
Total time 25 ms
Dwell time 2.5 ms
Pass 10
Total time 25 ms
1 µm
Pass 1
Pass 10
9/10/2018
4:38:13 PM
dwell
30 µs
HV
5.00 kV
WD
4.4 mm
1 µm
MCN Helios NanoLab 600

Figure 5.9 Effect of a number of passes for a fixed dose of 1.01 × 10^{16} *ions/cm*^{2}. The left side of each image represents single-pass serpentine scan, and the right side of each image represents a 10-pass serpentine scan.

It can be observed from Figure 5.9 that the multi-pass serpentine scan leads to the straightening of the walls leading to a proper and thin-walled array of square walled nanoholes, whereas the single-pass serpentine scan provides a zigzag pattern. Hence, it is preferred to use a multi-pass scan to obtain an array of squares with the thinnest possible walls and proper morphology.

5.3.2.2 Circularly concentric zigzag nanostructures

Concentric scanning with an outer diameter of 5 μm was performed to obtain hexagon-shaped nanoholes and spiralling zigzag geometries, as shown in Figure 5.10. The same beam overlap was set radially for the concentric scanning, giving a pitch of −600% BO between adjacent spots. In order to get different doses over the 5 × 5 μm^2 area, the dwell time was varied from 0.001 to 0.025 *s*. Figure 5.10 shows a comparison of the obtained nanostructures from low, intermediate, and high-dose concentric scans. It is observed from Figure 5.10(a) that the low dose gives circular nanoholes similar to the serpentine scan, and on the increase in the dose, the hexagonal geometries are evolved (Figure 5.10(b)). For the higher dose, the walls form V-shape in the direction opposite to the scan propagation (Figure 5.10(c)).

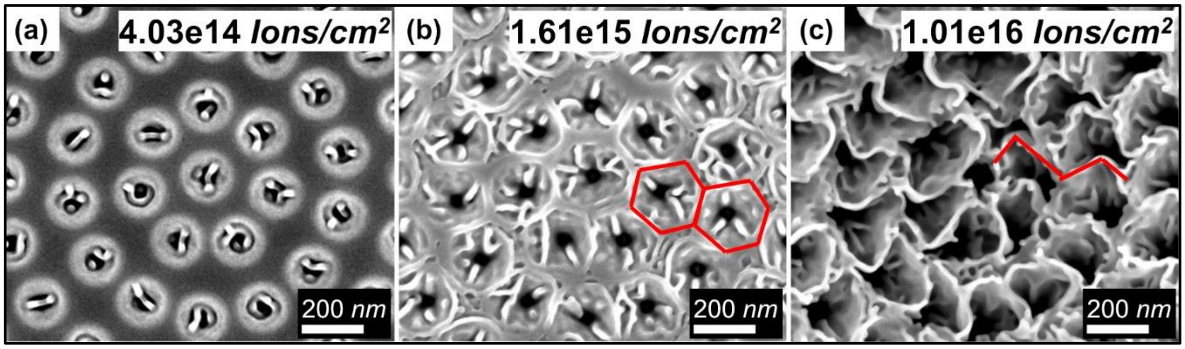

Figure 5.10 Evolution of hexagon-like and V-shaped nanostructures with dose (red lines represent geometric shapes), (a) low dose of 4.03×10^{14} *ions/cm*^{2}, (b) intermediate dose of 1.61×10^{15} *ions/cm*^{2}, and (c) high dose of 1.01×10^{16} *ions/cm*^{2}.

It is observed from Figure 5.10(b) that six beam spots surround any typical spot on the co-centrally scanned area; interaction of boundaries of these adjacent spots leads to the formation of hexagon-shaped nanowalled structures for the intermediate beam doses similar to the results in Figure 5.4. However, for the larger beam doses, the wall forms the zigzag nanostructures concentrically spiralled with pointing opposite to the scan propagation.

5.3.2.3 Corrugated, nano-mushrooms and nanohole-needle shaped structures

The Ga^+ FIB was irradiated with 30 *kV* energy at a small current of 9.7 *pA* to fabricate periodic complex-shaped self-organized nanostructures on the germanium surface. SEM images of the periodic and self-organized complex nanostructures are shown in Figure 5.11. Based on the beam overlap and beam current settings, varied morphologies of the protruding nanostructures are obtained, such as corrugated (Figure 5.11(a)), nano-scaled mushrooms (Figure 5.11(b)), and nanoneedle-nanohole dual-structures (Figure 5.11(c)).

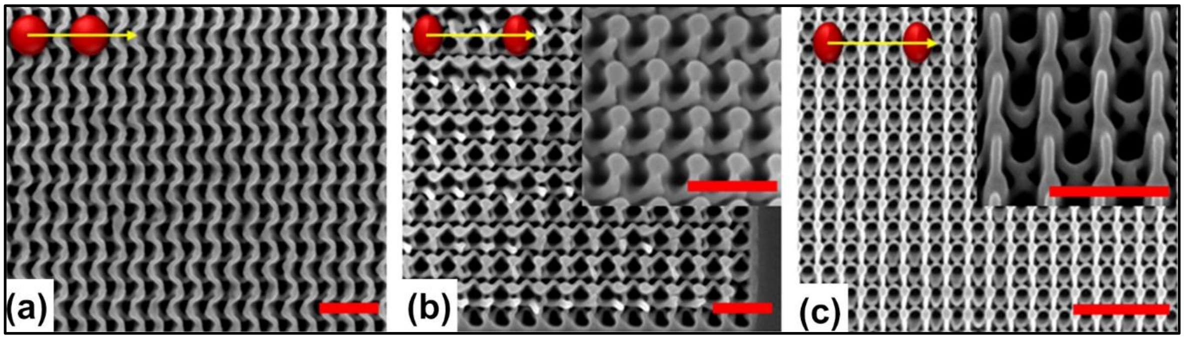

Figure 5.11 Complex-shaped self-organization (a) Corrugated, (b) Nano-mushrooms (inset, tilted at 30°), and (c) dual-nanostructures resembling nano-holes connected with nano-needles (inset, tilted at 30°).

Corrugated nanostructures are formed with a single pass scanning of FIB with −400% beam overlap and dwell time of 10 *ms*. Nano-mushrooms and dual-structured nano-features are obtained due to slightly elongated FIB with −600% beam overlap (Figure 5.11(b & c)). Nano-mushrooms are produced with a dwell time of 3.8 *ms* in 10-pass scanning, and dual-structures are produced with a dwell time of 3.2 *ms* in 20-pass scanning. It should be noted that for the elongated FIB spot, change in the dwell time and the number of passes make a substantial impact on the morphology due to preferred self-organization.

The demonstrated methodologies for varied morphologies provide highly controlled manipulation of the single-spot FIB milling process to realize the complex morphologies of the nanostructures. The achieved control on the transformation of nanoholes can lead to developing a fast and easy fabrication procedure for desired polygonal and complex geometries by engineering each focused ion beam spot.

5.3.3 Investigation on the mechanism of self-organization

Further analysis, to investigate the phase change and mechanism behind morphology transition, was performed by transmission electron microscopy (TEM) and Raman spectroscopy. During the TEM experiments, high-resolution cross-sectional imaging, acquisition of selected area electron diffraction (SAED) and Energy-dispersive X-ray spectroscopy were carried out for the FIB treated germanium surface. Also, the Raman spectra were acquired to study crystallographic changes in the nanostructures created by FIB irradiation.

5.3.3.1 Characterizations via transmission electron microscopy (TEM)

To characterize the phase change and mechanism behind the morphology transition, transmission electron microscopy (TEM) for a cross-section from typical square nanostructures is done. The TEM specimen (lamella) preparation for the square nanostructures, by cross-sectioning the region of nanostructures via FIB milling, is detailed in Figure 5.12.

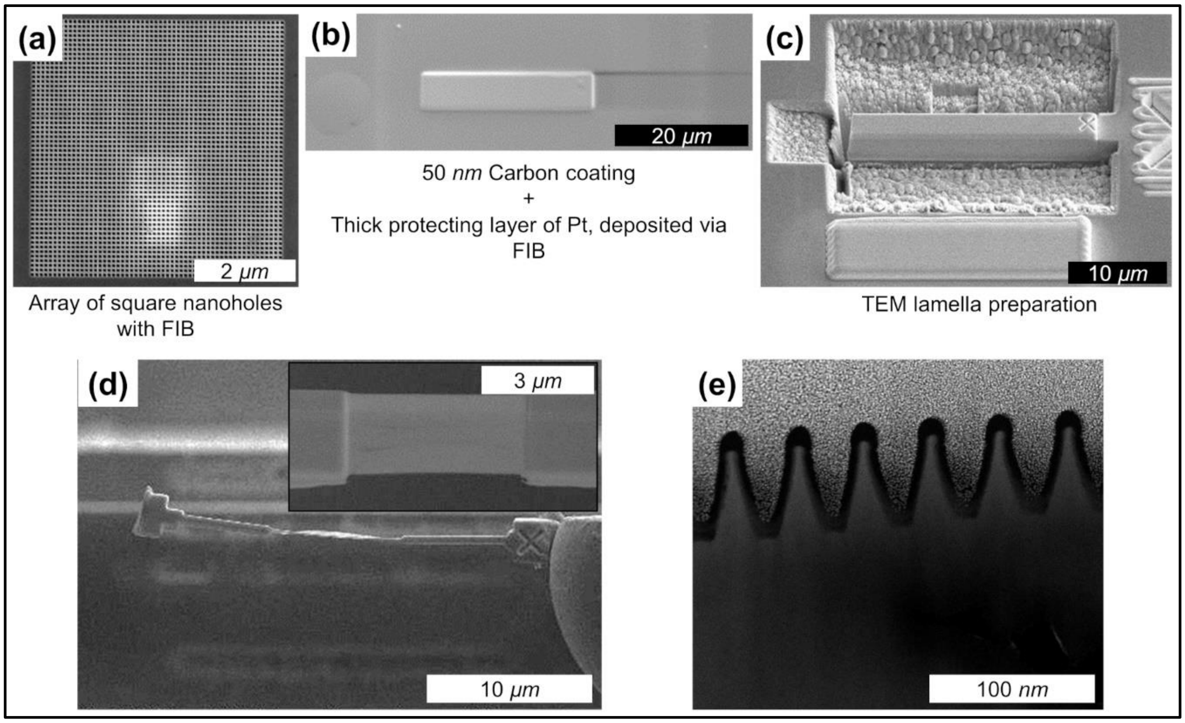
(a)
2 μm
Array of square nanoholes with FIB
(b)
20 μm
50 nm Carbon coating
+
Thick protecting layer of Pt, deposited via FIB
(c)
10 μm
TEM lamella preparation
(d)
3 μm
10 μm
(e)
100 nm

Figure 5.12 (a) SEM image of a patterned array of square nanostructures where the TEM lamella was prepared, (b) SEM image of protected layer deposition on the patterned area of (a), (c) FIB milling for preparation of lamella, (d) SEM images of the lamella lift-out, and (e) STEM image in of the prepared lamella.

Before lamella preparation, the patterned region (see Figure 5.12(a)) was coated with protective layers (Figure 5.12(b)) to avoid damage during the cross-sectioning by FIB. The array of square nanostructures (see Figure 5.12(a)) was covered by deposition of ~50 *nm* thick protection layer of carbon using evaporative carbon coater (Cressington 208, Ted Pella INC, USA) as seen in Figure 5.12(b). In addition to the protection while preparing TEM lamella, the carbon layer was expected to provide an excellent contrast to the germanium nanostructures with respect to the surroundings while taking TEM images. On the coated carbon layer, the thick platinum layer was deposited by the FIB assistance deposition method. Then the TEM lamella was prepared using focused ion beam milling and polishing using FIB-SEM system (Model Helios G4 UX, Thermo Fisher Scientific (FEI)) followed by lifting-out using micromanipulator and stored to use for TEM observation. The scanning transmission electron microscopy (STEM) image of the prepared lamella acquired by a high angle annular dark-field (HAADF) detector is shown in Figure 5.12(e).

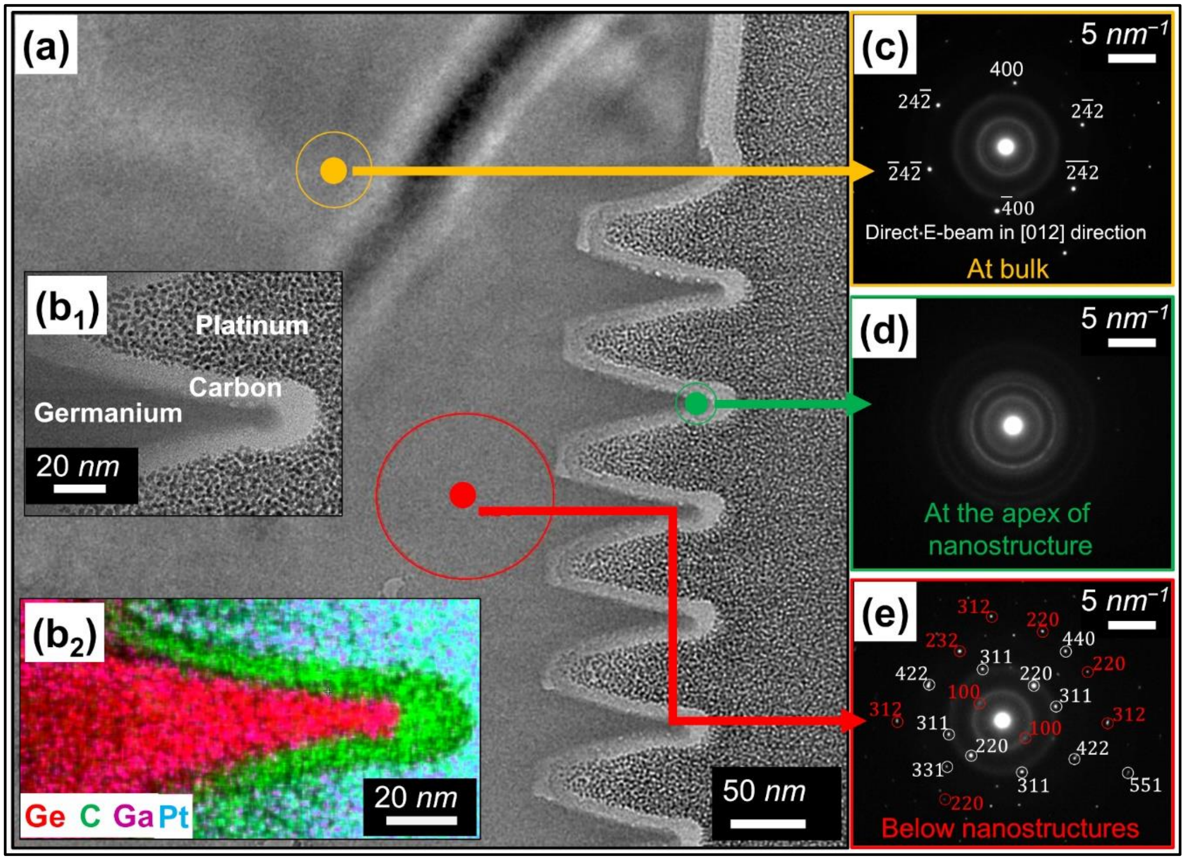
(a)
(b$_1$)
Platinum
Carbon
Germanium
20 nm
(b$_2$)
Ge C Ga Pt
20 nm
50 nm
(c)
5 nm^{-1}
400
$24\bar{2}$
$2\bar{4}2$
$\bar{2}4\bar{2}$
$\bar{2}\bar{4}2$
$\bar{4}00$
Direct-E-beam in [012] direction
At bulk
(d)
5 nm^{-1}
At the apex of nanostructure
(e)
5 nm^{-1}
312
220
232
440
311
422
220
220
100
311
312
311
100
312
220
422
331
311
551
220
Below nanostructures

Figure 5.13 (a) Cross-sectional TEM image of nanostructures. (b_1 & b_2) High-resolution TEM image and EDS elemental map for nanostructure showing a clear distinction between germanium with coated carbon and platinum. (c-e) Selected area electron diffraction (SAED) patterns for different regions: at the bulk (c), at the apex of nanostructure (d) and below the nanostructures (e). The indices for dc-Ge are indicated in white (c & e), and that for hd-Ge are indicated in red (e).

Low magnification and high magnification images acquired by TEM are shown in Figure 5.13(a) and Figure 5.13(b_1 & b_2), respectively. It is evident from the observation that the walls are protruding out of the surface in excellent agreement with AFM and SEM micrographs. The Energy-dispersive X-ray spectroscopy (EDS) was acquired using the same TEM instrument in the nanostructured wall region during the TEM imaging. Figure 5.13 (b_2) is Energy-dispersive X-ray spectroscopy (EDS) mapping acquired for the high-resolution TEM image in Figure 5.13 (b_1).

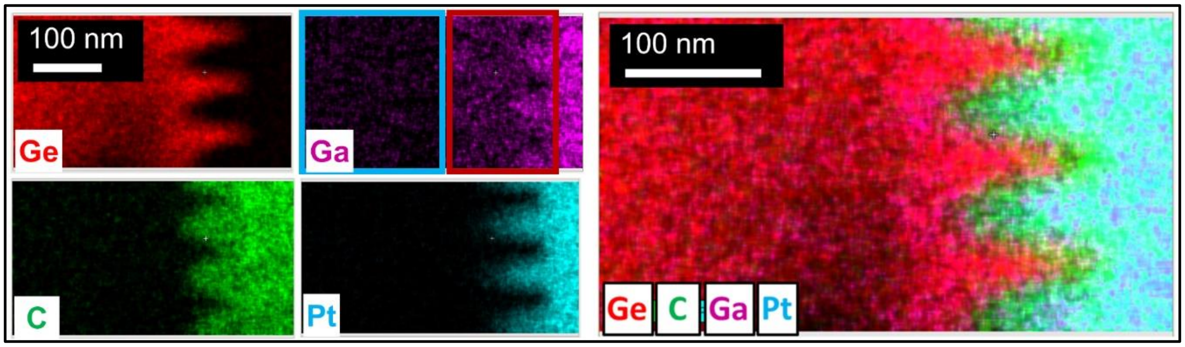

Figure 5.14 The EDS mapping of elements through a cross-section of the nanostructures.

The high magnification images (Figure 5.13(b_1 & b_2)) show a contrast between the germanium and the protecting layers. Moreover, the high-resolution EDS elemental map in Figure 5.13(b_1) shows the implantation of Ga in the Ge nanostructures. The low-resolution EDS was taken to check the Ga implantation in bulk, as shown in Figure 5.14. The gradually decreasing Ga implantation at the nanostructured region (red box in Figure 5.14(Ga)) is attributed to the FIB treatment during the fabrication process of the nanostructures. FIB irradiation experiment for self-organized nanostructures would lead to Ga implantation high at the top surface and lower at a depth of the sample. The uniform presence of Ga (blue box in Figure 5.14(Ga)) is at the bulk of the specimen. This uniform Ga implantation in a blue box (Figure 5.14(Ga)) is attributed to the Ga implantation during lamella preparation by FIB milling operation.

Figure 5.13(c-e) shows selected area electron diffraction (SAED) patterns acquired by an electron beam at three different positions along the cross-sectional region of the specimen:

(1) at the bulk (Figure 5.13(c)), (2) at the apex of nanostructure (Figure 5.13(d)) and (3) below the nanostructures (Figure 5.13(e)). At the bulk of the specimen, single-crystalline germanium with zone axis [012] is identified from the SAED pattern (Figure 5.13(c)).

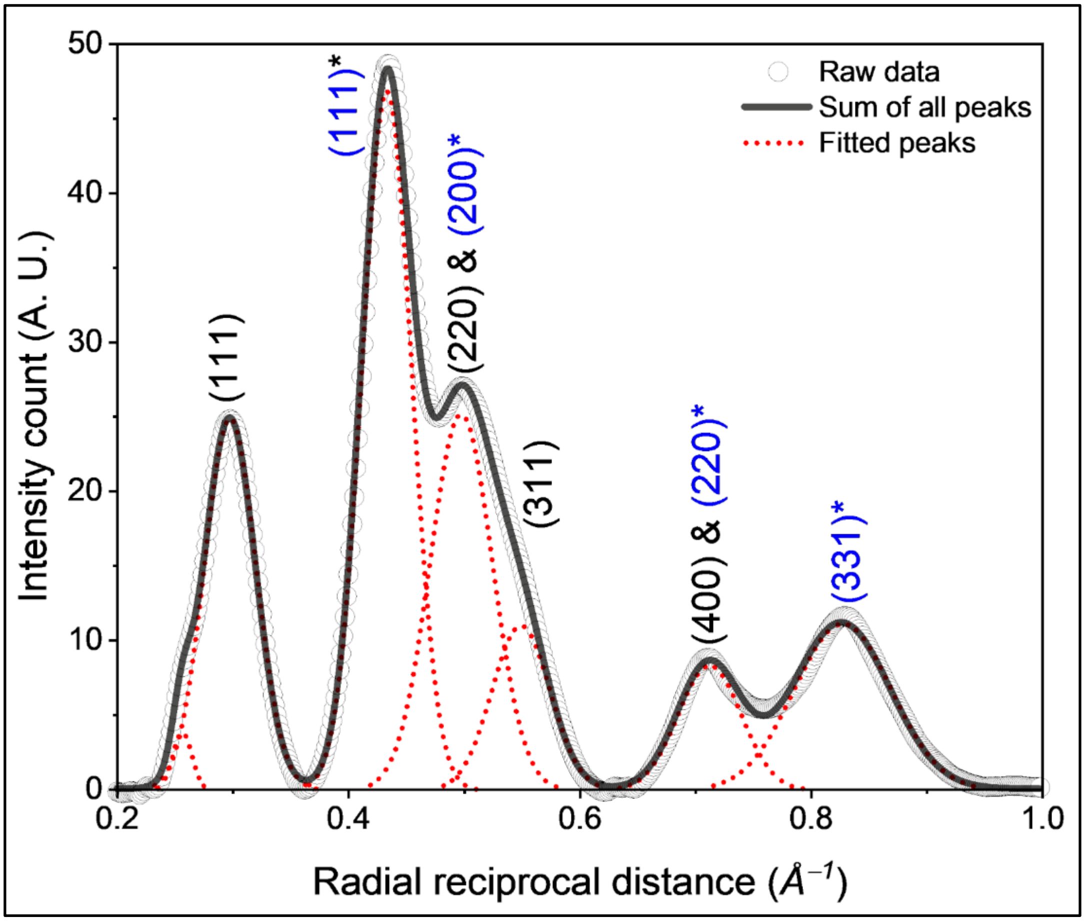

Figure 5.15 Azimuthally averaged intensity profile for the selected area diffraction ring pattern at the apex of nanostructures.

As evident from Figure 5.13(d), the structures are found to be amorphous at the tip of the walls. The crystallographic plane identification carried out for the selected area electron diffraction (SAED) is shown in Figure 5.13(d). The azimuthal averaged intensity distribution is plotted with a function of radial distance from the center in Figure 5.15. The diffraction peaks for apex region are matching with diamond cubic germanium (i.e., (111), (220), (311), & (400)) and face-cantered cubic platinum (i.e., (111)*, (200)*, (220)* & (331)*; The peaks with asterisk *). The appearance of platinum peaks is due to reflections from the surrounding areas of the point of interest as the protection layer of platinum is coated on the nanostructures. It is observed from the intensity plot that the diffraction profile is broadened, indicating an amorphous germanium phase. Thus, the diffraction peak analysis for this SAED pattern in Figure 5.13(d) revealed that the electron diffraction plot matches an amorphous phase of diamond cubic germanium.

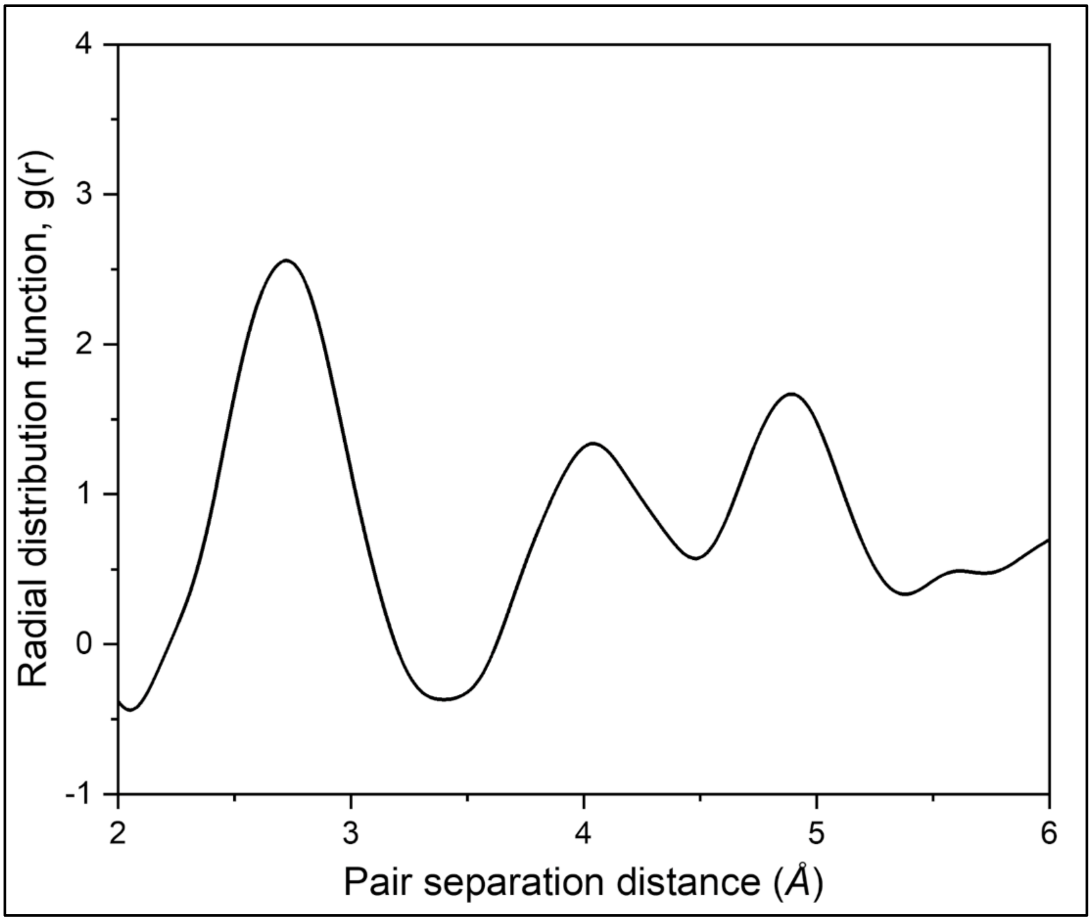

Figure 5.16 Radial distribution function calculated for the selected area electron diffraction ring pattern at the apex of nanostructures.

Also, radial distribution function (RDF) was determined from the SAED pattern for this amorphous region (Figure 5.13(d)) and represented in Figure 5.16. During RDF calculations from the diffraction ring pattern, the crystal structure was assumed to be diamond cubic germanium for simplicity. A very low intensity with a broad nature of each RDF peak suggests amorphization of the material at the apex of the nanostructures. Thus, diffraction peak analysis for the SAED pattern at the apex of nanostructures revealed an amorphous phase of amorphous diamond cubic germanium, which suggests significant amorphization at the apex of nanostructure walls due to ion beam irradiation.

A SAED image (Figure 5.13(e)) below the patterned area exhibit multiple reflections, emerging from different crystalline orientations within this region compared to the single crystal bulk germanium, due to ion irradiation induced strain. In Figure 5.13(e), the diffraction spots match closely with calculated interplanar spacings from diamond cubic germanium (dc-Ge) and hexagonal diamond germanium (hd-Ge) [141] as elaborated in Appendix A (on page number 155). For this comparison, the lattice parameters for dc-Ge was a = 5.658 $Å$ and that for hd-Ge were a = 3.94 $Å$ & c = 6.55 $Å$ [141]. Though dc-Ge and hd-Ge lattices exhibit some interplanar spacings having closer values, there are a significant number of diffraction spots that match with the hd-Ge phase better, as demonstrated in Appendix A (on page number 155). The site-specific high pressure and high temperature during ions irradiation, instigated from the collision cascade, lead to the creation of strained zones. Such strained zones, with an interstitial and a vacancy formed at the tetragonal Ge sites, attribute to phase changes comprising of amorphization and hexagonal diamond phase [57]. Thus, the existence of hd-Ge phase with different orientation of dc-Ge diffraction pattern confirms the damage due to irradiation collision cascade in the region below nanostructures.

5.3.3.2 Characterizations via Raman spectroscopy

The Raman spectroscopy is an essential tool to investigate the changes in the crystallographic properties of the material while undergoing microstructural damage and strain [142–144]. In order to study the effect of ion beam irradiation, Raman spectra were acquired for the surface of square nanostructures. The Raman spectra for bare and nanostructured germanium surfaces are shown in Figure 5.17. It has been observed that, for the germanium nanostructures, in addition to the characteristic Raman shift for diamond cubic germanium (dc-Ge) at 301 cm^{-1} (Figure 5.17(a-b)), there exist additional (see Figure 5.17(b)) Raman shift peaks at 270 cm^{-1} for amorphous germanium (a-Ge) and 290 cm^{-1} for hexagonal diamond germanium (hd-Ge).

The diffraction pattern at the apex of nanostructures (Figure 5.13(d)) suggests the amorphization due to ion irradiation induced phase transition as observed by the Raman spectroscopy (Figure 5.17(b)). The diffraction pattern for the germanium region, affected by the ion irradiation induced collision cascade below the nanostructures, confirms the existence of hd-Ge phase (Figure 5.13(e)). The existence of the hd-Ge phase suggests the phase transformation consistent with the Raman spectroscopy. Earlier, the Raman spectroscopy has revealed the undergoing microstructural damage, amorphization, and strain-induced phase transformation in the germanium crystal [142–144]. The strained and porous germanium is known to exhibit a hexagonal diamond phase, giving Ge-Ge Raman shift at 290 cm^{-1}, which is due to a metastable high-pressure phase of strained/porous germanium [142–145].

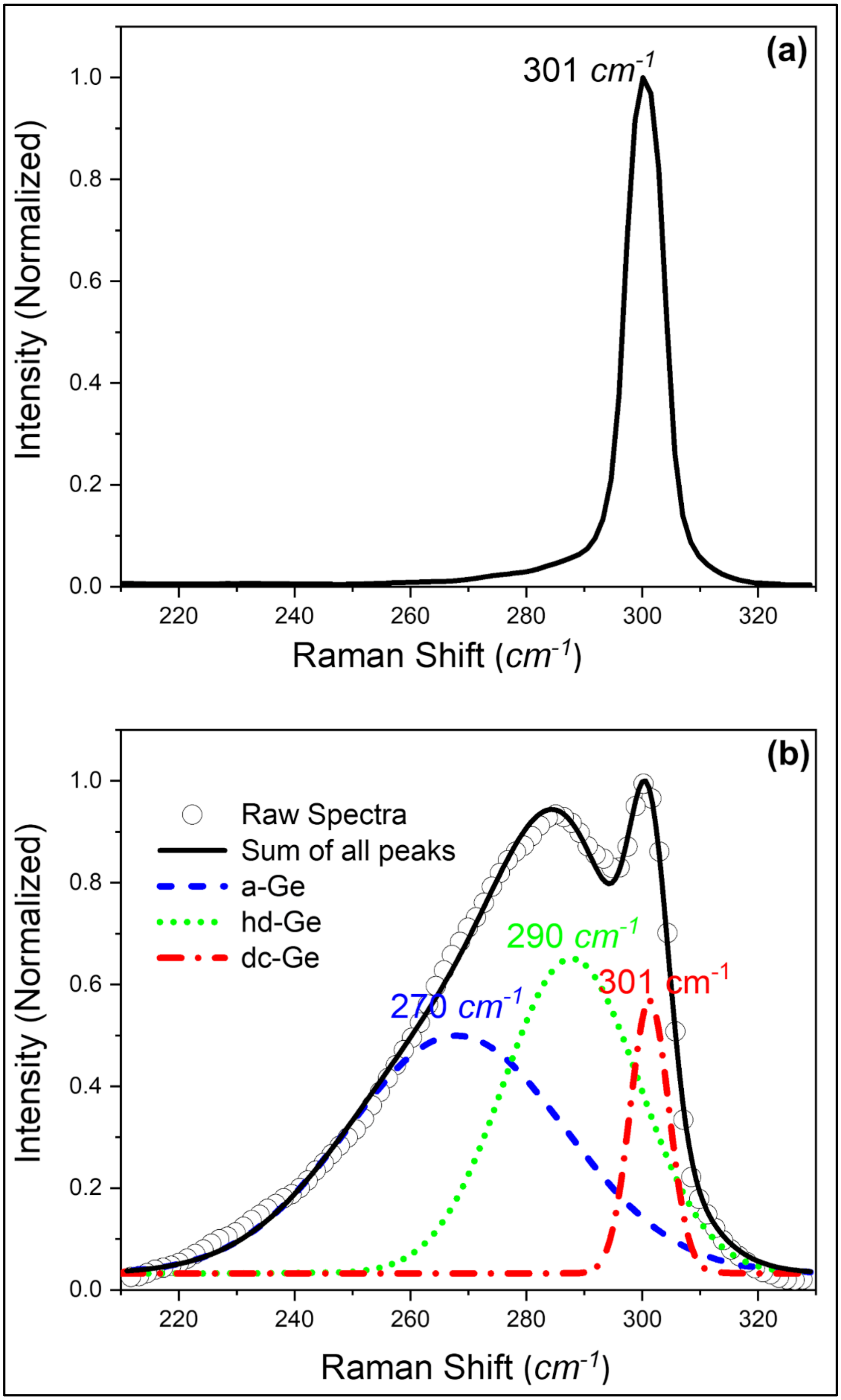

Figure 5.17 Raman spectra for (a) bare germanium and (b) the nanostructured Ge surface.

The observed crystalline phase transformation can lead to variations in morphology to minimize the surface energy of the structures providing smoothing, porosity, sponge, or nanodots [56,57]. Here, the unique self-organization mechanism is attributed to the interaction of impinging ions with the germanium surface atoms. On ion beam bombardment, the surface undergoes processes such as sputtering and defect formation. Also, the formation of melt-pool due to ion impingement results in a drastic change in the local volume due to a change in the density at the ion impingement site. Researchers have reported that the atoms lying on the germanium surface undergo site-specific confined viscous-flow due to thermal spikes induced by the bombardment of energetic ions [137,138,56]. The quasi-periodic nanoholes formation on the germanium at the very surface level (i.e., up to a few nm depth) due to broad ion beam irradiation was attributed to the viscous flow of the amorphous layer formed due to ion beam irradiation [137,56]. The site-specific localized high pressure and high temperature during FIB irradiation, originated from the collision cascade, lead to creating strained zones with an interstitial and a vacancy formation attribute to amorphization with existing vacancies in the tetragonal Ge sites [57]. The protruding morphology of the self-organized nanostructures was confirmed from micrographs acquired by SEM as well as AFM, and the morphology transition due to a phase change during FIB treatment is confirmed by Raman spectroscopy and TEM.

The phase change and defect formation on ion beam bombardment at the beam-overlapping region provide strengthening to the atoms instead of complete erosion. It has been observed that the amorphization and phase change effects contribute to the mass diffusion similar to the viscous flow in the affected regions [56,57]. On the ion bombardment over the nanostructured surface, Rayleigh–Plateau Liquid-Like Instabilities leads to an increase in the roughness and breaking of nanostructures; this is responsible for complete etching (sputtering) of the region with the beam overlap in materials such as silicon [146,147]. However, in the germanium surface at a specific dose and beam overlap, the viscous-flow dynamics of the surface are correct, and the surface exhibit reorganization under the effect of Saffman-Taylor instability. This leads to the occurrence of viscous-fingering [146–149]. On ion beam bombardment, the surface undergoes processes such as sputtering and defect formation. At optimized dose and beam overlap between adjacent holes, atoms lying on the overlapping region reorganize and flow like a viscous media allowing the surface reorganization under the effect of Saffman-Taylor instability [146–149].

The protrusion of nanostructures is attributed to increased volume (swelling) driven by amorphization and phase change on the ion beam irradiation. Viscous-fingering involving mass diffusion and surface reorganization forces the affected atoms to organize in a way to reduce the surface energy, and nanostructures are formed at the midpoints between the adjacent nanoholes. In contrast to the common sputtering governed milling phenomenon [28,139,140], in the present report, the overlapped region is found to undergo self-organization. And, instead of getting eroded as conventionally expected, it forms a straight wall protruding out of the surface providing better control over the morphology of the nanoholes induced by a single FIB-spot resulting in a designed polygonal nanostructure.

5.3.4 Optical absorption

The periodic arrays of germanium nanostructured polygon could exhibit a vital role for improved light-matter interactions [103,132]. Earlier, improved optical absorption has been demonstrated for germanium nanostructures [131,132]. Quasi-periodic Ge nanoripples have shown nearly 95% broadband light absorption with wide acceptance angle due to enhanced light trapping involving multiple reflections amongst the nanostructures [132]. To check the optical absorption behaviour of the nanostructures, the reflectance spectra were acquired using a J&M Micro UV-Vis microscope spectrometer. The acquired absorptance spectra for polygonal germanium nanostructured and bare germanium surface are shown in Figure 5.18. It can be observed that the broadband light absorption behaviour by germanium polygons is in agreement with the quasi-periodic germanium nanoripples reported in the previous chapter [132]. The broadband anti-reflectance is attributed to multi-reflection induced light trapping as well as absorption due to the graded refractive index for the nanostructured germanium over the bare germanium surface.

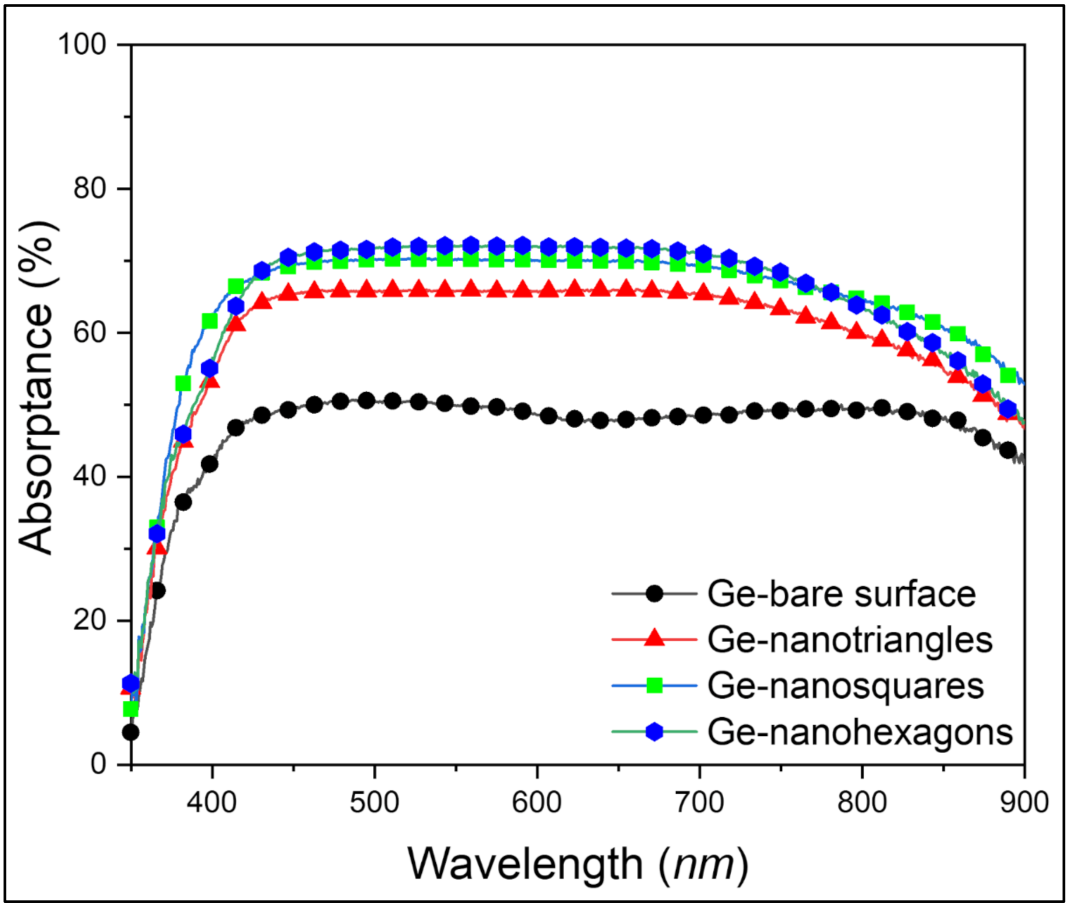

Figure 5.18 UV-Vis absorptance spectra for bare germanium and germanium nanostructures.

The absorption is higher for the hexagonal nanoholes due to their greater number density per unit surface area compared to the triangular nanoholes. The square nanoholes show an intermediate absorption as the number density per unit surface area is in-between that of hexagons and triangles. The UV-Vis spectroscopy suggested the antireflection with morphology dependency for the periodic nanostructures. The broadband light absorption by these polygonal nanostructures indicates potential exploitations to enhance light-matter interactions towards efficient detectors and sensors.

5.4 Summary

A novel approach to fabricate nanoscale polygonal holes induced by focused ion beam irradiation is presented. Here, the polygonal nanoholes are not formed due to the conventional direct milling dominant strategy where polygons can be created by milling an array of pixels for desired polygonal geometry, but the protruding polygonal nanoholes are grown out of the surface at each FIB pixel due to self-organization of the nanoholes on germanium surface via controlled ion beam scanning. The engineering of each spot during FIB dwelling has been carried out to produce periodic polygonal morphologies such as square, triangular, hexagonal, pentagonal and octagonal. Also, complex 3D structures such as spirals, corrugated, zigzag and mushroom-shaped nanostructures are demonstrated by self-organization. The process of self-organization by viscous-fingering provided the ability to manipulate the morphology of each FIB spot. This is a unique capability for miniaturization in the field of nanofabrication. The demonstrated approach has the potential to address the roadblocking challenges in the field of nanofabrication. Thus, the unique but straightforward process for periodic as well as protruding polygon-shaped nanoholes fabrication process is demonstrated.

Chapter 6

Focused Ion Beam Induced Self-Organization: Investigations by Molecular Dynamics Simulations

Focused ion beam induced self-organization for periodic and morphologically controlled nanostructures is attractive due to the easy process, and its potential towards a few nanometers scaled features. However, the self-organization mechanism is not well understood. A detailed study of interactions between ion beam and materials using atomic-level investigations using tools like molecular dynamics (MD) simulations can reveal insight into the underlining mechanism. This chapter presents a molecular dynamics investigation of self-organization on germanium (100) surface with gallium focused ion beam bombardment. For the realistic effect Gaussian beam has been set up in the simulations. The simulations show melt-pool assisted amorphization and phase transformation on ion beam irradiation over the germanium surface. The viscous-fingering driven self-organization at a nanoscale level is assisted by the site-specific melt-pool and phase transformation during the FIB irradiation.

6.1 Introduction

The previous chapters demonstrated the controlled realization and evolution of various nanostructures such as aligned-nanoripples and periodic polygonal nanostructures on the Ge surface by FIB induced self-organization. However, the understanding of the mechanism behind the interesting self-organization towards complex morphologies is a challenge. The atomistic studies of ion-solid interactions by capturing the effect of transferred kinetic energy from the incident ions onto the target material could be useful to investigate the self-organization mechanism behind the polygonal formation [60–67]. The molecular dynamics (MD) simulations can be utilized to investigate the interaction between ions and materials [60–67]. These MD simulations are focused on the energy transfer between the impingement ions resulting in the thermalization and atomic displacements in the target material. The MD simulations can provide insights into the essential characteristics such as crystallographic phase transformation, local thermalization, material self-diffusion, and irradiation-induced alteration in mechanical properties [60,62,67,68]. Thus, MD simulations can be useful to predict and understand the ion beam induced effects on the target materials.

The MD simulations have been applied to study the mechanism of nanopores formation and cutting processes when energetic ions are bombarded over 2-D materials such as graphene [65,66]. The simulations revealed that the controlled focused ion beam irradiation is responsible for joining the two graphene sheets at the site of nanopore formation. The defect and mechanical properties are also possible to investigate by utilizing MD simulations. The crystallographic damage and morphology of nanoholes in the single crystal silicon were found to be dependent on the orientation of the exposed facet and the angle of incident of ion bombardment [67]. The nanopore creation on the silicon membrane was driven by the boiling of atoms at the collision sites [65]. The reports on molecular dynamics simulations using LAMMPS (Large-scale Atomic/Molecular Massively Parallel Simulator) for investigating Ga^+ ion beams with germanium and silicon surfaces suggest the utilization of hybrid Stillinger−Weber (SW) [62,70,71] and Ziegler–Biersack–Littnark (ZBL) potentials [59]. Earlier, the ZBL potential was used for interactions of bombarding ions with Ge [62], which resulted in the amorphization of germanium upon ion irradiations. This demonstrated the effectiveness of ZBL parameters for interactions of irradiated ions with germanium. Recently, MD simulations were employed to estimate the alteration in the mechanical properties of nanowires resulting in the site-specific bending of nanowires due to FIB irradiation [68]. Hence, atomistic investigations by molecular dynamics simulations can be useful to understand the mechanism, by careful consideration of thermal and crystalline damage, for the self-organization observed in the previous chapter (Chapter 5).

In the following sections, the MD interaction of gaussian-shaped gallium nano-focused ion beam with diamond cubic germanium crystal has been reported. The temperature evolution and change in crystallinity have been studied due to the irradiation of the ion beam. The thermalization at the ion impingement site has been investigated towards the creation of melt-pool due to ion irradiation. Further, four spot ion impingements have been carried out to check the self-organization with an increase in the irradiation dose.

6.2 Molecular dynamics (MD) simulations

In order to investigate the morphology and crystallographic phase transition due to ion beam irradiation, the molecular dynamics (MD) simulation was carried out using LAMMPS (Large-scale Atomic/Molecular Massively Parallel Simulator) molecular dynamics simulation package [69]. The interactions between Ge-Ge can be defined by the Stillinger−Weber (SW) potential [62,70,71], and the high-energy collision interactions between Ga^+ ions and Ge atoms can be defined by the Ziegler–Biersack–Littnark (ZBL) potential [59,62]. As reported by Posselt et al. [71] in the atomistic study of the recrystallization and phase transformation in germanium crystal using the molecular dynamics simulations, the energy E in terms of Stillinger−Weber (SW) potential for the system of atoms can be expressed as [62,70,71],

$$E = \sum_{i<j} \Phi_2(i,j) + \sum_{\substack{i \neq j \\ j<k}} \Phi_3(i,j,k) = \sum_{i<j} \epsilon \Phi_2(r_{ij}) + \sum_{\substack{i \neq j \\ j<k}} \epsilon \Phi_3(r_{ij}, r_{jk}, \theta_{ijk}) \tag{6.1}$$

Equation 6.1 represents the combination of two- and three-body part of interactions represented by Φ_2 and Φ_3, respectively. The two-body function ensures interactions between all the neighbors j with the atom i within the cutoff distance a. Whereas the three-body function ensures interactions of all the neighbors j and k with the atom i within the cutoff distance a. r_{ij} and r_{jk} represent the distances of atom j and atom k from atom i, respectively. θ_{ijk} denotes the angle between the vectors r_{ij} and r_{jk}, which is used in the three-body interactions. The two- and three-body interaction functions for SW potential can be given by,

$$\Phi_2(r_{ij}) = A\left[B\left(\frac{\sigma}{r_{ij}}\right)^p - \left(\frac{\sigma}{r_{ij}}\right)^q\right] exp\left(\frac{1}{\frac{r_{ij}}{\sigma} - a}\right) \sum_{\substack{i \neq j \\ j<k}} \Phi_3(i,j,k) \tag{6.2}$$

$$\Phi_3(r_{ij}, r_{jk}, \theta_{ijk}) = \lambda\left(\cos\theta_{ijk} + \frac{1}{3}\right)^2 exp\left(\frac{\gamma}{\frac{r_{ij}}{\sigma} - a} + \frac{\gamma}{\frac{r_{ik}}{\sigma} - a}\right) \tag{6.3}$$

Where σ and ϵ are distance and energy scaling parameters, respectively. These scaling parameters define the lattice constant and cohesive energy of germanium. The parameters such as A, B, p, and q are for two-body interactions. While λ, γ and θ are used only for three-body interaction functions with the function of interatomic distances and angles, but γ is defined by a pair of atoms. The SW potential with the parameters used by Posselt et al. [71] provides the acceptable intuition of all the condensed germanium phases such as crystalline, amorphous and liquid states. The essential parameters for SW defining the Ge-Ge interactions are listed in Table 6.1 below,

Table 6.1 Parameters for the SW potential used the MD simulations [71]

Scaling		Two-body function				Three-body function		Cutoff
ϵ **(*eV*)**	σ **(*Å*)**	***A***	***B***	***p***	***q***	λ	γ	***a***
1.93	2.181	7.049556277	0.6022245584	4	0	19.5	1.19	1.8

The high-energy collision interactions between Ga$^+$ and Ge atoms was defined by the Ziegler–Biersack–Littnark (ZBL) potential [59,62]. The ZBL is known as a screened electrostatic potential describing nuclear-nuclear repulsions to include the energetic collisions between interacting atoms. The ZBL potential can be given by [59,62],

$$E_{ij}^{ZBL} = \frac{1}{4\pi\epsilon_0}\frac{Z_i Z_j e^2}{r_{ij}}\emptyset\left(\frac{r_{ij}}{a}\right) + S\left(r_{ij}\right) \tag{6.4}$$

Where Z_i and Z_j are atomic numbers of the first atom types and the second atom types, respectively. ϵ_0 is vacuum permittivity (8.85 × 10^{-12} *F/m*) and $\emptyset(x)$ is the screening function, which can be expressed as,

$$\emptyset(x) = 0.18175e^{-3.19980x} + 0.50986e^{-0.94229x} + 0.28022e^{-0.40290x} + 0.02817e^{-0.20162x}$$

$$a = \frac{0.46850}{Z_i^{0.23}+Z_j^{0.23}} \text{ and } \frac{r_{ij}}{a} = x$$

An additional switching function $S\left(r_{ij}\right)$ ensures ramping of the energy, force, and potential curvature smoothly to zero between the inner cutoff (i.e., the distance between the pair where switching function begins) and outer cutoff (i.e., the distance defining the global cutoff for the ZBL interactions between the pair of atoms). The switching function is applied to each pairwise interaction.

The simulation of Ga beam bombardment was performed on the germanium crystal with a diamond cubic lattice. The MD simulations were performed using the Cray XC computing system with 1X BDW processor (18 cores) and an accelerator (1X P100, 16 *GB*). The open visualization tool (OVITO) [150] was used for the visualization and analysis of the results obtained from MD simulations. Three regions are defined in the germanium crystal (of size 20 *nm* × 20 *nm* × 14 *nm*), namely, fixed, thermal and sputter region. The FIB gun region was defined along the central vertical axis of germanium crystal at 1 *nm* over the top of the surface. The diameter of the FIB gun was taken as 2 *nm* diameter. The central rectangular region with size 16 *nm* × 16 *nm* × 11 *nm* was kept as Newtonian atoms, which is called sputter region (grey). The bottom 1 *nm* thick layer (green) was fixed in space to hold the simulation domain, as shown in Figure 6.1 steadily. The thermal region (blue) was 3 *nm* thick around the sides and 2 *nm* thick at the bottom of the sputter (Newtonian) region.

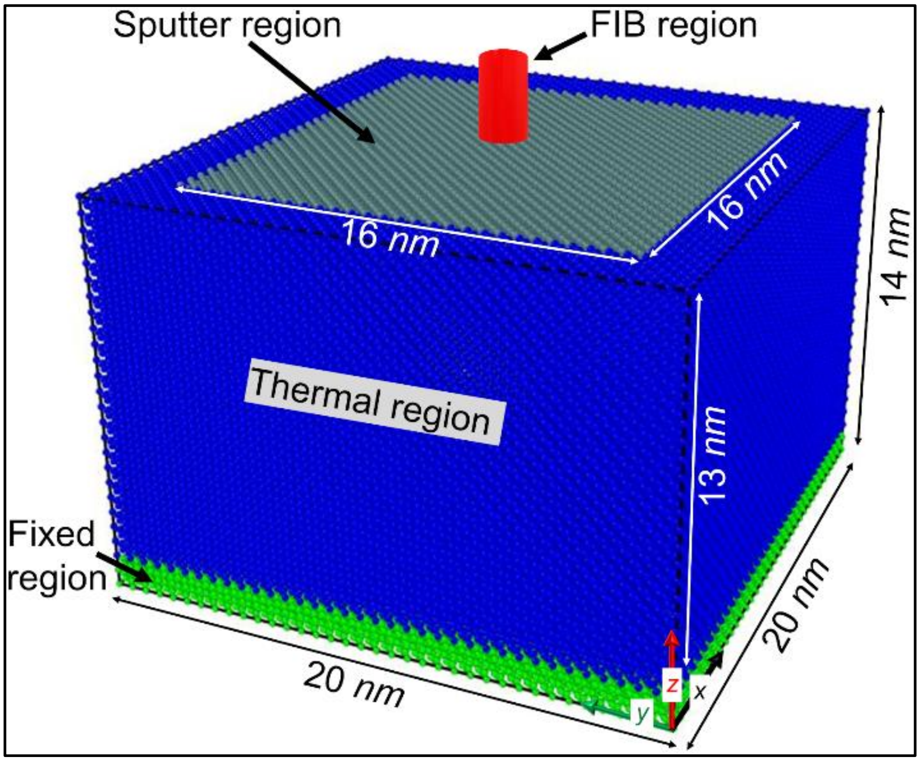

Figure 6.1 The perspective 3D view of the MD simulation set-up with different regions in the simulation domain and FIB region at the top.

6.3 Results and discussion

In addition to the sputtering of the atoms, the thermalization due to the ion irradiation plays a vital role in the crystallographic damage and hole creation on the target surface. Hence, to investigate the irradiation induced damage on the germanium crystal, the temperature evolution and change in crystallinity were investigated as discussed in the following sections.

6.3.1 Temperature evolution

In conventional ion beam milling, the overlapped region between the adjacent beam positions is expected to erode with an increase in the dose (Figure 5.1). However, here it is found that the overlapping region protrudes out of the surface and takes the shape of a straight wall. This suggests that there exists a phase transformation during the Ga^+ FIB irradiation on the germanium surface. Earlier, it was reported that on ion beam irradiation, the germanium surface exhibits melt-pool assisted amorphization and phase change [57,56,62]. This formation of melt-pool assisted amorphization could be the driving force for present self-organization. During the experiments, the energy of Ga^+ was 30 *kV*, however, in the MD simulations it was 2 *kV* (velocity of 744 *Å/ps*) to limit the size of the simulation domain for a feasible computation requirement.

The microcanonical ensemble NVE integration was used for all the atomic dynamics. The thermal region was kept as a thermostat (300 *K*) to absorb the kinetic energy imparted by the ion bombardment to the sputter region. The FIB milling studies revealed that the ion flux at the center of the beam is higher and it is lower at the beam edge (radially), and the intensity across the beam can be represented by Gaussian distribution [67,151–153]. Hence, the ion beam intensity across diameter was taken as Gaussian distribution for the irradiation in the MD simulation to represent the realistic Gaussian distribution of the FIB beam [67,151–153].

The kinetic energy of Ga ion was 2 *kV* with the Gaussian beam intensity distribution (with FWHM 0.8 *nm*) as depicted in Figure 6.2(a), and the gun diameter was 2 *nm*. The set Gaussian distribution produces a typical ion distribution along the beam cross-section, as seen in Figure 6.2(b). The simulations were carried out with variable time steps (0.005 to 0.5 *fs*) to restrict the maximum displacement of 0.02 *Å* in any time step.

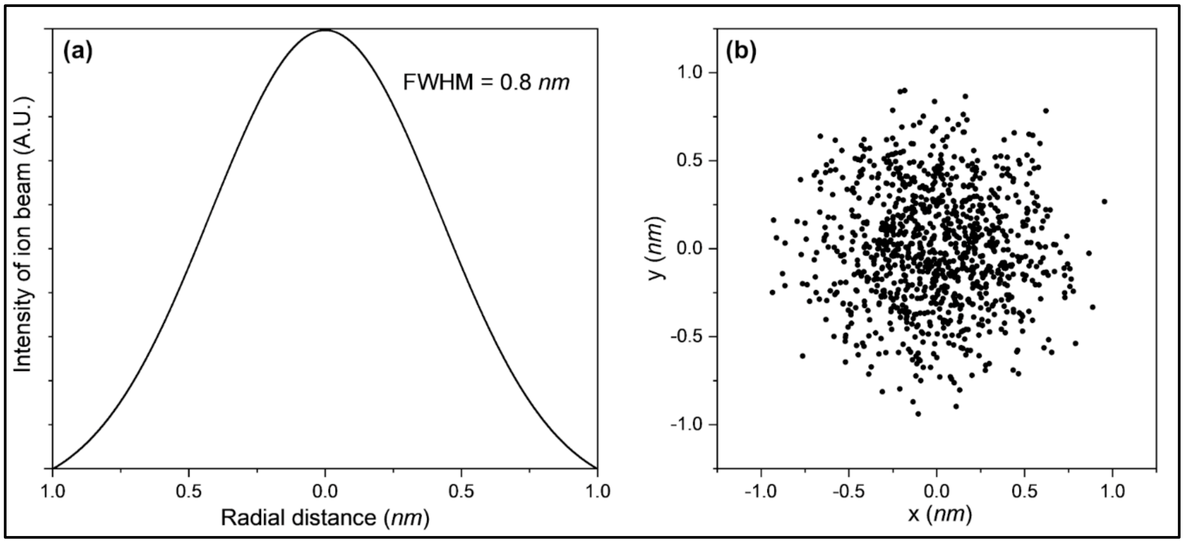

Figure 6.2 (a) The ion beam intensity across the diameter of for the radial distribution of ions. (b) The representation for a typical ion distribution in the beam cross-section corresponding to parameters in (a).

Before the irradiation of ions, the germanium crystal was equilibrated at room temperature for 30 *ps*. In total, 100 ions were bombarded, each at an interval of 10 *ps*. The relaxation time of 10 *ps* was set after each ion impingement to ensure the thermal stability of the system, as reported in the reference [62]. Here, to ensure the faster simulation running time, the ion beam current in the simulations was taken relatively higher (16 *nA*) than the experimental value (50 *pA*). The thermostat and the interval of ion impingement also ensured the realistic temperature spike in the sputter region with the cooling of the sputter region after each ion bombardment (see Figure 6.3(a)). The average temperature of the sputter region decreased down to room temperature after the 30 *ps* of the last ion impingement (see inset of Figure 6.3(a)). The temperature, being a canonical ensemble quantity, can be estimated by using the average kinetic energy of the atoms in the crystals as reported in the reference [72] to estimate the per atom temperature in the affected region.

The temperature of germanium atoms in the sputter region was estimated using the average kinetic energy of the atoms in the 1 *nm* radius of the central atom by the following equation,

$$\frac{1}{2}\sum_i^N m_i v_i^2 = \frac{3}{2} N T k_b \tag{6.5}$$

Where m_i and v_i are atomic mass and velocity of *i*th atom; *N* is the total number of atoms, including the central atom (inside the radius of 1 *nm* from the central atom); k_b is Boltzmann constant. Thus, *T* would give the calculated value of temperature for the central atom from the spatial average of all the atomic sites lying in the 1 *nm* radius of the central atom. There are typically 184 germanium atoms in 1 *nm* for diamond cubic lattice (as the atomic radius for Ge is 1.39 *Å*), which is a significant number of atoms to estimate per-atom temperature by the method mentioned above. The cross-sectional snapshots of the per-atom temperature distribution for atoms in *yz*-plane after the last ion irradiation are shown in Figure 6.3(b). The red coloured region in Figure 6.3(b) shows that the temperature of germanium atoms is higher than the melting point (T_m = 1211 *K*) of germanium, suggesting localized melting with the Ga^+ ion bombardment. We can call this volume (a spherical volume of ~4 *nm* diameter) a localized melt zone [62,154].

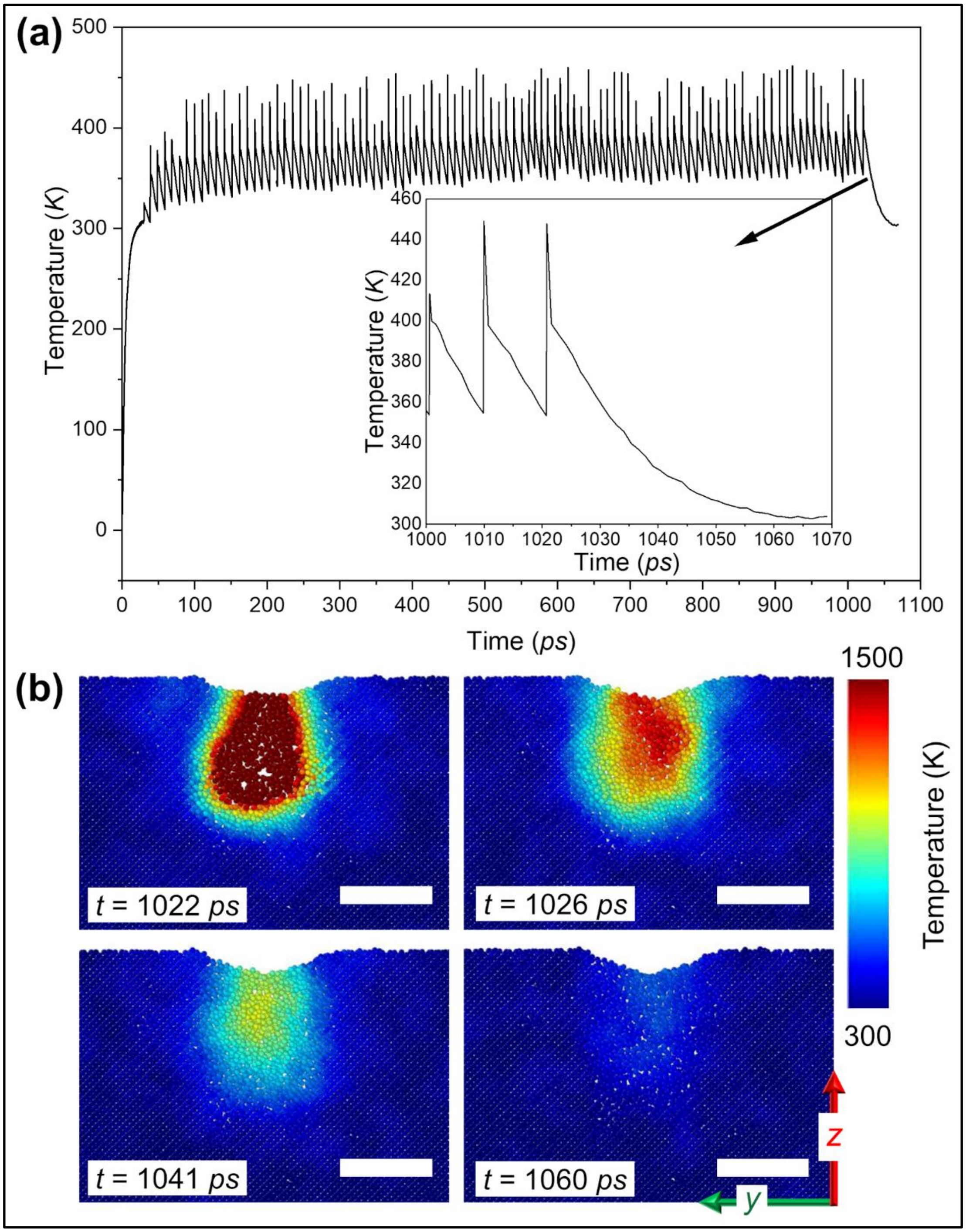

Figure 6.3 (a) The evolution of the temperature, from the MD simulation of Ga$^+$ FIB irradiation on Ge for the sputter region, shows the temperature spike with each ion impingement. Inset is the magnified view of temperature at the end of the irradiation time. (b) Snapshots illustrating the time evolution of temperature distribution on the yz-plane of the sputter region. The scale bars are of 4 *nm*.

The collision cascade due to ion impingement is stopped at 1022 *ps*, i.e., 2 *ps* after the last ion impingement. As seen from the inset of Figure 6.3(a), the thermal spike begins to cool down at 1022 *ps*. Further, as seen from Figure 6.3(b), at time t = 1022 *ps*, the local temperature distribution shows that the central atoms have a temperature higher than the melting point, representing the melt zone. However, the average temperature is below 400 *K* for the sputter region. The average temperature of the sputter region reduces gradually with time, giving the melt zone temperature of ~1300 *K*, ~900 *K* and ~600 *K* at t = 1026, 1041 and 1060 *ps*, and the corresponding average temperature of the sputter region being 380, 325 and 305 *K*, respectively.

It should be noted here that the ion beam energy and total ions/spot are as low as 2 *kV* and 100 *ions/spot*, respectively, compared to the experimental values of 30 *kV* and dose/pixel of 5.62×10^6 *ions/spot*. Hence, during the experiment, the size of nanoholes and range of melt zone are relatively larger than the present simulations and with an increase in dose, the depth of nanoholes increases [139,62,67]. The increase in the depth of nanoholes with an increase in irradiation time leads to higher melt zone volume.

6.3.2 Crystallinity changes

The atomic displacements for Ge atoms in the sputter region were calculated with the open visualization tool OVITO tool [150]. The kinetic energy from the impinging gallium ion transfer to some of the germanium atoms. This kinetic energy transfer occurs due to elastic collision by impinging ions, and a few germanium atoms experience displacement with a translation velocity along the crystal. After the collision with the incidence ion, the germanium atoms lead to a collision cascade resulting in multiple germanium atoms getting displaced. The trajectories of this translation movement of the germanium atoms were captured, and the magnitude of atomic displacements before the irradiation (at *t* = 30 *ps*) and after the irradiation (at *t* = 1060 *ps*) was estimated. The 3D and cross-sectional views of the atomic displacements are as shown in Figure 6.4. It can be seen from Figure 6.4(b & d) that the atoms in the melt zone region have been found to have undergone a high magnitude of displacement (upto 7 *nm*, red coloured atoms in Figure 6.4). Such a high magnitude of translations for a low energy (2 *kV*) irradiation suggests massive atomic displacements for the high energy irradiation (30 *kV*) during the FIB experiments in Chapter 5.

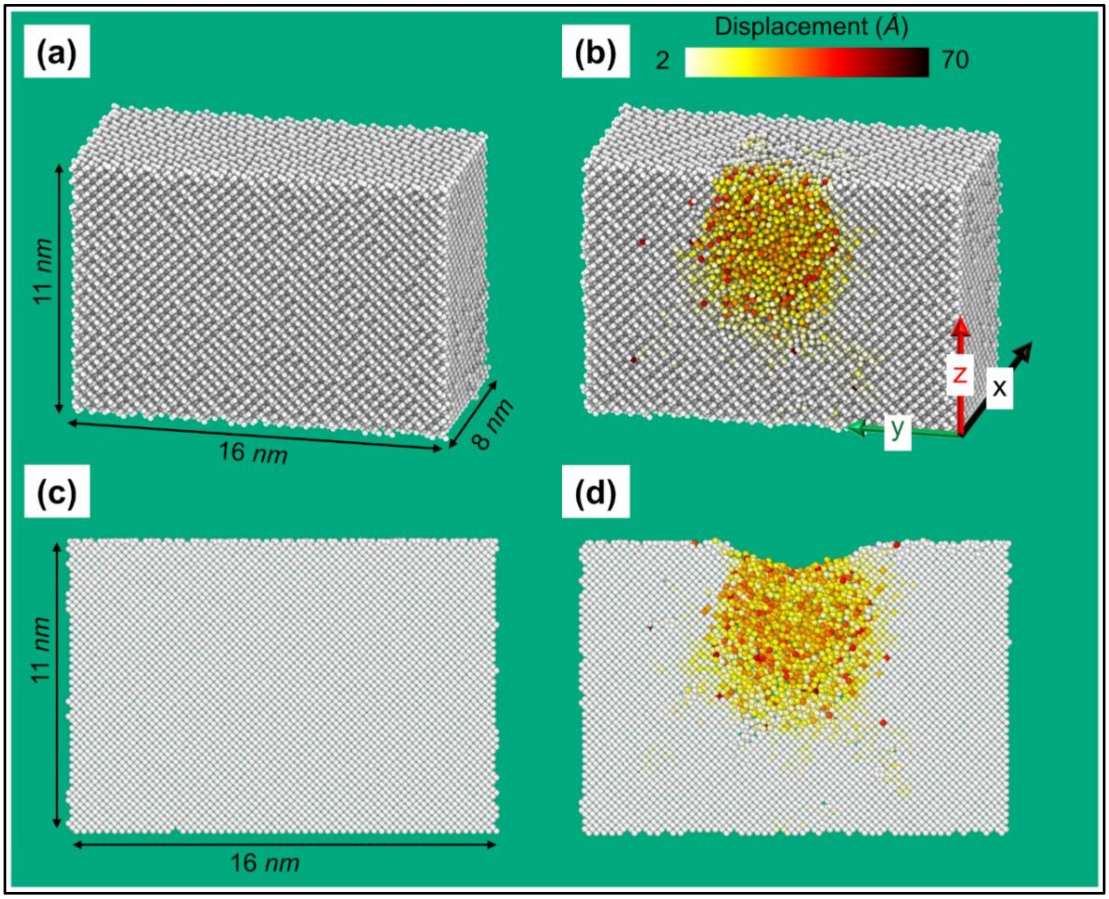

Figure 6.4. The 3D view of sliced sputter region for the atomic displacement (a) before and (b) after irradiation. The cross-sectional view of the sputter region for atomic displacement (c) before irradiation (at *t* = 30 *ps*) and (d) after irradiation (at *t* = 1060 *ps*).

The site-specific heat treatment and atomic displacement during the ion beam irradiation lead to the change in crystallographic arrangements of atoms. Hence, it is useful to check the radial distribution function of the sputter region in order to estimate crystallinity change in the germanium crystal. The resulting crystallographic changes in the germanium crystal can be seem in Figure 6.5 from the radial distribution function (RDF) before and after the irradiation for the sputter region. Reduction in the crystallinity of the germanium due to ion irradiation was indicated from the intensity reduction in the discrete peaks of the RDF.

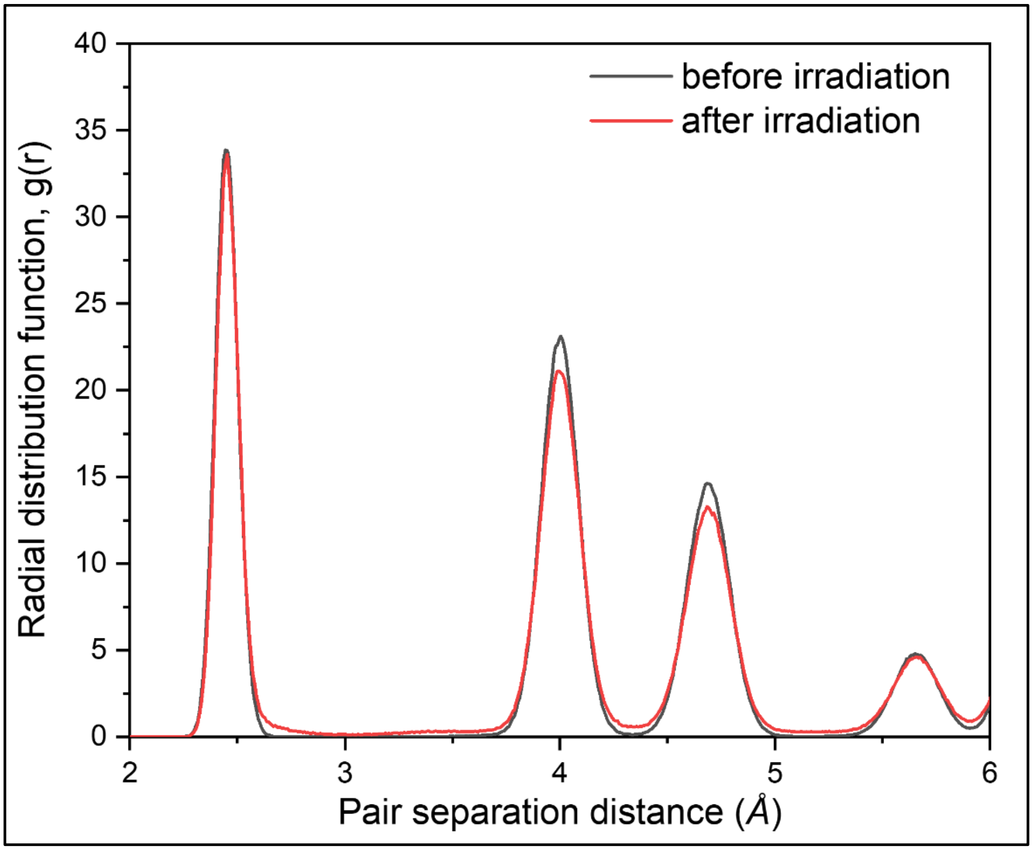

Figure 6.5 Effect of irradiation on the RDF (Radial distribution function) of the sputter region for damage in crystallinity due to Ga^+ FIB irradiation on the Germanium surface.

In order to identify crystal structure for the atomic sites, modified common neighbour analysis upto the second neighbour list was performed [155]. As seen in Figure 6.6, the amorphous (white coloured), cubical diamond (blue coloured) and hexagonal diamond (orange coloured) sites are found to be present in the melt pool zone. Similar to the cubic diamond lattice, the hexagonal diamond lattice has a tetrahedrally bonded site. The hexagonal diamond lattice is present in the polycrystalline germanium matrix when it undergoes strain or heat treatment [156–158]. The presence of hexagonal diamond cubic germanium and amorphization was also observed from the Raman spectroscopy (Figure 5.17(b)) and diffraction patterns acquired using TEM (Figure 5.13(d & e) in Chapter 5.

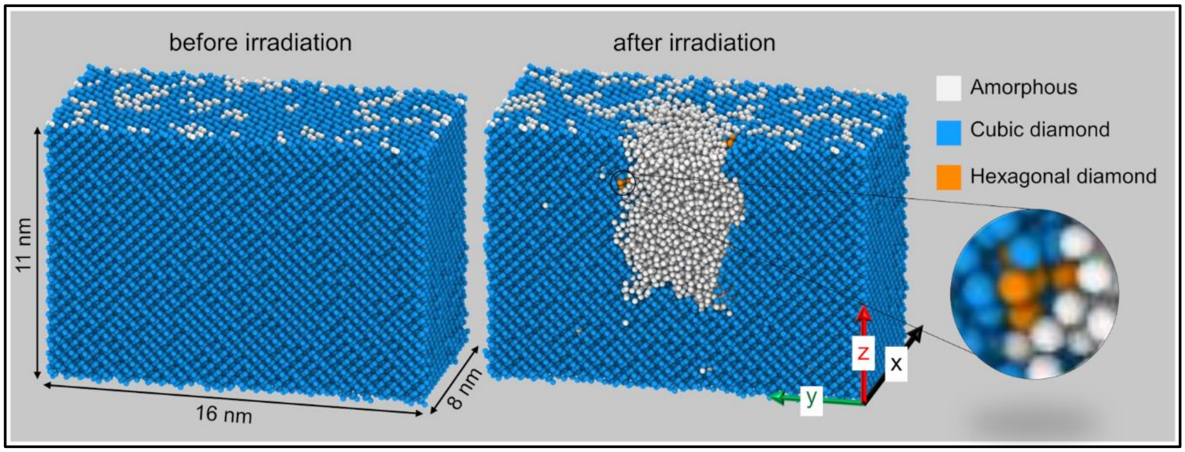

Figure 6.6 3D sliced view of the sputter region for the crystallinity changes due to Ga^+ FIB irradiation on the Germanium surface.

6.3.3 Demonstrating FIB induced self-organization

In order to check the self-organization similar to the experimental results for the polygon formation in Chapter 5 (see Figure 5.2), four FIB spots were set up at −200% beam overlap on the germanium crystal of the size as used in the previous single spot simulations. Gallium ions were bombarded with 5 *keV* energy (velocity of 1176 *Å/ps*), and the total dose for each FIB gun was 200 *ions/spot*. The other simulation parameters were the same as previous simulations of the single spot impingement. At each spot, 200 ions were bombarded, each at an interval of 10 *ps*. Thus, the total number of irradiated ions was 800. The raster scanning of FIB irradiation was performed in a manner such that a single ion is bombarded per spot at each scan. The snapshots for the top view of the germanium crystal after the simulation are shown in Figure 6.7. The red spheres represent germanium atoms, and the blue spheres represent gallium ions in the simulation domain space.

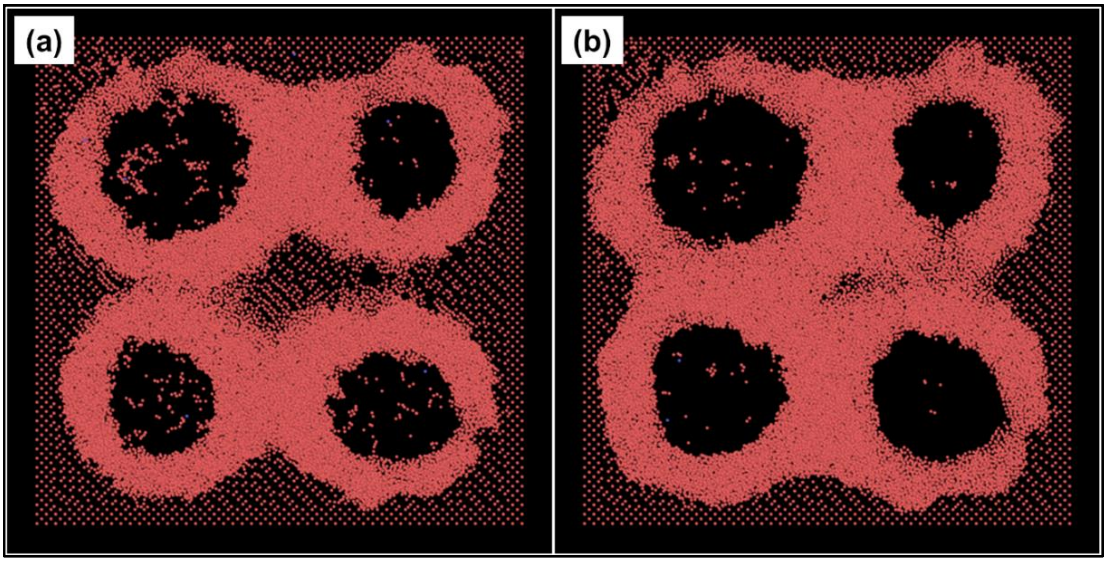

Figure 6.7 Top view of self-organization simulation via four FIB spots. The snapshots are after irradiation of (a) 150 ions per spot and (b) 200 ions per spot. These top views of the germanium crystal region are of the scale 20 *nm* × 20 *nm*.

Each top view in Figure 6.7 represents a slice of the top 5 *nm* surface. It is clear from the top view that the sputtered region is circular for low dose as the boundaries of adjacent spots are far, and sputtered regions do not interact with each other (Figure 6.7(a)). However, for higher doses (Figure 6.7(b)), the boundaries are closer due to an increase in the sputtered region, and they start interacting with each other. It can be noted that the boundaries seem to strengthen and takes a straight shape (Figure 6.7(b)) instead of a curved shape of the initial circular sputtered region (Figure 6.7(a)). The simulation region being small, there are limitations when investigating the dynamics of surface reorganization such as melt-pool assisted diffusion as the boundaries and collision cascade reach up to the thermal and fix regions of a germanium crystal. Defining a larger simulation region is not feasible due to computational limits; hence, these simulations of four-spot ion beam impingement are needed to be optimized to a great extent for a thorough investigation of dynamics governing self-organization with scaled-up MD simulations.

6.3.4 Proposed mechanism of polygon formation via viscous-fingering

Contrary to the common sputtering phenomenon seen in silicon, in the experimental results in Chapter 5, the overlapped region is found to undergo phase transformation. Thus, instead of getting eroded as conventionally expected, it forms a straight wall protruding out of the surface providing better control over the morphology of the nanoholes induced by a single FIB spot. As suggested by MD simulations, the combined effect of melt-pool (Figure 6.3) assisted amorphization and phase change (Figure 6.5 and Figure 6.6) contribute to the mass diffusion up to a short range and mimics the viscous flow in the affected regions [57,56,62]. Such phase transformation can lead to variations in morphology to minimize the surface energy of the structures providing smoothing, porosity, sponge, or nanodots [56,57,154]. Here, the unique self-organization mechanism is attributed to the interaction of impinging ions with the germanium surface atoms. On ion beam bombardment, the surface undergoes processes such as sputtering and defect formation. The phase change and defect formation on ion beam bombardment at the beam-overlapping region provide strengthening to the atoms against complete sputtering. The combined effect of melt-pool assisted amorphization and phase transformation contribute to the mass diffusion up to a short range. Which mimics the confined viscous flow in the affected regions [57,56,62]. It has been reported that the fingering patterns emerge along the interface of a viscous fluid to minimize the surface energies when the flow of viscous media is affected by resistance such as the flow of less viscous fluid [148,159], air [160], or particles [161]. This process of fingering pattern formation is called Saffman-Taylor instability, also widely known as viscous-fingering [148,159]. The controlled viscous-fingering with the utilization of modified Hele Show cell, which has periodic pores, leads to the formation of polygonal formations at millimeter-scale [148,159]. The results of the formation of ordered polygons in the previous chapter (SEM images in Figure 5.2) seem to mimic the ordered polygonal fingering in the Hele Show cell due to viscous-fingering at the nanoscale. Thus, the viscous-flow of the amorphous surface at walls between adjoining nanoholes under the overlapping region is forced to reorganize radially along the vertical axis of the incident ion beam. The phase transformation and viscous-flow on ion beam bombardment at the beam-overlapping region inhibit the complete sputtering of the atoms on collision with incident ions.

The other interesting aspect observed is a protrusion of nanostructures (AFM results in Figure 5.6) above the target surface, suggesting the potential for 3D structure fabrication. The protrusion is attributed to increased volume (swelling) driven by amorphization and phase transformation on the ion beam induced reorganization (Selected area electron diffraction in Figure 5.13(d-e) and Raman spectroscopy results in Figure 5.17). Further, the viscous-fingering, involving mass diffusion and surface reorganization, forces the affected atoms to organize in a way to reduce the surface energy, and straightened walls are formed at the midpoints between the adjoining nanoholes. Subsequently, polygonal morphologies are evolved based on the placement of the FIB spot (SEM images in Figure 5.2). At optimized dose and beam overlap between adjacent holes, atoms lying on the overlapping region reorganize and flow like a viscous media allowing the surface reorganization under the effect of Saffman-Taylor instability, which leads to the occurrence of viscous-fingering to minimize the surface energy [146–149].

Thus, the mechanism for the formation of polygonal nanoholes can be summarised in three stages as seen in Figure 5.1(b): (i) initial circular nanoholes with low dose irradiation due to milling process as melt-pool zones are far apart and do not interact with each other, (ii) with an increase in the dose the size of the nanoholes increases and melt-pool zones of neighbouring nanoholes start interacting with each other, (iii) on the further increase in the dose the walls between adjoining nanoholes strengthen due to the viscous-fingering phenomenon, and periodic polygonal nanoholes are formed. In contrast to the common sputtering governed milling phenomenon, [28,139,140] in the present report, the overlapped region is found to undergo self-organization. Instead of getting sputtered as conventionally expected, the material forms a straight wall protruding out of the surface providing better control over the morphology of the nanoholes induced by a single FIB-spot, resulting in a designed polygonal nanostructure.

6.4 Summary

The molecular dynamics simulations reveal melt-pool assisted amorphization and phase transformation on ion beam irradiation over the germanium surface. 2 *keV* energy gallium ion beam is found to create site-specific temperature in the germanium above the melting point. It is evident that the higher energy ion beam will lead to the formation of a melt-zone having a larger volume for a relatively longer duration. Strengthening the existence of metastable germanium phase from TEM and Raman spectroscopy in the previous chapter, MD results suggest hexagonal diamond phase in the matrix of amorphous/polycrystalline germanium after ion beam irradiation. Saffman-Taylor instability is the driving force behind the unique morphology of the nanoholes in the germanium surface. The mechanism behind the morphology transition is found to be governed by the viscous-fingering effect at a nanoscale level, which is assisted by the site-specific melt-pool and phase transformation during the FIB irradiation. The large-scale molecular dynamics simulations are necessary to understand the dynamics of surface reorganization on ion beam bombardment.

Chapter 7

Conclusions and Outlook

This chapter provides an overview on the conclusions of this thesis and presents an outlook on the directions for futures research.

7.1 Conclusions

In this thesis, the research work demonstrates the manipulation of the ion beam induced self-organization resulting in the varied morphologies of the nanostructures. The irradiation of broad argon ion beam on gold and silicon was studied, and simply a change in rotational conditions resulted in the morphological tunning of the self-organized nanostructures. Moreover, starting from the quasi-periodic nanoripples to highly periodic and protruding nanoscale polygons of germanium were achieved by the gallium focused ion beam. The electron microscopy, atomic force microscopy, Raman spectroscopy, and atomistic investigations with molecular dynamics simulations were carried out to characterize as well as to investigate the self-organized morphologies and the underlying mechanism. The summary of conclusions is as follows,

- Demonstrated the formation of self-organized gold nanocones by argon ion beam bombardment on a large area. It has been observed that the rotation of the sample during ion beam sputtering plays a significant role in defining the final morphology of the nanostructures.
- A hybrid tri-layered gold-nanocone/graphene/gold-nanohole structure is proposed and numerically investigated with electromagnetic simulations using the FDTD method. The results obtained from numerical simulations reveal that the proposed

structure gives a high SERS enhancement factor of the order of 10^9 for the graphene layer of 1 *nm* thickness. Hence, the proposed hybrid plasmonic structure has the potential to provide a highly sensitive SERS signal, and it would be useful for efficient molecular sensing.

- Formation of nanoripples with variant orientations such as parallel and perpendicular to the ion beam scanning direction is demonstrated. The results provide a novel approach to manipulate the orientation of nanoripples by simply changing the beam overlap and thus enabling the fabrication of varied nanoripples on a defined area. Using this approach, different nanoripple orientations can be achieved at the normal incidence of the focused ion beam itself, which is advantageous over the conventional approach of varying incident angle.
- The broadband light trapping for the FIB induced germanium nanoripples both experimentally and through FDTD simulations was demonstrated. The resultant light absorptance is about 95% for the visible light range. Such broadband light absorption in nanostructured germanium can lead to higher efficiency in photovoltaic based devices.
- A novel approach with viscous-fingering at the nanoscale to fabricate nanoscale polygonal holes induced by focused ion beam irradiation is presented. Here, the polygonal nanoholes are not formed due to the conventional direct milling dominant strategy where polygons can be created by milling arrays of pixels for desired polygonal geometry, but the protruding polygonal nanoholes are grown out of the surface at each FIB pixel due to the self-organization of the nanoholes on germanium surface via controlled ion beam scanning.

- The research demonstrates the engineering of each spot during FIB dwelling to produce periodic polygonal morphologies such as square, triangular, hexagonal, pentagonal, and octagonal. Hence, in addition to the precise nanoscale control on self-organization, the study also fosters the advancement in FIB processes towards manipulating the individual nanoholes (induced by each FIB-spots), offering a unique and novel capability in the field of FIB-nanofabrication.
- To check the effect of FIB irradiation on germanium, atomistic simulations with molecular dynamics (MD) were carried out for interactions of bombarding Ga^+ ions with Ge crystal. The influence of thermalization and crystallographic changes in the germanium on Ga^+ irradiation was investigated by molecular dynamics (MD) simulations. The MD simulations predicted the site-specific temperature spike creating a melt-pool assisted phase transformation resulting in hexagonal diamond lattice sites of Ge within the amorphous phase of Ge at the ion impingement regions. These results agree with the results from selected area electron diffraction and Raman spectroscopy for the polygonal nanostructures.
- The mechanism behind the morphology transition is driven by a viscous-fingering effect at a nanoscale level, which is assisted by the site-specific melt-pool formation and phase transformation during the FIB irradiation on the germanium surface. The presented findings will open new avenues on the easy fabrication of nanoscale 3D structures and towards high-efficiency germanium based photovoltaic as well as photonics applications

7.2 Directions for future research and developments

The demonstrated approach for varied polygonal nanostructures by easy single spot FIB processing has the potential to address the roadblocking challenges in the field of nanofabrication. Thus, the unique but straightforward process for periodic as well as protruding polygon-shaped nanoholes fabrication process is demonstrated. Such germanium nanostructures can be significantly useful for bio-sensing, photodiodes, and microfluidics. Using the FIB system with a low beam current or with different ion sources can lead to obtaining yet smaller polygons of the size lesser than 10 *nm*. For example, He^+ FIB can provide a probe size of ~5 *nm*, which could be utilized to realize the smaller polygonal nanostructures by the presented strategies. The future experiment on FIB self-organization can be extended on the other similar materials, in terms of similar sensitivity with ion beams, such as copper, aluminium and silver, etc. Future research on the presented self-organization for other materials would enable us with a plethora of applications. Different FIB sources exhibit unique and varied interactions with different materials samples due to material-dependent sensitivity, sputter yield, and mechanical/thermal properties of materials. Hence, there are unique and diverse scopes for future research to utilize the presented self-organization methods for materials scientists to develop advanced applications of nanostructures.

The present study has the potential to provide an easy way of controlling the orientation of nanoripples, which can aid in the design of high-efficiency germanium-based photovoltaic devices. Germanium nanostructures exhibit localized surface plasmon resonance in the infrared spectrum [162]. Hence, a localized surface plasmon resonance (LSPR) and light confinement enhanced infrared photodetector can be designed as represented in Figure 7.1.

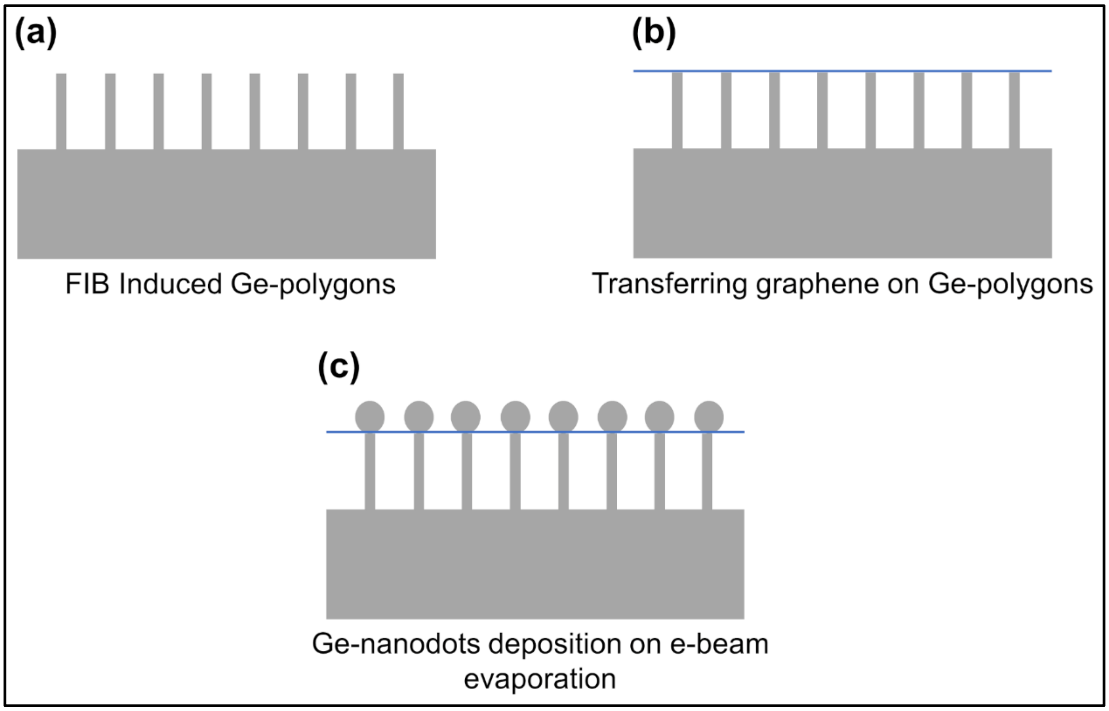
(a)
FIB Induced Ge-polygons
(b)
Transferring graphene on Ge-polygons
(c)
Ge-nanodots deposition on e-beam evaporation

Figure 7.1 Schematic for fabrication of Gee-nanodots/Graphene/Ge-nanostructures for LSPR in IR region

The hybrid, tri-layered Ge-nanodots/Graphene/Ge-nanostructures, the photodetector can be fabricated in two steps: (1) transferring graphene on FIB induced self-organized germanium polygons (Figure 7.1(b)), and then (2) germanium nanoclusters can be deposited on Graphene/Ge-nanostructures using electron beam evaporation technique (Figure 7.1(c)). Owing to the enhanced optical absorption in the broad wavelength range, amorphous Si/Ge photodetector can be designed from the self-organized germanium nanostructures [130]. The device can be prepared from FIB-induced germanium nanostructures by thermal deposition of the silicon layer on the germanium nanostructures.

The presented controlled fingering pattern formation with viscous-fingering can be exploited to develop a theoretical model at nanoscale fingering based on Saffman-Taylor instabilities on ion beam irradiation. The attempts to connect this observed nanoscaled viscous-fingering with the macroscaled viscous-fingering occurring in a Hele Show cell will provide an essential aspect of the phenomenon, which could be useful to achieve such self-organization into different kind of materials. The theoretical MD simulations demonstrated in this thesis could also be used to predict the feasibility of similar self-organization in different metal and semiconducting materials. The essential requirement of viscous-fingering driven self-organization would be that the material of interest should exhibit similar response as germanium on ion irradiation with optimized crystallographic and thermalization conditions. The mass transport (diffusion) and surface re-organization could be studied to strengthen the understanding of the morphology transitions. The theoretical knowledge acquired through extensive experiments on different materials and MD simulations could be extended towards developing a robust model for complex morphologies and manipulating nano-/pico-scaled structures.

References

[1] H. Haken, *Synergetics: An Introduction*, 3rd ed. (Springer-Verlag, Berlin Heidelberg, 1983).

[2] T. Y. Kim, S. W. Kwon, S. J. Park, D. H. Yoon, K. S. Suh, and W. S. Yang, *Self-Organized Graphene Patterns*, Adv. Mater. **23**, 2734 (2011).

[3] T. Bobek, N. Mikuszeit, J. Camarero, S. Kyrsta, L. Yang, M. Á. Niño, C. Hofer, L. Gridneva, D. Arvanitis, R. Miranda, J. J. de Miguel, C. Teichert, and H. Kurz, *Self-Organized Hexagonal Patterns of Independent Magnetic Nanodots*, Adv. Mater. **19**, 4375 (2007).

[4] H. Reinhardt, M. Kroll, S. L. Karstens, S. Schlabach, N. A. Hampp, and U. Tallarek, *Nanoscaled Fractal Superstructures via Laser Patterning—A Versatile Route to Metallic Hierarchical Porous Materials*, Adv. Mater. Interfaces 2000253 (2020).

[5] R. M. Bradley and J. M. E. Harper, *Theory of Ripple Topography Induced by Ion Bombardment*, J. Vac. Sci. Technol. A **6**, 2390 (1988).

[6] U. Valbusa, C. Boragno, and F. B. de Mongeot, *Nanostructuring Surfaces by Ion Sputtering*, J. Phys.: Condens. Matter **14**, 8153 (2002).

[7] L. Sack and C. Scoffoni, *Leaf Venation: Structure, Function, Development, Evolution, Ecology and Applications in the Past, Present and Future*, New Phytologist **198**, 983 (2013).

[8] L. M. S. Aas, M. Kildemo, C. Martella, M. C. Giordano, D. Chiappe, and F. Buatier de Mongeot, *Optical Properties of Biaxial Nanopatterned Gold Plasmonic Nanowired Grid Polarizer*, Optics Express **21**, 30918 (2013).

[9] J. Munoz-Garcia, L. Vazquez, R. Cuerno, J. A. Sanchez-Garcia, M. Castro, and R. Gago, *Self-Organized Surface Nanopatterning by Ion Beam Sputtering*, in *Toward Functional Nanomaterials*, edited by Z. M. Wang (Springer US, 2009), pp. 323–398.

[10] J. Wu, G. Chen, Z. Zeng, S. Li, X. Xu, Z. M. Wang, and G. J. Salamo, *Ordered SrTiO3 Nanoripples Induced by Focused Ion Beam*, Nano-Micro Lett. **4**, 243 (2012).

[11] D. Repetto, M. C. Giordano, C. Martella, and F. Buatier de Mongeot, *Transparent Aluminium Nanowire Electrodes with Optical and Electrical Anisotropic Response Fabricated by Defocused Ion Beam Sputtering*, Appl. Surf. Sci. **327**, 444 (2015).

[12] T. Basu, D. A. Pearson, R. M. Bradley, and T. Som, *Temporal Evolution of a Silicon Surface Subject to Low Energy Ion Irradiation and Concurrent Sample Rotation*, Appl. Surf. Sci. **379**, 480 (2016).

[13] C. D’Andrea, B. Fazio, P. G. Gucciardi, M. C. Giordano, C. Martella, D. Chiappe, A. Toma, F. Buatier de Mongeot, F. Tantussi, P. Vasanthakumar, F. Fuso, and M. Allegrini, *SERS Enhancement and Field Confinement in Nanosensors Based on*

Self-Organized Gold Nanowires Produced by Ion-Beam Sputtering, J. Phys. Chem. C **118**, 8571 (2014).

[14] B. Ziberi, Ion Beam Induced Pattern Formation on Si and Ge Surfaces, Leibniz Institute of Surface Modification, Leipzig University, 2006.

[15] M. Teichmann, J. Lorbeer, B. Ziberi, F. Frost, and B. Rauschenbach, *Pattern Formation on Ge by Low Energy Ion Beam Erosion*, New J. Phys. **15**, 103029 (2013).

[16] D. P. Datta, S. K. Garg, T. Basu, B. Satpati, H. Hofsäss, D. Kanjilal, and T. Som, *Temporal Evolution of Ge Surface Topography under KeV Ion Irradiation: Combined Effects of Curvature-Dependent Sputter Erosion and Atomic Redistribution*, Applied Surface Science **360, Part A**, 131 (2016).

[17] S. K. Garg, D. P. Datta, D. Kanjilal, and T. Som, *Aspects of Ions Induced Texture Evolution on Ge Surface: A Statistical Assessment*, Nuclear Instruments and Methods in Physics Research Section B: Beam Interactions with Materials and Atoms (n.d.).

[18] S. Reyntjens and R. Puers, *A Review of Focused Ion Beam Applications in Microsystem Technology*, J. Micromech. Microeng. **11**, 287 (2001).

[19] R. M. Langford, *Focused Ion Beam Systems: Application to Micro- and Nanofabrication*, in *Encyclopedia of Materials: Science and Technology (Second Edition)*, edited by K. H. J. B. W. C. C. F. I. J. K. M. Veyssière (Elsevier, Oxford, 2010), pp. 1–13.

[20] N. Yao and A. Epstein, *Surface Nanofabrication Using Focused Ion Beam*, Vol. 3 (Formatex, 2010).

[21] K. Gamo, *Nanofabrication by FIB*, Microelectronic Engineering **32**, 159 (1996).

[22] M. J. Vasile, Z. Niu, R. Nassar, W. Zhang, and S. Liu, *Focused Ion Beam Milling: Depth Control for Three-Dimensional Microfabrication*, Journal of Vacuum Science & Technology B: Microelectronics and Nanometer Structures Processing, Measurement, and Phenomena **15**, 2350 (1997).

[23] Y. Fu and N. K. A. Bryan, *Fabrication of Three-Dimensional Microstructures by Two-Dimensional Slice by Slice Approaching via Focused Ion Beam Milling*, Journal of Vacuum Science & Technology B: Microelectronics and Nanometer Structures Processing, Measurement, and Phenomena **22**, 1672 (2004).

[24] A. A. Tseng, *Recent Developments in Nanofabrication Using Focused Ion Beams*, Small **1**, 924 (2005).

[25] C. S. Kim, J. Park, W. S. Chu, D. Y. Jang, S. D. Kim, and S. H. Ahn, *Fabrication of Silicon Micro-Mould for Polymer Replication Using Focused Ion Beam*, Microelectronic Engineering **86**, 556 (2009).

[26] G. Seniutinas, A. Balčytis, I. Reklaitis, F. Chen, J. Davis, C. David, and S. Juodkazis, *Tipping Solutions: Emerging 3D Nano-Fabrication/ -Imaging Technologies*, Nanophotonics **6**, 923 (2017).

[27] A. Sharma, S. B.N, K. N. Bhat, and A. K. Naik, *Gallium-Doped Piezoresistive Sensor With Optimized Focused Ion Beam Implantation*, Journal of Microelectromechanical Systems (2017).

[28] S. Kasani, K. Curtin, and N. Wu, *A Review of 2D and 3D Plasmonic Nanostructure Array Patterns: Fabrication, Light Management and Sensing Applications*, Nanophotonics **8**, 2065 (2019).

[29] C. Lehrer, L. Frey, S. Petersen, and H. Ryssel, *Limitations of Focused Ion Beam Nanomachining*, Journal of Vacuum Science & Technology B: Microelectronics and Nanometer Structures Processing, Measurement, and Phenomena **19**, 2533 (2001).

[30] C.-S. Kim, S.-H. Ahn, and D.-Y. Jang, *Review: Developments in Micro/Nanoscale Fabrication by Focused Ion Beams*, Vacuum **86**, 1014 (2012).

[31] B. Ziberi, F. Frost, Th. Höche, and B. Rauschenbach, *Ripple Pattern Formation on Silicon Surfaces by Low-Energy Ion-Beam Erosion: Experiment and Theory*, Phys. Rev. B **72**, 235310 (2005).

[32] A. V. Krasheninnikov and F. Banhart, *Engineering of Nanostructured Carbon Materials with Electron or Ion Beams*, Nature Materials **6**, 723 (2007).

[33] D. Lucot, J. Gierak, A. Ouerghi, E. Bourhis, G. Faini, and D. Mailly, *Deposition and FIB Direct Patterning of Nanowires and Nanorings into Suspended Sheets of Graphene*, Microelectronic Engineering **86**, 882 (2009).

[34] J. Kotakoski, C. Brand, Y. Lilach, O. Cheshnovsky, C. Mangler, M. Arndt, and J. C. Meyer, *Toward Two-Dimensional All-Carbon Heterostructures via Ion Beam Patterning of Single-Layer Graphene*, Nano Lett. **15**, 5944 (2015).

[35] W. C. L. Hopman, F. Ay, W. Hu, V. J. Gadgil, L. Kuipers, M. Pollnau, and R. M. de Ridder, *Focused Ion Beam Scan Routine, Dwell Time and Dose Optimization for Submicrometre Period Planar Photonic Crystal Components and Stamps in Silicon*, Nanotechnology **18**, 195305/1 (2007).

[36] J. Igaki, R. Kometani, K. Nakamatsu, K. Kanda, Y. Haruyama, Y. Ochiai, J. Fujita, T. Kaito, and S. Matsui, *Three-Dimensional Rotor Fabrication by Focused-Ion-Beam Chemical-Vapor-Deposition*, Microelectronic Engineering **83**, 1221 (2006).

[37] W. J. MoberlyChan, *Dual-Beam Focused Ion Beam/Electron Microscopy Processing and Metrology of Redeposition during Ion–Surface 3D Interactions, from Micromachining to Self-Organized Picostructures*, Journal of Physics: Condensed Matter **21**, 224013 (2009).

[38] W. J. MoberlyChan and R. Schalek, *Ion Beam Induced Surface Modulations from Nano to Pico: Optimizing Deposition During Erosion and Erosion During Deposition*, MRS Proceedings **1059**, 1059 (2007).

[39] J. E. E. Baglin, *Ion Beam Nanoscale Fabrication and Lithography—A Review*, Applied Surface Science **258**, 4103 (2012).

[40] Y. Zhang and G. Ran, *Self-Assembly of Well-Ordered and Highly Uniform Nanoripples Induced by Focused Ion Beam*, Physica E: Low-Dimensional Systems

and Nanostructures **41**, 1848 (2009).

[41] M. A. Makeev, R. Cuerno, and A.-L. Barabási, *Morphology of Ion-Sputtered Surfaces*, Nuclear Instruments and Methods in Physics Research Section B: Beam Interactions with Materials and Atoms **197**, 185 (2002).

[42] E. Chason, J. Erlebacher, M. J. Aziz, J. A. Floro, and M. B. Sinclair, *Dynamics of Pattern Formation during Low-Energy Ion Bombardment of Si(0 0 1)*, Nuclear Instruments and Methods in Physics Research Section B: Beam Interactions with Materials and Atoms **178**, 55 (2001).

[43] S. Peter, *Theory of Sputtering. I. Sputtering Yield of Amorphous and Polycrystalline Targets*, Physical Review **184**, 383 (1969).

[44] P. Sigmund, *A Mechanism of Surface Micro-Roughening by Ion Bombardment*, Journal of Materials Scienece **8**, 1545 (1973).

[45] R. M. Bradley and H. Hofsäss, *A Modification to the Sigmund Model of Ion Sputtering*, Journal of Applied Physics **116**, 234304 (2014).

[46] A. Datta, Y.-R. Wu, and Y. L. Wang, *Real-Time Observation of Ripple Structure Formation on a Diamond Surface under Focused Ion-Beam Bombardment*, Phys. Rev. B **63**, 125407 (2001).

[47] A. Keller and S. Facsko, *Tuning the Quality of Nanoscale Ripple Patterns by Sequential Ion-Beam Sputtering*, Physical Review B **82**, (2010).

[48] H. George, A.-D. Brown, M. R. McGrath, J. D. Erlebacher, and M. J. Aziz, *Quantifying the Order of Spontaneous Ripple Patterns on Ion-Irradiated Si (111)*, in *MRS Proceedings*, Vol. 908 (Cambridge Univ Press, 2005), pp. 0908-OO02.

[49] W. Zhou, A. Cuenat, and M. J. Aziz, *Formation of Self-Organized Nanostructures on Ge during Focused Ion Beam Sputtering*, in *Conference Series-Institute of Physics*, edited by A. G. Cullis and P. A. Midgley, Vol. 180 (Philadelphia; Institute of Physics; 1999, 2003), pp. 625–628.

[50] X. Xu, J. Wu, X. Wang, H. Li, Z. Zhou, and Z. M. Wang, *Site-Controlled Fabrication of Ga Nanodroplets by Focused Ion Beam*, Applied Physics Letters **104**, 133104 (2014).

[51] X. Xu, J. Wu, X. Wang, M. Zhang, J. Li, Z. Shi, H. Li, Z. Zhou, H. Ji, X. Niu, and Z. M. Wang, *Ion-Beam-Directed Self-Ordering of Ga Nanodroplets on GaAs Surfaces*, Nanoscale Res Lett **11**, 38 (2016).

[52] M. Kang, T. W. Saucer, M. V. Warren, J. H. Wu, H. Sun, V. Sih, and R. S. Goldman, *Surface Plasmon Resonances of Ga Nanoparticle Arrays*, Applied Physics Letters **101**, 081905 (2012).

[53] R. Ribeiro-Andrade, A. Malachias, D. R. Miquita, T. L. Vasconcelos, R. Kawabata, M. P. Pires, P. L. Souza, and W. N. Rodrigues, *Study of Growth Properties of InAs Islands on Patterned InP Substrates Defined by Focused Ion Beam*, Physica E: Low-Dimensional Systems and Nanostructures **87**, 59 (2017).

[54] V. Callegari and P. M. Nellen, *Spontaneous Growth of Uniformly Distributed In*

Nanodots and InI3 Nanowires on InP Induced by a Focused Ion Beam, Phys. Stat. Sol. (a) **204**, 1665 (2007).

[55] W. MoberlyChan, *Surface Modification Energized by FIB: The Influence of Etch Rates & Aspect Ratio on Ripple Wavelengths*, MRS Proceedings **960**, 0960 (2006).

[56] M. Fritzsche, A. Muecklich, and S. Facsko, *Nanohole Pattern Formation on Germanium Induced by Focused Ion Beam and Broad Beam Ga+ Irradiation*, Appl. Phys. Lett. **100**, 223108 (2012).

[57] R. Böttger, K.-H. Heinig, L. Bischoff, B. Liedke, and S. Facsko, *From Holes to Sponge at Irradiated Ge Surfaces with Increasing Ion Energy—an Effect of Defect Kinetics?*, Appl. Phys. A **113**, 53 (2013).

[58] P. Süle and K.-H. Heinig, *The Molecular Dynamics Simulation of Ion-Induced Ripple Growth*, The Journal of Chemical Physics **131**, 204704 (2009).

[59] J. F. Ziegler and J. P. Biersack, *The Stopping and Range of Ions in Matter*, in *Treatise on Heavy-Ion Science: Volume 6: Astrophysics, Chemistry, and Condensed Matter*, edited by D. A. Bromley (Springer US, Boston, MA, 1985), pp. 93–129.

[60] S. Satake, N. Inoue, J. Taniguchi, and M. Shibahara, *Molecular Dynamics Simulation for Focused Ion Beam Processing: A Comparison between Computational Domain and Potential Energy*, Journal of Physics: Conference Series **106**, 012013 (2008).

[61] J. J. Végh and D. B. Graves, *Molecular Dynamics Simulations of Sub-10 Nm Wavelength Surface Rippling by CF3 Ion Beams*, Plasma Sources Sci. Technol. **19**, 045005 (2010).

[62] C. Anders, K.-H. Heinig, and H. M. Urbassek, *Polyatomic Bismuth Impacts into Germanium: Molecular Dynamics Study*, Phys. Rev. B **87**, (2013).

[63] J. Muñoz-García, L. Vázquez, M. Castro, R. Gago, A. Redondo-Cubero, A. Moreno-Barrado, and R. Cuerno, *Self-Organized Nanopatterning of Silicon Surfaces by Ion Beam Sputtering*, Materials Science and Engineering: R: Reports **86**, 1 (2014).

[64] X. Wu, H. Zhao, M. Zhong, H. Murakawa, and M. Tsukamoto, *Molecular Dynamics Simulation of Graphene Sheets Joining under Ion Beam Irradiation*, Carbon **66**, 31 (2014).

[65] K. Das, J. B. Freund, and H. T. Johnson, *A FIB Induced Boiling Mechanism for Rapid Nanopore Formation*, Nanotechnology **25**, 035303 (2014).

[66] Z. Bai, L. Zhang, H. Li, and L. Liu, *Nanopore Creation in Graphene by Ion Beam Irradiation: Geometry, Quality, and Efficiency*, ACS Appl. Mater. Interfaces **8**, 24803 (2016).

[67] P. Wang, Q. Chen, Y. Xing, Y. Li, C. Fang, and X. Qiu, *Molecular Dynamic Simulation of Orientation-Dependent Effect on Silicon Crystalline during Sputtering Process of Focused Ion Beam*, Microsyst. Technol. **25**, 1413 (2019).

[68] V. Garg, B. Kamaliya, R. K. Singh, A. S. Panwar, J. Fu, and R. G. Mote, *Controlled*

Manipulation and Multiscale Modeling of Suspended Silicon Nanostructures under Site-Specific Ion Irradiation, ACS Appl. Mater. Interfaces **12**, 6581 (2020).

[69] S. Plimpton, *Fast Parallel Algorithms for Short-Range Molecular Dynamics*, J. Comput. Phys. **117**, 1 (1995).

[70] Zi Jian, Zhang Kaiming, and Xie Xide, *Modification of Stillinger-Weber Potentials for Si and Ge*, Phys. Rev. B **41**, 12915 (1990).

[71] M. Posselt and A. Gabriel, *Atomistic Simulation of Amorphous Germanium and Its Solid Phase Epitaxial Recrystallization*, Phys. Rev. B **80**, 045202 (2009).

[72] S. Z. Chavoshi and X. Luo, *Atomic-Scale Characterization of Occurring Phenomena during Hot Nanometric Cutting of Single Crystal 3C–SiC*, RSC Adv. **6**, 71409 (2016).

[73] J. Zhou, M. Hildebrandt, and M. Lu, *Self-Organized Antireflecting Nano-Cone Arrays on Si (100) Induced by Ion Bombardment*, Journal of Applied Physics **109**, 053513 (2011).

[74] T. Basu, J. R. Mohanty, and T. Som, *Unusual Pattern Formation on Si(100) Due to Low Energy Ion Bombardment*, Applied Surface Science **258**, 9944 (2012).

[75] S.-C. Song, Y. Qiu, H.-C. Hao, and M. Lu, *Effects of Crystallographic Plane and Co-Deposited Element on the Growth of Ion-Sputter Induced Si Nano-Cone Arrays: A Mechanism Study*, Appl. Phys. A **119**, 1033 (2015).

[76] J. K. Yoon, K. Kim, and K. S. Shin, *Raman Scattering of 4-Aminobenzenethiol Sandwiched between Au Nanoparticles and a Macroscopically Smooth Au Substrate: Effect of Size of Au Nanoparticles*, J. Phy. Chem. C **113**, 1769 (2009).

[77] J. M. Kontio, H. Husu, J. Simonen, M. J. Huttunen, J. Tommila, M. Pessa, and M. Kauranen, *Nanoimprint Fabrication of Gold Nanocones with ~10 Nm Tips for Enhanced Optical Interactions*, Opt. Lett. **34**, 1979 (2009).

[78] X. Li, J. Zhu, and B. Wei, *Hybrid Nanostructures of Metal/Two-Dimensional Nanomaterials for Plasmon-Enhanced Applications*, Chem. Soc. Rev. **45**, 3145 (2016).

[79] Z. Zhan, L. Liu, W. Wang, Z. Cao, A. Martinelli, E. Wang, Y. Cao, J. Chen, A. Yurgens, and J. Sun, *Ultrahigh Surface-Enhanced Raman Scattering of Graphene from Au/Graphene/Au Sandwiched Structures with Subnanometer Gap*, Adv. Optical Mater. **4**, 2021 (2016).

[80] P. Zheng, X. Shi, K. Curtin, F. Yang, and N. Wu, *Detection of Mercury(II) with a Surface-Enhanced Raman Scattering Sensor Based on Functionalized Gold Nanoparticles*, Mater. Res. Express **4**, 055017 (2017).

[81] M. Banik, A. Nag, P. Z. El-Khoury, A. Rodriguez Perez, N. Guarrotxena, G. C. Bazan, and V. A. Apkarian, *Surface-Enhanced Raman Scattering of a Single Nanodumbbell: Dibenzyldithio-Linked Silver Nanospheres*, J. Phys. Chem. C **116**, 10415 (2012).

[82] X. Zhu, L. Shi, M. S. Schmidt, A. Boisen, O. Hansen, J. Zi, S. Xiao, and N. A.

Mortensen, *Enhanced Light–Matter Interactions in Graphene-Covered Gold Nanovoid Arrays*, Nano Lett. **13**, 4690 (2013).

[83] E. J. Blackie, E. C. Le Ru, and P. G. Etchegoin, *Single-Molecule Surface-Enhanced Raman Spectroscopy of Nonresonant Molecules*, J. Am. Chem. Soc. **131**, 14466 (2009).

[84] E. C. Le Ru, E. Blackie, M. Meyer, and P. G. Etchegoin, *Surface Enhanced Raman Scattering Enhancement Factors: A Comprehensive Study*, J. Phys. Chem. C **111**, 13794 (2007).

[85] D. Paria, K. Roy, H. J. Singh, S. Kumar, S. Raghavan, A. Ghosh, and A. Ghosh, *Ultrahigh Field Enhancement and Photoresponse in Atomically Separated Arrays of Plasmonic Dimers*, Adv. Mater. **27**, 1751 (2015).

[86] G. Das, M. Morett, B. Torre, M. Allione, A. Giugni, and E. D. Fabrizio, *Graphene: A Building Foundation for Efficient Plasmonic SERS Device*, Biochem. Anal. Biochem. **06**, (2017).

[87] N. Reckinger, A. Vlad, S. Melinte, J.-F. Colomer, and M. Sarrazin, *Graphene-Coated Holey Metal Films: Tunable Molecular Sensing by Surface Plasmon Resonance*, Applied Physics Letters **102**, 211108 (2013).

[88] Y. Wang, Z. Ni, H. Hu, Y. Hao, C. P. Wong, T. Yu, J. T. L. Thong, and Z. X. Shen, *Gold on Graphene as a Substrate for Surface Enhanced Raman Scattering Study*, Appl. Phys. Lett. **97**, 163111 (2010).

[89] M. Kalbac, V. Vales, and J. Vejpravova, *The Effect of a Thin Gold Layer on Graphene: A Raman Spectroscopy Study*, RSC Adv. **4**, 60929 (2014).

[90] C. J. Shearer, A. D. Slattery, A. J. Stapleton, J. G. Shapter, and C. T. Gibson, *Accurate Thickness Measurement of Graphene*, Nanotechnology **27**, 125704 (2016).

[91] Z. Qin, M. Taylor, M. Hwang, K. Bertoldi, and M. J. Buehler, *Effect of Wrinkles on the Surface Area of Graphene: Toward the Design of Nanoelectronics*, Nano Lett. **14**, 6520 (2014).

[92] G. W. Hanson, *Dyadic Green's Functions and Guided Surface Waves for a Surface Conductivity Model of Graphene*, J. Appl. Phy. **103**, 064302 (2008).

[93] L. A. Falkovsky, *Optical Properties of Graphene*, J. Phys. Conf. Ser. **129**, 012004 (2008).

[94] X. Zhu, L. Shi, M. S. Schmidt, A. Boisen, O. Hansen, J. Zi, S. Xiao, and N. A. Mortensen, *Enhanced Light–Matter Interactions in Graphene-Covered Gold Nanovoid Arrays*, Nano Lett. **13**, 4690 (2013).

[95] E. D. Palik, editor , *Handbook of Optical Constants of Solids*, in *Handbook of Optical Constants of Solids*, Vol. 1 (Academic Press, Burlington, 1997), pp. 465–478.

[96] P. B. Johnson and R.-W. Christy, *Optical Constants of the Noble Metals*, Physical Review B **6**, 4370 (1972).

[97] S. D. Standridge, G. C. Schatz, and J. T. Hupp, *Toward Plasmonic Solar Cells: Protection of Silver Nanoparticles via Atomic Layer Deposition of TiO2*, Langmuir **25**, 2596 (2009).

[98] D. Dominguez, H. Tiznado, H. A. Borbon-Nuñez, F. Muñoz-Muñoz, J. M. Romo-Herrera, and G. Soto, *Enhancing the Oxidation Resistance of Diamond Powder by the Application of Al2O3 Conformal Coat by Atomic Layer Deposition*, Diam. Relat. Mater. **69**, 108 (2016).

[99] Y. Yu, Z. Zhang, X. Yin, A. Kvit, Q. Liao, Z. Kang, X. Yan, Y. Zhang, and X. Wang, *Enhanced Photoelectrochemical Efficiency and Stability Using a Conformal TiO_2 Film on a Black Silicon Photoanode*, Nat. Energy **2**, 17045 (2017).

[100] Q. Han, Y. Fu, L. Jin, J. Zhao, Z. Xu, F. Fang, J. Gao, and W. Yu, *Germanium Nanopyramid Arrays Showing Near-100% Absorption in the Visible Regime*, Nano Research **8**, 2216 (2015).

[101] D. Cavalcoli, G. Impellizzeri, L. Romano, M. Miritello, M. G. Grimaldi, and B. Fraboni, *Optical Properties of Nanoporous Germanium Thin Films*, ACS Appl. Mater. Interfaces **7**, 16992 (2015).

[102] C. Kang, J. W. Leem, I. Maeng, T. H. Kim, J. S. Lee, J. S. Yu, and C.-S. Kee, *Strong Emission of Terahertz Radiation from Nanostructured Ge Surfaces*, Appl. Phys. Lett. **106**, 261106 (2015).

[103] L. Baldassarre, E. Sakat, J. Frigerio, A. Samarelli, K. Gallacher, E. Calandrini, G. Isella, D. J. Paul, M. Ortolani, and P. Biagioni, *Midinfrared Plasmon-Enhanced Spectroscopy with Germanium Antennas on Silicon Substrates*, Nano Lett. **15**, 7225 (2015).

[104] W.-K. Lee, S. Yu, C. J. Engel, T. Reese, D. Rhee, W. Chen, and T. W. Odom, *Concurrent Design of Quasi-Random Photonic Nanostructures*, PNAS 201704711 (2017).

[105] S. Rubanov and P. R. Munroe, *The Application of FIB Milling for Specimen Preparation from Crystalline Germanium*, Micron **35**, 549 (2004).

[106] H. X. Qian and W. Zhou, *Self-Organization of Ripples on Ti Irradiated with Focused Ion Beam*, Applied Surface Science **258**, 1924 (2012).

[107] C. Schoendorfer, A. Lugstein, L. Bischoff, Y. J. Hyun, P. Pongratz, and E. Bertagnolli, *FIB Induced Growth of Antimony Nanowires*, Microelectronic Engineering **84**, 1440 (2007).

[108] S. M. Allameh, N. Yao, and W. O. Soboyejo, *Synthesis of Self-Assembled Nanoscale Structures by Focused Ion-Beam Induced Deposition*, Scr. Mater. **50**, 915 (2004).

[109] T. Som and D. Kanjilal, *Applications of Ion Beam Produced Patterned Substrates in Plasmonics*, in *Nanofabrication by Ion-Beam Sputtering: Fundamentals and Applications* (CRC Press, 2012), pp. 318–348.

[110] A. Toma, D. Chiappe, D. Massabò, C. Boragno, and F. Buatier de Mongeot, *Self-Organized Metal Nanowire Arrays with Tunable Optical Anisotropy*, Applied

Physics Letters **93**, 163104 (2008).

[111] P. Chaudhari, J. Lacey, J. Doyle, E. Galligan, S.-C. A. Lien, A. Callegari, G. Hougham, N. D. Lang, P. S. Andry, R. John, K.-H. Yang, M. Lu, C. Cai, J. Speidell, S. Purushothaman, J. Ritsko, M. Samant, J. Stöhr, Y. Nakagawa, Y. Katoh, Y. Saitoh, K. Sakai, H. Satoh, S. Odahara, H. Nakano, J. Nakagaki, and Y. Shiota, *Atomic-Beam Alignment of Inorganic Materials for Liquid-Crystal Displays*, Nature **411**, 56 (2001).

[112] P. Bellon, S. J. Chey, J. E. Van Nostrand, M. Ghaly, D. G. Cahill, and R. S. Averback, *Surface Damage Produced by 20 KeV Ga Bombardment of Ge(001)*, Surface Science **339**, 135 (1995).

[113] I. H. Wilson, *The Effects of Self-ion Bombardment (30–500 KeV) on the Surface Topography of Single-crystal Germanium*, Journal of Applied Physics **53**, 1698 (1982).

[114] S. Ichim and M. J. Aziz, *Lateral Templating of Self-Organized Ripple Morphologies during Focused Ion Beam Milling of Ge*, Journal of Vacuum Science & Technology B: Microelectronics and Nanometer Structures **23**, 1068 (2005).

[115] D. Nečas and P. Klapetek, *Gwyddion: An Open-Source Software for SPM Data Analysis*, Centr.Eur.j.Phys. **10**, 181 (2012).

[116] R. F. Potter, *Germanium (Ge)*, in *Handbook of Optical Constants of Solids*, edited by E. D. Palik, Vol. 1 (Academic Press, Burlington, 1997), pp. 465–478.

[117] B. E. Yoldas, *Investigations of Porous Oxides as an Antireflective Coating for Glass Surfaces*, Appl. Opt. **19**, 1425 (1980).

[118] Y. Tamar, M. Tzabari, C. Haspel, and Y. Sasson, *Estimation of the Porosity and Refractive Index of Sol–Gel Silica Films Using High Resolution Electron Microscopy*, Solar Energy Materials and Solar Cells **130**, 246 (2014).

[119] K. J. Pascoe, Reflectivity and Transmissivity through Layered, Lossy Media: A User-Friendly Approach, Technical Report, Wright Patterson Air Force Base: Ohio, USA, 2001.

[120] J. S. C. Prentice, *Coherent, Partially Coherent and Incoherent Light Absorption in Thin-Film Multilayer Structures*, Journal of Physics D: Applied Physics **33**, 3139 (2000).

[121] D. J. Poxson, F. W. Mont, M. F. Schubert, J. K. Kim, J. Cho, and E. F. Schubert, *Demonstration of Optical Interference Filters Utilizing Tunable Refractive Index Layers*, Optics Express **18**, A594 (2010).

[122] J. W. Leem, Y. M. Song, and J. S. Yu, *Broadband Antireflective Germanium Surfaces Based on Subwavelength Structures for Photovoltaic Cell Applications*, Opt. Express, **19**, 26308 (2011).

[123] M. Chen, H. Chang, A. S. P. Chang, S.-Y. Lin, J.-Q. Xi, and E. F. Schubert, *Design of Optical Path for Wide-Angle Gradient-Index Antireflection Coatings*, Appl. Opt., AO **46**, 6533 (2007).

[124] M. Grydlik, M. T. Lusk, F. Hackl, A. Polimeni, T. Fromherz, W. Jantsch, F. Schäffler, and M. Brehm, *Laser Level Scheme of Self-Interstitials in Epitaxial Ge Dots Encapsulated in Si*, Nano Lett. **16**, 6802 (2016).

[125] M. Grydlik, F. Hackl, H. Groiss, M. Glaser, A. Halilovic, T. Fromherz, W. Jantsch, F. Schäffler, and M. Brehm, *Lasing from Glassy Ge Quantum Dots in Crystalline Si*, ACS Photonics **3**, 298 (2016).

[126] G. Pellegrini, L. Baldassare, V. Giliberti, J. Frigerio, K. Gallacher, D. J. Paul, G. Isella, M. Ortolani, and P. Biagioni, *Benchmarking the Use of Heavily Doped Ge for Plasmonics and Sensing in the Mid-Infrared*, ACS Photonics **5**, 3601 (2018).

[127] G. Grinblat, Y. Li, M. P. Nielsen, R. F. Oulton, and S. A. Maier, *Enhanced Third Harmonic Generation in Single Germanium Nanodisks Excited at the Anapole Mode*, Nano Lett. **16**, 4635 (2016).

[128] F. Neubrech, C. Huck, K. Weber, A. Pucci, and H. Giessen, *Surface-Enhanced Infrared Spectroscopy Using Resonant Nanoantennas*, Chem. Rev. **117**, 5110 (2017).

[129] S. Ossicini, M. Amato, R. Guerra, M. Palummo, and O. Pulci, *Silicon and Germanium Nanostructures for Photovoltaic Applications: Ab-Initio Results*, Nanoscale Res. Lett. **5**, 1637 (2010).

[130] M. Steglich, M. Zilk, F. Schrempel, A. Tünnermann, and E.-B. Kley, *Improvement of Ge-on-Si Photodiodes by Black Silicon Light Trapping*, Appl. Phys. Lett. **102**, 111110 (2013).

[131] A. Podolian, A. Nadtochiy, O. Korotchenkov, B. Romanyuk, V. Melnik, and V. Popov, *Enhanced Photoresponse of Ge/Si Nanostructures by Combining Amorphous Silicon Deposition and Annealing*, J. Appl. Phys. **124**, 095703 (2018).

[132] B. Kamaliya, R. G. Mote, M. Aslam, and J. Fu, *Enhanced Light Trapping by Focused Ion Beam (FIB) Induced Self-Organized Nanoripples on Germanium (100) Surface*, APL Mater. **6**, 036106 (2018).

[133] W.-J. Lee, J. W. Ma, J. M. Bae, K.-S. Jeong, M.-H. Cho, C. Kang, and J.-S. Wi, *Strongly Enhanced THz Emission Caused by Localized Surface Charges in Semiconducting Germanium Nanowires*, Sci. Rep. **3**, 1984 (2013).

[134] D. Sabbagh, J. Schmidt, S. Winnerl, M. Helm, L. Di Gaspare, M. De Seta, M. Virgilio, and M. Ortolani, *Electron Dynamics in Silicon–Germanium Terahertz Quantum Fountain Structures*, ACS Photonics **3**, 403 (2016).

[135] D. J. Paul, K. Gallacher, R. W. Millar, V. Giliberti, E. Calandrini, L. Baldassarre, M. P. Fischer, J. Frigerio, A. Ballabio, E. Sakat, G. Pellegrini, D. Brida, G. Isella, M. Ortolani, and P. Biagioni, *N-Ge on Si for Mid-Infrared Plasmonic Sensors*, in *2017 IEEE Photonics Society Summer Topical Meeting Series (SUM)* (2017), pp. 125–126.

[136] R. Goodarzi, F. Hajiesmaeilbaigi, and E. Bostandoost, *Self-Organized Fractal-like Structures Formation on the Silicon Wafer Surface Using the Femtosecond Laser Pulses*, Opt. Lasers Eng. **128**, 106008 (2020).

[137] Q. Wei, X. Zhou, B. Joshi, Y. Chen, K.-D. Li, Q. Wei, K. Sun, and L. Wang, *Self-Assembly of Ordered Semiconductor Nanoholes by Ion Beam Sputtering*, Adv. Mater. **21**, 2865 (2009).

[138] J. C. Kim, D. G. Cahill, and R. S. Averback, *Surface Defects Created by 20keV Xe Ion Irradiation of Ge(111),* Surf. Sci. **574**, 175 (2005).

[139] V. Garg, R. G. Mote, and J. Fu, *Focused Ion Beam Direct Fabrication of Subwavelength Nanostructures on Silicon for Multicolor Generation*, Adv. Mater. Technol. **3**, 1800100 (2018).

[140] V. Garg, R. G. Mote, and J. Fu, *Rapid Prototyping of Highly Ordered Subwavelength Silicon Nanostructures with Enhanced Light Trapping*, Opt. Mater. **94**, 75 (2019).

[141] G. Dushaq, A. Nayfeh, and M. Rasras, *Hexagonal Germanium Formation at Room Temperature Using Controlled Penetration Depth Nano-Indentation*, Sci. Rep. **9**, 1 (2019).

[142] R. J. Kobliska, S. A. Solin, M. Selders, R. K. Chang, R. Alben, M. F. Thorpe, and D. Weaire, *Raman Scattering from Phonons in Polymorphs of Si and Ge*, Phys. Rev. Lett. **29**, 725 (1972).

[143] M. Wakaki, M. Iwase, Y. Show, K. Koyama, S. Sato, S. Nozaki, and H. Morisaki, *Raman Spectroscopy of Germanium Films Deposited with Cluster-Beam Technique*, Physica B Condens. Matter **219–220**, 535 (1996).

[144] D. Jung, J. Faucher, S. Mukherjee, A. Akey, D. J. Ironside, M. Cabral, X. Sang, J. Lebeau, S. R. Bank, T. Buonassisi, O. Moutanabbir, and M. L. Lee, *Highly Tensile-Strained Ge/InAlAs Nanocomposites*, Nat. Commun. **8**, 14204 (2017).

[145] P. Alfaro-Calderón, M. Cruz-Irisson, and C. Wang-Chen, *Theory of Raman Scattering by Phonons in Germanium Nanostructures*, Nanoscale Res. Lett. **3**, 55 (2007).

[146] A. K. Raychaudhuri, *Instabilities in Focused Ion-Beam-Patterned Nanostructures*, in *FIB Nanostructures*, edited by Z. M. Wang (Springer International Publishing, 2013), pp. 435–463.

[147] G. Carter and V. Vishnyakov, *Roughening and Ripple Instabilities on Ion-Bombarded Si*, Physical Review B **54**, 17647 (1996).

[148] T. ul Islam and P. S. Gandhi, *Viscous Fingering in Multiport Hele Shaw Cell for Controlled Shaping of Fluids*, Sci. Rep. **7**, 1 (2017).

[149] H. T. Johnson, *Effects of Stress on Formation and Properties of Semiconductor Nanostructures*, in *Material Substructures in Complex Bodies*, edited by G. Capriz and P. M. Mariano (Elsevier Science Ltd, Oxford, 2007), pp. 284–313.

[150] A. Stukowski, *Visualization and Analysis of Atomistic Simulation Data with OVITO–the Open Visualization Tool*, Modelling Simul. Mater. Sci. Eng. **18**, 015012 (2009).

[151] E. Chang, K. Toula, and V. Ray, *Reconstructing Focused Ion Beam Current Density*

Profile by Iterative Simulation Methodology, Journal of Vacuum Science & Technology B, Nanotechnology and Microelectronics: Materials, Processing, Measurement, and Phenomena **34**, 06KO01 (2016).

[152] H. Luo, R. Jing, Y. Cui, H. Wang, and R. Wang, *Improvement of Fabrication Precision of Focused Ion Beam by Introducing Simultaneous Electron Beam*, Progress in Natural Science: Materials International **20**, 111 (2010).

[153] S. Tan, R. Livengood, Y. Greenzweig, Y. Drezner, and D. Shima, *Probe Current Distribution Characterization Technique for Focused Ion Beam*, Journal of Vacuum Science & Technology B, Nanotechnology and Microelectronics: Materials, Processing, Measurement, and Phenomena **30**, 06F606 (2012).

[154] L. Bischoff, R. Bottger, P. Philipp, and B. Schmidt, *Nanostructures by Mass-Separated FIB*, in *FIB Nanostructures*, edited by Z. M. Wang (Springer International Publishing, 2013), pp. 465–525.

[155] E. Maras, O. Trushin, A. Stukowski, T. Ala-Nissila, and H. Jónsson, *Global Transition Path Search for Dislocation Formation in Ge on Si(001)*, Comput Phys Commun **205**, 13 (2016).

[156] J. R. Parsons and C. W. Hoelke, *Crystallography of Hexagonal Germanium*, Nature **301**, 591 (1983).

[157] M. Okugawa, R. Nakamura, M. Ishimaru, H. Yasuda, and H. Numakura, *Thermal Crystallization of Sputter-Deposited Amorphous Ge Films: Competition of Diamond Cubic and Hexagonal Phases*, AIP Adv. **6**, 125035 (2016).

[158] L. Q. Huston, B. C. Johnson, B. Haberl, S. Wong, J. S. Williams, and J. E. Bradby, *Thermal Stability of Simple Tetragonal and Hexagonal Diamond Germanium*, J. Appl. Phys. **122**, 175108 (2017).

[159] T. T. Al-Housseiny and H. A. Stone, *Controlling Viscous Fingering in Tapered Hele-Shaw Cells*, Phys. Fluids **25**, 092102 (2013).

[160] A. Leshchiner, M. Thrasher, M. B. Mineev-Weinstein, and H. L. Swinney, *Harmonic Moment Dynamics in Laplacian Growth*, Phys. Rev. E **81**, 016206 (2010).

[161] R. Luo, Y. Chen, and S. Lee, *Particle-Induced Viscous Fingering: Review and Outlook*, Phys. Rev. Fluids **3**, 110502 (2018).

[162] R. Lu, C.-W. Ge, Y.-F. Zou, K. Zheng, D.-D. Wang, T.-F. Zhang, and L.-B. Luo, *A Localized Surface Plasmon Resonance and Light Confinement-Enhanced near-Infrared Light Photodetector*, Laser & Photonics Reviews **10**, 595 (2016).

Appendix A

Indexing SAD diffraction pattern in Figure 5.13(e):

The crystallographic plane identification was carried out for the mixed crystalline germanium phase below the nanostructures shown in the selected area electron diffraction (SAED) pattern (Figure 5.13(e)). First, the positions of diffraction dots were marked, as shown in Figure A.1. Then, the interplanar spacing values were measured and compared with calculated interplanar spacings for dc-Ge and hd-Ge, as shown in Table A.1.

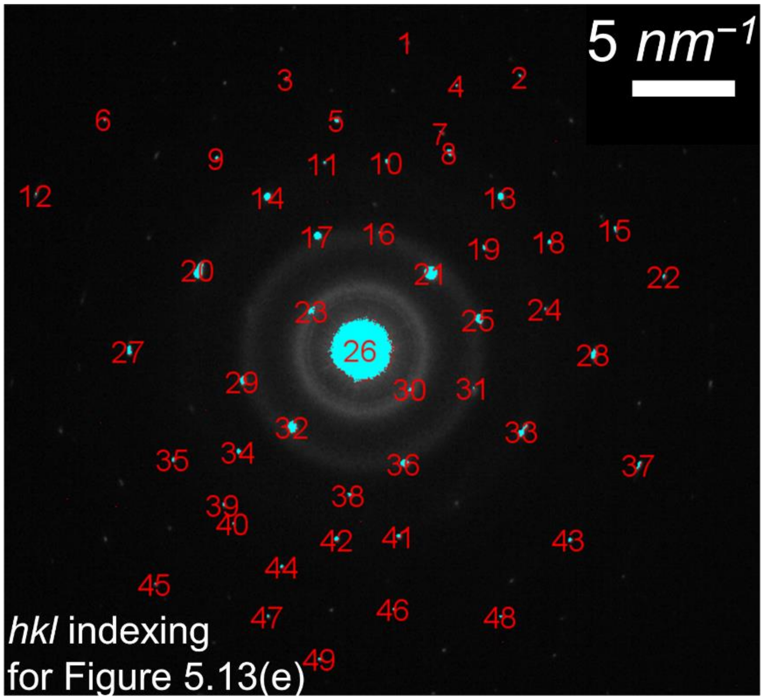
5 nm^{-1}
1
2
3
4
5
6
7
8
9
10
11
12
13
14
15
16
17
18
19
20
21
22
23
24
25
26
27
28
29
30
31
32
33
34
35
36
37
38
39
40
41
42
43
44
45
46
47
48
49
hkl indexing
for Figure 5.13(e)

Figure A.1 Diffraction spots in the electron diffraction pattern below the nanostructures (i.e., for the SAED pattern shown in Figure 5.13(e) of the main text). The numbering indicates the spots that are indexed in Table A.1.

The measured values of interplanar spacing were compared with the calculated d-spacing values of diamond cubic germanium (i.e., dc-Ge with a lattice constant a = 5.658 $Å$) and hexagonal diamond germanium (i.e., hd-Ge with lattice constants a = 3.94 $Å$ & c = 6.55

Å) [141], and are shown in Table A.1. There is an excellent agreement between the measured and calculated d-spacing values. Some of the interplanar spacings for dc-Ge and hd-Ge are very close, as can be observed from Table A.1, there are a significant number of diffraction spots that match with interplanar spacings from hd-Ge better than the closest interplanar spacings from dc-Ge. Hence, the existence of hd-Ge phase within the matrix of dc-Ge was identified to agree with the Raman spectroscopy and molecular dynamics studies.

Table A.1 Comparing the measured interplanar distances with calculated values for (*hkl*) indices of dc-Ge and hd-Ge. For any diffraction spot, if the calculated d-spacing values of both the phases match with the measured d-spacing value, then the closest interplanar distance is shown with red coloured indices.

Spot No.	Measured d (Å)	Calculated d (Å) / *(hkl)*		Spot No.	Measured d (Å)	Calculated d (Å) / *(hkl)*	
		dc-Ge	**hd-Ge**			**dc-Ge**	**hd-Ge**
1	0.686 ± 0.024	0.691(733)	-	25	1.751 ± 0.061	1.706(311)	-
2	0.673 ± 0.031	0.667(660)	-	27	0.916 ± 0.029	0.895(620)	0.909(312)
3	0.757 ± 0.017	0.756(642)	-	28	0.917 ± 0.029	0.895(620)	0.909(312)
4	0.759 ± 0.017	0.756(642)	-	29	1.739 ± 0.041	1.706(311)	-
5	0.920 ± 0.029	0.895(620)	0.909(312)	30	3.368 ± 0.086	-	3.412(100)
6	0.617 ± 0.061	0.653(751)	-	31	1.797 ± 0.060	-	-
7	0.920 ± 0.015	-	0.909(312)	32	2.049 ± 0.072	2.000(220)	-
8	0.986 ± 0.019	1.000(440)	0.985(220)	33	1.177 ± 0.045	1.155(422)	1.200(232)
9	0.886 ± 0.015	0.895(620)	-	34	1.333 ± 0.044	1.298(331)	1.289(210)
10	1.120 ± 0.023	-	1.137(300)	35	0.976 ± 0.019	-	0.985(220)
11	1.117 ± 0.023	-	1.137(300)	36	1.753 ± 0.061	1.706(311)	-
12	0.589 ± 0.092	0.653(751)	-	37	0.709 ± 0.025	0.707(800)	-
13	1.029 ± 0.039	1.000(440)	-	38	1.460 ± 0.066	1.414(400)	1.513(202)
14	1.185 ± 0.023	-	1.200(232)	39	1.027 ± 0.039	1.000(440)	-
15	0.757 ± 0.017	0.756(642)	-	40	0.984 ± 0.019	1.000(440)	0.985(220)
16	1.800 ± 0.059	-	-	41	1.119 ± 0.045	1.155(422)	1.137(300)
17	1.748 ± 0.061	1.706(311)	-	42	1.115 ± 0.045	1.155(422)	1.137(300)
18	0.983 ± 0.019	1.000(440)	0.985(220)	43	0.754 ± 0.017	0.756(642)	-
19	1.335 ± 0.043	1.706(311)		44	0.921 ± 0.029	0.895(620)	0.909(312)
20	1.177 ± 0.023	1.155(422)	1.200(232)	45	0.681 ± 0.024	0.691(733)	-
21	2.056 ± 0.072	2.000(220)	-	46	0.814 ± 0.025	0.817(444)	-
22	0.684 ± 0.024	0.691(733)	-	47	0.754 ± 0.017	0.756(642)	-
23	3.349 ± 0.086	3.267(111)	3.412(100)	48	0.708 ± 0.024	0.707(800)	-
24	1.129 ± 0.045	1.155(422)	1.137(300)	49	0.681 ± 0.024	0.691(733)	-

Publications

Journal Publications:

1. B. Kamaliya, R. G. Mote, M. Aslam, and J. Fu, "Enhanced Light Trapping by Focused Ion Beam (FIB) Induced Self-Organized Nanoripples on Germanium (100) Surface", APL Materials, Vol. 6, No. 3, 36106 (2018).
2. B. Kamaliya, R. G. Mote, M. Aslam, and J. Fu, "Improved Enhancement Factor for SERS Using Broad Ion Beam Induced Self-Organized Gold Nanocones", MRS Advances, Vol. 4, No. 11-12, 697-703 (2019).
3. B. Kamaliya, V. Garg, A. Liu, Y. Chen, M. Aslam, J. Fu, and R. G. Mote, "Tailoring Surface Self-Organization for Nanoscale Polygonal Morphology on Germanium", Advanced Materials, Vol. 33, No. 21, 2008668 (2021).

Conference Proceedings/Presentations:

1. B. Kamaliya, R.G. Mote, M. Aslam, and J. Fu, "Ion beam induced uniformly distributed self-organized Nano-cones on gold and silicon surfaces", in 4th International Conference on Nano Structuring by Ion Beam (ICNIB 2017), Devi Ahilya University, Indore during October 11-13, 2017.
2. B. Kamaliya, R.G. Mote, M. Aslam, and J. Fu, "Improved Enhancement Factor for SERS Using Broad Ion Beam Induced Self-Organized Gold Nanocones", 2018 MRS Fall Meeting, Boston, Massachusetts during November 25-30, 2018.
3. B. Kamaliya. V. Garg, R. G. Mote, M. Aslam and J. Fu, "Controlled Self-Organization on Germanium Using Focused Ion Beam (FIB): From Quasi-periodic Nanoripples to Well-ordered Periodic Nanostructures", Microscopy and Microanalysis, vol. 26, no. S2, pp. 1–4, 2010, M&M 2020, Milwaukee, WI, USA, August 3-8, 2020.

Cover art appeared as Frontispiece in Advanced Materials (21/2021):

- B. Kamaliya, V. Garg, A. Liu, E. Chen, M. Aslam, J. Fu, R. Mote, Hierarchical Structures: Tailoring Surface Self-Organization for Nanoscale Polygonal Morphology on Germanium, Advanced Materials, Vol. 33, No. 21, 2170164 (2021).

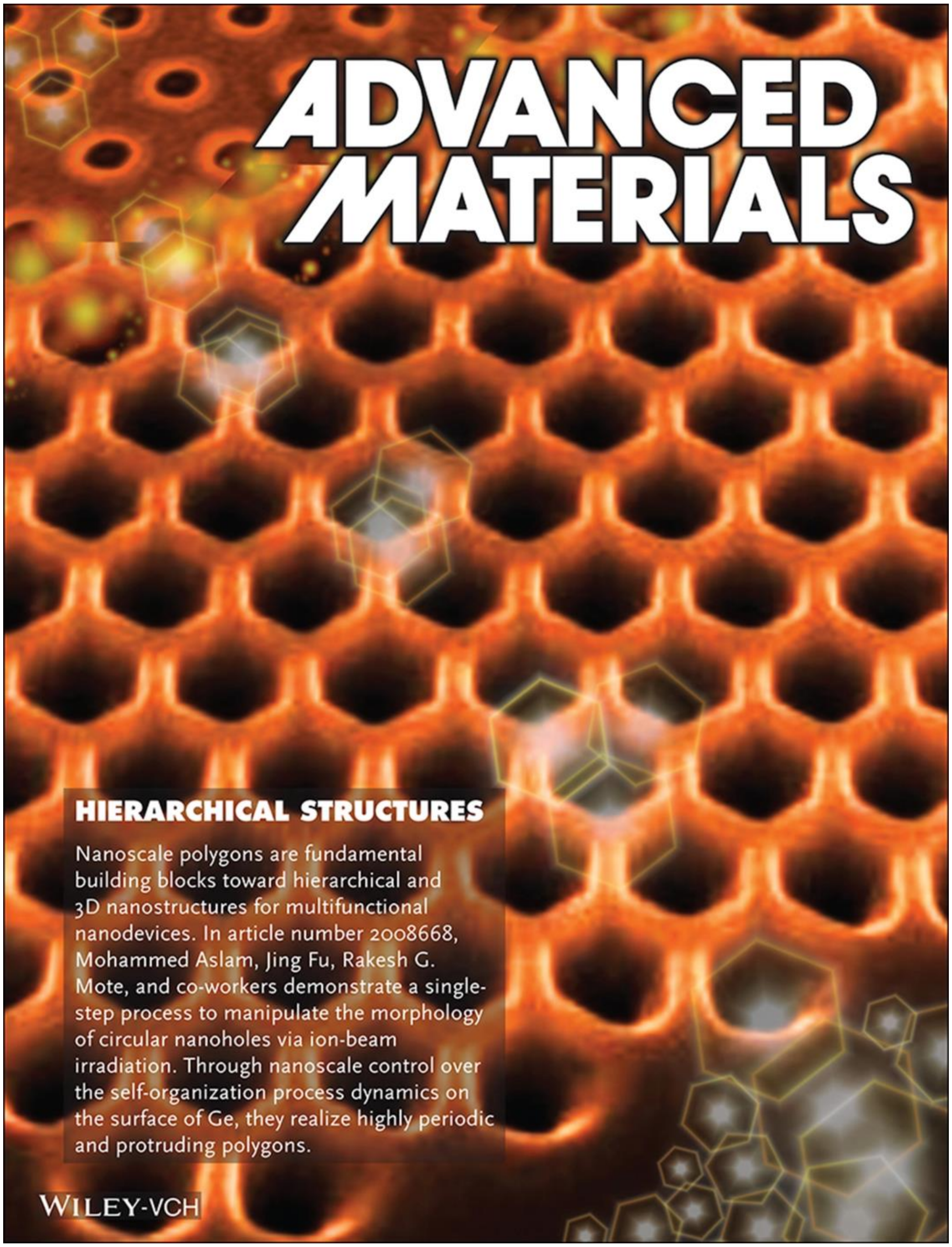

ADVANCED MATERIALS

HIERARCHICAL STRUCTURES

Nanoscale polygons are fundamental building blocks toward hierarchical and 3D nanostructures for multifunctional nanodevices. In article number 2008668, Mohammed Aslam, Jing Fu, Rakesh G. Mote, and co-workers demonstrate a single-step process to manipulate the morphology of circular nanoholes via ion-beam irradiation. Through nanoscale control over the self-organization process dynamics on the surface of Ge, they realize highly periodic and protruding polygons.

WILEY-VCH

Acknowledgements

With immense pleasure, I want to convey my sincere thanks to my supervisors, Prof. Rakesh G. Mote, Prof. Jing Fu and Prof. Mohammed Aslam, without whom this thesis would not have been possible, for their constant encouragement and guidance towards the completion of my research work. I am grateful to Prof. Mote, for always showing faith and confidence in me with immense support and for his rigorous involvement in my research project. I am thankful to Prof. Aslam and Prof. Jing, for their help and involvement in my PhD studies. I express my gratitude to all my supervisors for giving me this opportunity to work in their research group. Their excellent guidance with enthusiasm and critical assessment has been a driving force to accomplish in the best possible way. I thank Prof. Mohammed Aslam for extending his support towards my enrolment in the Department of Physics. I thank Prof. Jing for his encouragement and financial support during the extension of my Monash stay, which was crucial to finish the vital experimental work needed to complete this dissertation.

I convey my sincere thanks to research progress committee members Prof. Pradeep Dixit, Prof. Shankar Sharma V. Tatiparti, and Prof. Wenyi Yan for their valuable feedback and assessment. I thank Prof. Ajay Panwar for teaching the molecular dynamics simulations and for valuable discussions. I am thankful to Prof. Saurabh Lodha for providing germanium wafer samples during the commencement of my research work. I am grateful to Prof. Ramesh Singh for providing access to the lab facilities at Machine Tools Lab (MTL).

I thank Dr. Amelia Liu, Monash Centre for Electron Microscopy (MCEM), for FIB training and her involvement in the interpretations of TEM results. I thank Dr. Emily Chen and Mr. Nicholas McDougall, MCEM, for their help in TEM measurements. I am thankful to Dr. Peter Miller, Dr. Xiya Fang, Dr. Zhou Xu (Ben), Dr. Renji Pan, and all MCEM staff for their outstanding support. I thank Dr. Hemayat Uddin, Dr. Fatima Eftekhari and Dr. Guangyuan Si, for their help on the facilities at Melbourne Centre for Nanofabrication (MCN). I am thankful to Dr. Finlay Shank, School of Chemistry, for his help on Raman and UV visible spectroscopy. I am thankful to all the members of project staff, teaching assistants of Centre of Excellence in Nanoelectronics (CEN), Sophisticated Analytical Instrument Facility

(SAIF), Centre for Research in Nanotechnology & Science (CRNTS), and Metallurgical Engineering & Materials Science (MEMS) at IIT Bombay for their help in the experiments.

I thank IITB-Monash Research Academy, for giving me this outstanding opportunity and for the financial support. I acknowledge the financial assistance received from the Vice-Chancellor's International Inter-Campus PhD Travel Grant during my extended stay at the Monash. I am thankful to the staff at IITB Monash Research Academy, IIT Bombay, and Monash University, for their immense support during my PhD studies. I convey my sincere thanks to Prof. Murali Sastry and Mr. M. S. Unnikrishnan for the support and access to the facilities during my tenure. I am grateful to Dr. Kyatanahali Nagabhushana, Mr. Adrian Gertler, Mrs. Kuheli Banerjee, Mrs. Jayasree Narayanan, Mrs. Laya Vijayan, Mrs. Beena Pillai, Mr. Kiran More, Mrs. Nancy Sowho, Mr. Stelios Konstantinidis, Ms. Fiona Pyrczak, Mr. Shripal Singh, Mr. Ashok Gonaka, Mr. Nilesh Ghule, and others for helping through the administrative formalities including paperwork, approvals, etc.

I take this opportunity to thank my wonderful friends and colleagues, whom I was privileged to meet, for playing a vital role throughout my tenure. I am grateful to acknowledge the crucial part of Vivek Garg for his generous support and invaluable inputs. I express my gratitude to my lab mates and friends Mayur Darak, Anandita Singh, Mukesh Tak, Ganesan G., Mrinmoy Roy, Bhawna, Salman Siddiqui, Manoj Jangid, Yeonuk Kim, Shuo Zhang, Shi Qiu, Sagar Agnihotri, Laxman Malla, Abhishek Mukherjee, Nisha Chhikara, Chitresh B., Palak Garg, Anchal Yadav, Abin Varghese, Arif Ibrahim, Uzma Memon, Anurag Ladage, Himanshu S., and Tanesh Gamot for their help in many ways.

Last but foremost, I thank and appreciate my mother, siblings, and all the family members for their absolute support, love, and care during my studies. I thank my amazing nephews and nieces, for often visiting me during my campus stay and for making my vacation trips memorable. I wish to thank my ex-wife, Reema, for her support and considerations during my PhD journey. I take this occasion to offer special gratitude and highest regards to my father, who, although no longer with us, remains inspiring by his example and dedication.

– Bhaveshkumar Kamaliya